Elucidating Interactions within Photoautotroph-Methanotroph Cocultures at Both Systems and Molecular Levels

by

Kiumars Badr

A dissertation submitted to the Graduate Faculty of
Auburn University
in partial fulfillment of the
requirements for the Degree of
Doctor of Philosophy

Auburn, Alabama
August 7, 2021

Keywords: Photoautotroph, Methanotroph, Cocultures, Biogas Conversion, Kinetic Models, Genome-Scale Models

Approved by

Jin Wang, Chair, Walt and Virginia Woltosz Endowed Professor of Chemical Engineering
Q. Peter He, Co-chair, Associate Professor of Chemical Engineering
Andrew Adamczyk, Assistant Professor of Chemical Engineering
Alexander Beliaev, Biologist (Team Lead), Pacific Northwest National Laboratory
Marina Kalyuzhnaya, Associate Professor of Biology, San Diego State University
Evert Duin, Professor of Chemistry and Biochemistry

Abstract

In the US, the biogas produced from anaerobic digestion (AD) of industrial, municipal and agricultural waste streams has a great potential as a renewable feedstock. To tap into the immense biogas potential while reducing greenhouse gas (GHG) emissions, effective biotechnologies such as methanotroph-photoautotroph (M-P) coculture that can operate at ambient pressure and temperature without requiring biogas cleaning/upgrading are urgently needed. Although it has been recognized that microbial communities offer a number of advantages over monocultures, the utilization of microbial communities for biotechnological applications have been limited. This work aims to help change that by developing effective experimental and computational tools to enable the exploration of interactions in microbial communities.

This study investigates and addresses the following major challenges in developing an M-P coculture-based biotechnology: (1) lack of experimental and computational tools to efficiently and accurately characterize the coculture in real-time; (2) lack of tools and methodologies in determining largely unknown interspecies dependencies and their contributions among the species; (3) lack of understanding and modeling strategies to quantitatively characterize the highly complex dynamics of the coculture cells and their metabolic interactions over time, which hinders the design and scale-up of M-P photobioreactors, as well as the optimization and control of operation conditions.

In this work, the advantages of the M-P coculture over sequential photoautotroph and methanotroph single cultures for biogas conversion are investigated. An experimental-computational protocol is proposed for fast, easy and accurate quantitative characterization of M-P cocultures. A semi-structured kinetic model is proposed that can accurately predict the coculture growth under a wide range of cultivation conditions. A genome-scale metabolic network model

(GEM) is employed to develop steady-state M-P coculture models, to postulate potential molecular interactions responsible for the enhanced growth observed in the coculture. The kinetic model and coculture GEM model were utilized to develop a dynamic GEM model that can determine the metabolic flux profile and contribution of mutualistic interactions over time.

Acknowledgments

First, I would like to thank God. I consider myself to be truly blessed to have pursued and obtained my PhD from Auburn.

I would like to express my sincere and immeasurable appreciation for my advisor, Dr. Jin Wang, for supporting and believing me during these past five years. She held me to a standard much higher than I imagined for myself. Thank you for your motivation, your immense knowledge, and your hard questioning that made me a better researcher and tougher person. Her guidance and support helped me in all the time of research and writing of this thesis. I could not have imagined having a better advisor and mentor for my PhD study. I also want to thank Dr. Peter He for patiently listening and kindly guiding me with his thoughtful and delicate observation on my research that enabled me to understand the research from different perspectives. Beside my advisor and co-advisor, I would like to thank the rest of my committee members Dr. Marina Kalyuzhnaya, Dr. Alexander Beliaev, Dr. Andrew Adamczyk and Dr. Evert Duin for their encouragement, insightful comments, and assistance in completing this work.

I owe many thanks to my current and former group members who have served many roles including teachers, assistants, and most importantly, friends. I especially would like to thank Dr. Matthew Hilliard (my teacher in computational work, my assistant in experimental work and my best friend); Dr. Devarshi Shah (my teacher in computational work, my friend with countless conversations both work and non-work related), Dr. Kyle Stone (my teacher in experimental work, my friend and senior member of our group); and Dr. Nathan Roberts (my teacher any time I needed him). I am also thankful for my fellow graduate students and life-long friends, Dr. Iman Hassani who motivated me to start the graduate school journey and always was there for me; Morgan, Kirby, William and Kian who have helped my experience at Auburn to be

pleasant and memorable; and thank all of my friends for your encouragement, support, and off-campus gatherings that were a source of solace throughout graduate school, and each of you will hold a special place in my heart forever.

Finally, I am greatly indebted to my family and friends who have been unwavering in their spiritual, emotional, and physical support throughout this endeavor. I am truly thankful for my parents, Jamshid and Mehraz, and my siblings, Mitra and Amin, for inspiring me and always believing in me throughout the difficult times. I wouldn't be where I am today without them.

Table of Contents

List of Tables

List of Figures

List of Abbreviations

AD	Anaerobic digestion
ATP	Adenosine triphosphate
cFBA	community flux balance analysis
CHP	Combined heat and power
COD	Chemical oxygen demand
E-C	Experimental-computational
EPA	Environmental Protection Agency
FAO	Food and Agriculture organization
FBA	Flux balance analysis
FOG	Fats, oils and grease
GC	Gas chromatograph
gDCW	gram dry cell weight
GEM	Genome-Scale Metabolic
GHGs	Greenhouse gases
HTL	Hydrothermal liquefaction
MGD	Million gallons per day
MSE	Mean squared error
NADPH	Nicotinamide adenine dinucleotide phosphate
NETs	Negative emissions technologies
OD	Optical density
oxyPPP	oxidative pentose phosphate pathway

P:M	Photoautotroph:Methanotroph Ratio
PAR	Photosynthetically active radiation
PCA	Principal Component Analysis
PhPP	Phenotype Phase Plane Analysis
SCP	Single cell protein
SID	System Identification
TCA	tri-carboxylic acid cycle
TIC	Total inorganic carbon
TOC	Total organic carbon
VOC	Volatile organic acids
WRRF	Water resource recovery facility
WWTP	Wastewater treatment plant

Chapter 1: Introduction

1.1 Greenhouse gases and its environmental impact

Greenhouse gases (GHGs) in the atmosphere have an important influence on the climate of our planet. Simply stated, GHGs impede the outward flow of infrared radiation more effectively than they impede incoming solar radiation. Because of this asymmetry, the earth, its atmosphere, and its oceans are warmer than they would be in the absence of such gases [1].

The major GHGs are water vapor, carbon dioxide (CO_2), methane (CH_4), and nitrous oxide (N_2O). Without the naturally occurring GHGs (primarily water vapor and CO_2), the earth's average temperature would be about 33°C (59°F) colder than it is [2], and the planet would be much less suitable for human habitation. The possible warming due to increased concentrations of these gases is called "greenhouse warming." An overview of U.S. GHGs emissions is shown in **Figure 1** [3].

While CO_2 emissions come from a variety of natural sources, human-related emissions are responsible for the increase that has occurred in the atmosphere since the industrial revolution [4]. The main human activity that emits CO_2 is the combustion of fossil fuels (coal, natural gas, and oil) for energy and transportation, although certain industrial processes and land-use changes also emit CO_2. The main sources of CO_2 emissions in the United States are shown in **Figure 2**a. CO_2 is constantly being exchanged among the atmosphere, ocean, and land surface as it is both produced and absorbed by many microorganisms, plants, and animals. However, emissions and removal of CO_2 by these natural processes tend to balance, absent anthropogenic impacts [5].

In 2019, CH_4 accounted for about 10 percent of all U.S. GHG emissions from human activities [6]. Methane's lifetime in the atmosphere is much shorter than CO_2, but CH_4 is more efficient at trapping radiation than CO_2 [6]. Pound for pound, the comparative impact of CH_4 is 25 times greater than CO_2 over a 100-year period [7].

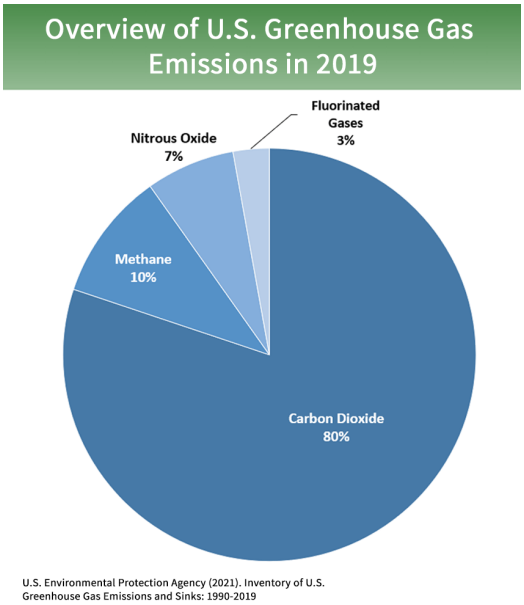

Figure 1. Total U.S. Emissions in 2019 = 6,558 Million Metric Tons of CO_2 equivalent (excludes land sector). Percentages may not add up to 100% due to independent rounding [3].

CH_4 is emitted from energy, industry, agriculture, land use, and waste management activities, are shown in **Figure 2**b. Domestic livestock such as cattle, swine, sheep, and goats produce CH_4 as part of their normal digestive process. These animals have a fore-stomach (or rumen) containing microbes called methanogens, which are capable of digesting coarse plant material and which produce methane as a by-product of digestion (enteric fermentation): this methane is released to the atmosphere by the animal belching [8]. Also, when animal manure is stored or managed in lagoons or holding tanks, CH_4 is produced [6]. Natural gas and petroleum systems are the second largest source of CH_4 emissions in the United States. CH_4 is generated in landfills as waste decomposes and in the treatment of wastewater. Landfills are the third-largest source of CH_4 emissions in the United States [9]. CH_4 is also generated from domestic and industrial wastewater treatment and from composting and anerobic digestion. CH_4 is also emitted

from several natural sources. Natural wetlands are the largest source, emitting CH_4 from bacteria that decompose organic materials in the absence of oxygen [6].

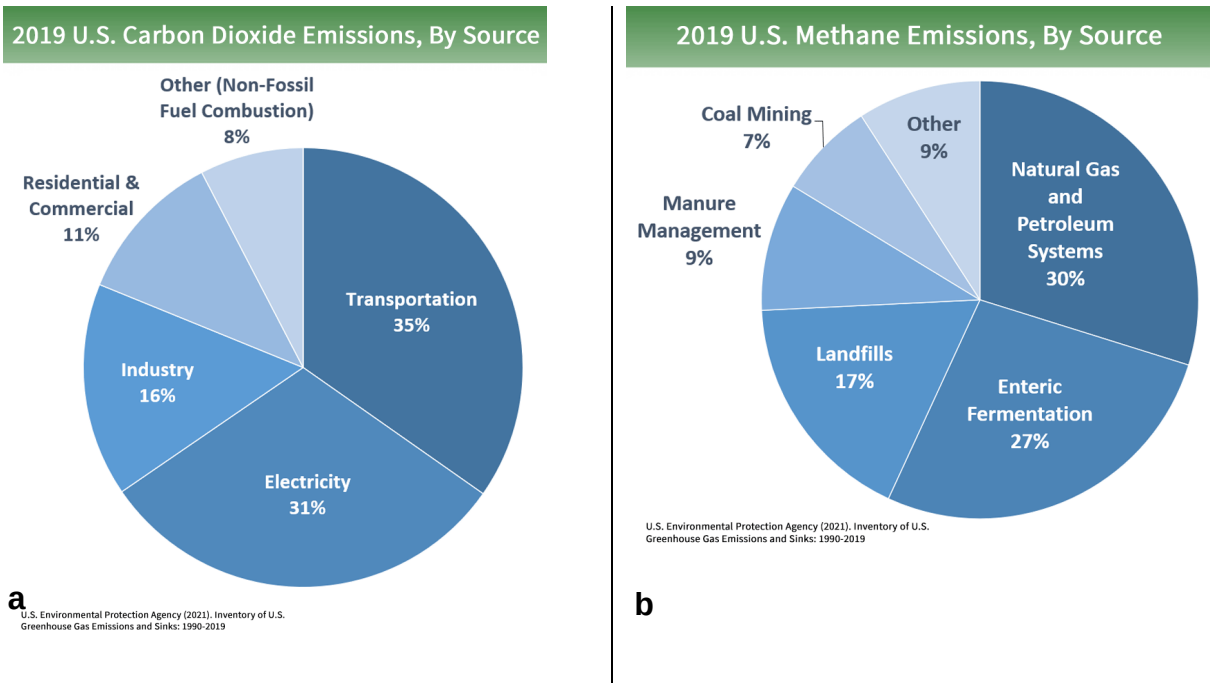

Figure 2. Source of U.S. (a) CO_2 and (b) CH_4 emissions in 2019. All emission estimates from the *Inventory of U.S. GHG Emissions and Sinks: 1990–2019* (excludes land sector) [3].

1.1.1 Impacts of climate change

Climate change will have many kinds of impacts. Climate change will affect ecosystems and human systems—such as agricultural, transportation, and health infrastructure—in ways we are only beginning to understand (see **Figure 3**). There will be positive and negative impacts of climate change, even within a single region. For example, warmer temperatures may bring longer growing seasons in some regions, benefiting those farmers who can adapt to the new conditions but potentially harming native plant and animal species [10]. In general, the larger and faster the changes in climate are, the more difficult it will be for human and natural systems to adapt [10].

Unfortunately, the regions that will be most severely affected are often the regions that are the least able to adapt.

Developed nations, including the United States, also will be affected. For example, most models indicate that snowpack is likely to decline on many mountain ranges in the West, which would bring adverse impacts on fish populations, hydropower, water recreation, and water availability for agricultural, industrial, and residential use [11]. However, wealthy nations have a better chance of using science and technology to anticipate and adapt to sea level rise, threats to agriculture, and other climate impacts.

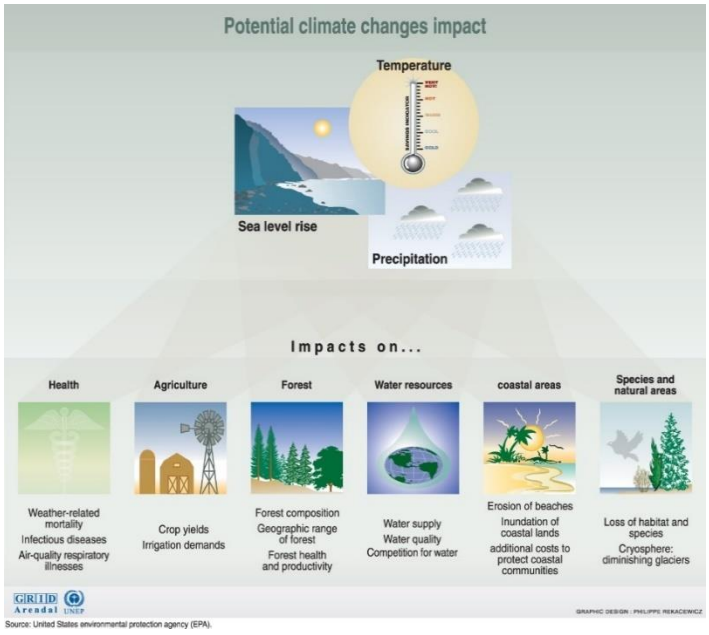

Figure 3. Climate changes could have potentially wide-ranging effects on both the natural environment and human activities and economies. Source: U.S. Environmental Protection Agency [12].

Polar regions are already experiencing major changes in climate. Like the proverbial canary in the coal mine, changes in the polar regions can be an early warning of things to come for the rest of the planet, and the environmental changes now being witnessed at higher latitudes are

alarming. For example, Arctic Sea ice cover is decreasing rapidly, and glaciers are retreating and thinning. NASA data show that Arctic Sea ice shrunk to a new record low in 2007 [13]; 24 percent lower than the previous record (2005), and 40 percent lower than the long-term average [13].

A number of ecosystem changes, such as plants flowering earlier in the year and declines in animal species that depend on sea ice for habitat, have been attributed to the strong warming observed at northern latitudes [14]. Changing climate is also having human impacts: some Alaskan villages have been moved to higher ground in response to increasing storm damage, and the thawing of permafrost is undermining infrastructure, affecting houses, roads, and pipelines in northern communities around the world [14].

1.1.2 Reducing GHGs Emissions

Most climate and integrated assessment models project that the concentration of atmospheric CO_2 would have to stop increasing (and perhaps start decreasing) by the second half of the century for there to be a reasonable chance of limiting warming and the associated dangerous climate impacts. The focus of climate mitigation is to reduce energy sector emissions by 80-100 percent, requiring massive deployment of low-carbon technologies between now and 2050 [15]. Most climate mitigation technologies are intended to decrease the rate at which we take additional carbon from fossil fuel reservoirs and ecosystems and add it to the atmosphere as CO_2. These include renewable electricity, increased energy efficiency, and carbon capture and storage of emissions from fossil power plants [16].

Progress toward these targets could be made by deploying negative emissions technologies (NETs), which remove carbon from the atmosphere and sequester it [15]. Under the present conditions, where fossil CO_2 is continuously added to the atmosphere, removing CO_2 from the atmosphere and storing it has exactly the same impact on the atmosphere and climate as

simultaneously preventing emission of an equal amount of CO_2 [15]. These negative emissions technologies, or NETs, have received much less attention by researchers than traditional mitigation technologies. NETs have been part of the portfolio to achieve net emissions reductions, at least since reforestation, afforestation, and soil sequestration were brought into the United Nations Framework Convention on Climate Change, albeit as mitigation options, more than two decades ago. Recent analyses found that deploying NETs may be less expensive and less disruptive than reducing some emissions, such as a substantial portion of agricultural and land-use emissions and some transportation emissions [15].

Using biological processes to increase carbon stocks in microorganism, forests, and wetlands is the first way to mitigate GHGs, and then the second way is production of energy from biomass, while capturing and storing the resulting CO_2 emissions. Third, using chemical processes to capture CO_2 directly from the air and then sequester it in geologic reservoirs, and forth, enhancing geologic processes that capture CO_2 from the atmosphere and permanently bind it with rocks. In this work, we satisfy first two ways of GHGs mitigation by using a novel coculture system. Since source of GHGs are broad and different, our group focus on biogas, specifically the biogas produced from anaerobic digestions of waste treatment facilities.

1.2 Immense potential of biogas- products and challenges

1.2.1 Biogas production

Here is an overview of the proposed biotechnology in capturing biogas and producing high value fuels and chemicals (**Figure 4**).

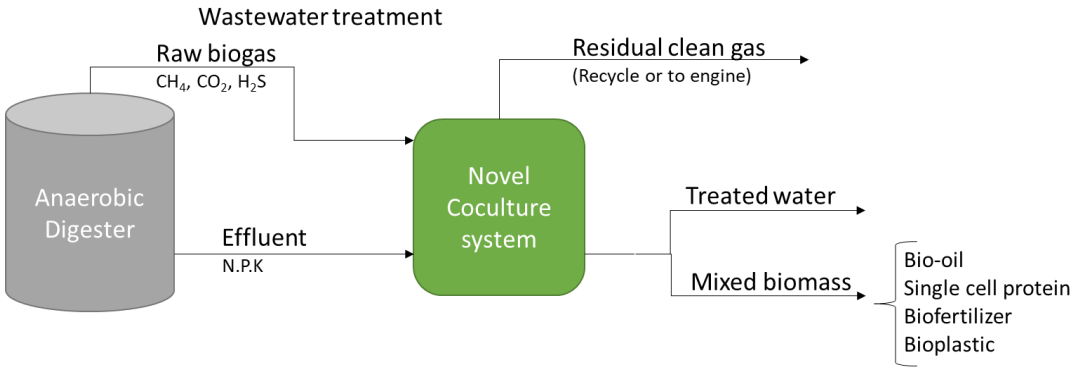

Figure 4. An overview of biotechnology (the coculture system) in wastewater treatment industry

Biogas is a renewable and valuable energy resource as a byproduct of anaerobic digestion. Anaerobic digestion is a series of biological processes in which microorganisms digest plant and/or animal material in sealed containers, producing biogas, which is a mixture of CH_4, CO_2 and other gases. The organic material left over, known as digestate, is rich in organic matter and nutrients such as nitrogen, phosphate and potash. Typically, biogas contains 50-70% CH_4 and 30-50% CO_2 and the ratio of these two gases in biogas depends on the substrate, operating conditions and pH among other factors [17]. At water resource recovery facilities (WRRFs), the anaerobic digester substrate usually comprises of the sludge from the primary settling basin as well as waste activated sludge from the secondary clarifier tanks. However, co-digestion of organic wastes with sludge is applied as a strategy for increasing the digester gas production and yield [18]. Fats, oil and grease (FOG) is a lipid-rich organic waste that that is currently utilized in numerous WRRFs across the United States. As a result, biogas production at WRRFs will benefit from improved efficiency and conversion of waste to energy. This energy may be used in many different ways.

1.2.2 Biogas utilization and challenges

1.3 Co-culture biomass as feedstock for valuable products

Photoautotrophs and methanotrophs have immense potential as renewable feedstocks - the microbial biomass can be used for producing a variety of products. Under different operating conditions, both photoautotrophs and methanotrophs can accumulate various energy compounds (carbohydrates, proteins and lipids) to use as feed, other products and especially for energy products as biofuels.

1.3.1 Biofuel potential

The limited supply of fossil fuel as well as its negative effects on the environment (contribution to global warming) has led to the reduction of fossil fuels for energy. Consequently, balancing the increasing global energy demand while decreasing use of traditional fossil fuel has prompted continued research into alternative fuels from sustainable feedstock. Photoautotroph has attracted significant interest to the scientific community as a renewable resource of energetic compounds (carbohydrates, lipids) which can be converted to biofuels [29]. Biofuels consist of biodiesel, bio-oil or bioethanol. First generation biofuels are acquired from crops. Three major challenges of first-generation biofuels are: 1-reduced human food production, 2-increased use of arable land and 3-environmental damage [29].

Second generation biofuels utilized non-crop feedstocks such as agricultural and forest residue, grass and waste oil; however, its production has is not profitable as it requires expensive technology. Third generation biofuels are promising in overcoming the challenges posed by 1st and ^{2nd} generation biofuels [30,31]. Advantages of third generation biofuels include:

1. Rapid growth rate of photoautotroph as compared to plants as feedstock

2. Cultivation of photoautotroph on various waste nutrient sources promotes bioremediation through efficient removal of mainly inorganic N and P.

3. Higher photosynthetic efficiencies (4-5%) can be reached as compared to plant (1-2%) [29].

1.3.1.1 Bioethanol

Photoautotroph contains carbohydrates that serve as the feedstock for fermentative bioethanol production. Carbohydrates are present in microalgae and cyanobacteria as either stored (glycogen, starch) or as a structural component of the cell wall (cellulose, sulphated polysaccharides). Different physical (bead milling, freeing, agitation, high pressure homogenization), chemical (acidic or alkaline hydrolysis), and enzymatic pretreatments are required to release the carbohydrate content. It is important to note that the lack of lignin in microalgae requires less harsh pretreatment as compared to 1st generation bioethanol. Then microalgal biomass is hydrolyzed to convert polymeric carbohydrate to glucose (most abundant monomeric sugar) for subsequent fermentation by yeast or bacteria. Low carbohydrate content in photoautotroph will not favor economic production of bioethanol; thus, there are increasing efforts to enhance and optimize the carbohydrate content of photoautotroph cells through manipulation of the culture conditions (irradiance, temperature, CO_2 supply, pH and nutrients) [29,32,33]. Some of the challenges of third generation bioethanol are dewatering algae culture, pretreating biomass for releasing carbohydrates, and optimizing the fermentation process.

1.3.1.2 Bio-oil

Photoautotroph biomass have gained ground as feedstock for high-value biofuels due to their energy-rich biomolecules (carbohydrate, protein and lipids). However, high nutrient cost coupled with the use of limited freshwater sources pose significant challenges for commercial

application. The AD effluent and biogas produced at WRRFs is a convenient and sustainable source of essential nutrients (nitrogen, phosphorus and trace metals) and carbon substrate (CO_2) required for high growth rates and biomass production. The significant advantages offered through this approach are 1) reduction in environmental pollution by capturing the nutrients and 2) low-cost biomass production which can be used for production bioenergy such as biofuels. However, the energy and cost-intensive downstream processing of microalgal biomass for biodiesel production is a major drawback for the economic feasibility of converting microalgae to biofuels. Producing biodiesel from lipids by the conventional transesterification process is energy intensive as the biomass has to be dried and the residual biomass containing proteins and carbohydrates are not utilized [34]. The traditional transesterification process also utilizes hazardous organic solvents [35] which can increase operating costs. Furthermore, acquiring high lipid content of photoautotroph is usually stimulated by nutrient depletion which in turn would affect photoautotroph growth rates and biomass productivity. In order to address these shortcomings, researchers are focusing on converting photoautotroph biomass to biofuels through hydrothermal liquefaction (HTL). HTL greatly reduces the energy input as wet biomass can be directly converted to biocrude and all components of the biomass can be converted to biocrude. HTL is more ecofriendly as it does not involve harmful solvents for oil extraction. Thus, integration of the methanotroph- photoautotroph co-culture for bioconversion of wastewater treatment to biocrude can yield significant economic and environmental benefits while addressing the shortfalls of the microbial biomass to biodiesel process.

1.3.2 Single cell protein

Global consumption demands of animal-derived protein is predicted to require 1,250 million tons of meat and dairy to be produced annually by 2050 [36]. However, increasing meat

production faces the major limitation of low feed conversion ratio by beef, pork and poultry [36,37]. Additionally, meeting increased protein demands from plant-based sources such as bean will be limited by the arable land and water requirements. Seafood, wild-catch and aquaculture is reported as the largest animal protein industry in the world and over the past two decades the largest increase in animal protein sectors results from aquaculture. By lowering the feed production cost, aquaculture has the potential to become more a sustainable animal protein industry towards meeting global protein demands.

Single cell protein (SCP) is protein produced by microbial cells and has been investigated for decades for enhancing protein content in animal feed. Especially when waste side streams of carbon and nutrients are valorized, and arable land is not required [38]. By weight percent, the protein in meat, milk and soybean are about 45%, 25% and 35%, respectively [36]. Various microorganisms identified as suitable for SCP are algae (cyanobacteria and microalgae), bacteria (methanotrophs) and yeast (Candid, Saccharomyces, etc.) amongst others. Vitamin, amino acid, fat and high protein content [36,38] of these microorganisms make them attractive at animal feed supplement. Advantages of SCP processes over conventional plant and animal sources of protein include higher efficiency in substrate conversion and high productivity derived from fast growth rate of microorganisms. In addition, these microorganisms afford the ability to utilize carbon from waste feedstocks originating from agricultural, municipal and industrial sources while recovering harmful pollutants. For example, agricultural and municipal waste streams have been increasingly investigated as a cheap and economical medium for methanotrophic bacteria, yeast and microalgae cultivation with intended use as single cell protein [36]. This approach is intended to produce SCP more economically while utilizing the microorganism for bioremediation. The gaseous carbon (CO_2, CH_4) from waste gas streams of anaerobic digesters serves as substrate for photoautotroph

and methanotrophic bacteria eliminating the threat of release of GHGs. Organic compounds in wastewater have also demonstrated the potential for promoting microalgal growth. Furthermore, photoautotroph and methanotrophic bacteria are capable of reducing pollutants by assimilating nitrogen, phosphorus and COD from wastewater effluents [24,39]. Conversely, the SCP process has a principal disadvantage of high nucleic acid content which can cause health disorders [36,38] such as kidney and bladder stones in long-lived animals. Any use in short-lived animals requires further processing [40]. Secondly, animal feed supplemented with SCP originating from waste feedstock substrates may introduce toxic and carcinogenic compounds into animal feed. Extensive testing of SCP products is performed before being marketed for animal feed [36,40]. Photoautotroph can survive in high concentrations of heavy metals whereas excessive concentrations of heavy metals can be detrimental to animals. Another challenge is the technical and economic cost of harvesting microorganisms cultivated for SCP. Lastly, wide-spread commercial application of SCP from wastewater treatment will heavily rely on addressing production cost by reducing downstream product modification and separation processes.

1.3.3 Biofertilizers

Microalgae and cyanobacteria have gained interest for use as biofertilizers since research in the last few decades have indicated that these microbes are of significant agricultural importance. Of the various type of biofertilizers, algal-derived biofertilizers have demonstrated considerable benefits such as contributing to the improvements in crop yields, plant growth and soil quality as a result of the stimulation of soil microbial interactions [41]. These interactions aid in plant growth by improving soil nitrogen, secretion of essential metabolites and organic carbon, mineralization, release of macro and micro-nutrients and production of growth hormones [42,43]. Nitrogen-fixing cyanobacteria has shown to enhance the N availability in the soil especially as

they do not compete with plants for their N demand. Swarnalakshmi et al. 2013 has reported a reduction in chemical fertilizer use when algal cells were inoculated in soil of wheat crop [44]. Excessive nitrogen in soil creates an environmental concern of leaching; however, as compared to chemical fertilizer, excessive N is biologically fixed to the soil in complex chemical forms. Consequently, leaching through biofertilizers is thought to be low as leaching is only increased after release of inorganic forms of N [41].

Another contribution of microalgae- and cyanobacterial-based biofertilization is mineralization and solubilization of macro- and micro-nutrients that can improve plant growth [45]. Photoautotroph can also secrete siderophores which are organic compounds that help chelate iron or copper such that they are made available to plants and other microbes. Furthermore, there are reports of increased micronutrients (Fe, Mn, Cu, and Zn) in plants when a consortia including microalgae, bacteria and cyanobacteria was used [46].

Photoautotroph also has the potential to secrete phytohormones (growth hormones) which can play critical roles in the development of plants. Various hormones such as cytokinin and auxin are reportedly produced intracellularly in green microalgae and some strains can also excrete hormones in the cell broth [47,48]. Besides microalgae, methanotrophs may also play a role in plant growth by shaping bacterial communities in paddy rice root [49]. Therefore, utilization of photoautotrophs and methanotrophs as biofertilizer can be a good agronomic practice for stimulating plant growth and crop yield.

Cultivation of photoautotroph and methanotrophic bacteria for biofertilizer require large amounts of nutrients. As growth media can be a large fraction of production costs, utilization of wastewater as low-cost medium is critical for improving economic viability. As discussed in earlier sections, municipal wastewater effluents can contain macronutrients (N, P, K) as well as micronutrients (Fe,

Cu, Mn, Zn) required for good growth of algae and methanotrophic bacteria. By this approach, both wastewater treatment and biomass production can be achieved. However, use of wastewater as cultivation media pose potential challenges. Municipal wastewater contains heavy metals that can accumulate in photoautotroph and hinder its use as fertilizer. Besides, biomass production on unsterilized wastewater effluents is the most economically viable method, but there is the risk of transferring viruses and other potentially harmful bacteria to crops and plants. The use of algal and methanotrophic fertilizer cultivated on wastewater for crop and vegetable fertilizer will depend on the source of the wastewater and the quality of biomass produced. Thus, growth of the co-culture on appropriate wastewater effluents has the potential to be used as an environmentally friendly biofertilizer when the biomass produced meets the biomass feedstock quality requirements. Lastly, co-culture biomass as biofertilizer can also reduce GHG emissions through methanotrophic CH_4 oxidation and microalgal CO_2 bio fixation. Also, the production of chemical fertilizer is an energy intensive process that result in GHG emissions. Thus, increasing biofertilizer use will also reduce GHG emissions from chemical-based fertilizers.

1.3.4 Bioplastics

The world-wide demand for petroleum-based plastics is increasing as a variety of consumer products utilize these plastics due to their strength, low weight and resistance to degradation by water, light and chemicals [50]. While these properties make plastics attractive and suitable for use in numerous applications and products, petroleum-based plastics have raised both economic and environmental concerns. Polystyrene is a widely used plastic, but its production is an energy costly process and the use of crude oil as a conventional plastic feedstock consumes an already diminishing resource. Further, the resistance to degradation by petroleum-based plastics increase

the amount of solid waste that has to be managed by landfills and waste generated by resin production can cause air and water pollution [50].

To meet increasing plastic consumption demands in a sustainable manner, bioplastics from natural feedstocks offer an alternative to conventional plastics. Starch and cellulose derived from corn, wheat, oil seeds have been used as a feedstock for bioplastics [51]. Also, proteins in crops (e.g. soybean and sunflower) also serves as a base material for bioplastics [52]. A major limitation of crop-derived bioplastics is the competition of these crops for food and feed. Furthermore, these crops require time to grow, arable land, water and fertilizer to produce sufficient amounts the crop biomass necessary for offsetting petroleum-based plastic feedstocks.

In recent years, microalgae have presented as an attractive, alternative for bioplastics feedstock. Microalgae biomass can reach relatively high fractions of protein (30-70%) that render them suitable for use in bioplastics. Some of the advantages of microalgal feedstock for bioplastics include rapid microalgal growth in comparison to terrestrial crops, elimination competition for food, feed and arable land. Moreover, microalgae can be sustainably cultivated on waste streams where AD liquid digestate serves as a low-cost and economical nutrient (N & P) source and CO_2 in biogas is a gaseous substrate for microalgal growth which renders a more economical process but also remediating water for reuse and reducing GHG emissions. Recent studies suggest that microalgal biomass with the proper protein content can be used in bioplastics. In addition to microalgae, methanotroph biomass also contains high fractions of protein that make them proper for use in bioplastics.

Consequently, once the methanotroph-photoautotroph co-culture contains a proper fraction of protein that yields the desired bioplastic properties, the co-culture technology can potentially be a suitable biomass feedstock for bioplastics.

Chapter 2: Photoautotroph-Methanotroph coculture- A flexible platform for efficient biological CO_2-CH_4 co-utilization

Abstract

Industrial, municipal, and agricultural waste streams containing stranded organic carbon, which can be converted into biogas through anaerobic digestion. It has been demonstrated that biogas has immense potential as a renewable feedstock for producing high-density fuels and commodity chemicals. However, the utilization of biogas represents a significant challenge due to its low pressure and presence of contaminants such as H_2S, ammonia, and volatile organic carbon compounds. To tap into this immense potential, effective biotechnologies that co-utilize both CO_2 and CH_4 are needed. Using the basic metabolic coupling principles used by natural consortia, we have demonstrated that photoautotroph- methanotroph co-cultures offers a flexible and highly promising platform for biological CO_2/CH_4 co-utilization.

Redrafted after:

Badr K, Hilliard M, Roberts N, He QP, Wang J. Photoautotroph-Methanotroph Coculture–A Flexible Platform for Efficient Biological CO_2-CH_4 Co-utilization. *IFAC-PapersOnLine*. 2019;52(1):916-921.

2.1 Introduction

Industrial, municipal, and agricultural waste streams containing stranded organic carbon represent a significant and underutilized feedstock to produce fuels and chemicals. Biogas, which contains 50%~70% CH_4, 30%~40% CO_2 and trace amount of contaminants such as H_2S and NH_3, can be produced during anaerobic digestion of various waste streams. CO_2 and CH_4 are the two leading GHGs that cause global warming and many detrimental effects to the earth's ecosystem, including climate change. If the anaerobic digestion of waste material happens in an uncontrolled

fashion such as in landfill, the produced biogas would be released into atmosphere and cause global warming; at the same time, CH_4 is a valuable fuel; if anaerobic digestion happens in a controlled condition such as within an anaerobic digester, the produced biogas can be further processed to generate electricity or simply used for heating.

It has been shown that biogas has immense potential as a renewable feedstock for producing high-density fuels and commodity chemicals. EPA estimates that currently US biogas production potential from animal farms alone is 654 billion cubic feet per year, which could displace 7.5 billion gallon of gasoline [53]. However, the utilization of biogas represents a significant challenge due to its low pressure and presence of contaminants such as H_2S, ammonia, and volatile organic carbon compounds. As a result, although anaerobic digester (AD) is a mature technology that can offer significant environmental and social benefits, as well as the enormous energy and economic potential, the deployment of AD is rather limited. For example, As of August 2017, out of 8113 US dairy and swine farms identified by AgSTAR as candidates for profitable AD biogas recovery systems, only 250 (3% of total potential) manure AD biogas recovery systems were in operation [53]. In addition, most of the AD produced biogas is currently flared or used for heating/cooking with only a fraction to generate electricity or upgraded to a liquefied transportation fuel. Specifically, among all livestock farms that have AD installed, only ~3% of them use biogas to produce CNG and 30% of them use biogas for electricity generation [54]. In short, the low value of biogas is the main factor that hinders the wide adoption of AD and exploration of biogas potential as a feedstock for production of high-density fuels and commodity chemicals. To tap into the immense potential of biogas produced from waste streams, effective biotechnologies that can operate at ambient pressure, temperature and are economically viable at small to mid-scale are needed, especially the ones that could co-utilize both CH_4 and CO_2.

Recent studies have demonstrated that natural microbial communities have developed a highly efficient way to recover the energy and capture carbon from both CH_4 and CO_2 through metabolic coupling of CH_4 oxidation to oxygenic photosynthesis [55–57]. This coupling represents a major sink of both CH_4 and CO_2 at oxic-anoxic interfaces across various aquatic and terrestrial ecosystems, where the methanotrophic activity is fuelled by *in situ* photosynthetic production of O_2. Specifically, recent findings suggest that the coupling of CH_4 oxidation (by aerobic methanotroph) and oxygenic photosynthesis (by peat moss or photosynthetic algae) is prevalent in nature [56,57].

2.2 Current status

These recent findings suggest that the coculture of photoautotroph and methanotroph presents not only a feasible, but also a highly promising strategy for simultaneous conversion of biogas (both CO_2 and CH_4) into useful products, including high density fuel, commodity chemicals and animal feed, etc. In fact, such coupling has been partially validated in laboratory settings. (1) It was reported that coculture of *Scenedesmus sp.* (microalgae) and *Methylocystis parvus* (methanotroph) can achieve total microbial conversion of both CH_4 (60%) and CO_2 (40%) in a synthetic biogas without external O_2 supply [58]; (2) coculture of *Synechococcus* PCC 7002 (cyanobacteria) and *Methylomicrobium alcaliphilum* (methanotroph) exhibit robust growth on diverse gas mixtures including raw biogas and synthetic natural gas [59]; (3) coculture of *Chlorella sorokiniana* (microalgae) and *Methylococcus capsulatus* (methanotroph) can recovery nutrient contained in waste water from a potato processing plant and produce single cell protein as animal feed [24].

As the very first attempts to explore the potential of photoautotroph-methanotroph for biogas conversion, these published research mainly aimed to demonstrate the feasibility of the

coculture for CO_2/CH_4 co-utilization, without any efforts to mathematically model the coculture and to examine the potential interactions within the cocultures. In addition, it is important to realize that currently how to effectively characterize the coculture still present significant challenges to such research effort. Specifically, how to track the individual biomass concentration in a mixed culture in real-time is still an unsolved problem; in addition, in the photoautotroph-methanotroph coculture, both strains contribute to the production and consumption of CO_2 and O_2, which adds additional difficulty to the characterization of the coculture.

Using the principles that drive the natural consortia, we have assembled and investigated several different photoautotroph-methanotroph cocultures that exhibit stable growth under varying substrate delivery and illumination regimes. In addition, we have developed experimental and computation protocols to characterize of the coculture accurately, easily and frequently. These protocols are the key enables to the quantitative examination of the photoautotroph-methanotroph coculture systems. Finally, we have developed an unstructured kinetic model that can accurately capture the growth of each individual strains in the coculture under various growth conditions. In this chapter, we briefly present our progress in understanding the photoautotroph-methanotroph coculture.

2.3 Strains and their characteristics for our model coculture system

While several saltwater cocultures have been established, the coculture pair of focus will be *Methylomicrobium buryatense* 5GB1 and *Arthrospira platensis* (*Spirulina platensis*) (**Figure 5**). These microbes grow well in similar pH ranges and temperatures, and their medium components are comparable (our group previously found the optimum medium for this pair). *A. platensis*, the most cultivated and a nutritionally enriched filamentous cyanobacterium, is widely used as an alternative protein source for cultured fish, a feed supplement, and a source of fine

chemicals [25,60,61]. To summarize, methanotrophs are bacteria that assimilate CH_4 (largely through aerobic processes) for their sole source of carbon and energy. *M. buryatense* 5GB1 is a relatively fast-growing methanotroph [62].

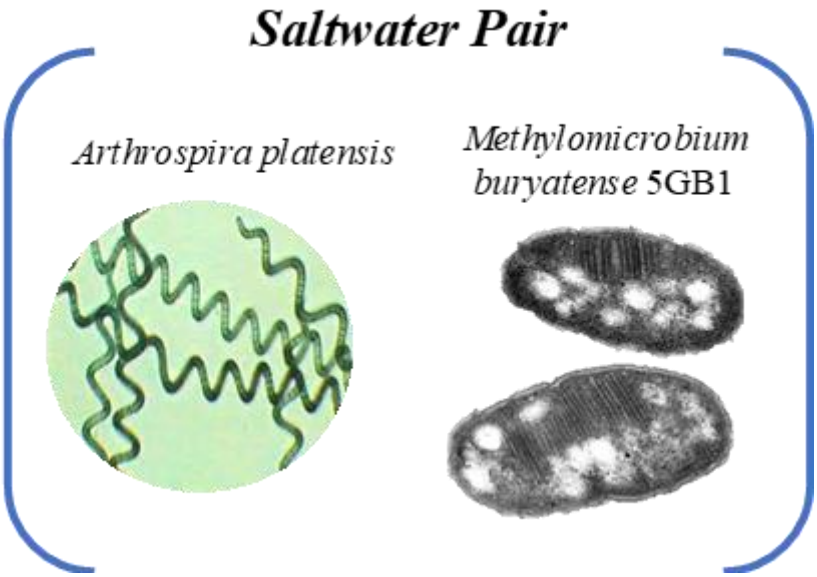

Figure 5. The saltwater pair was used in this work as the model coculture system

2.4 Advantage of the coculture platform over sequential single cultures

From an engineering perspective, coupling photosynthesis to methanotrophic metabolism offers several advantages for the design of robust microbial catalysts for biogas conversion, as listed in **Figure 6**. **Figure 6** shows that the exchange of the *in situ* produced O_2 and CO_2 appears to be a major synergistic interaction between the two strains; in addition, there may be other potential "metabolic links" that could promote or inhibit the growth of the coculture.

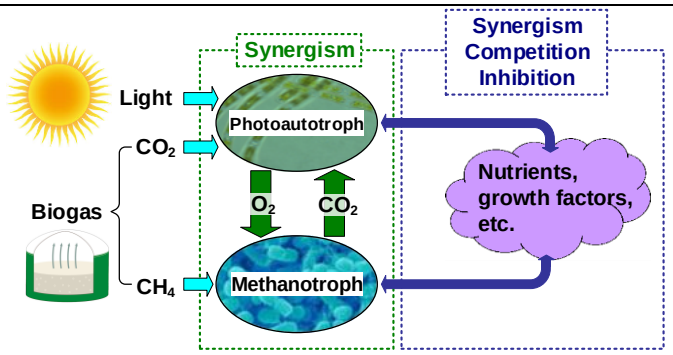

Potential advantages of the coculture:

- Exchange of *in situ* produced O_2 and CO_2 dramatically reduces mass transfer resistance of the two gas substrates
- *In situ* O_2 consumption removes inhibition on photoautotroph and eliminates risk of explosion
- Interdependent yet compartmentalized configuration of the coculture offers flexibility and more options for metabolic engineering

Figure 6. Photoautotroph-methanotroph coculture: potential interactions and its advantages

However, the synergy caused by substrate exchange could also be achieved through culturing the two strains separately and sequentially (photoautotroph then methanotroph). Therefore, the first question we aimed to answer is the following: are there clear benefits of using the coculture than using single cultures sequentially for biogas conversion. In fact, this is a critical question applicable to any consortia-based biotechnologies, as the operation of the mixed culture can be more challenging than maintaining two single cultures sequentially.

To answer this question, we have conducted the comparison experiments for three cases as shown in **Figure 7**, using *Arthrosipira platensis* (cyanobacterium) - *Methylomicrobium buryatense* (methanotroph) - as the model coculture system. Case A is the coculture; Case B is the sequential culture of cyanobacterium followed by methanotroph, with the amount of O_2 produced by the cyanobacterium injected into the single culture of methanotroph; Case C simulates the effect of

the exchange of *in situ* produced O_2 between the coculture, where the amount of O_2 produced by the cyanobacterium in the coculture was injected into the methanotroph single culture.

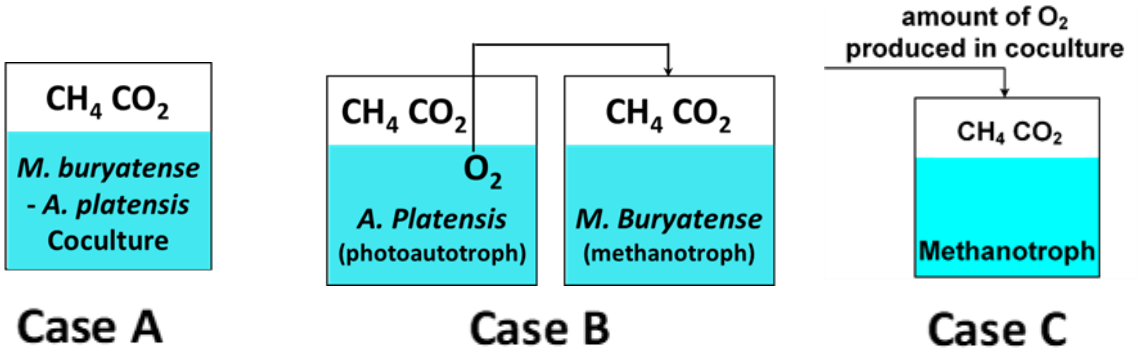

Figure 7. Preliminary comparison experiments to demonstrate the advantages of coculture.

All experiments were carried out in 250ml serum bottles with 100ml media under batch operations, with gas phase composition 70% CH_4 and 30% CO_2, light:dark cycle of 16:8, and light intensity of 180 µmol/m^2/s. **Figure 8**(a) compares the growth of the methanotroph in the three cases over 4 days (4 light periods and 3 dark periods), and **Figure 8** (b) compares the growth of cyanobacterium in case A and B for the same period (as CO_2 is available from head space, case C does not apply to cyanobacterium), and **Figure 8** (c) compares the O_2 produced by cyanobacterium in Cases A and B. **Figure 8** clearly shows that both cyanobacterium and methanotroph in coculture (Case A) grew significantly faster than the sequentially operated single cultures (Case B). In addition, the improvement of the methanotroph growth cannot be fully explained by the availability of the extra O_2 produced in coculture (Case C). **Figure 8** (b) and (c) further confirmed that cyanobacterium in the coculture grow faster than the single culture and produce more O_2. Together, **Figure 8** suggests that there could be other factors that promote cell growth of both strains in the coculture; in other words, the photoautotroph-methanotroph coculture offer significantly more benefit than sequentially operated single cultures.

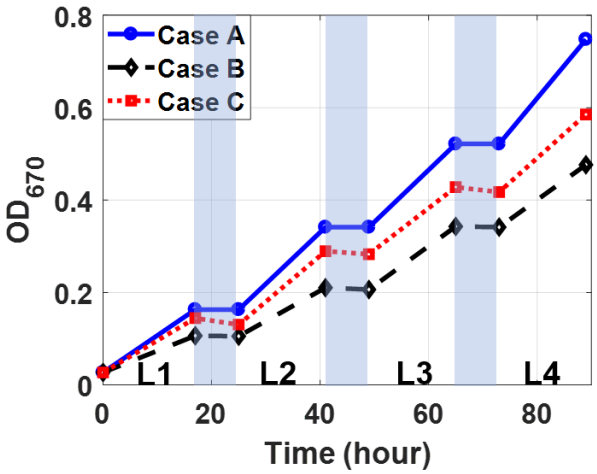

(a) Methanotroph

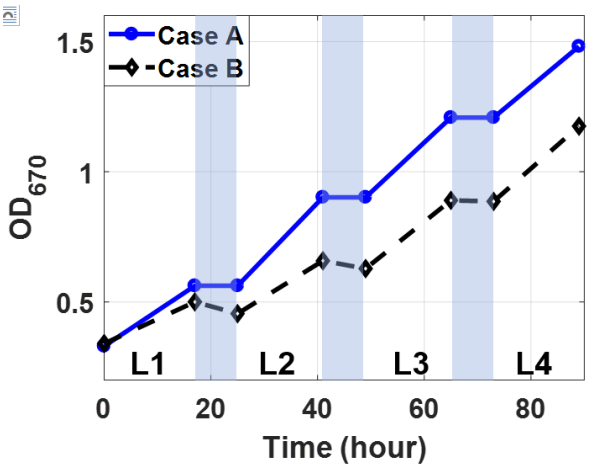

(b) Microalgae

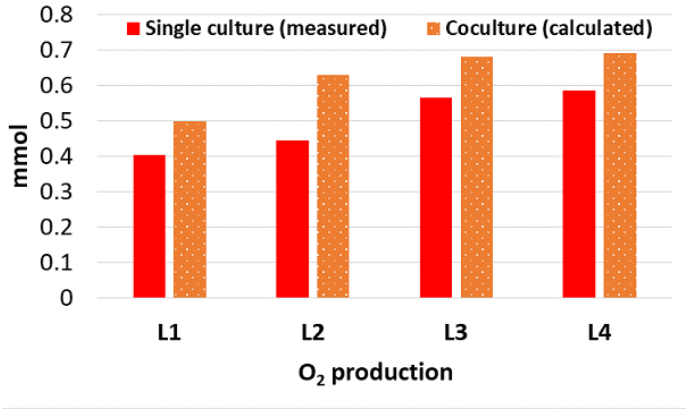

(c) O_2 production

Figure 8. Comparison experiments show that both strains growth much faster in coculture (Case A) than in sequential (Case B) as shown in (a) and (b). (c) shows that with the same inoculum, microalgae produce more O_2 in coculture than in single couture; Even with coculture O_2 amount injected into methanotroph single culture (Case C), its growth is still slower than coculture as shown in (a), suggesting other factors that play a role in enhancing coculture growth. Shaded periods indicate dark cycles and light cycles are denoted as L followed by a number.

Next, to verify the flexibility of the coculture platform, our group has demonstrated that several pairs of the photoautotroph-methanotroph cocultures can form self-regulating systems that can maintain functional homeostasis in response to external or environmental perturbations [63].

Among them, some pairs prefer high salt and alkaline condition which we term as saltwater pair, and some prefer neutral pH and very low salt condition which we term as freshwater pair. For each pair, we have identified the range of liquid media that enable stable growth of the coculture; validated the stability of the coculture over multiple transfer; conducted H_2S tolerance test and verified that fresh water pairs can maintain healthy growth for H_2S up to 3000ppm while saltwater pair can tolerate even higher concentration of H_2S; finally, by using digestate collected from Columbus Water Works, we showed that after adaptation, the freshwater pairs can growth well on digestate diluted using clarifier water (the water ready to be discharged from the water treatment facility), and even better than synthetic media [63].

2.5 Investigation of the cocultures at both systems and molecular level

Multispecies associations are ubiquitous in nature as they provide key ecosystem services such as carbon, nutrient, and metal cycling. It was shown that a mixed culture could offer a number of advantages over a conventional single-culture, such as complete utilization of substrate, better stability and robustness, higher product yield, higher growth rate, as well as the capability to carry out multistep transformation that would be impossible for a single organism.

Despite these potential significant advantages, utilization of mixed cultures for biotechnological applications in bioenergy and related areas have been limited partially due to the ***methodological gaps***. Specifically, the methodological gap refers to the lack of effective, fast and low-cost analytical ***tools*** to characterize mixed culture systems frequently or in real-time. In the next chapter (Chapter 3), we report the experimental and computational protocols that we have developed to quantitatively characterize the photoautotroph-methanotroph coculture.

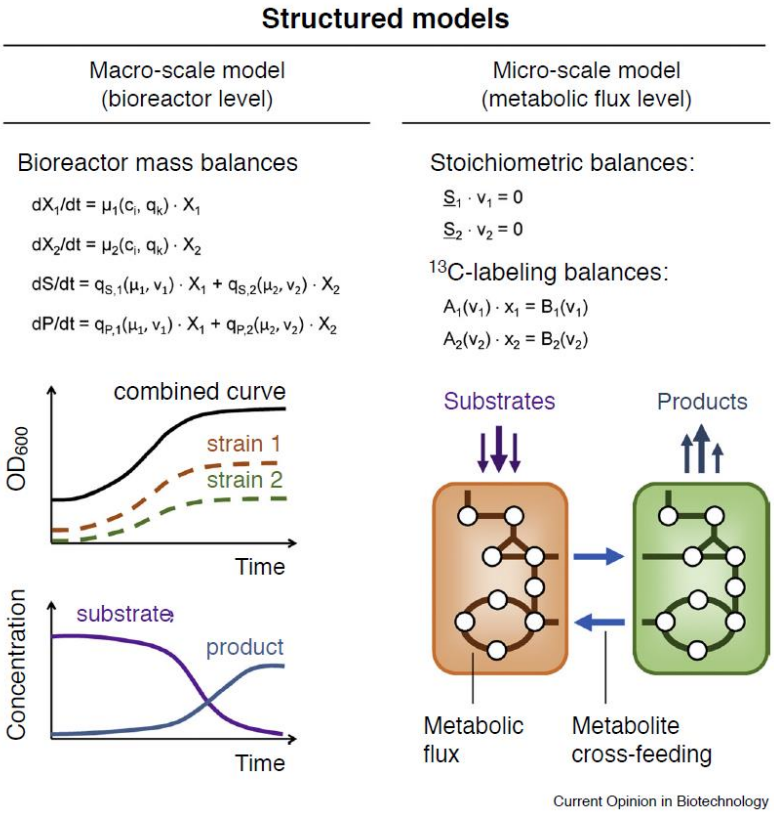

Figure 9. Bioreactor level (Mathematical) models focus on describing population dynamics and evaluating the stability of communities under various conditions or perturbations. Metabolic models focus on cellular metabolism and explicit cross-feeding interactions to predict population properties of microbiomes [64].

Given the prevalence and importance of microbiomes in nature, much effort has been invested in the past decade to unravel the members, structures, functions, interactions, and governing principles of microbial communities [65]. With the advent of next-generation sequencing, metagenomics first emerged as an important tool in the study of microbial communities. It allowed quantitative analysis of the diversity, composition, and dynamics of these systems [66]. Statistical modeling approaches, such as multiple linear regression and multi-dimensional cluster analysis, were then used to interpret the wealth of metagenomics data to identify microbial community trends and correlations between metagenomics data and other

observable system variables [67]. These statistical modeling approaches provided new hypotheses regarding potential interactions and functions of communities. However, metagenomics data alone could not predict causal relationships in microbial communities. For this, new computational models were needed that allowed a more systematic and rigorous interpretation and interrogation of the huge amount of heterogeneous data that was generated [68] (**Figure 9**). Once a model was constructed, systems biological properties could be analysed by comparing model simulations with experimentally observed data. Mathematical models of microbial communities thus provided critical tools for generating and testing biological hypotheses to better understand and predict the dynamics and interactions among community members [69].

Therefore, there are ***knowledge gaps*** that have made the utilization of mixed cultures for biotechnological applications limited. Specifically, how the coculture grow at various conditions and also what interactions happen between the species when they grow together. In the Chapter 4, we investigate the coculture system and their interaction in ***systems level*** by developing mathematical models. In the Chapters 5 and 6, we elucidate the interactions within the coculture in ***molecular level*** by developing metabolic models.

Chapter 3: Fast and Easy Quantitative Characterization of Methanotroph-Photoautotroph Cocultures

Abstract

Recent research has demonstrated that synthetic methanotroph-photoautotroph cocultures offer a highly promising route to convert biogas into value-added products. However, there is a lack of techniques for fast and accurate characterization of cocultures, such as determining the individual biomass concentration of each organism in real-time. To address this unsolved challenge, we propose an experimental-computational protocol for fast, easy and accurate quantitative characterization of the methanotroph-photoautotroph cocultures. Besides determining the individual biomass concentration of each organism in the coculture, the protocol can also obtain the individual consumption and production rates of O_2 and CO_2 for the methanotroph and photoautotroph, respectively. The accuracy and effectiveness of the proposed protocol was demonstrated using two model coculture pairs, *Methylomicrobium alcaliphilum* 20ZR - *Synechococcus sp.* PCC7002 that prefers high pH high salt condition, and *Methylococcus capsulatus* - *Chlorella sorokiniana* that prefers low salt and neutral pH medium. The performance of the proposed protocol was compared with a flowcytometry based cell counting approach. The experimental results show that the proposed protocol is much easier to carry out and delivers faster and more accurate results in measuring individual biomass concentration than the cell counting approach without requiring any special equipment.

Redrafted after:

Badr K, Whelan W, He QP, Wang J. Fast and easy quantitative characterization of methanotroph–photoautotroph cocultures. *Biotechnol Bioeng*. 2021;118(2):703-714.

3.1 Introduction

Biogas is comprised primarily of methane (CH_4, 50%~70%) and carbon dioxide (CO_2, 30% ~50%). It can be produced through AD of various organic waste sources, including landfill waste; animal manure; wastewater sludge; and industrial, institutional, and commercial organic wastes. CO_2 and CH_4 are the two leading GHGs that cause many detrimental effects to our ecosystem, including climate change. On the other hand, CH_4 is also a valuable fuel. It is estimated that currently US biogas production potential is 654 billion cubic feet per year, which could displace 7.5 billion gallon of gasoline [70]. Although waste-derived biogas has immense potential as a renewable feedstock for producing high-density fuels and commodity chemicals, the contaminants (e.g., H_2S, NH_3, and volatile organic carbon (VOC) compounds) present significant challenges to biogas utilization. Currently the AD-derived biogas is primarily used for heating/cooking or flared, with only a small fraction for electricity generation due the cost associated with biogas clean-up [70]. To tap into this immense potential, effective technologies that can co-utilize both CO_2 and CH_4 without costly biogas clean-up are needed.

Recent studies have demonstrated that natural microbial communities have developed a highly efficient way to recover the energy and capture carbon from natural biogas streams through interspecies metabolic coupling of CH_4 oxidation to oxygenic photosynthesis [55,56,71]. **Figure 10**(a) illustrates the key synergistic interactions within the methanotroph-photoautotroph coculture: the photoautotroph converts CO_2 into biomass while producing O_2 via photosynthesis and the methanotroph utilizes the *in situ* produced O_2 to convert CH_4 into biomass while producing CO_2 for the photoautotroph. **Figure 10**(b) depicts the total mass balance and key substrate exchanges in the coculture.

Following the principles that drive the natural consortia, different synthetic methanotroph-photoautotroph (e.g., cyanobacteria or microalgae) cocultures have been demonstrated to

simultaneously convert both CH_4 and CO_2 into microbial biomass without external oxygen supply [58,72–75]. The biogas-derived coculture biomass could be further processed to produce biofuels (such as biodiesel), directly used as single cell protein for animal feed supplement or serves as feedstock to produce bioplastics. In addition, the coculture could be engineered to produce other value-added chemicals (such as succinate or lactic acid) using biogas as feedstock. Therefore, the methanotroph-photoautotroph coculture offers a highly promising biological platform for waste-to-value conversion.

In order to develop methanotroph-photoautotroph based biotechnology for biogas conversion, a key prerequisite is an effective tool to enable fast, easy and accurate characterization of each organism in the coculture in terms of biomass growth and biogas conversion performance. However, currently no such tool is available. In fact, one major challenge associated with characterizing any mixed culture is the accurate determination of the individual biomass concentration for each microorganism. Existing approaches to quantify individual biomass concentration in mixed culture include molecular biological, biochemical, and microbiological method [76,77]. However, these methods require either expensive equipment such as flow cytometry, community genome sequencing, or time-consuming and challenging techniques, such as RNA/DNA extraction, isolation, or amplification. Therefore, these approaches are suitable for off-line, infrequent characterization of mixed culture, and cannot provide the frequent or real-time measurements desired for dynamic modelling of the coculture systems. As a result, among the published methanotroph-photoautotroph research, only Hill et al. (2017) tracked the individual biomass concentration over time through cell counting using flow cytometry, while others just reported the total optical density of the coculture over time without differentiating the contribution from the methanotroph and the photoautotroph [58,75].

Besides individual biomass concentration, the individual substrate consumption rates and product excretion rates of each organism are needed in order to develop a kinetic model for the coculture. However, when there is cross-feeding in the coculture (i.e., any exchange of metabolite(s) between different organisms), it is highly challenging to obtain the individual consumption/production rates because they cannot be measured directly. For the case of methanotroph-photoautotroph coculture, as shown in **Figure 10**(b), both O_2 and CO_2 are cross-feeding metabolites: O_2 is produced by the photoautotroph while consumed by the methanotroph, while CO_2 is produced by the methanotroph and consumed by the photoautotroph. However, what can be directly measured are the overall or total consumption/production rates of O_2 and CO_2 by the coculture, not individual rates by each organism. Currently how to use the measured overall rate to infer or estimate the individual consumption/production rates remains an unsolved problem. It is worth noting that in our experiments, oftentimes no oxygen was detectable in the gas phase or liquid phase, as all the O_2 produced by the photoautotroph was consumed by the methanotroph *in situ*.

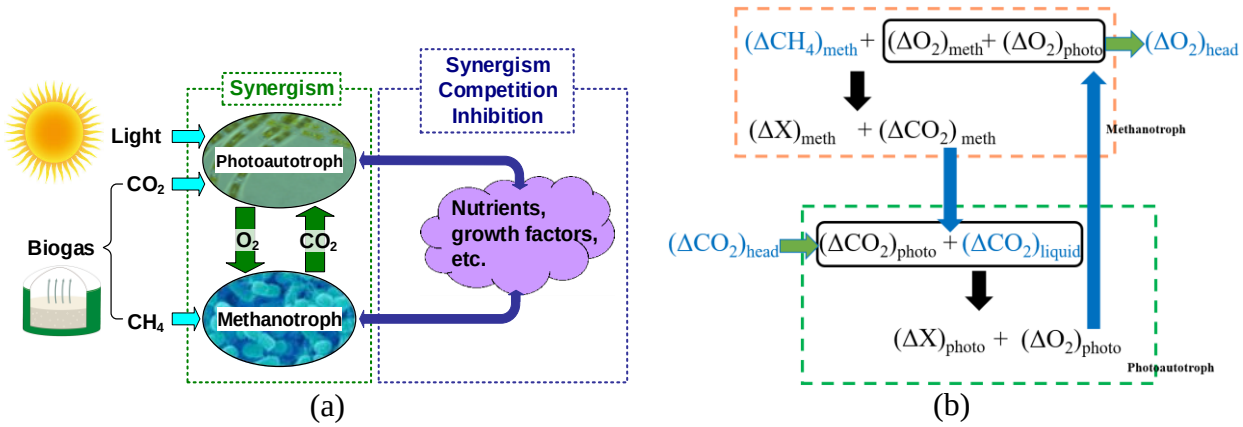

Figure 10. (a) The interdependency within methanotroph-photoautotroph cocultures; (b) Total mass balance and substrate exchange within the coculture, where X denotes biomass, and the subscripts "$meth$" and "$photo$" denote methanotroph and photoautotroph, respectively; Δ indicates the amount of change in the variable; blue-coloured variables are

directed measured and black coloured variables are calculated based on the cell growth stoichiometry. For example, $(\Delta O_2)_{meth}$ is the consumed oxygen by methanotroph.

To address the above-mentioned challenges, we have developed an experimental-computational (E-C) protocol to fully characterize the synthetic methanotroph-photoautotroph coculture based on the overall mass balance and each organism's growth stoichiometry. Besides tracking the biomass concentration of each organism in the coculture over time, the E-C protocol also obtains estimates on the substrate consumption rates (CH_4 and O_2 uptake rates for the methanotroph and CO_2 uptake rate for the photoautotroph) and product secretion rates (CO_2 for the methanotroph and O_2 for the photoautotroph). Such quantitative characterizations will enable better understanding of the coculture growth kinetics, and will lay the foundation for the development of the coculture-based biotechnology to convert biogas into valuable products. The E-C protocol only requires the commonly measured variables including total optical density for the coculture (UV/Vis spectroscopy), gas phase composition (GC), dissolved CO_2 in the culture broth (total carbon analyser). Therefore, the E-C protocol does not require any special equipment, and it does not require any special sample preparation such as DNA/RNA extraction or cell fixation in order to achieve the above-mentioned characterizations.

In this chapter, we use one methanotroph-cyanobacteria pair and one methanotroph-microalgae pair to demonstrate the performance of the developed protocol; To validate its accuracy, we compared the individual biomass concentrations obtained by the E-C protocol with cell counting results obtained using flow cytometry. In this work, the methanotroph-cyanobacteria coculture pair is *Methylomicrobium alcaliphilum* 20ZR - *Synechococcus sp.* PCC7002 , which prefers high salt and high pH medium and has demonstrated robust growth on different concentrations of biogas [72]. The methanotroph-microalgae coculture pair is *Methylococcus*

capsulatus - *Chlorella sorokiniana*, which prefers low salt and neutral pH medium and has been used for wastewater treatment [75].

3.2 Materials and Methods

3.2.1 Microorganism and growth media

Methylomicrobium alcaliphilum 20ZR was provided by Dr. Marina Kalyuzhnaya, San Diego State University, and *Synechococcus sp.* PCC7002 was provided by Dr. Alexander Beliaev, Pacific Northwest National Lab. *M. alcaliphilum* 20ZR cells were grown in modified P-medium. *Synechococcus sp.* PCC7002 cells were grown in A+ medium. For the coculture, the growth media consisted of 10% P-medium and 90% A+ medium.

Methylococcus capsulatus was acquired from the American Type Culture Collection (ATCC 33009), and *Chlorella sorokiniana* (UTEX 2805) was acquired from UTEX Culture Collection of Algae. *M. capsulatus Bath* cells were grown in NMS medium. *C. sorokiniana* cells were grown in N8 medium. For the coculture, the growth media consisted of 10% NMS medium and 90% N8 medium. It is worth to mention that all species have different size. Methanotrophs are colourless and photoautotroph species have different chlorophyll which make them light and dark green colour.

3.2.2 Sampling procedure

Composition of gas samples was analysed using GC (Agilent 7890B gas chromatograph customized with FID, TCD, Unibeads IS 60/80 mesh and MolSieve 5A 60/80 SST columns). It is worth noting that the consumption and production of various gases will result in changes in system pressure (for batch operations) or off-gas flow rate (for continuous operations). These changes would cause significant errors in the estimated gas component uptake and production rates if they

were not accounted for. To address it, our group have previously developed a protocol [78], which is followed in this work. The optical density of each liquid sample was measured using a Beckman Coulter DU® 730 UV/Vis spectrophotometer at OD750. To determine the amount of the dissolved CO_2 in the liquid phase, we first removed cell mass through centrifugation, then measure the total inorganic carbon (TIC) using a Shimadzu TOC-V_{CSN} Analyzer, also following the procedures reported in [78].

3.2.3 Cell counting through flow cytometry

For *M. alcaliphilum* 20ZR - *S. sp.* PCC7002 pair, two 0.5 mL samples of culture broth were taken and each sample was immediately treated with 0.25 mL of 50 mM EDTA and 0.25 mL of 4% paraformaldehyde to fix the cells. After 10 minutes of fixation, the samples were centrifuged at 10,000 RPM and 0.5 ml of supernatant was removed, then each sample was treated with 0.5 mL of 0.05% Tween-20 detergent for 20 minutes (away from light) to minimize cells sticking to each other. Next, after removing Tween-20 through centrifugation, the samples were washed and re-suspended in DI water. For *M. capsulatus – C. sorokiniana* pair, the overall procedure is similar, with the differences being that the samples were first treated with 0.2% Tween-20 detergent for 20 minutes and then treated with 200 mM EDTA and 4% paraformaldehyde for 20 minutes to fix the cells. After sample preparation, 25 µL of the re-suspended sample was counted on a Beckman Coulter Cytoflex LX cytometer with 6 active lasers and 21 channels for fluorescence detection. FlowJo Version 10.6.1 was used to analyze the data obtained from the flow cytometer. As both the cyanobacteria and microalgae used in this work are green, and both methanotrophs are white, different filter of excitation wavelengths were used to help differentiate the cells in the coculture. For *M. alcaliphilum* 20ZR - *S. sp.* PCC7002 pair, the forward scatter (FSC-H) was paired with the filter of excitation wavelength at 610nm (Y610-mCHERRY-H fluorochrome) to separate the two

populations. For *M. capsulatus – C. sorokiniana* pair, the FSC-H was paired with the filter of excitation wavelength of 710nm (Y710-PC5.5-H) to separate the two populations.

3.2.4 Calibration and testing for the cell counting approach

To establish the calibration relationship between biomass concentration and cell counting results, we first conducted cell counting experiments for each single culture (*M. alcaliphilum* 20ZR, *S. sp.* PCC7002, *M. capsulatus* and *C. sorokiniana*). For each strain, cell counting was performed for 4 different biomass concentrations, with triplicates for each sample. To validate the effectiveness of the cell counting approach, we prepared static coculture samples by mixing given amounts of each individual microorganisms together. For each coculture pair, six coculture samples with different compositions were tested with triplicates.

3.2.5 Demonstration of the E-C protocol in characterizing coculture dynamic growth

In these experiments, the E-C protocol was applied to characterize the dynamic growth of both model coculture pairs. To validate the E-C protocol's accuracy, the individual biomass concentration within the coculture was also measured through cell counting using flow cytometry for comparison. For each coculture pair, three different inoculum concentrations were tested with duplicates. For the *M. alcaliphilum* 20ZR - *S. sp.* PCC7002 pair, the inoculum OD ratios between the methanotroph and the cyanobacteria were 1:15, 1:10, and 1:5, with the same amount of methanotroph for all three cases. For the *M. capsulatus* - *C. sorokiniana* pair, the inoculum OD ratios were 1:3, 1:2 and 1:1, also with the same amount of methanotroph for all three cases. Before and after the inoculation, all vials were flushed with the feeding gas (80% CH_4 and 20% CO_2), and were put under the same light intensity (190 μmol/m^2/s). The coculture growth lasted for 3 days

and was sampled once daily. The vials were flushed with feeding gas to replenish the gas phase after each sampling.

3.3 Modeling Framework for the Experimental-Computational Protocol

The protocol was developed based on each organism's growth stoichiometry, the substrate exchange relationship within the coculture as shown in **Figure 10**(b), and the total mass balance. Eqns. (1) and (2) show the growth stoichiometry for the methanotroph and photoautotroph, respectively.

$$CH_4 + \left(Y_{\frac{O_2}{CH_4}}\right)_{meth} O_2 \rightarrow \left(Y_{\frac{X}{CH_4}}\right)_{meth} X_{meth} + \left(Y_{\frac{CO_2}{CH_4}}\right)_{meth} CO_2 \quad (1)$$

$$CO_2 + \left(Y_{\frac{H_2O}{CO_2}}\right)_{photo} H_2O \rightarrow \left(Y_{\frac{X}{CO_2}}\right)_{photo} X_{photo} + \left(Y_{\frac{O_2}{CO_2}}\right)_{photo} O_2 \quad (2)$$

where X denotes biomass, and the subscripts "$meth$" and "$photo$" denote methanotroph and photoautotroph, respectively; $Y_{\frac{a}{b}}$ denotes the stoichiometric coefficients between "a" and "b", where "b" is CH_4 for methanotroph and CO_2 for photoautotroph. These coefficients can be obtained from literature (Akberdin et al., 2018; Bernstein et al., 2016; Kliphuis et al., 2011). If the coculture growth medium is vastly different from what is commonly used for the single culture and could affect the microorganism's growth stoichiometry, then experimental data of the single

Table 1. Stoichiometric coefficient values used in this work

	Methanotroph	
Coefficient	*M. alcaliphilum* 20ZR	*M. capsulatus*
$Y_{\frac{O_2}{CH_4}}$	1.26 (Akberdin et al., 2018) [82]	1.60 [This study]
$Y_{\frac{CO_2}{CH_4}}$	0.48 (Akberdin et al., 2018) [82]	0.33 [This study]
$Y_{\frac{x}{CH_4}}$	9.60 (Akberdin et al., 2018) [82]	10.60 [This study]
	Photoautotroph	

	S. sp. PCC7002	*C. sorokiniana*
$Y_{\frac{O_2}{CO_2}}$	1.28 [This study]	1.34 [This study]
$Y_{\frac{x}{CO_2}}$	23.73 [This study]	23.68 [This study]
$Y_{\frac{x}{O_2}}$	18.53 (Bernstein, 2016) [80]	17.67 (Kliphuis et al., 2011) [81]

culture cultivated on the coculture medium should be used to estimate the coefficients. The coefficients used in this work are listed in **Table 1**. The yields for coculture could be different compared to single culture, however, we used the same yields (reported or experimentally achieved) for single culture. The error of the calculation is very small that the mentioned difference could not affect the accuracy of the model. Moreover, all the yields for biomass (x) are in the unit of gram/mol of substrate and other yields are mol/mol.

As shown in **Figure 10** (b), only the methanotroph within the coculture can consume CH_4, therefore the amount of cell growth for methanotroph can be estimated based on the measured CH_4 consumption (i.e., ΔCH_4). Similarly, the amount of the O_2 required for CH_4 consumption and the amount of CO_2 produced can be estimated using stoichiometric coefficients as follows.

$$(\Delta X)_{meth} = \left(Y_{\frac{x}{CH_4}}\right)_{meth} \Delta CH_4 \tag{3}$$

$$(\Delta O_2)_{meth} = \left(Y_{\frac{O_2}{CH_4}}\right)_{meth} \Delta CH_4 \tag{4}$$

$$(\Delta CO_2)_{meth} = \left(Y_{\frac{CO_2}{CH_4}}\right)_{meth} \Delta CH_4 \tag{5}$$

Next, based on the overall mass balance of O_2 and CO_2, as shown in Eqns (6) and (7), we can determine the amount of CO_2 consumed and the amount of O_2 produced by the photoautotroph. The subscript “gas” and “liquid” denote the measurements obtained from headspace samples and liquid samples, respectively.

$$(\Delta O_2)_{gas} = (\Delta O_2)_{photo} - (\Delta O_2)_{meth} \quad (6)$$

$$(\Delta CO_2)_{gas} = (\Delta CO_2)_{meth} - (\Delta CO_2)_{photo} - (\Delta CO_2)_{liquid} \quad (7)$$

where CO_2 and O_2 in the gas phase (*i.e.*, $(\Delta CO_2)_{gas}$, $(\Delta O_2)_{gas}$) are measured through GC, and the dissolved CO_2 in the liquid phase (*i.e.*, $(\Delta CO_2)_{liquid}$) are measured through total carbon analyser. In Eqn (6), we neglect the contribution from dissolved O_2 due to its small solubility in aqueous solutions; however, in Eqn. (7), dissolved CO_2 has to be considered due to its much larger solubility in aqueous solutions, especially under high pH conditions. Although it is difficult to determine the amount of dissolved CO_2 in one sample due to the carbonate (CO_3^{2-}) and bicarbonate (HCO_3^-) salts contained in the culture medium and the equilibrium among different forms of dissolved CO_2, the change in dissolved CO_2 between two sampling points can be easily determined by the difference in the total inorganic carbon content of these two samples. Therefore, based on the overall mass balances (i.e., Eqns (6) and (7)), the amount of CO_2 consumed and O_2 produced by photoautotroph can be obtained, as shown in Eqns (8) and (9).

$$(\Delta O_2)_{photo} = (\Delta O_2)_{gas} + (\Delta O_2)_{meth} \quad (8)$$

$$(\Delta CO_2)_{photo} = (\Delta CO_2)_{meth} - (\Delta CO_2)_{gas} - (\Delta CO_2)_{liquid} \quad (9)$$

With the amount of CO_2 consumed and O_2 produced by the photoautotroph available, the amount of biomass produced by photoautotroph growth can be obtained through two ways using growth stoichiometry, either from CO_2 consumption (Eqn. (10)) or from O_2 production (Eqn. (11)).

$$(\Delta X)_{photo-1} = \left(Y_{\frac{X}{CO_2}}\right)_{photo} (\Delta CO_2)_{photo} \quad (10)$$

$$(\Delta X)_{photo-2} = \left(Y_{\frac{X}{O_2}}\right)_{photo} (\Delta O_2)_{photo} \quad (11)$$

where biomass yield with respect to O_2 can be obtained as the following:

$$\left(Y_{\frac{X}{O_2}}\right)_{photo} = \left(Y_{\frac{X}{CO_2}}\right)_{photo} \Big/ \left(Y_{\frac{O_2}{CO_2}}\right)_{photo} \quad (12)$$

In this work, we use the average of these two approaches to estimate photoautotroph biomass accumulation, as shown Eqn. (13).

$$(\Delta X)_{photo} = \frac{1}{2}\left[(\Delta X)_{photo-1} + (\Delta X)_{photo-2}\right] \quad (13)$$

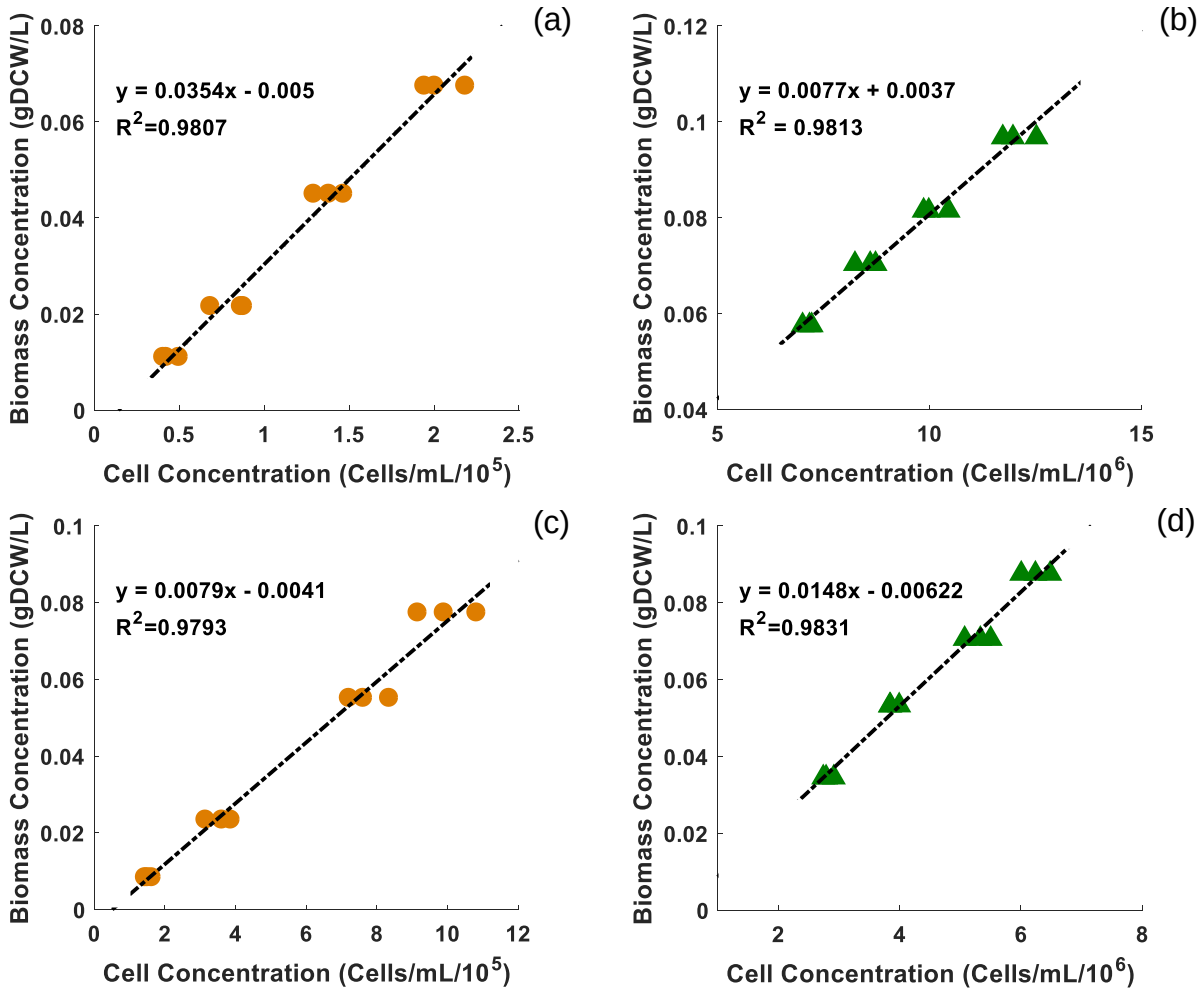

Figure 11. Flow cytometry calibration curves with single cultures. (a) *M. alcaliphilum* 20ZR; (b) *S. sp.* PCC7002; (c) *M. capsulatus*; (d) *C. sorokiniana*

3.4 Results and Discussion

3.4.1 Calibration and validation of the cell counting approach

The flow cytometry calibration plots for each microorganism are given in **Figure 11**. These results confirmed excellent linear relationship between biomass concentration and the cell counting results, with R^2 ranging 0.979 – 0.983. **Figure 11** also shows that cell counting with flow cytometry is more reliable/consistent when cell concentrations are low. Using the calibration relationship obtained from the single cultures, we validated the accuracy of the flow cytometry measurements using static coculture samples with known individual biomass concentrations. For each coculture pair, six samples with different compositions were tested. The individual biomass concentrations for each microorganism in the cocultures measured using flow cytometry are plotted against the known concentrations in **Figure 12** (a) ~ (d), with the detailed results provided in **Table 2**. As shown in these figures, the measured individual biomass concentrations (converted from cell counting based on the calibration curves in **Figure 11**) show good agreement with the known concentrations. However, there are relatively large variations among the triplicates for each sample, especially for higher concentrations, which is consistent with the similar trend observed in the calibration curves in **Figure 11**. In addition, when the same sample was measured multiple times, the measurements showed same level of variations, suggesting the source of the variation was cell counting. One possible reason for such large variation is the non-uniform distribution of the cells in the liquid sample, and the small sample volumes (25 µL) for cell counting makes such variation more pronounced for higher concentrations, as observed in both calibration and validation experiments. Another possible reason, which we believe is more important for mixed culture samples, is the effect of sample fixation process on cell counting. As shown in **Figure 12** (c), for the *M. capsulatus – C. sorokiniana* coculture which turned out to be more challenging in

sample preparation, the measurement error for *M. capsulatus* was consistently larger for both low and high cell density samples.

Table 2. Detailed flow cytometry cell counting results on the static coculture samples with known individual biomass concentrations

Sample Number	Known Concentration (gDCW/L)		Concentration measured by cell counting ± STD (gDCW/L)		Error%	
	M. alcaliphilum 20ZR	*S. sp.* PCC7002	*M. alcaliphilum* 20ZR	*S. sp.* PCC7002	*M. alcaliphilum* 20ZR	*S. sp.* PCC7002
1	0.0154	0.0876	0.0146±0.0007	0.0843±0.0030	5.41%	3.71%
2	0.0232	0.0827	0.0209±0.0016	0.0784±0.0028	9.81%	5.15%
3	0.0132	0.0751	0.0132±0.0009	0.0736±0.0027	0.38%	1.94%
4	0.0199	0.0709	0.0190±0.0016	0.0705±0.0025	4.45%	0.50%
5	0.0110	0.0626	0.0109±0.0011	0.0625±0.0017	1.07%	0.15%
6	0.0165	0.0591	0.0148±0.0006	0.0597±0.0005	10.55%	1.13%
	M. capsulatus	*C. sorokiniana*	*M. capsulatus*	*C. sorokiniana*	*M. capsulatus*	*C. sorokiniana*
1	0.0159	0.0736	0.0156±0.0022	0.0692±0.0053	1.93%	5.99%
2	0.0298	0.0646	0.0295±0.0040	0.0657±0.0068	1.11%	1.70%
3	0.0367	0.0601	0.0335±0.0038	0.0578±0.0018	8.89%	3.79%
4	0.0228	0.0511	0.0236±0.0034	0.0504±0.0019	3.31%	1.41%
5	0.0395	0.0403	0.0339±0.0048	0.0369±0.0028	14.3%	8.29%
6	0.0507	0.0331	0.0453±0.0035	0.0330±0.0008	10.6%	0.25%

In this work, we had to optimize the sample fixation protocols multiple times in order to obtain the acceptable validation results. **Figure 12** (e) and (f) compare the cell counting results for a same static coculture sample. **Figure 12** (e) was obtained following the cell fixation protocol initially developed for the salt water pair, while **Figure 12** (f) following the protocol optimized for the fresh water pair. The known and measured individual biomass concentration are provided in **Table 3**. The large measurement errors shown in **Figure 12** (e) (-88.3% for *M. capsulatus* and 18.0% for *C. sorokiniana*) indicate that some methanotroph cells stuck to the microalgae cells and the flow cytometer could not separate them properly. With the optimized protocol, methanotroph cells were much better separated from microalgae cells, which resulted in significantly reduced

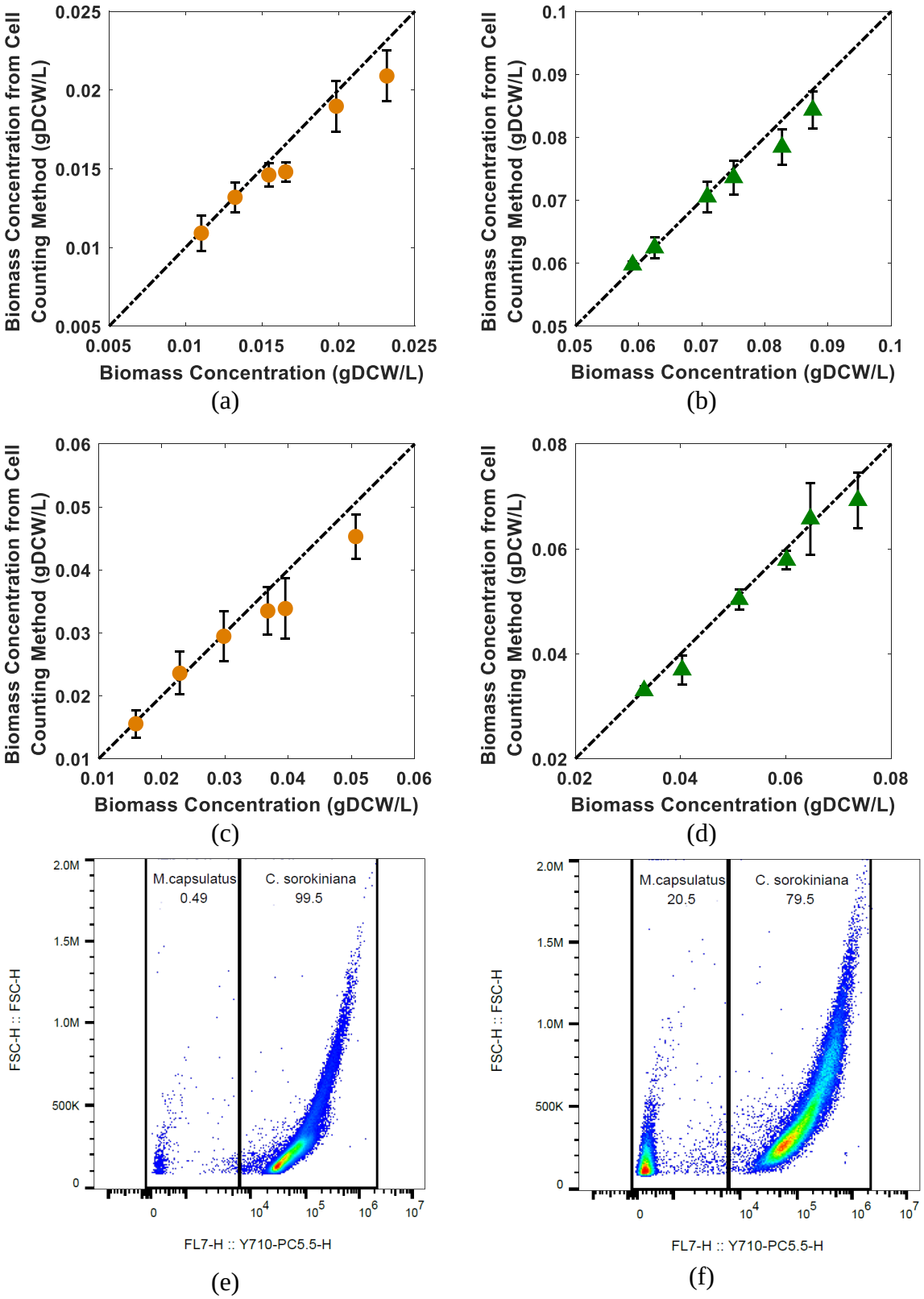

Figure 12. Validation of flow cytometry measurements using static coculture samples with known individual biomass concentrations for coculture pairs of *M. alcaliphilum* 20ZR - *S. sp.*

PCC7002 and *M. capsulatus* - *C. sorokiniana*. (a) *M. alcaliphilum* 20ZR; (b) *S. sp.* PCC7002; (c) *M. capsulatus*; (d) *C. sorokiniana*; (e) Erroneous cell counting by flow cytometry when an inadequate sample fixation protocol is used; (f) Significantly improved cell counting by flow cytometry after optimizing sample fixation protocol. (e) and (f) used the same statically mixed coculture sample with known individual biomass concentrations listed in **Table 3**.

measurement error (-7.9% for *M. capsulatus* and -6.5% for *C. sorokiniana*). Currently the flow cytometry has been commonly used to characterize the composition of synthetic microbiome. This example highlights the importance of performing validation experiments to confirm the appropriateness of the experimental protocol and the accuracy of the cell counting result to avoid misleading conclusions.

Table 3. Effect of cell fixation protocols on cell counting using flow cytometry

Species	Known Concentration (gDCW/L)	Before optimizing protocol (Figure 2(e))		After optimizing protocol (Figure 2(f))	
		Concentration from cell counting (gDCW/L)	Error%	Concentration from cell counting (gDCW/L)	Error%
M. capsulatus	0.0367	0.0043	-88.3%	0.0338	-7.9%
C. sorokiniana	0.0601	0.0709	18.0%	0.0562	-6.5%

3.4.2 Validation of E-C protocol using dynamic growth of the coculture

The E-C protocol is not applicable to the static coculture with known concentrations, as it is based on the growth stoichiometry of individual microorganisms. Therefore, in this subsection, we use coculture batch growth experiments to demonstrate and validate the E-C protocol. With the validity of the cell counting method established, the individual biomass concentration obtained

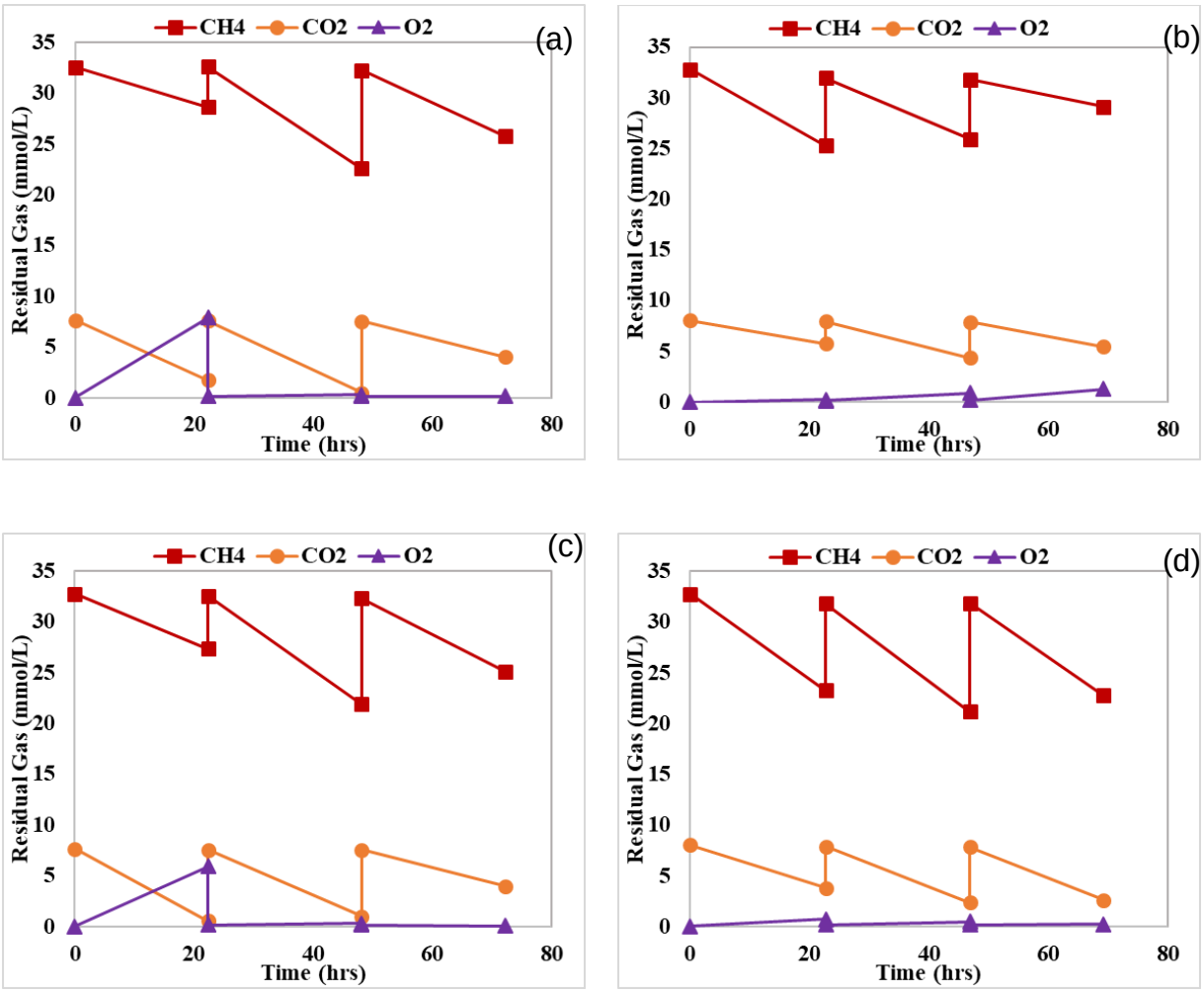

Figure 13. Gas phase composition over three days: (a) salt water coculture pair *M. alcaliphilum* 20ZR – *S. sp.* PCC7002 for inoculum OD ratio of 1:15; (b) fresh water coculture pair *M. alcaliphilum* 20ZR – *S. sp.* PCC7002 for inoculum OD ratio of 1:3; (c) salt water coculture pair *M. alcaliphilum* 20ZR – *S. sp.* PCC7002 for inoculum OD ratio of 1:5; (d) fresh water coculture pair *M. alcaliphilum* 20ZR – *S. sp.* PCC7002 for inoculum OD ratio of 1:1.

from the cell counting method were used to validate the E-C protocol. **Figure 14** (a) and (b) plot the total OD of the coculture over 3 days for the salt water pair and fresh water pair, respectively; and **Figure 14** (c) and (d) plot the gas phase composition for each coculture pair for one inoculum ratio (1:10 for the salt water pair and 1:2 for the fresh water pair), respectively. The gas compositions for the other inoculum ratios are provided in **Figure 13**. For the fresh water methanotroph-microalgae pair, higher inoculum concentration of the microalgae resulted in better

growth of the coculture. This is because the microalgae grows much slower than the methanotroph, so the methanotroph growth is limited by O_2 availability. Therefore, more microalgae in the inoculum enabled better growth of the methanotroph. For the salt water pair, higher inoculation concentration of the cyanobacteria did not have much impact on coculture growth. This is because the cyanobacteria grew much faster than the methanotroph, and the methanotroph growth is limited by mass transfer of CH_4 from gas phase.

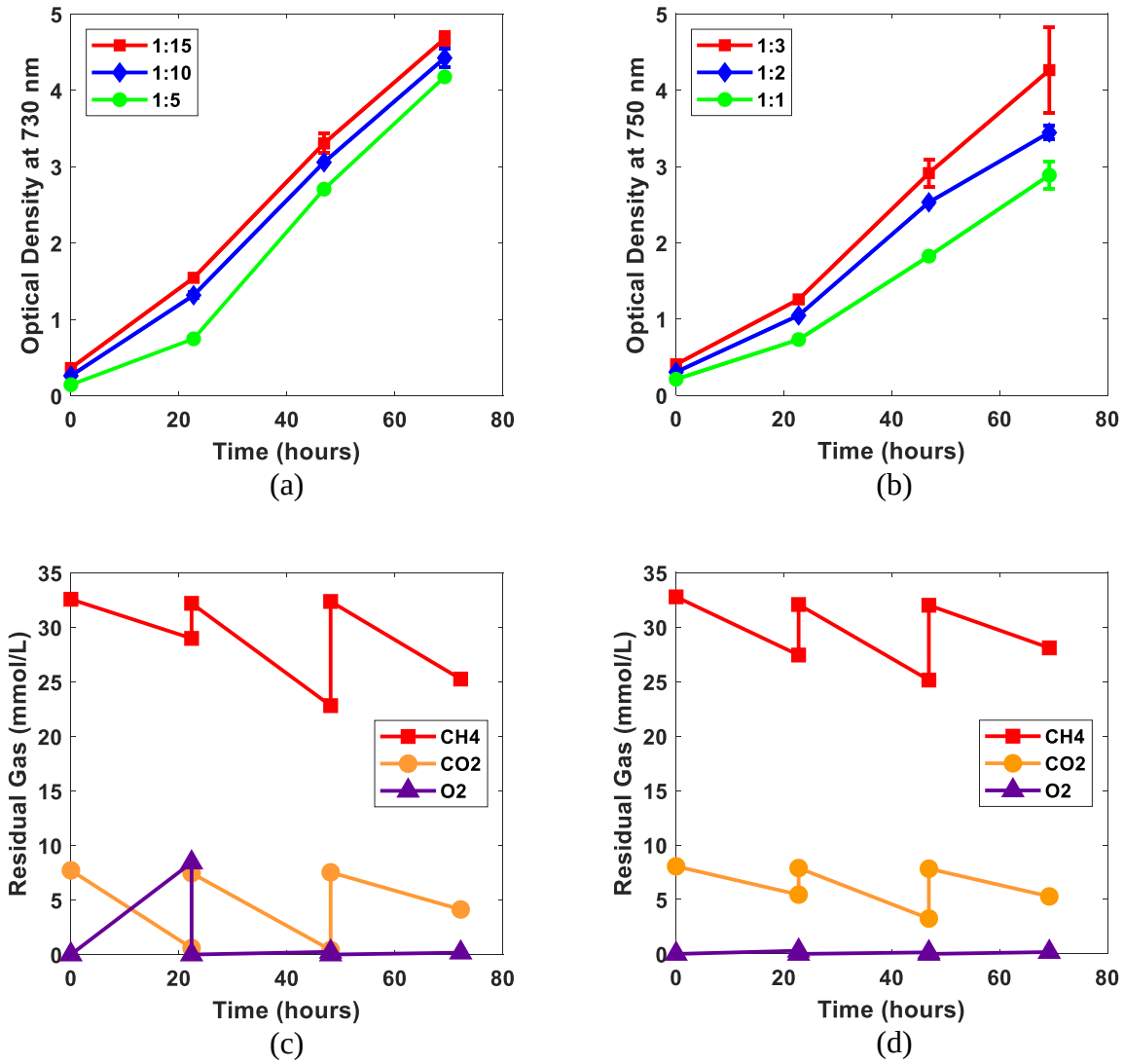

Figure 14. (a) Measured total OD of the salt water coculture pair *M. alcaliphilum* 20ZR – *S. sp.* PCC7002 over three days for inoculum OD ratio of 1:15, 1:10, and 1:5; (b) Measured total

OD of the fresh water coculture pair *M. capsulatus* – *C. sorokiniana* over three days for inoculum OD ratio of 1:3, 1:2, and 1:1; (c) Gas phase composition of salt water coculture pair *M. alcaliphilum* 20ZR – *S. sp.* PCC7002 over three days for inoculum OD ratio of 1:10; (d) Gas phase composition of fresh water coculture pair *M. alcaliphilum* 20ZR – *S. sp.* PCC7002 over three days for inoculum OD ratio of 1:2.

Figure 15 compares the individual biomass concentration measured through the cell counting approach and the E-C protocol for both coculture pairs, where each point represents one of the duplicates, and the error bar represents the standard deviation from three cell counting measurements for the same sample. As can be seen from these figures, the results obtained from the two approaches correlated very well, particularly at low biomass concentrations. The R^2 for the linear relationship between the results from the E-C protocol and cell counting approach ranges 0.90 – 0.98, which validates the results obtained from the E-C protocol.

However, **Figure 15** also shows that the agreement between the cell counting approach and the E-C protocol deteriorates at higher concentrations of coculture growth. To determine which approach performs better, we calculated the total OD for each sample using the measured individual biomass concentrations, and plotted them against the measured total OD. The results are shown in **Figure 16** (a) and (b) for the salt water pair and the fresh water pair respectively. Both figures showed that the total OD calculated from the E-C protocol were almost exactly the same as the measured total OD. On the other hand, the total OD calculated from the cell counting approach showed larger deviation from the measured total OD, particularly at higher concentrations. The bar chart of the mean squared error (MSE) of predictions in the total OD based on six experimental runs (three inoculum concentrations with duplicates) are plotted in **Figure 16**. The error bar represents one standard deviation of MSE's. Student's *t*-test shows that the MSE's of the cell counting is statistically significantly larger than that of the E-C protocol, with a p-value

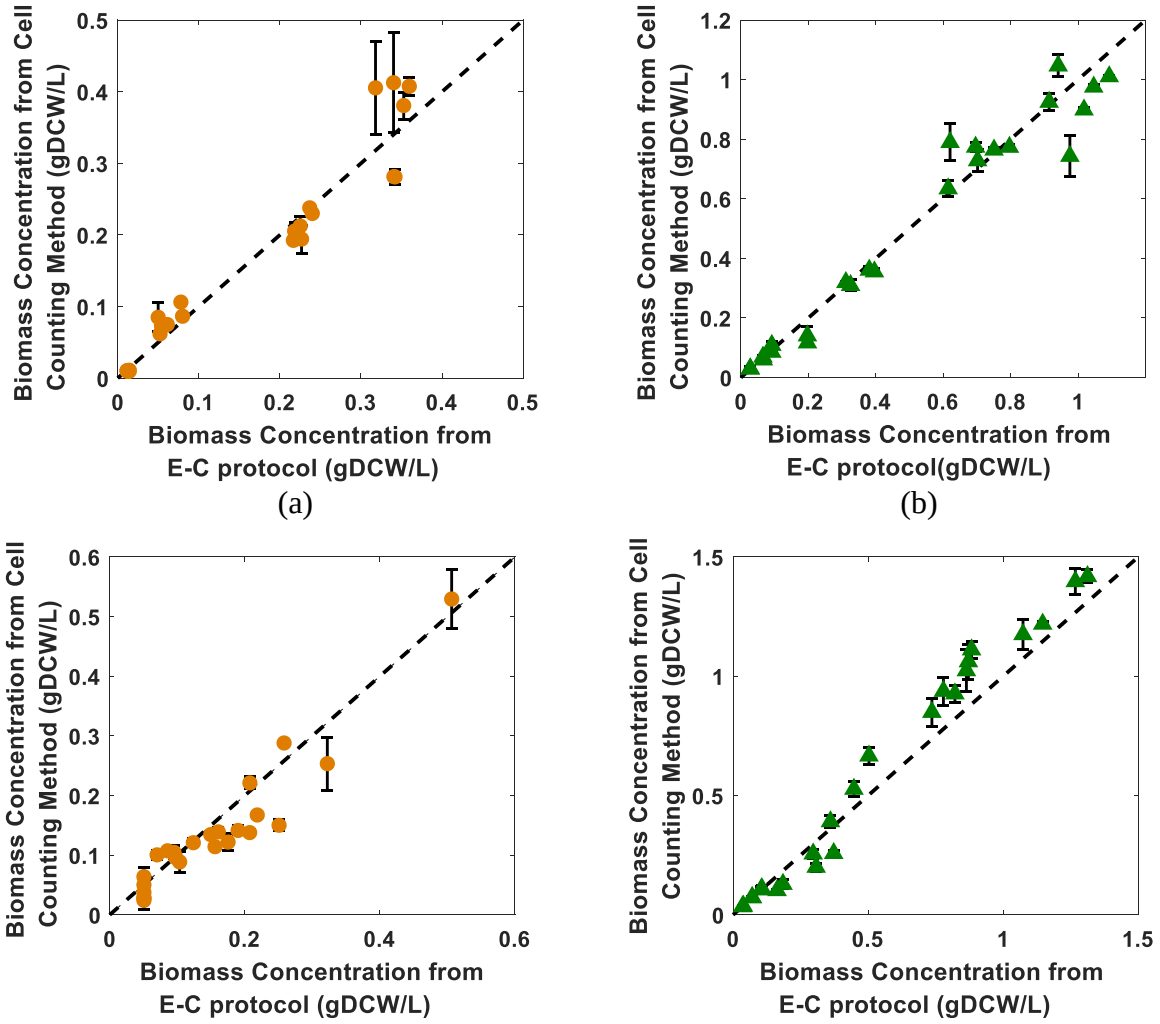

Figure 15. Individual biomass concentration measured through the cell counting approach and the E-C protocol for both coculture pairs, where each point represents one of the duplicate samples, and the error bar represents the standard deviation from three cell counting measurements for the same sample. (a) *M. alcaliphilum* 20ZR; (b) *S. sp.* PCC7002; (c) *M. capsulatus*; (d) *C. sorokiniana*.

Table 4. Biomass concentration vs OD calibration Relationship

M. alcaliphilum 20ZR	Conc(gDCW/L) = OD_{730}×0.4411+0.006
S. sp. PCC7002	Conc(gDCW/L) = OD_{730}×0.2582+0.003
M. capsulatus	Conc(gDCW/L) = OD_{730}×0.5566-0.005
C. sorokiniana	Conc(gDCW/L) = OD_{730}×0.3607-0.003

of 0.0158 for the salt water pair and 0.0030 for the fresh water pair. The calibration relationship between biomass concentration (gDCW/L) and OD for all four strains were obtained through cell drying experiment in house, and are provided in**Table 4**.

Besides obtaining individual biomass concentration for each microorganism in the coculture accurately and quickly, the E-C protocol also provides estimates of individual substrate consumption rates and product excretion rates. **Figure 17** (a) and (b) plot the individual

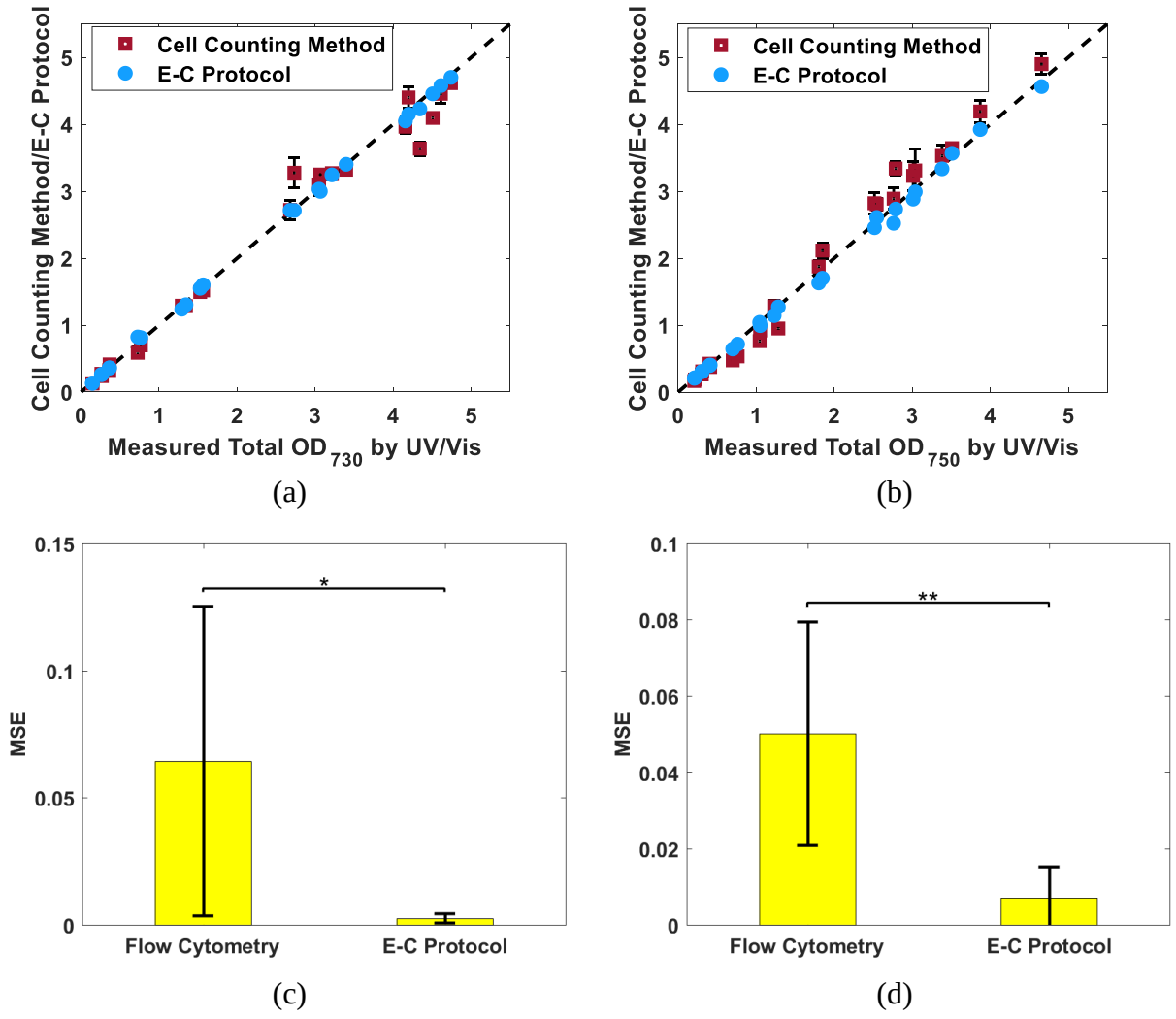

Figure 16. (a) and (b) are the comparison of the measured total OD vs. the total OD calculated using the individual biomass concentrations obtained through cell counting and the E-C protocol: (a) the salt water coculture pair *M. alcaliphilum* 20ZR – *S. sp.* PCC7002; (b) the fresh water coculture pair *M. capsulatus* – *C. sorokiniana*. (c) and (d) are bar chart of MSE

in total OD predictions based on six experimental runs (three inoculum concentrations with duplicates): (c) the salt water coculture pair *M. alcaliphilum* 20ZR – *S. sp.* PCC7002; (d) the fresh water coculture pair *M. capsulatus* – *C. sorokiniana*. The error bar represents one standard deviation of the six MSE's. Student's *t*-tests were performed to compare MSE's of two approaches where symbol '*' denotes p-value ≤ 0.05; '**' denotes p-value ≤ 0.01, indicating the performance improvement of the E-C protocol over flow cytometry is statistically significant at 95% confidence level for the salt water pair and at 99% confidence level for the fresh water pair.

consumption and production rates of O_2 and CO_2 respectively by *M. alcaliphilum* 20ZR and *S. sp.* PCC7002 over a three-day period for the inoculum ratio of 1:10, and **Figure 17** (c) and (d) plot those values for *M. capsulatus* – *C. sorokiniana*, for the inoculum ratio of 1:2.

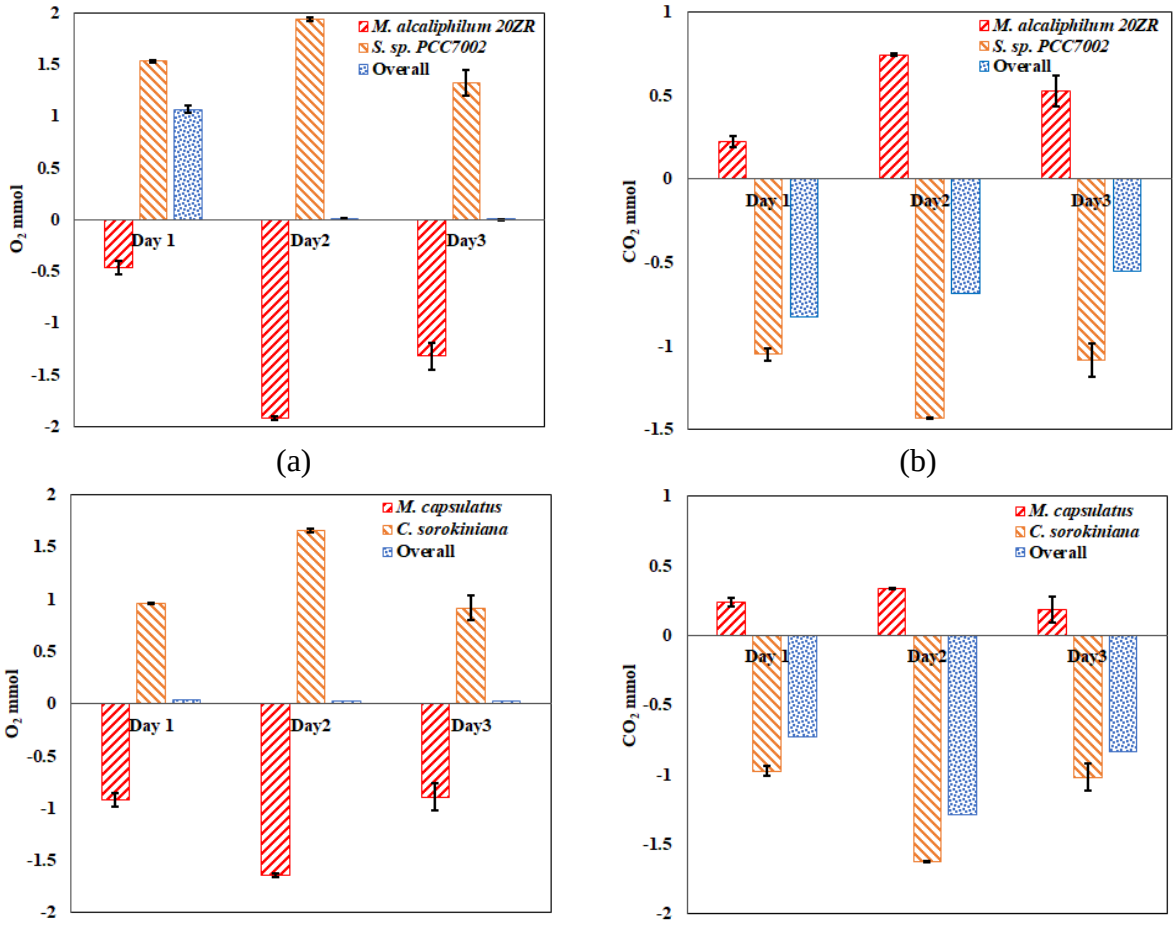

Figure 17. Individual and overall consumption/production rates of O_2 and CO_2 over the growth period of 3 days: (a) O_2 for salt water *M. alcaliphilum* 20ZR – *S. sp.* PCC7002 pair at 1:10 inoculum OD ratio; (b) CO_2 for salt water *M. alcaliphilum* 20ZR – *S. sp.* PCC7002 pair at

1:10 inoculum OD ratio; (c) O_2 for fresh water *M. capsulatus – C. sorokiniana* pair at 1:2 inoculum OD ratio; (d) CO_2 for fresh water *M. capsulatus – C. sorokiniana* pair at 1:2 inoculum OD ratio.

Figure 17 shows that although for many cases very small amounts of O_2 were detected in the gas phase (e.g., day 2 and 3 for the salt water pair and all 3 days for the fresh water pair), significant amount of O_2 was produced by the photoautotroph, which was completely consumed *in situ* by the methanotroph. Similarly, **Figure 17** shows that the actual amount of CO_2 consumed by the photoautotroph was much larger than what was directly measured in the experiment, because the CO_2 produced by the methanotroph would be preferably consumed by the photoautotroph, as it was produced *in situ* and did not involve the mass transfer resistance from gas to liquid.

3.5 Conclusions

It has been recognized that methanotroph-photoautotroph cocultures offer a highly promising biological platform for biogas conversion. Through the interspecies metabolic coupling of CH_4 oxidation to oxygenic photosynthesis, the coculture can simultaneously convert both CH_4 and CO_2 into microbial biomass without external oxygen supply. However, one key obstacle in developing methanotroph-photoautotroph based biotechnology for biogas conversion is the lack of an effective tool for fast, accurate and frequent characterization of the coculture growth dynamics. In this work, based on the organism's growth stoichiometry, the interspecies metabolic coupling and the total mass balance, we developed an E-C protocol to characterize the coculture. The E-C protocol provides not only accurate estimates of the individual biomass concentration within the coculture, but also the individual substrate consumption and product excretion rates of each organism. To the best of our knowledge, the developed E-C protocol is the first ever approach that

could obtain individual substrate consumption and product excretion rates for methanotroph-photoautotroph or any other cocultures.

The accuracy of the developed E-C protocol was validated by cell counting approach using flow cytometry. In addition, by comparing the predicted total OD from the individual biomass concentration with the measured total OD, we showed that the E-C protocol provided better accuracy than the cell counting approach through statistical testing. It is worth noting that the developed E-C protocol only requires commonly used analytical equipment to provide quick and accurate characterization of the methanotroph-photoautotroph cocultures.

Finally, we showed that it is very important to use static cocultures with known concentration to validate the cell counting method, as the cell fixation protocol could result in severely skewed cell counting results. Currently, although cell counting with flow cytometry has become increasingly common in determining the individual biomass concentration in mixed culture or microbiome, very few publications have presented validation results on their cell counting approaches.

3.6 Acknowledgements

This work was supported by U.S. Department of Energy, Office of Science, Office of Biological and Environmental Research, Genomic Science Program (DE-SC0019181), and Department of Education (P200A180002). The authors declare that there is no conflict of interest.

Chapter 4: Semi-structured kinetic modeling for methanotroph-photoautotroph cocultures

Abstract

Through metabolic coupling of CH_4 oxidation and oxygenic photosynthesis, methanotroph-photoautotroph (M-P) cocultures offer a highly promising technology platform for biogas conversion. Real-time accurate characterization of the M-P coculture and kinetic models that can accurately predict the coculture growth under different conditions are key enablers of the M-P coculture based biotechnologies. In our recent work, we have developed an experimental-computational protocol to accurately characterize the M-P coculture in real-time. In this work, we present a semi-structured kinetic model for the M-P coculture that explicitly models the exchange of *in situ* produced O_2 and CO_2. Using *Methylomicrobium buryatense* 5GB1- *Arthrospira platensis* as the model coculture and a series of designed experiments, it was demonstrated that the semi-structured kinetic model can accurately predict the coculture growth under a wide range of growth conditions. In addition, the mechanistic details provided by the validated model enabled fundamental understanding on the coculture growth dynamics.

Redrafted after:

Badr K, He QP, Wang J. Semi-structured kinetic modeling for methanotroph-photoautotroph cocultures. *Bioresource technology*. 2021 (submitted).

4.1 Introduction

Industrial, municipal, and agricultural waste streams containing stranded organic carbon represent a significant and underutilized feedstock to produce fuels and chemicals. Among different waste management approaches, anaerobic digestion (AD) is a mature and efficient solution for handling organic waste streams and mitigating pathogens and odor. During the AD

process, a large fraction (up to 60%) of organic matter is broken down into biogas (50%~70% CH_4, 30%~40% CO_2 and trace amount of contaminants such as H_2S and NH_3). CO_2 and CH_4 are the two leading (GHGs) that cause global warming and many detrimental effects to the earth's ecosystem, and AD enables the containment of biogas produced from waste degradation that otherwise would be released into atmosphere. AD produced biogas can be used to produce energy, including electricity, heat and compress natural gas. In addition, AD contributes significantly to prevent the leaching of excessive amount of N and P into soil and water (both surface and ground water) caused by waste storage (especially manure storage), which has caused severe eutrophication; AD is also highly effective in mitigating odor associated with waste storage and decomposition, as well as removing pathogens that can pose significant risk to animal and human health.

Currently biogas production is led by the European Union and the United States, with other regions (such as Asia, Latin America and Africa) increasingly deploying the technology [83–85]. In 2000, global biogas production was 280 Petajoule, and in 2014, global biogas production increased to 1280 Petajoule, representing an increase of 457% [86]. The biogas potential as a feedstock for producing energy and commodity chemicals is immense across the world. For example, in the United States, more than 2100 biogas plants were operating in 2017, compared to the estimated potential of 13,000 biogas plants that could be built (8241 in farms, 1086 at land fill sites and 3681 at waste water treatment plants) [87]; in Europe, biogas production reached 18 billion m^3 in 2015, while the potential of biogas production is estimated to be about 78 billion m^3 [88]. In China, about 9 billion m^3 biomethane was generated in 2014, compared to the estimated potential of 200-250 billion m^3 biomethane annually [89,90].

Because of the presence of contaminants such as H_2S, ammonia, and volatile organic carbon compounds, the utilization of biogas beyond heat and electricity generation is quite limited. The significant capital expanse (CapEx) and maintain cost required to remove the contaminants, as well as the low value of the products (heat and electricity) results in unfavorable return-of-investment for biogas production. Therefore, despite the fact that AD is a mature technology that can offer significant environmental and social benefits, as well as the enormous energy potential, the deployment of AD is still quite limited. Specifically, for the US, out of 8113 US dairy and swine farms identified by AgSTAR as candidates for profitable AD biogas recovery systems, only 250 (3% of total potential) manure AD biogas recovery systems were in operation in 2017 [19]. To tap into the immense potential of biogas produced from waste streams, effective biotechnologies that can operate at ambient pressure, temperature without requiring biogas cleaning/upgrading and are economically viable at small to mid-scale are needed. In addition, the technologies that can co-utilize both CH_4 and CO_2 are particularly attractive.

Recent studies have demonstrated that natural microbial communities have developed a highly efficient approach to recover energy and recycle carbon from both CH_4 and CO_2 through metabolic coupling of CH_4 oxidation to oxygenic photosynthesis [55–57], as illustrated in **Figure 18**a. This coupling enables significant reductions of CH_4 and CO_2 emission at oxic-anoxic interfaces across various aquatic and terrestrial ecosystems, where the *in situ* photosynthetic production of O_2 enables methanotrophic activities [55]. Inspired by these research findings, different methanotroph-photoautotroph (M-P) cocultures have been examined recently for biogas conversion. For example, van der Ha et al. [58] reported that a coculture of *Methylocystis parvus-Scenedesmus sp.* could completely convert a synthetic biogas (60% CH_4, 40% CO_2) into microbial biomass without external oxygen supply; Hill et al. [59] demonstrated that *Methylomicrobium*

alcaliphilum- *Synechococcus* PCC 7002 could maintain stable growth on gas mixtures with wide range of composistions, including raw biogas and synthetic biogas; Most recently, Rasouli et al. [24] and Roberts et al. [63] showed that *Methylococcus capsulatus*- *Chlorella sorokiniana* can efficiently recover nutrient (N and P) contained in waste water while converting biogas into microbial biomass.

These recent developments clearly demonstrated that M-P cocultures offer a highly promising biotechnology platform for biogas conversion. For the development of various biotechnologies. kinetic models that can accurately predict microbial growth and product excretion patterns under different conditions serve as an essential tool. A high-quality kinetic model provides a foundation to guide the design, optimization and scale up of the bioreactors, as well as the optimization of the operation conditions and controls of the bioreactor. However, most of the existing results on the M-P coculture are limited to qualitative proof-of-concept experiments, and there is a lack of quantitative understanding on the growth kinetics of the M-P coculture. Given the added complexity of the M-P cocultures, i.e., *in situ* exchange of CO_2 and O_2 between the methanotroph and the photoautotroph, as well as the largely unknown interspecies interactions, obtaining a kinetic model is highly challenging, but also imperative for the development of the coculture-based biogas conversion technologies.

A prerequisite to the development of a coculture kinetic model is the time-series measurements of individual biomass concentrations in the coculture, as well as the individual substrate uptake rates and product excretion rates. Currently, there is a lack of effective tools to obtain the real-time, accurate measurements for each species in the coculture needed for kinetic modeling. To address this challenge, we recently developed an experimental-computational (E-C) protocol to deliver fast, easy and accurate quantitative characterization of the M-P coculture. The

E-C protocol only uses easily measured variables such as gas compositions and total inorganic carbon in liquid broth, and doesn't require specialized equipment such as flow cytometer, or advanced technologies such as next-generation sequencing. Based on each organism's growth stoichiometry, the interspecies metabolic coupling of O_2/CO_2, and the total mass balance, the E-C protocol provides not only accurate estimates of the individual biomass concentration, but also the individual substrate consumption and product excretion rates. The accuracy of the E-C protocol was validated via the cell counting approach using flow cytometry on two model M-P coculture pairs. In addition, by comparing the total OD predicted using the individual biomass concentration determined through either the E-C protocol or flow cytometer with that directly measured via a UV/Vis spectrometer, it was demonstrated through statistical testing that the E-C protocol delivered better accuracy than the cell counting approach using flow cytometer. More details of the E-C protocol can be found in [91].

Enabled by the real-time characterization of the M-P coculture, in this work we report a semi-structured kinetic model that can accurately predict the individual growth rate, as well as the individual consumption/production rates of O_2 and CO_2 for the methanotroph and photoautotroph in the coculture under a wide range of growth conditions. We term the developed kinetic model "semi-structured", because the exchange of *in situ* produced O_2 and CO_2 between the two species explicitly captured in the model. The rest of the paper is organized as the following: Method and Material are covered in Section 4.2, which also include the details of the developed semi-structure kinetic model; Results (both experimental and computational) and discussion are provided in Section 4.3, and Conclusions are provided in Section 4.4.

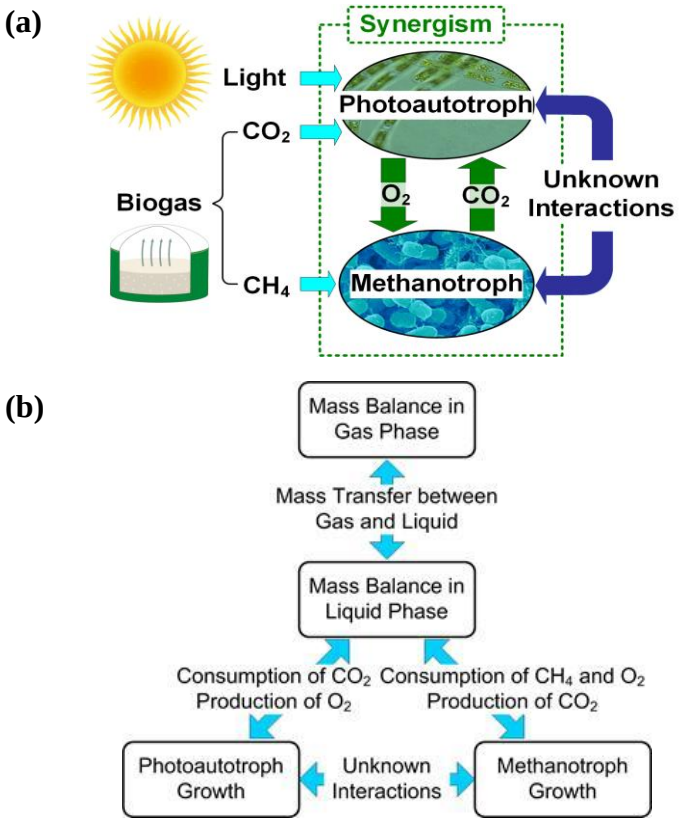

Figure 18. (a) Illustration of metabolic coupling of methane oxidation to oxygenic photosynthesis, (b) an overview of the semi-structured kinetic modeling framework

4.2 Method and Material

4.2.1 Strains and media

Methylomicrobium buryatense 5GB1 (provided by Prof. Mary Lidstrom, University of Washington) and *Arthrospira platensis* (UTEX LB 2340) were grown under coculture and axenic conditions. All cultures were grown in one of the two previous described minimal salts media, NMS2 medium [62] or Zarrouk medium [92], or the mixture of these media (10% NMS2 and 90% Zarrouk).

4.2.2 Batch cultivations

The growth experiments of the *M. buryatense* 5GB1- *A. platensis* coculture and their sequential single culture were conducted using sealed 250 ml serum bottles with working volumes

of 100 ml. All bottles placed in a rotary shaker set at 200 rpm, with a temperature of 30°C and pH kept at 8.8-9. Various factors were tested to examine their effect on the coculture growth, and the conditions for each set of designed experiments are listed **Table 5**.

Table 5. Various conditions for each set of designed coculture experiments

Experiment (Case)	System	Condition	Gas (CH_4:CO_2:O_2)*	Inoculum ratio (P:M)	Light intensity (μmol/m^2 s)
A	Coculture	a	70:30:0	12.5 : 1	180
		b			60
B	Light intensities	a	80:20:0	12.5 : 1	180
		b			140
		c			100
		d			60
C	Gas compositions	a	20:10:0	12.5 : 1	180
		b	60:30:0		
		c	60:30:10		
		d	80:20:0		
D	Inoculum ratios	a	80:20:0	12.5 : 1	180
		b		8.5 : 1	
		c		4 : 1	
		d		1.5 : 1	
E	Coculture vs Sequential single culture	coculture	70:30:0	12.5 : 1	180
		A. platensis	70:30:0	Inoculum conc. (0.218 gDCW/L)	
		M. buryatense	70:30:0**	Inoculum conc. (0.018 gDCW/L)	

* Volume/mole percentage. N_2 is the inert gas to make up to 100% when needed.
** The oxygen produced by the single photoautotroph was injected to the single methanotroph

For each growth experiment, after inoculation, the bottles were flushed with appropriate feed gas for 15 minutes, and the bottles were refed every 24 hours. All experiments were carried out with triplicates. Gas and liquid samples were taken twice per day, before and after feeding. Compositions of the gas samples were analyzed following a protocol we published previously [78]. For the liquid samples, total optical density (OD), pH and total inorganic carbon (TIC) were measured following our previous work [63]. Individual biomass concentrations were determined using the E-C protocol [91].

4.3 Semi-structured kinetic modeling framework for the M-P coculture

Figure 18b provides an overview of the semi-structured kinetic modeling framework for the M-P coculture. The overall kinetic model consists of four components: (1) biomass growth of the photoautotroph; (2) biomass growth of the methanotroph; (3) mass balance in liquid phase; and (4) mass balance in gas phase. The interdependency among different components is also shown in the figure, where the growth of each organism in the coculture is coupled with the gas phase composition changes through the mass balances in the liquid and gas phase. As gas composition can be measured accurately, such coupling provides an additional route for model validation.

Table 6. Variables used in the semi-structured kinetic model

j	:	superscript indicating different microorganism; M = methanotroph, P = photoautotroph;
i	:	subscript indicating different metabolite, (e.g., CH_4, O_2, CO_2, or a = light intensity);
k	:	subscript indicating concentration of different phases; g = gas, l = liquid;
X^j	:	biomass concentration of species j (g/L);
μ^j_{max}	:	maximum growth rate of species j (1/hr);
μ^j	:	growth rate of species j (1/hr);
$K^j_{S,i}$	:	half saturation constant of substrate i for species j, (mmol/L);
v^j_i	:	consumption/production rate of metabolite i for species j, (mmol/g hr);
$[\,i\,]_k$	:	concentration of metabolite i in phase k, (mmol/L);
H^e_i	:	effective Henry's constant for gas substrate i, (-);
$Y^j_{a/b}$	:	yield coefficient between metabolite i and biomass for species j; $i = CH_4, O_2, or\ CO_2$; $j = M\ or\ P$ (mmol/g)
I	:	light intensity, (μmol photons m^{-2} s^{-1});
V_k	:	volume of liquid and gas phase in the system, (L);
$k_L a_i$	:	volumetric mass transfer coefficient for substrate i, (1/hr).

In the semi-structured kinetic modeling framework, cell growth is described using Monod equations; the substrate consumption rates and product excretion rates are determined through the yield coefficients between the corresponding substrate/product and the biomass. We term the coculture kinetic model a semi-structured model, as the exchange of *in situ* produced O_2 and CO_2 were explicitly modeled in the framework, while the other potential interspecies interactions were captured through lumped parameters, i.e., maximum growth rate of each organism. **Table 6** listed the notations of the variables utilized in this work. In the following, we describe each modeling component in detail.

4.3.1 Growth of the photoautotroph

The growth of the photoautotroph is described using Monod model, as shown in Eqn. (14), where CO_2 and light energy input (I_a) are the two substrates. CO_2 uptake rate and O_2 production rate are determined through the corresponding yield coefficients with respect to biomass production, i.e., Eqns (15) & (16); As the available light energy to the cells in the culture broth depends on the biomass concentration due to the "self-shading" effect, we use the Beer-Lambert law for light distribution to estimate the light attenuation effect [93]. As shown in Eqn. (17), I_0 is the direct measurement of incident light intensity ($\mu mol\, m^{-2}s^{-1}$); m is the absorption coefficient, $m = aI_0 + b$, where the model parameters (i.e., a and b) were estimated using coculture growth experiments under the highest and lowest incident light intensities (180 $\mu mol\, m^{-2}s^{-1}$and 60 $\mu mol\, m^{-2}s^{-1}$respectively in this work).

$$\mu^{P} = \mu^{P}_{max} \cdot \frac{[CO_2]_l}{K^P_{S,CO_2}+[CO_2]_l} \cdot \frac{I_a}{K^P_{S,I}+I_a} \quad (14)$$

$$v^P_{CO_2} = \mu^P . Y_{CO_2/X^P} \quad (15)$$

$$v^P_{O_2} = \mu^P . Y_{O_2/X^P} \quad (16)$$

$$I_a = I_0 \exp\left[-m(X^M + X^P)\right] \quad (17)$$

4.3.2 Growth of the methanotroph

Similar to the photoautotroph, the growth of the methanotroph is also described using Monod model, as shown in Eqn. (18), where CH_4 and O_2 are the substrates. CH_4 and O_2 uptake rates, as well as CO_2 production rate are determined through the corresponding yield coefficients as shown in Eqns (19) - (21).

$$\mu^{M} = \mu^{M}_{max} \cdot \frac{[O_2]_l}{K^M_{S,O_2}+[O_2]_l} \cdot \frac{[CH_4]_l}{K^M_{S,CH_4}+[CH_4]_l} \quad (18)$$

$$v^M_{CH_4} = \mu^M . Y_{CH_4/X^M} \quad (19)$$

$$v_{O_2}^M = \mu^M . Y_{O_2/X^M} \quad (20)$$

$$v_{CO_2}^M = \mu^M . Y_{CO_2/X^M} \quad (21)$$

4.3.3 Mass balance in liquid phase

The mass balance in the liquid phase links the coculture growth and gas phase composition changes. In this work, the dissolved CH_4 and O_2 concentrations in the liquid phase were not measured, therefore cannot be used for model validation. In fact, the dissolved CH_4 concentration has hardly been reported in the literature due to the lack of CH_4 probes. The dissolved O_2 concentration was not measured due to limited volume of the serum bottle. In addition, as the growth of the methanotroph is usually under oxygen-limited condition, the dissolved O_2 concentration can be close to zero and may not be detectable, which is the case for all the conditions tested in this work except for the case where external O_2 is provided through feed gas.

For different gas components, the mass balance consists of the amount of the gas component transferred from the gas phase, as well as the amount produced and/or consumed by the methanotroph or photoautotroph. In this way, the exchange of *in situ* produced CO_2 and O_2 can be directly captured by its corresponding mass balance, as shown in Eqn. (23) and (24). Finally, Eqns. (25) and (26) describe the biomass accumulation in the liquid phase.

$$\frac{d[CH_4]_l}{dt} = k_l a_{CH_4}\left(H_{CH_4}^e [CH_4]_g - [CH_4]_l\right) - v_{CH_4}^M X^M \quad (22)$$

$$\frac{d[O_2]_l}{dt} = k_l a_{O_2}\left(H_{O_2}^e [O_2]_g - [O_2]_l\right) - v_{O_2}^M X^M + v_{O_2}^P X^P \quad (23)$$

$$\frac{d[CO_2]_l}{dt} = k_l a_{CO_2}\left(H_{CO_2}^e [CO_2]_g - [CO_2]_l\right) - v_{CO_2}^P X^P + v_{CO_2}^M X^M \quad (24)$$

$$\frac{dX^P}{dt} = \mu^P X^P \quad (25)$$

$$\frac{dX^M}{dt} = \mu^M X^M \quad (26)$$

The above mass balance equations were derived based on the assumption of batch cultivation, which can be easily modified to continuous cultivation.

As indicated in Eqns. (22) – (24), we assume ideal mixing of the liquid phase and ignore the mass transfer resistance associated with the transport of the dissolved gas substrate across the bulk liquid phase to reach the cells. This simplification is reasonable, as in this work the liquid volume was small (100 ml) and the vials were under continuous rotation (200 rpm). As shown in "Result and Discussion", this simplification was validated by the experimental results, as the model predictions (both individual biomass concentrations and gas phase compositions) showed excellence agreement with experimental measurement under wide range of growth conditions.

4.3.4 Mass balance in gas phase

The concentration of different gas components in the gas phase is linked to those in the liquid phase through mass transfer between the two phases. As shown in Eqns. (27) – (29), we assume the distribution of various gas components between the gas and liquid phase are at equilibrium all the time. In order to capture the effect of the biomass and culture medium on the solubility of different gas components, we used effective Henry's constant to determine the solubility of different gas components in the coculture broth

$$\frac{d[CH_4]_g}{dt} = -k_l a_{CH_4}(H^e_{CH_4}[CH_4]_g - [CH_4]_l)\frac{V_L}{V_G} \quad (27)$$

$$\frac{d[O_2]_g}{dt} = -k_l a_{O_2}(H^e_{O_2}[O_2]_g - [O_2]_l)\frac{V_L}{V_G} \quad (28)$$

$$\frac{d[CO_2]_g}{dt} = -k_l a_{CO_2}(H^e_{CO_2}[CO_2]_g - [CO_2]_l)\frac{V_L}{V_G} \quad (29)$$

It is worth noting that it has been very challenging to determine the partition of CO_2 between the gas phase and liquid culture broth, mainly due to the dissociation of dissolved CO_2 into HCO_3^- and CO_3^{2-} ($CO_2 \leftrightarrow H_2CO_3 \leftrightarrow HCO_3^- + H^+ \leftrightarrow HCO_3^- + 2H^+$). To address this challenge, we didn't

differentiate the various forms of dissolved CO_2, instead, we lumped them all into a "total dissolved CO_2" that can be tracked experimentally by measuring total inorganic carbon (TIC) of the liquid sample. Then the partition of the CO_2 between the gas and liquid phase (i.e., total dissolved CO_2) can be determined using a linear empirical relationship obtained through designed experiments.

Since gas phase composition can be measured accurately, the coupling of the gas phase, liquid phase and coculture growth provides an additional route to validate the kinetic model. If the model predicted gas phase composition agrees with the experimental measurements over time, it would be very convincing that the semi-structured kinetic model can accurately describe the coculture growth dynamics, and many details predicted by the kinetic model that are difficult to obtain experimentally could help reveal what actually happened in the coculture liquid broth.

4.4 Results and Discussion

In this work, using *M. buryatense* 5GB1 and *A. platensis* as the model coculture, we first use batch growth experiments to demonstrate that the semi-structured kinetic model can adequately capture and accurately describe the growth dynamics of the M-P coculture. The parameters involved in the semi-structured kinetic model were determined based on literature as well as data obtained from just two coculture batch growth experiments (under the same condition except with different light intensities) as a training step. Next, we examine the effect of different environmental factors on the coculture growth, which include light intensity, gas composition and inoculum ratio, as the testing step. The experimental measurements obtained under a wide range of growth conditions were compared with model predictions (using the same set of model parameters) to validate the model. Once validated, the mechanistic details that are difficult to measure experimentally can be obtained through *in silico* experiments using the kinetic model to

obtain fundamental understanding on the M-P coculture growth dynamics. An overview of training and validating (testing) the model is shown in **Table 7**. Finally, by comparing the coculture growth with sequential single culture growth using both wet lab experiments and kinetic modeling, we were able to confirm the existence of other emergent metabolic interactions, in addition to the exchange of the *in situ* produced O_2 and CO_2, as well as to quantify the effect of these unknown metabolic interactions on coculture growth.

Table 7. An overview of training and testing the Semi structured kinetic model

Semi structured kinetic model	
Step	**Used Experiments**
Training (fitting)	A (two conditions)
Validating (testing)	B (four conditions)
	C (four conditions)
	D (four conditions)

4.4.1 The semi-structured kinetic model accurately captures the coculture growth dynamics

Table 8. Optimized values of model parameters based on literature and experimental data

Parameter	Obtained value	Unit	Ref.	Parameter	Obtained value	Unit	Ref.
$\mu^{P}_{max}{}^{\text{single}}$	0.024	hr^{-1}	[94]	$Y^{P}_{\frac{CO_2}{X^P}}$	31.85	$mmol/gDCW$	[95]
$\mu^{M}_{max}{}^{\text{single}}$	0.098	hr^{-1}	This study	$Y^{P}_{\frac{CO_2}{X^P}}$	40.82	$mmol/gDCW$	[96]
$\mu^{P}_{max}{}^{\text{coculture}}$	0.034	hr^{-1}	This study	$Y^{M}_{\frac{CH_4}{X^M}}$	85.47	$mmol/gDCW$	[97,98]
$\mu^{M}_{max}{}^{\text{coculture}}$	0.145	hr^{-1}	This study	$Y^{M}_{\frac{CO_2}{X^M}}$	40.98	$mmol/gDCW$	[97]
K^{P}_{S,CO_2}	0.240	$mmol\ L^{-1}$	[99]	$Y^{M}_{\frac{O_2}{X^M}}$	114.94	$mmol/gDCW$	[97]
K^{M}_{S,O_2}	0.005	$mmol\ L^{-1}$	[100]	H_{CH_4}	0.0014	$mol\ L^{-1}\ atm^{-1}$	[101]
K^{M}_{S,CH_4}	0.028	$mmol\ L^{-1}$	[100,102]	H_{O_2}	0.0013	$mol\ L^{-1}\ atm^{-1}$	[101]
$K^{P}_{S,I}$	4.33	$\mu mol\ m^{-2}s^{-1}$	This study	H_{CO_2}	0.035	$mol\ L^{-1}\ atm^{-1}$	[101]
a	-0.0175	-	This study	$H^{e}_{CH_4}$	0.0341	-	This study
b	6.40	-	This study	$H^{e}_{O_2}$	0.0317	-	This study
$k_L a_{CH_4}$	100	h^{-1}	[103]	$H^{e}_{CO_2}$	1.6120	-	This study
$k_L a_{O_2}$	$1.17 \times k_L a_{CH_4}$	h^{-1}	[104]				
$k_L a_{CO_2}$	$0.90 \times k_L a_{CH_4}$	h^{-1}	[105]				

In this subsection, we use the model fitting performance to demonstrate that the semi-structured kinetic model can adequately capture and accurately describe the growth dynamics of the coculture. The conditions for the designed coculture growth experiments in this subsection are listed in **Table 5** (Experiment A). Specifically, the coculture was cultivated under continuous illumination with light intensity of 60 or 180 $\mu mol\ m^{-2}s^{-1}$, inoculum ratio of 12.5 :1 (P:M) and gas composition of 70%CH_4, 30% CO_2.

The model parameters were determined based on available literature data and fitting to the experimental data (Experiment A). The fitted model parameters for the coculture of *M. buryatense* 5GB1-*A. platensis* are provided in **Table 8**, and were utilized in all the model predictions for the rest of the paper.

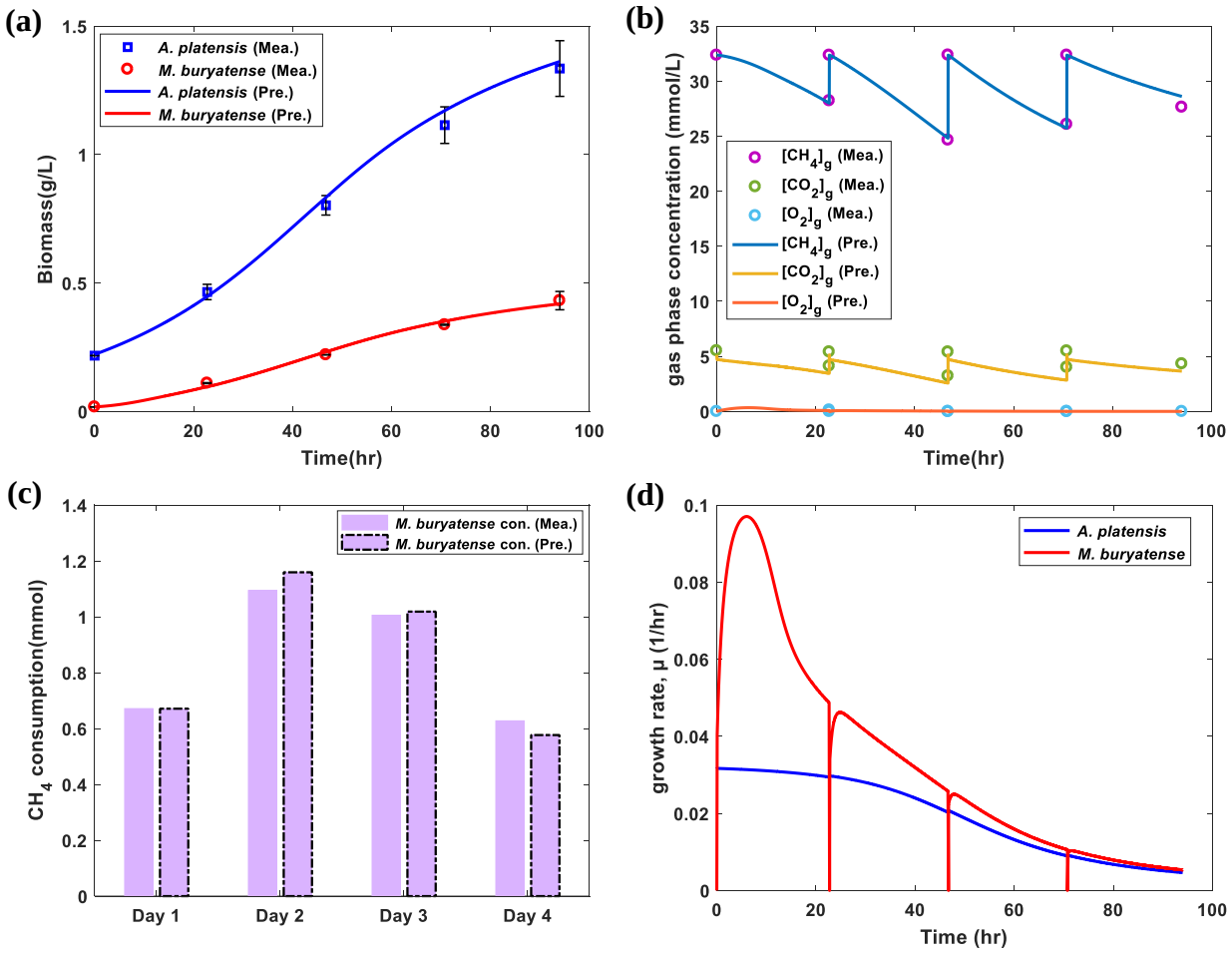

Figure 19. Comparison of the experimental measurements with the model prediction for various variables, (a) the individual biomass concentrations, (b) gas composition, (c) CH_4 consumption for each day, (d) individual growth rates (model prediction only).

Figure 19 compares the experimental measurements with the model prediction for various variables: the individual biomass concentrations (**Figure 19**a, measurements obtained through the E-C protocol), gas composition (**Figure 19**b), CH_4 consumption for each day (**Figure 19**c) and individual growth rates (**Figure 19**d, model prediction only). The reset of the gas phase composition every 24 hours was due to the refeeding that happened daily. Similarly, the model predicted growth rate for the methanotroph dropped to zero after refeeding because dissolved O_2 became zero due to refeeding.

These results showed excellent agreement between the model fitting and experimental measurements, which clearly demonstrated that the semi-structured kinetic model can adequately capture and accurately describe the growth dynamics of the coculture. Specifically, the excellent agreement between the measured and model predicted gas phase composition over time confirmed that the integration of the four modeling components were accurate.

For the rest of the paper, the same set of model parameters were utilized to predict the coculture growth under different conditions, which were compared with experimental measurements to further validate the model. Once validated, the semi-structured kinetic model provides many details that cannot be directly measured in real-time, which not only allowed us to gain better understanding of the coculture growth dynamics, but also enabled us to test different hypotheses easily.

4.4.2 The effect of light intensity

We hypothesize that photosynthesis rate is a key factor that determines the coculture growth rate, as the growth of the methanotroph depends on the O_2 availability and the CO_2 produced by the methanotroph could fuel additional growth of the photoautotroph. To test this hypothesis, we performed the set of designed experiments as shown in **Table 5**, Experiment B. These set of experiments were conducted under the same growth conditions except the different light intensities (60, 100, 140, 180 $\mu mol\ m^{-2}s^{-1}$).

The model predicted individual biomass concentrations (**Figure 20**a for *M. buryatense* 5GB1 and **Figure 20**b for *A. platensis*) were first compared with experimental measurements to validate the model. The excellent agreement between experimental measurements and model predictions under different light intensities clearly validated the accuracy of the semi-structured kinetic model. Further, **Figure 20**a & b shows that increasing light intensity not only enhanced the growth of *A. platensis*, but also the growth of the *M. buryatense* 5GB1, confirming our hypothesis.

Figure 20c & d plotted the model predicted individual growth rates for *M. buryatense* 5GB1 and *A. platensis* respectively, and there are two interesting observations. First, the growth rate of *A. platensis* kept decreasing over the course of the batch experiment; while the growth rate of *M. buryatense* 5GB1 initially increased and reached a maximum, then kept decreasing afterward. Second, the enhancement on cell growth rates driven by higher light intensity diminished over time. The decreasing cell growth rates and diminishing improvement on cell growth over time could be attributed to two possible reasons. One reason is the carbon substrate limitation - due to the mass transfer resistance, the total amount of gas components transferred from the gas phase to the liquid phase would be limited; therefore, with the increasing biomass over time, the specific carbon uptake rate per unit biomass would decrease and cause decreasing cell growth rate; the other possible reason is the light availability limitation due to self-shading

effect: as the total biomass concentration in the liquid broth increased, light attenuation caused by self-shading could limit the photosynthesis rate which in turn reduces the cell growth rate of the photoautotroph. In this work, the limitation of macronutrient is not considered as a potential reason, as the coculture medium contained sufficient amount of nutrient by design.

To determine the underlying reason for the decreasing cell growth rates and the diminishing effect on cell growth enhancement, we first examined the total substrate uptake rate (CH_4 and O_2 for *M. buryatense* 5GB1 and CO_2 for *A. platensis*), which are plotted in **Figure 20**e. If carbon substrate limitation caused by the combination of mass transfer resistance and increasing biomass were the true cause, the total substrate uptake rates (mmol/hr) would initially increase as the biomass concentration increases, then reach a maximum and maintain at the maximum, where the maximum would be determined by the mass transfer rate of the gas substrate. However, as shown in **Figure 20**e, the total substrate uptake rates first increased as expected, but then decreased. In addition, the total uptake of CH_4, O_2 and CO_2 all followed the same trend. This suggest that carbon substrate limitation was not the reason for the decreasing cell growth and diminish enhancement observed in the experiment. As discussed in the next subsection, the CO_2 needed for photosynthesis was mainly provided through dissolved CO_2 due to the high pH medium, and was never in limitation in this research. Therefore, the decreasing CO_2 uptake rate was most likely driving by the limitation of light availability due to self-shading effect, and the reduced O_2 supply at higher biomass concentration in turn limited the CH_4 uptake rate. As the coculture biomass concentration increased, the light availability limitation resulted in the decrease of total substrate uptakes rates, which resulted in the decreasing of cell growth rates for both *A. platensis* and *M. buryatense* 5GB1; in addition, although higher light intensity enables the faster growth of the

coculture initially, the faster increase in the coculture biomass also resulted in more severe light attenuation, which resulted in the diminishing effect on cell growth enhancement over time.

To verify this explanation, we conducted *in silico* experiment to simulate the coculture growth without self-shading effect. This was achieved by simply setting $I_a = I_o$, and the resulting total substrate uptake rates are shown in **Figure 20**f. When the biomass concentration was low, it is clear that the total substrate consumption rate, with or without considering self-shading effect, did not show much difference. All three gas components initially were at the similar level and self-shading effect was negligible as those in **Figure 20**e; however, when the coculture biomass concentration became higher and self-shading effect became dominant, the simulated coculture growth without self-shading effect showed substrate uptake rates kept increasing over time. A local maximum was achieved at about 71 hours, where the total substrate consumption rates dropped to zero because of the substrate provided through gas phase had been completely consumed. Then at 72 hours when the vial was refed, the growth of coculture resumed and reached even higher level until the substrates were fully consumed again before next feeding. However, in the actual coculture growth with self-shading effect, the cell growth is limited by light availability far before mass transfer becomes the limiting factor.

The comparison of the individual biomass production and cell growth rate with and without self-shading effect showed that without self-shading effect, the total biomass achieved could be three times higher than the actual case with self-shading effect. This result suggest that light availability is usually the limiting factor when photosynthesis is involved, far before mass transfer becomes the limiting factor. Therefore, improving light availability should be the primary consideration for improving photo-synthesis rate and enhancing mass transfer of CO_2 the secondary consideration.

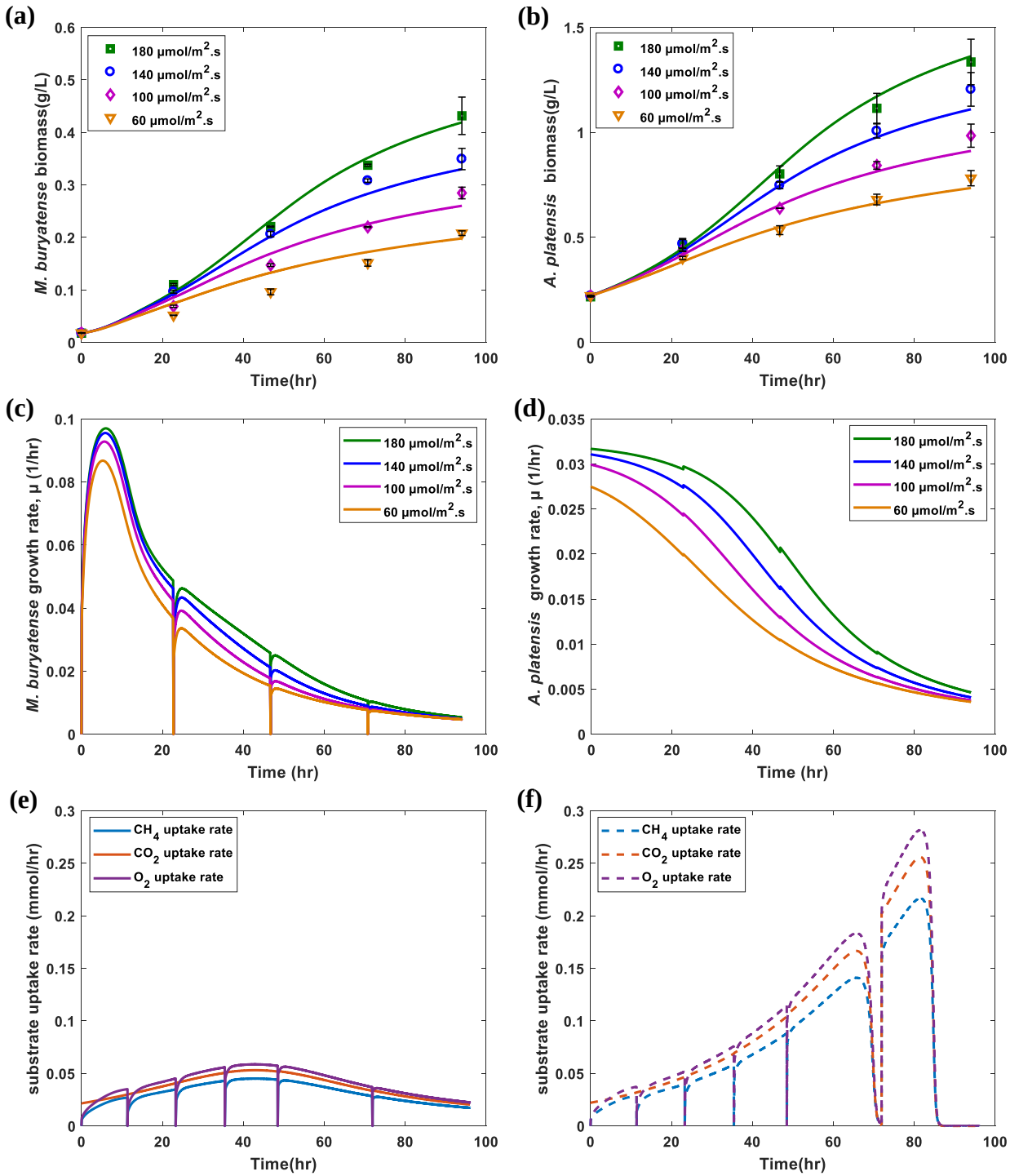

Figure 20. Comparison of the model predicted individual biomass concentrations with experimental measurements for (a) *M. buryatense* 5GB1 (b) *A. platensis*. The model predicted individual growth rates for (c) *M. buryatense* 5GB1 and (d) *A. platensis*. The model predicted total substrate uptake rate (e) with self-shading effect, (f) without self-shading effect.

It is worth noting that in the semi-structured kinetic model, ideal mixing of both gas phase and liquid phase was assumed. In general, such simplification is deemed reasonable for bench scale reactors with sufficient agitation. However, mass transfer resistance in the liquid phase cannot be ignored for large-scale bioreactors and must be considered for scale up.

4.4.3 The effect of gas composition

As the growth of methanotroph in the coculture is usually limited by the oxygen availability, the gas phase composition, in addition to the photosynthesis rate, could serve as a key manipulated variable to control the growth and population ratio of the coculture. In this section, we examine the effect of the gas phase composition on the coculture growth. As shown in **Table 5** (Experiment C), four different gas compositions (with CH_4:CO_2:O_2 of 20:10:0; 60:30:0; 60:30:10; 80:20:0) were compared, while the other growth conditions were fixed.

Figure 21a & b plot the individual biomass concentration and **Figure 21**c & d plot the growth rate under different gas compositions for *M. buryatense* 5GB1 and *A. platensis* respectively. **Figure 21**b suggests that different CO_2 content in the feed gas didn't have much impact on the growth of *A. platensis*, which can be attributed to the high pH medium and the way the bottle was fed. During the daily feeding, the bottle was flushed with the feed gas for 15 minutes to ensure the distribution equilibrium between the gas and liquid phase for different gas components was achieved. Due to the high pH of the culture broth (pH 8-9), there were large amount of CO_2 dissolved in the form of HCO_3^- and CO_3^{2-}. Therefore, the supply of CO_2 for phototroph growth was mainly through various forms of dissolved CO_2 (including CO_2 produced by the methanotroph) instead of the CO_2 contained in the headspace of the bottle. Regardless of the CO_2 content in the feed gas, the reduction of gas phase CO_2 concentration has been limited, and gas phase CO_2 was never depleted before the next feeding. **Figure 21**d confirmed that the

growth rate of *A. platensis* under different feed gas composition followed the same trajectory and overlapped with each other, further confirming that CO_2 supply was barely affected by changing CO_2 content in the feed gas.

Similarly, **Figure 21**a suggests that the CH_4 content in the feed gas has little effect on the growth of *M. buryatense* 5GB1; instead, it is the O_2 content in the feed gas that has significant impact on the growth of the methanotroph. When there was 10% of O_2 in the feed gas, *M. buryatense* 5GB1 showed significantly improved growth. As shown in **Figure 20**c, the growth rate of *M. buryatense* 5GB1 from different gas compositions large overlap with each other, except the one with 10% O_2 in the feed gas. For the condition with 10% O_2, *M. buryatense* 5GB1 showed significantly elevated growth right after the daily feeding when abundant amount of O_2 was available. As the external O_2 supply was quickly depleted, the growth rate of *M. buryatense* 5GB1 dropped to a level that was lower than the conditions without external O_2 supply. Since the amount of O_2 produced by *A. platensis* were almost the same across the different conditions, the higher biomass concentration of *M. buryatense* 5GB1 resulted from external O_2 supply resulted in lower specific O_2 uptake rate and therefore lower growth rate after the external supply was depleted. In addition, these results confirm that O_2 content in the feed gas can serve as an effective "control knob" for the coculture growth. By adding 10% of O_2 into gas phase, we can achieve largely different methanotroph biomass concentration and steady-state population ratio.

Figure 21e & f both measure the gas phase compositions for the cases with and without external oxygen supply (60:30:0 and 60:30:10). With 10% O_2 in the feed gas, the kinetic model predicted that significant CH_4 consumption occurred right after the feeding, then CH_4 consumption slowed down after external O_2 supply was exhausted and the growth of *M. buryatense* 5GB1 had to rely on the O_2 produced by *A. platensis*. It is worth noting that the dynamic details revealed by

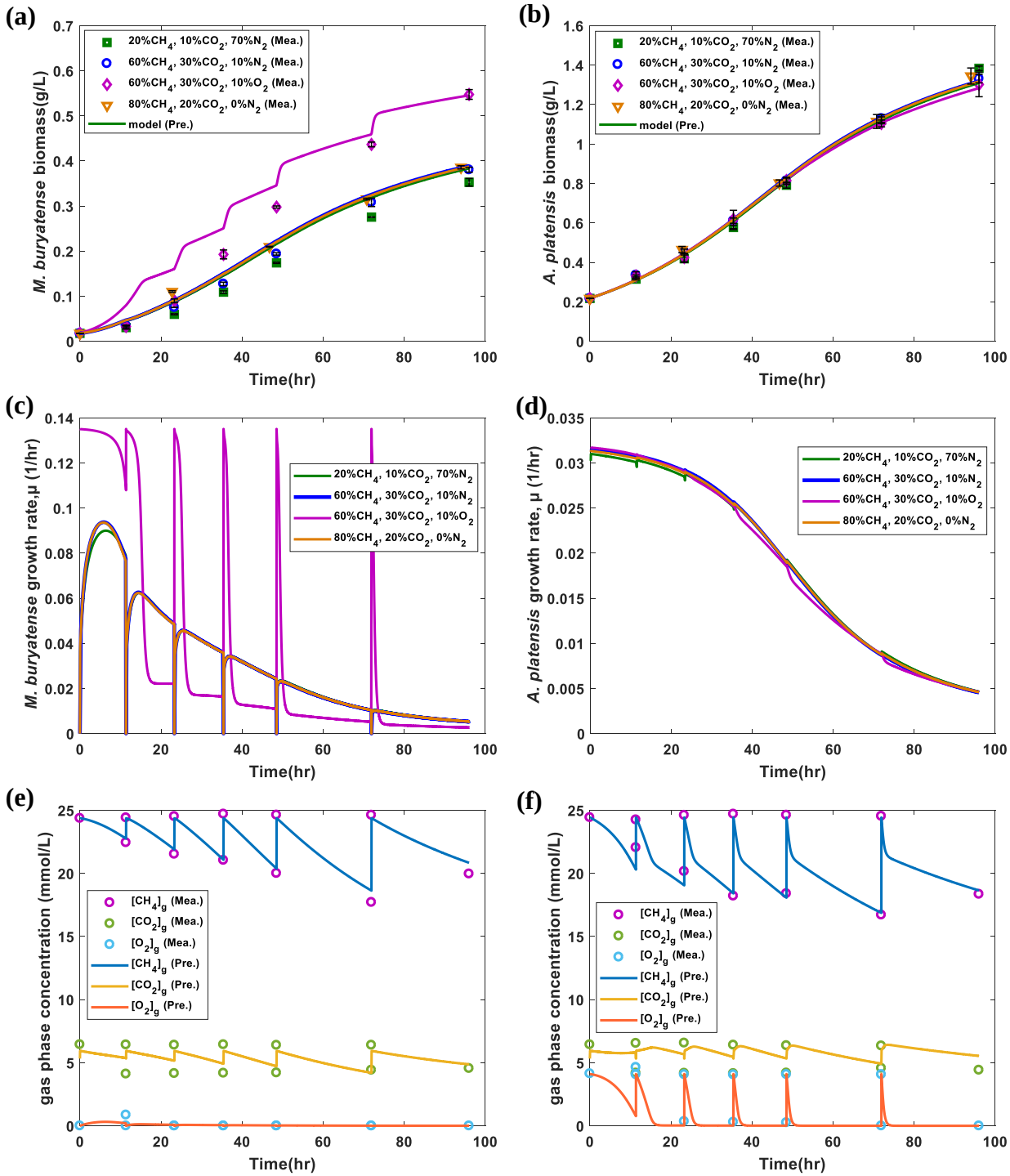

Figure 21. The individual biomass concentration for (a) *M. buryatense* 5GB1 and (b) *A. platensis*. The growth rate under different gas compositions for (c) *M. buryatense* 5GB1 and (d) *A. platensis*. The gas phase compositions for the experiments (e) with and (f) without external oxygen supply.

the semi-structured kinetic model can be difficult to capture through experimental measurements alone. The limited gas phase measurements completely missed the two-stage growth of *M. buryatense* 5GB1, i.e., with and without external O_2 supply, as the gas phase measurements showed very similar pattern between the two conditions.

These results further demonstrated the predict power of the semi-structured model, as the model predictions showed excellent agreement with the experimental data in almost all experiments. For the case with external O_2 supply, the model predicted biomass concentration for *M. buryatense* 5GB1 showed larger deviation from their measurements, this is likely due to the fact that the same sets of the fixed yield coefficients were utilized in the model, while the cells in the coculture likely experienced some adaptation to the coculture conditions, and exhibited somewhat different growth phenotype during the course of the coculture experiments.

4.4.4 The effect of inoculum ratio

Due to the different innate growth capabilities of the methanotroph and photoautotroph, different inoculum ratio could affect the coculture growth rate. However, given the interdependency between the photoautotroph and methanotroph, we hypothesize that regardless of the inoculum ratio, the P:M population ratio will transition to a steady-state that potentially maximize the carry-capacity of both populations under the given light intensity and gas composition. To exam the effect of the inoculum ratio on the coculture growth as well as to test the hypothesis, in this subsection, we compared 4 different inoculum ratios under the same growth condition as shown in **Table 5** (Experiment D), with P:M of 12.5:1, 8.5:1, 4:1, 1.5:1 respectively and all conditions have the same inoculum concentration of *M. buryatense* 5GB1.

Figure 22a & b plot the measured and model predicted individual biomass concentration for *M. buryatense* 5GB1 and *A. platensis* respectively. These results clearly showed that for the

model coculture, the higher the inoculum ratio, the faster the coculture growth. Since in the coculture, the maximum growth rate of *M. buryatense* 5GB1 (0.145 hr-1) was more than three times that of *A. platensis* (0.034 hr-1), higher inoculum of *A. platensis* would produce more O_2 to support faster growth of *M. buryatense* 5GB1. This is confirmed by the model predicted individual growth rates of *M. buryatense* 5GB1 and *A. platensis* (**Figure 22**c). It is worth noting that the growth rate of *A. platensis* with higher inoculum showed faster decline over time, further confirmed that the growth of the photoautotroph was limited by the light availability.

Figure 22 d plots the measured and predicted P:M population ratio over time. It clearly validated our hypothesis, as the coculture started with different inoculum ratios all converged to the same steady-state ratio (about 3:1). As O_2 availability is a major factor that determines the steady-state population ratio of the coculture, we expect that both light intensity and external O_2 supply would have a big impact on the steady-state population ratio. **Figure 22** e & f plotted the measured and predicted steady-state population ratio obtained from Experiment B and C respectively. **Figure 22**e suggests that the effect of different light intensity is rather limited, which appears to be contradicting to our expectation. However, this can be explained by the fact that the population ratio approaches steady-state, the light intensity (photon energy) available to cell growth was mainly determined by self-shading effect as shown in **Figure 20**c & d. The differences among cell growth rate for *M. buryatense* 5GB1 and *A. platensis* under different light intensities diminished as biomass density increased, which explains why there was limited impact from light intensity on the steady-state population ratio.

Figure 22e confirmed that external oxygen supply had significant impact on the steady-state population ratio, while different CO_2 concentration had negligible effect on the steady-state population ratio, as the main source of CO_2 supply came from dissolved CO_2.

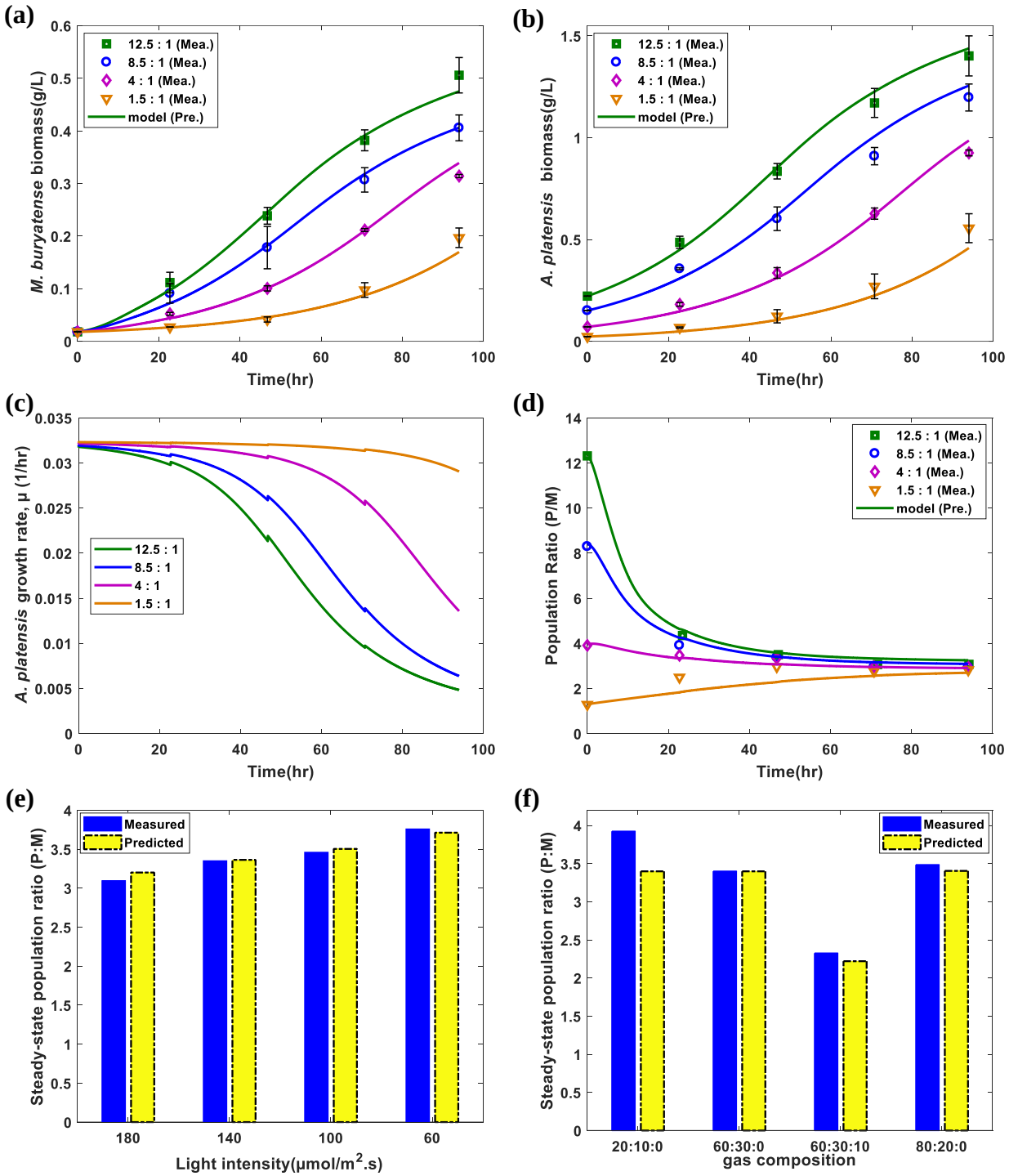

Figure 22. The measured and model predicted individual biomass concentration for (a) *M. buryatense* 5GB1 and (b) *A. platensis.* (c) The model predicted individual growth rates of *A. platensis.* (d) The measured and predicted P:M population ratio over time. The measured and predicted steady-state population ratio obtained from (e) Experiment B and (f) Experiment C.

4.4.5 The effect of other potential metabolic interactions

Besides the exchange of *in situ* produced O_2 and CO_2, there may exist other metabolic exchanges that could further enhance the growth of the M-P coculture. In the semi-structured kinetic model, the exchange of *in situ* produced O_2 and CO_2 are modelled explicitly, and the effect of any potential unknown "emergent interactions" can be captured by the lumped model parameters (*i.e.*, the maximum cell growth rates, μ^{max}, in the Monod model for both species). Therefore, using designed experiments (**Table 5**, Experiment E) to compare coculture with sequential single cultures and coupled with the kinetic modeling results, we could determine whether there exist additional metabolic exchanges in the M-P coculture and quantify the effect these unknown metabolic exchanges on the coculture growth.

Figure 23a illustrates the designed comparative experiment. In the sequential single culture experiment, the culture medium and inoculum concentration for *A. platensis* and *M. buryatense* 5GB1 were the same as those in the coculture experiment, and the amount of O_2 produced by the *A. platensis* single culture was injected into the single culture of *M. buryatense* 5GB1 to support methanotroph growth. **Figure 23**b & c compares the individual biomass concentration in the coculture and sequential single culture for both *M. buryatense* 5GB1 and *A. platensis* respectively. Again, the model predictions demonstrated excellent agreement with the measurements for both the coculture and sequential single culture. These figures also clearly showed that both species in the coculture exhibited significantly enhanced growth over those in the sequential single cultures. To determine whether the enhanced growth of both species in the coculture was due to any unknown metabolic interactions existed in the coculture, we used the experimental data collected from the sequential single culture to estimate the maximum cell growth rates for each species, while keeping the other parameters in the Monod model the same as those in the coculture model. As shown in **Table 8** for model parameters, both species in the coculture showed greatly enhanced

maximum growth rates, with 42% and 48% increase in the μ^{max}'s compared to those of the single cultures. The significances increase μ^{max} in the coculture for both species not only confirmed the existence of additional mutualistic interactions in the coculture besides O_2/CO_2 exchanges, but also quantified the effect these mutualistic interactions have on the growth of each species. In this work the maximum growth rate obtained for the *M. buryatense* 5GB1 single culture (0.098 hr^{-1}) was lower than the value reported in the literature (0.205 hr^{-1}) [106], which was most likely due to the fact that *M. buryatense* 5GB1 single culture was cultivated using the coculture medium and different agitation rate that those reputed in the literature. To confirm this was the reason, we have conducted multiple *M. buryatense* 5GB1 single culture cultivation experiments and obtained the lower μ^{max} consistently.

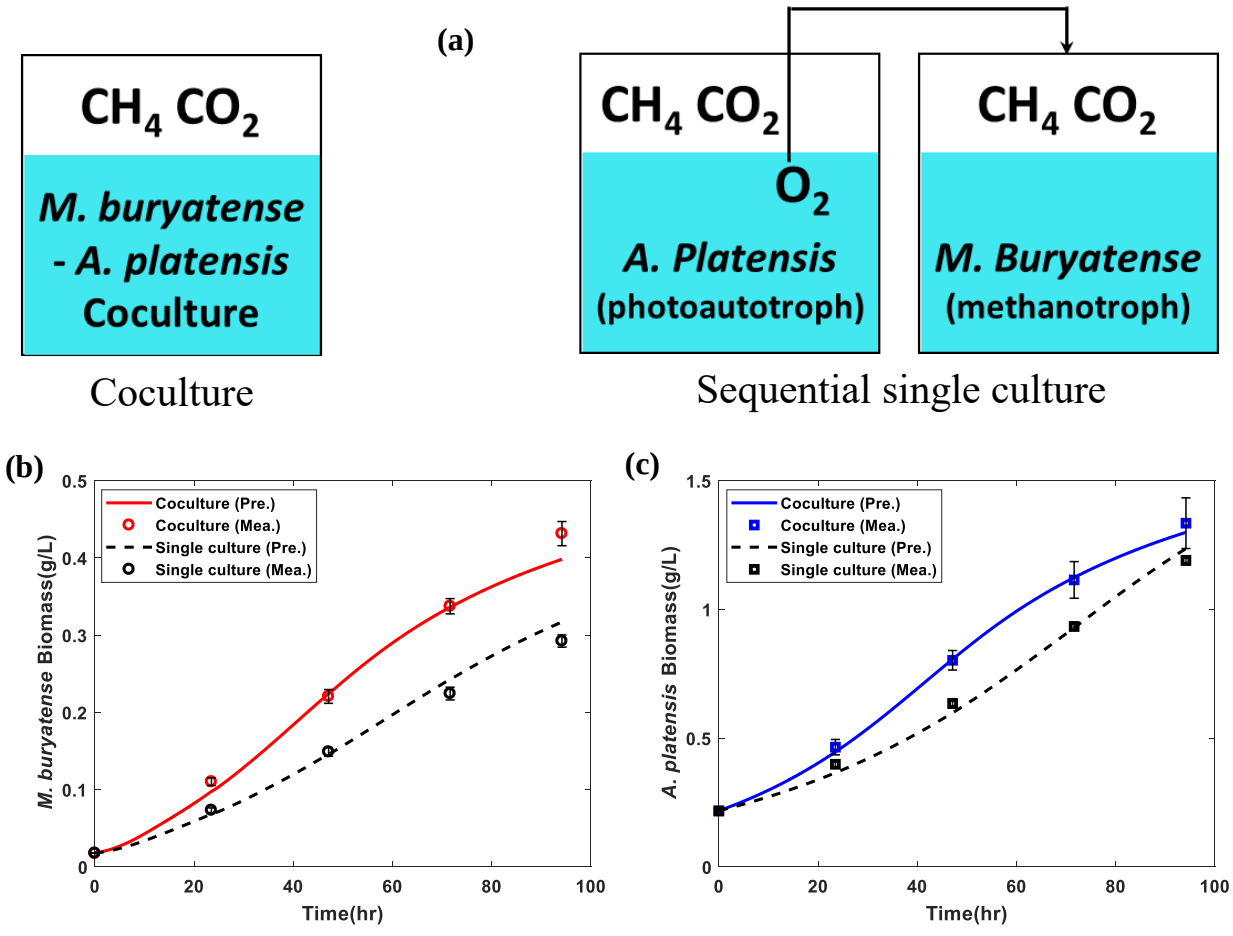

Figure 23. (a) Illustration of the designed comparative experiment. Comparison of the individual biomass concentration in the coculture and sequential single culture for (b) *M. buryatense* 5GB1 and (c) *A. platensis.*

4.5 Conclusion

In this work, we present a semi-structured kinetic modeling framework for methanotroph-photoautotroph cocultures. By explicitly modeling the exchange of *in situ* produced O_2 and CO_2, the semi-structured kinetic model can accurately predict the coculture growth dynamics under a wide range of growth conditions, demonstrated by a series of designed experiments using a model coculture *M. buryatense* 5GB1- *A. platensis*. This kinetic model provides a foundation for the design, optimization and control of photobioreactors needed for the coculture-based biogas conversion technologies. In addition, by coupling the individual biomass growth with gas phase composition changes, the modeling framework not only provides additional way to validate the model prediction, but also allows the testing of different hypotheses on the limiting factors of coculture growth. Specifically, the details provided by the model confirms that light availability, constrained by self-shading effect, is the limiting factor for coculture growth and it happens far before carbon substrate availability, limited by mass transfer resistance, becomes the limiting factor. Finally, by comparing the maximum growth rates obtained for *M. buryatense* 5GB1 and *A. platensis* using the coculture and sequential single culture experimental data, we confirmed that there exist additional emergent metabolic exchanges that further enhanced the growth both *M. buryatense* 5GB1 and *A. platensis.*

Chapter 5: Genome-scale metabolic models of *Arthrosipira platensis* - *Methylomicrobium buryatense* 5GB1 predict potential metabolic links

5.1 Introduction

5.1.1 Genome Scale Metabolic Models and Flux Balance Analysis

With continuous progress of omics technology, mathematical model representations of cellular metabolisms have grown in complexity and popularity. In doing so, *in silico* experimentation can provide insight on the effects of designed mutation and synthetic carbon flux through the metabolic network. Instead of focusing on individual genes or enzymes, genome-scale models enable researchers to envisage the cellular metabolism as a system comprised of many individual components that interact with each other to achieve a common goal. As a result, the field of Systems Biology has evolved to further elucidate the complex relationships that exist between genes and enzymes as well as intracellular metabolism and extracellular environmental conditions. At the core of Systems Biology are these genome-scale metabolic models (GEMs), which as the name suggests, are constructed based on the cell's genome to provide a map of the possible enzymes and their corresponding reaction pathways. As such, these models build a bridge to relate organism's genotype and phenotype by incorporating genomics and experimentally observed data into model building and establishing constraints [107,108].

Specifically, GEMS enable researchers to examine how a system (i.e., cellular metabolism) comprised of many individual components (i.e., reactions) interact to achieve a common objective. Models are created via a system of equations in a stoichiometric matrix that represents the reactions and metabolites that comprise an organism's metabolism via knowledge of the annotated genome. The rows represent the metabolites, and the columns represent the reactions taking place in the model. Each entry represents the stoichiometric coefficient of each metabolite. A negative entry accounts for metabolite consumption and a positive entry for metabolite production in all reactions.

Metabolites that are not involved in the reaction simply receive a zero value. Since the matrix developed is based on the complete stoichiometry of reactions, it is inherently mass balanced at steady state. It is important to note that most genome sequences are only partially characterized; therefore, modifications, such as various gap filling tools connected to genome bank, are made for improvement [107].

Models consist of hundreds or even thousands of reactions and metabolite. Universally, reactions far outnumber the metabolites in GEMs creating a stoichiometric matrix in the model that in turn, generates an underdetermined system of equations. Therefore, the most common technique for quantitative evaluation of GEMs is through constraint-based optimization. These constraints may be physicochemical, environmental, thermodynamic, or experimentally derived so that the solution space is logically reduced [109].

As the goal of GEMs is to understand and predict how cells utilize substrates, and how metabolites flow through the metabolic network to produce different products, several strategies have been developed over the past several years to solve for the flux distribution including flux balance analysis (FBA), elementary flux modes analysis (EFM), and ^{13}C-metabolic flux analysis to evaluate GEMs [110–112]. The model predicted flux through particular reactions are then compared to the experimentally measured flux values which are often limited to secreted products and biomass growth rate. For this research, FBA is used which is a powerful technique that treats the complex cellular metabolism as a linear programming problem. An objective function is defined and is used to calculate an optimal solution [111]. In this study, the objective function is set to maximize the predicted growth rate of the methanotroph or photoautotroph in the single culture or both in the coculture system. Reversibility data for reactions are used for the lower and upper bounds to constrain the possible reaction fluxes through each pathway and evaluated to

achieve the objective function (e.g., maximize growth). Constraints commonly applied to the model are uptake rates of the substrates and production rates from extracellular metabolites. For example, for model analysis of methanotroph, methane and oxygen are the substrates, while formate or CO_2 could be constrained for production rates if desired.

It is important to note that FBA does not require kinetic parameters, but uses defined constraints based on mass balances and bounds set by experimental data. This method does not incorporate regulatory effects of genes or enzyme activity [113]. Since FBA is a steady state approached, it uses time-invariant substrate (mmol g DCW^{-1} hr^{-1}) consumption rates and thus, primarily used for continuous experiments, but it can be used in batch experiments as well by calculating consumption/production rates between two sample points [114,115]. Dynamic flux balance analysis (DFBA) mostly has been used for batch experiments that will be discussed in the next chapter.

A basic overview of GEMs and the FBA process is shown in **Figure 24** [116]. Using the genome model to understand the placement and stoichiometry of known reactions, a stoichiometric matrix, S, can be produced. For example, the first reaction is the consumption of metabolite A and metabolite B and production of D. Thus, reaction (R1) will have a value of -1 for the consumption of A and B in the S table and a value of +1 for production of D. From this table, the concentration flux (dx/dt) over time is defined. FBA's key steady state assumption removes the derivative term and leaves Sv =0. The v matrix is the fluxes of individual reactions and is what is being solved by FBA. Using define bounds (lb and ub) of the metabolites and substrates, an optimal solution is found for the defined objective function (often the flux through the biomass equation called the growth rate).

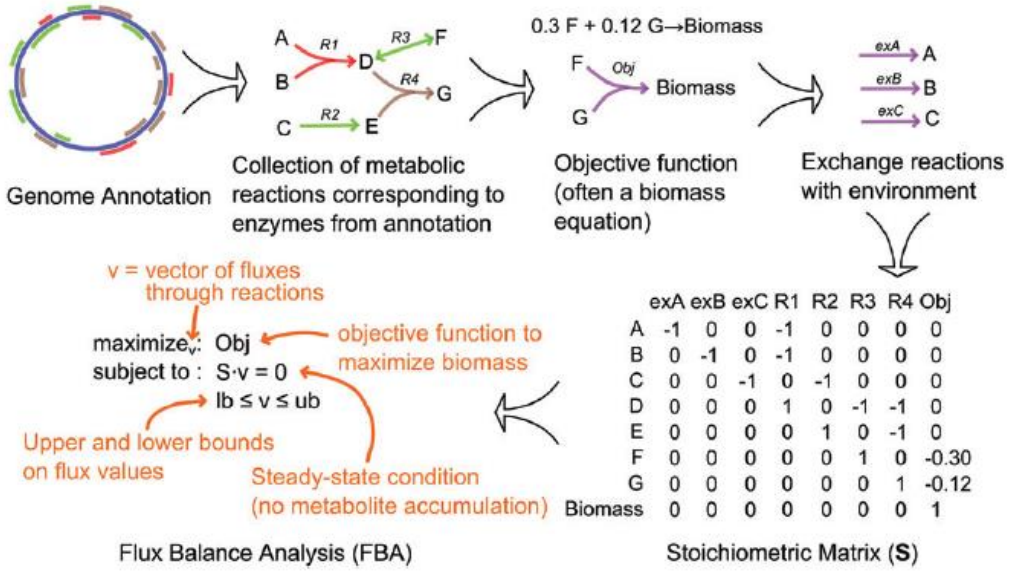

Figure 24. Summary of genome metabolic models and flux balance analysis [117]

5.1.2 Refinement of Genome-scale metabolic models

Similar to models developed in various science and engineering fields, the quality of a GEM determines the successfulness of its applications. Therefore, model validation plays an important role in GEM development. Besides assessing its size and connectivity, the current standard approach for GEM validation is to compare model predictions with experimental data under different conditions [118]. Most often the experimental data consist of measured cross-membrane fluxes, i.e., various substrate uptake rates, product excretion rates, and cell growth rate. Each experimental condition represents a single (although potentially high dimensional) point. For well-characterized organisms, point-matching approaches work well, because their metabolic network structures have been well-studied and well-defined. However, for some GEM, especially a less studied one, matching numerical experimental data over a few limited conditions does not

necessarily indicate a high-quality GEM and can result in very misleading conclusions. This was clearly demonstrated in our group study on the evaluation of the two GEMs of *s. stipitis* [119,120].

Therefore, at this work, we (1) use system identification-based framework to refine the model, (2) cure the model manually and (3) validate it with experimental data to assure our models are high-quality GEMs.

5.1.2.1 System identification-based GEM validation

Currently, GEM refinement is typically accomplished through trial-and-error by modifying different reactions in the model and examining whether model predictions improve. This process relies heavily on the modeler's knowledge and capability to sort out clues from various simulation results. Therefore, GEM refinement is usually labor intensive and time consuming [121,122]. To address this issue, our group has developed a system identification (SID) based framework for GEM validation [119]. In the SID framework, biological knowledge embedded in a GEM is first extracted from a series of designed *in silico* experiments through multivariate analysis methods such as principal component analysis (PCA); next, the extracted knowledge, such as how cells respond under a given stimulus, is visualized and compared with the existing knowledge for model validation and analysis. We term the proposed approach "knowledge-matching" as the simulation results are not directly compared with experimental data; instead, the knowledge captured by the model is compared with available knowledge.

5.1.2.1.1 The SID-based framework for GEM refinement

For GEM refinement, the biggest challenge is to identify the root cause of an erroneous model behavior. Because of the complex interconnectivity in a GEM, many times seemingly unrelated reactions located far away from the "problematic" reactions (i.e., reactions that are not

carried out in the expected way) play a key role in changing model behavior, and the experimental-matching validation does not provide information on such "hidden" relations.

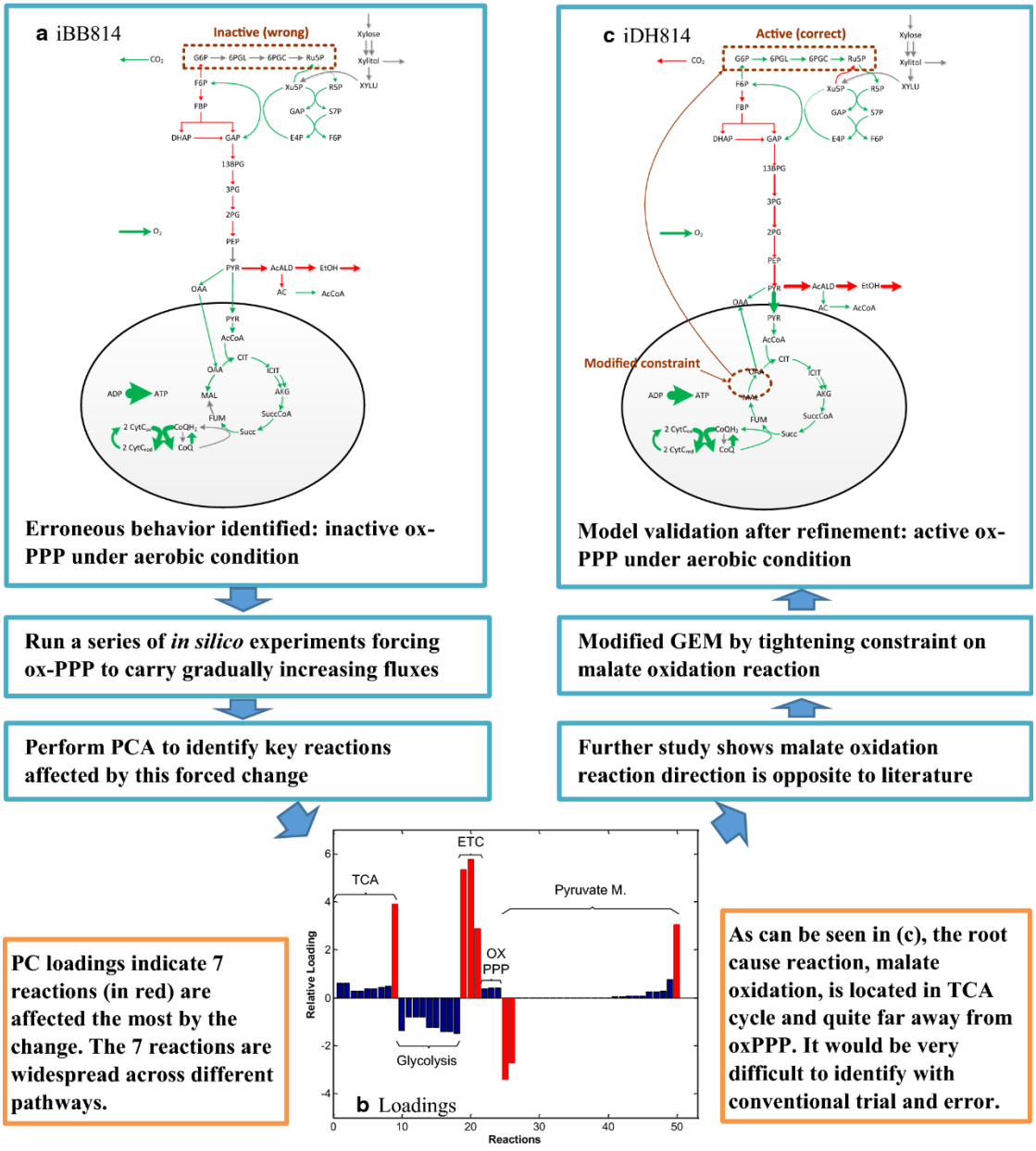

Figure 25. Demonstration of the SID based framework for GEM refinement [120]

Our group previously has shown how the SID-based framework can be applied to identify candidate root causes for a particular model faulty behavior, and in doing so, expedite GEM

refinement [120]. As an example, the refinement of iBB814 for one particular error has been illustrated the four steps in the SID-guided GEM refinement as shown in **Figure 25**.

This example shows that the malate oxidation reaction, the root cause of the erroneous model behavior, i.e. inactive oxyPPP under aerobic condition, is located quite away from oxyPPP pathway. Without the guidance of the SID framework, it could be very difficult to quickly identify this source of error. However, with the SID-based analysis, the overall network response provides key information to help quickly identify the root cause of the error.

In this work, we improve GEM of *Arthrospira platensis* and *Methylomicrobium buryatense* 5GB1 with existing knowledge (SID framework and manual curation) and then compare and validate them with experimental data.

5.2 Description and validation of the GEM of individual strains

5.2.1 Methanotroph: *Methylomicrobium buryatense* 5GB1

In 2015, a full metabolic model from the genome of 5GB1 was reconstructed [123]. The composition of the biomass flux (which represents growth rate) was designed from direct measurement of metabolites (i.e., amino acids, fatty acids, phospholipids, etc.), primary literature, and assumed values from well-studied organisms including *M. alcaliphilum* 20z and *E. coli.* The stoichiometric matrix for the model was further reduced by efforts of Dr. Marina Kalyuzhnaya's group, removing futile cycles and non- expressed reactions.

For the model, a few key assumptions and summarizations are made. The first is the grouping of the reactions involved in the electron transport chain where the cells produced the energetic unit ATP via aerobic respiration. Instead of accounting for the hydrogens pumped across the intercellular membranes for ATP generation, the overall reactions are summarized below assuming oxygen as the electron acceptor and NADH as the main electron donor.

$$2NADH/H^+ + O_2 + 6\,ADP + 6\,Pi + 8\,H^+ \leftrightarrow 2\,NAD + 8H_2O + 6\,ATP \quad (1)$$

The general equation for ETC above has been further broken down to the individual complexes [124,125]. The number of hydrogen ions pumped by these enzymes is of interest and thus are labeled specifically in these models. These labeled hydrogen ions are then used by the ATP synthase with a set ratio of hydrogen to ATP production. The process is called oxidative phosphorylation and it is assumed that 1 ATP is produced per 3 H^+ ions translocated across the membrane. For this particular study, the summarized form is maintained but this assumed ratio of ATP/H pumped is of interest.

The produced ATP can be used for metabolic reactions, non-growth associated maintenance, and growth associated maintenance. Non-growth associated maintenance is typical energy requirements by the cells to stay viable but is separate from the energy needed for reproduction. Growth associated maintenance is the energy utilized for cell duplication and growing biomass. In the GEM model, non-growth associated maintenance (NGAM) is accounted for via a reaction directing ATP to ADP at an initially assumed flux of 10.6 mmol ATP $gDCW^{-1}$ h^{-1}, while growth associated maintenance (GAM) was set via as a coefficient in the biomass flux at 23 mmol ATP $gDCW^{-1}$. Phenotype phase plane analysis also was performed to predict different phenotypes. For example, **Figure 26** shows 3D PhPP diagram with NGAM set to 10.6 mmolATP/(gDCW·hr). More information about GEM modeling, different phenotypes of 5GB1 and chosen parameters has been provided in Appendices **(B)**.

Furthermore, formate, acetate, and lactate are removed from the biomass equation and put in the model as separate byproducts. Formate and acetate have especially been known to be produced by 5GB1 under both methane and oxygen limited conditions [126,127]. However, the production in this particular methanotroph is not solely owed to a “fermentation mode” as seen in

the fellow methanotroph strain, *Methylomicrobium alcaliphilum* 20z [98]. Recent research indicates a redox balance and nutrient limitation (nitrate and trace elements such as copper) may play a larger role [128]. Moreover, Visio was used to visualize the model's central carbon pathway. Eventually, SID framework had applied at this step to assure the quality of the model after manual curation. Measured O_2, CH_4 uptake rate was put as the constraints into the model to interpret carbon distribution through central carbon network.

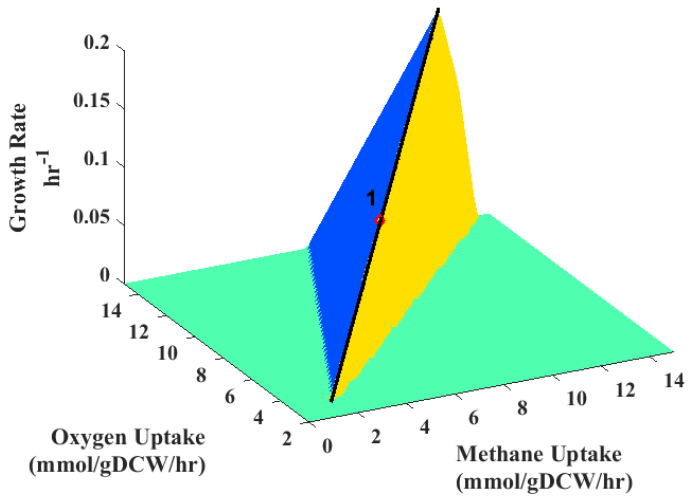

Figure 26. 3D PhPP diagram with NGAM set to 10.6 mmolATP/(gDCW·hr). The black line represents the line of optimality (LO).

The modified reconstruction model of *M. buryatense* 5GB1 was used and validated in different conditions of continuous experiments in our group (see Appendices **(B)**). However, at this work, in order to let organism to produce and consume metabolites in the coculture system, several reactions were added to the model to bring some metabolites (ammonium, amino acids, citrate, etc.) from cytoplasm to extracellular. The last version of the model is described in **Table 9**. The model prediction on single culture was explored using experimental data.

Table 9. Modified GEM reconstruction of iMb5G(B1)

unique metabolites	metabolic reactions	genes	compartments	Constraints for FBA simulation
403	520	313	3	Methane and Oxygen

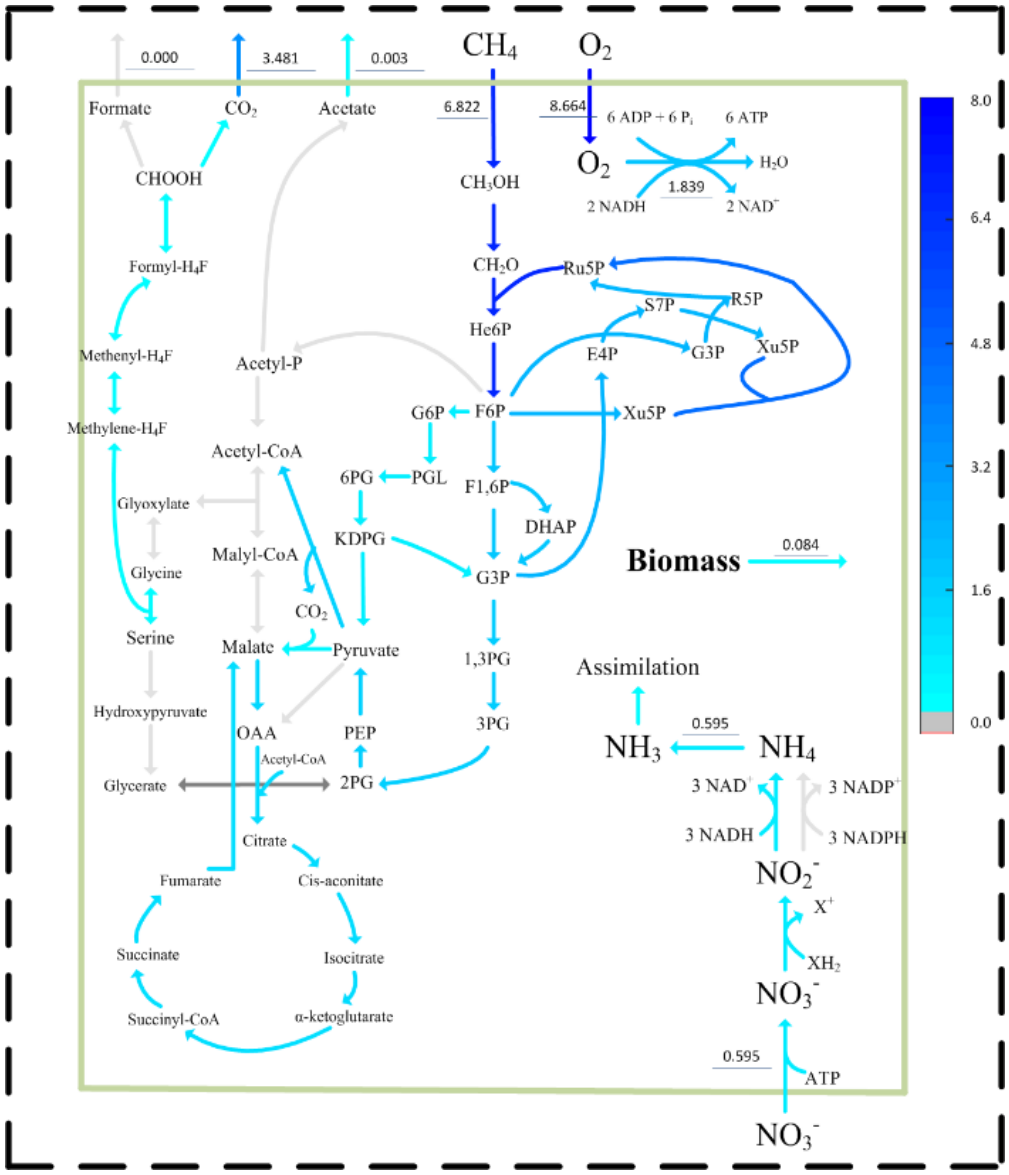

Figure 27. Model predicted fluxes for the model's central carbon network (CCN).

Single batch culture experiment of *M. buryatense* 5GB1 growth has performed in triplicate (Experiment for advantage of the coculture over sequential single cultures, see the Chapter 4). CH_4 and O_2 consumption rate were measured and put as constraints in the model (**Figure 27**, **Table 10**). Growth rate was used to validate the accuracy of the model (**Figure 28**). As it is shown the last version of the model could accurately capture growth rate of the methanotroph at the designed batch experiment.

Table 10. Constraints for validation of the *M. buryatense* 5GB1 model

Methanotroph	**CH_4 (constraint)**	**O_2 (constraint)**
Single culture (Experiment E)	-3.134	-4.319

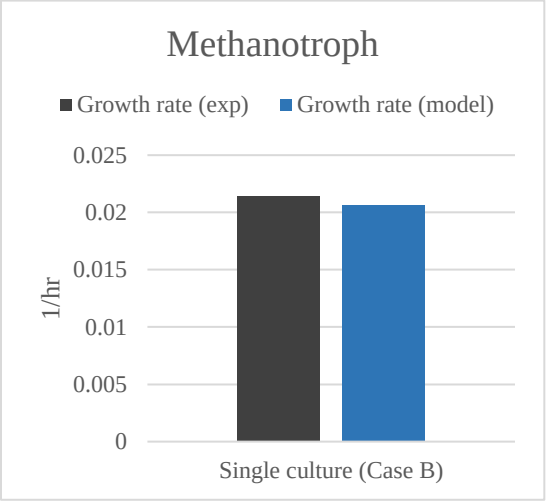

Figure 28. Comparison of the model prediction and experimental measurement for *M. buryatense* 5GB1 growth at condition Experiment E (chapter 4).

5.2.2 Photoautotroph: *Arthrospira platensis*

The reconstruction model for *A. platensis* NIES-39 [129] was used for this study, and several modifications were applied on the model. First, certain refinements using SID platform was performed. **Figure 29** shows central carbon flux of the model during SID refinement. **Figure**

29 (a) shows GEM model prediction at the beginning. The biomass prediction was much lower than expected. Therefore, after performing PCA in SID framework refinement, the major issue was identified to be the cyclic pathway between G3P and 13DPG as it is highlighted. In **Figure 29** (b) the cyclic pathway was addressed, however, there is no oxygen production. The issue was identified to be a reaction for glycine that needs to be blocked as it is shown in **Table 11**. The model could predict oxygen production at this step, however, there was some other irregularity, according to the existing knowledge, such as converting FDP to F6P or G6P to 6PGL as shown in **Figure 29** (c). As it is shown in **Figure 29** (d) all issues of the model were addressed using SID framework.

After preforming the refinements, which was mostly on central carbon pathway such as Pyruvate metabolism and Glycolysis / Gluconeogenesis, the model could predict the growth rate and oxygen production. Moreover, some further refinements applied to the model using the literature that have been studied on *A. platensis* [130,131], specifically focused on different pathways such as Photosynthesis and electron transport chain, Calvin cycle / Pentose phosphate pathway and Pyrimidine/ serine/glutamate metabolism. Furthermore, the ammonium uptake rate was set to zero and as an autotrophic condition, the photon uptake rate was set to a given value, and the glucose uptake rate was set to zero. Growth associated ATP maintenance of the model was set to 40 based on the recent literatures [130,132]. The **Table 11** shows the described modifications on the GEM model.

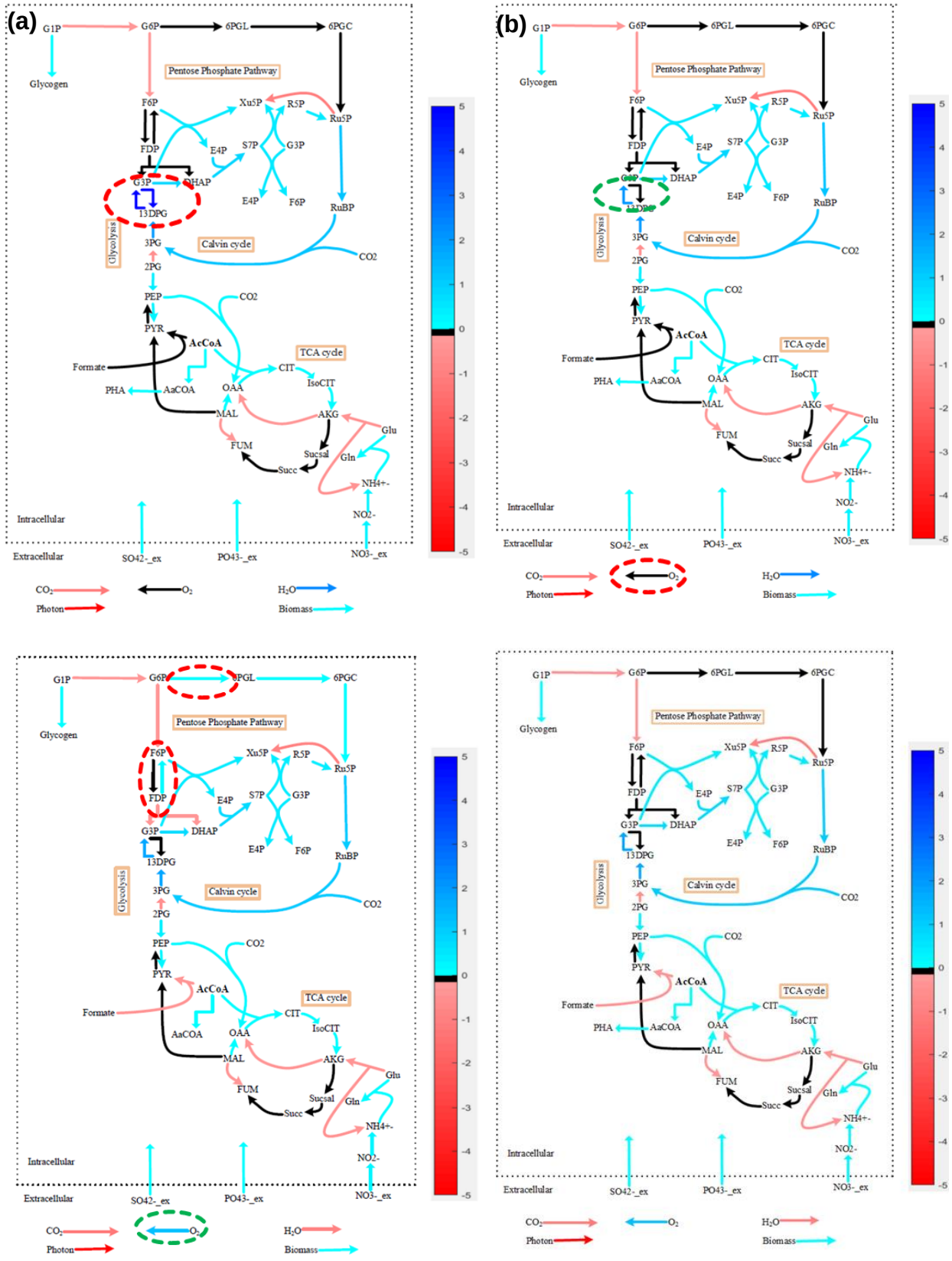
(a)
(b)
G1P
G6P
6PGL
6PGC
Glycogen
Pentose Phosphate Pathway
F6P
Xu5P
R5P
Ru5P
FDP
E4P
S7P
G3P
G3P
DHAP
13DPG
E4P
F6P
RuBP
Glycolysis
3PG
Calvin cycle
CO2
2PG
PEP
CO2
PYR
AcCoA
TCA cycle
Formate
CIT
IsoCIT
PHA
AaCOA
OAA
MAL
AKG
Glu
FUM
Sucsal
Gln
Succ
NH4+-
NO2-
Intracellular
Extracellular
SO42-_ex
PO43-_ex
NO3-_ex
CO2
O2
H2O
Photon
Biomass

Figure 29. Gem refinement steps of *A. platensis using* SID based framework.

Table 11. Selected modification on *A. platensis* NIES-39 GEM model using SID framework and existing knowledge

Reaction	Modification	Description and Reason
1 gly-L + nad + thf -> co2 + h + mlthf + nadh + nh4	blocked	Glycine, serine and threonine metabolism was excessive.
6 h + 2 fdrd + pq -> 2 fdox + 4 h[t] + pqh2	added	Photosynthesis and electron transport chain (Peltier, Aro, and Shikanai 2016)
atp + f6p -> adp + fdp + h	blocked	Calvin cycle / Pentose phosphate pathway; inactivated by light (Plaxton 1996)
g6p + nadp -> 6pgl + h + nadph	blocked	Pentose phosphate pathway; light inhibits it (Plaxton 1996)
fdp + h2o -> f6p + pi	blocked	Calvin cycle / Pentose phosphate pathway; light inactivates it (Lemaire 2004; Matsumoto 2008)
ser-L -> nh4 + pyr	blocked	Serine metabolism; This reaction is not present (KEGG)
glu-L + h2o + nadp <=> akg + h + nadph + nh4	Upper bound=0	Glutamate metabolism; This reaction is irreversible reaction (Muro-Pastor 2005)
gtp + h2o -> gmp + h + ppi	blocked	This reaction is not present (KEGG) Pyrimidine metabolism
dgtp + h2o -> dgmp + h + ppi	blocked	This reaction is not present (KEGG)
dutp + h2o -> dump + h + ppi	blocked	This reaction is not present (KEGG)
h2o + utp -> h + ppi + ump	blocked	This reaction is not present (KEGG)
10fthf + h2o -> for + h + thf	blocked	This reaction is not present (KEGG) One carbon pool by folate

Metabolites	Name
f6p	D-fructose-6-phosphate
fdp	D-fructose-1,6-bisphosphate
g6p	D-glucose-6-phosphate
g3p	Glyceraldehyde3-phosphate
13dpg	1,3-Bisphospho-D-glycerate
6pgl	6-phospho-D-glucono-1-5-lactone
ser-L	L-Serine
pyr	Pyruvate
glu-L	L-Glutamate
gly-L[c]	Glycine
mlthf	5-10-Methylenetetrahydrofolate
nh4	Ammonium
akg	2-Oxoglutarate
10fthf	10-Formyltetrahydrofolate
thf	Tetrahydrofolate
for	Formate
h[t]	H^+ in thylakoid

The original model had 735 metabolites and 745 reactions. In order to let organism to be able to produce and consume metabolites (such as ammonium, malate, succinate, amino acids,

etc.) in the coculture, several reactions was added to the model to bring the metabolites from cytoplasm to extracellular [131]. After the modification, the model had 796 reactions, however, many of the reactions were inactive or blocked. To address this issue and make the model simpler (without any effects on prediction), "ReducedModel" code in Cobra Toolbox was implemented to find blocked reactions which cannot carry any fluxes in the given simulation conditions and remove them from the model to form a reduced model (the unused metabolites were removed along the reactions). The GEM model of *A. platensis* NIES-39 has described at **Table 12**.

Table 12. Modified GEM reconstruction of *A. platensis* NIES-39

metabolites	metabolic reactions	compartments	Constraints for FBA simulation
508	579	4	Carbon dioxide and photon

* O_2, H_2O, sulfate, phosphate, and nitrate were assumed to be freely exchanged

At the end, the prediction of the model on *A. platensis* growth on single culture using experimental data (Experiment E, Chapter 4) was investigated. **Table 13** and **Figure 30** shows the model prediction results. There is an excellent agreement between model prediction and experimental measurements for oxygen production and growth rate of *A. platensis.*

Table 13. Constraints for single culture cyanobacteria GEM model

Cyanobacteria	**CO_2 (constraint)**	**Light photon(constraint)***
Single culture (Experiment E)	-0.681	-6.42

* This amount is the photon was received by the cells in unit of mmol/gDCW/hr (in the GEM model) which estimated by performing several *in silico* experiments and comparing with the experimental data (CO_2 uptake) at light intensity of 180 µmol photon/m^2/s

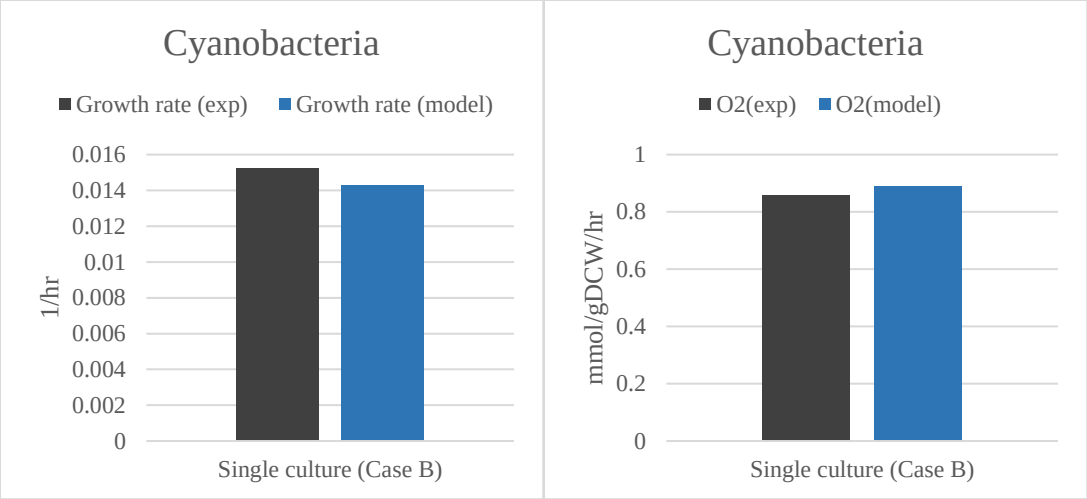

Figure 30. Comparison of the model prediction and experimental measurement for *A. platensis* growth and O_2 production at condition Experiment E (chapter 4).

In short, the GEM for the *A. platensis* refined to incorporate recent finding on photosynthetic electron transport components. The model predicted oxygen production and biomass growth showed a better agreement with experimental data.

5.3 Coculture modeling framework

In order to model the community, we have followed the approach proposed by SteadyCom [133] and microbe-microbe interactions in Microbiome Modeling Toolbox (MMT) [134] which are reformulation of cFBA [135] with the computational advantage that the number of LPs to be solved is independent of the number of organisms in the community. We used two GEM models to make sure the results are consistent and similar solution are predicted. Specific fluxes (mmol/gDCW/hr) are integrated as model constraints, where gDCW indicates grams of dry cell weight for all biomass in the coculture. Using these GEM models, we can account for species abundance in the community. The biomass of each species is calculated based on the community

biomass and the species ratio. In addition to this, steady-state and equal growth rate of species are assumed.

5.3.1 Coculture GEM reconstruction

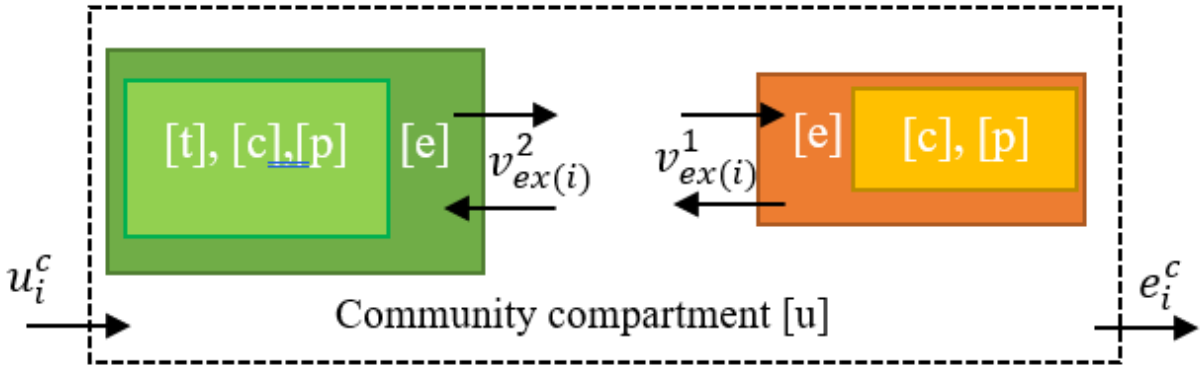

Figure 31. Dependencies applied to the coculture model to describe possible interactions. Both organisms have a common compartment to share the metabolites of their needs.

M. buryatense 5GB1 and *A. platensis* GEM models were combined to form one coculture model that shows syntrophic relations of the organisms when they grow together. To model the interaction between two strains, we used modified model of each organism and added a common compartment ([u], community compartment) to exchange of metabolites. It is worth to mention that unfortunately the model reconstructions had different name's format since they achieved form various database. The metabolite names could be totally different between different database/generators. To address this challenge, we used a developed code in our group to refine the metabolite names in the reconstruction models and make them all similar to universal format of metabolites.

Furthermore, to achieve a coculture GEM, all metabolites that were defined as extracellular ([e]) in its original models, will be defined as exchange metabolites in the common community

compartment of the model, [u]. Metabolites that are shared between species, will be exchanged through this common compartment, being first transported from the corresponding extracellular compartment to the community compartment, or vice versa. For example, acetate in extracellular of methanotroph (M1ac[e]), transferred to the community compartment as following: M1ac[e] <=> ac[u]. It is worth mentioning that multi-species generator recognizes extracellular reactions if there is "EX_" in their name. Therefore, all extracellular reaction names in the models curated manually based on the mentioned requirement. In principle, all metabolites that are present in both extracellular compartments and are defined in the community compartment, can be exchanged, being the directionality of the associated reactions favorable to produce the exchange. However, some dependencies have been assumed in the model based on experimental evidences. Finally, the coculture GEM model was transformed into MATLAB file.

Next, the coculture GEM model was developed by SteadyCom and MMT for predicting metabolic flux distributions for a growth rate of the coculture. **Figure 31** shows the compartments of the system. Where [c] shows cytoplasm, [p] periplasm, [t] thylakoid, [e] extra cellular, u_i^c community uptake rate, e_i^c community export rate.

5.3.2 Coculture GEM modelling for *E.coli* toy systems

To test the coculture GEM model before applying on our coculture system, a published *E.coli* model, iAF1260 [136], was used and a toy coculture system (followed by a literature [133]) was made by making two mutant of *E.coli* (**Figure 32**). Both biomass composition of mutants is the same. Therefore, mutants need both amino acids (Lys-L and Arg-L) to grow, even though the gene of an amino acid might be knockout in their cell.

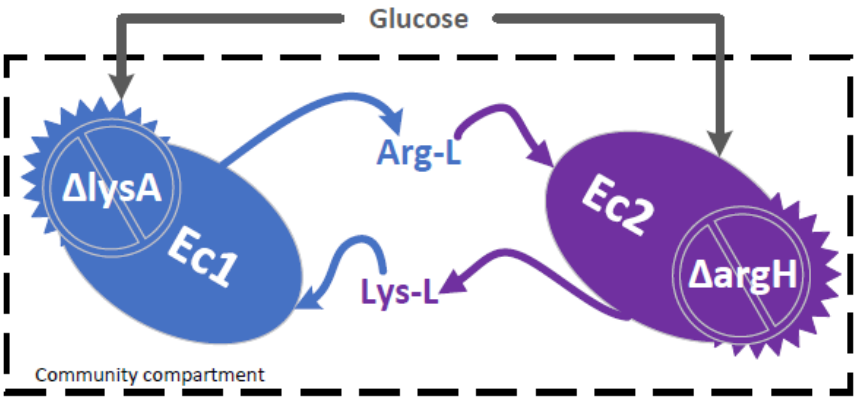

Figure 32. The designed toy model for investigation of Coculture GEM modeling. Ec1 is missing the gene for synthesis of Lys-L, and needs to uptake it from outside to grow. Ec2 is missing the gene for synthesis of Arg-L and needs to uptake it from outside to grow. Lys-L and Arg-L are part of the biomass composition of both mutants.

We considered three scenarios to show accuracy of the coculture GEM modeling. **Figure 33** shows different scenarios and model prediction results for coculture growth rate and each mutant abundance in the coculture. **Figure 33** (a) shows the scenario when there is unlimited Arg-L in the community compartment. As it is shown, Ec2 got the needed amino acid from the community, grew and became the dominant specie. **Figure 33** (b) shows the scenario when there is Arg-L in the community compartment, but it is limited by a constraint. As it is shown, Ec2 consumed the amino acid in the community compartment, but it also produces some Lys-L for Ec2 to get more Arg-L. But Ec2 is still has 82% of the coculture since there was some Arg-L in the community. And third scenario is when there is not any amino acid in the community compartment (**Figure 33** (c)). Therefore, the mutants need each other to get the required amino acid.

This modeling on *E. coli* toy model clearly shows the mutual intentions and metabolic links between the organisms which coculture GEM could predict it successfully.

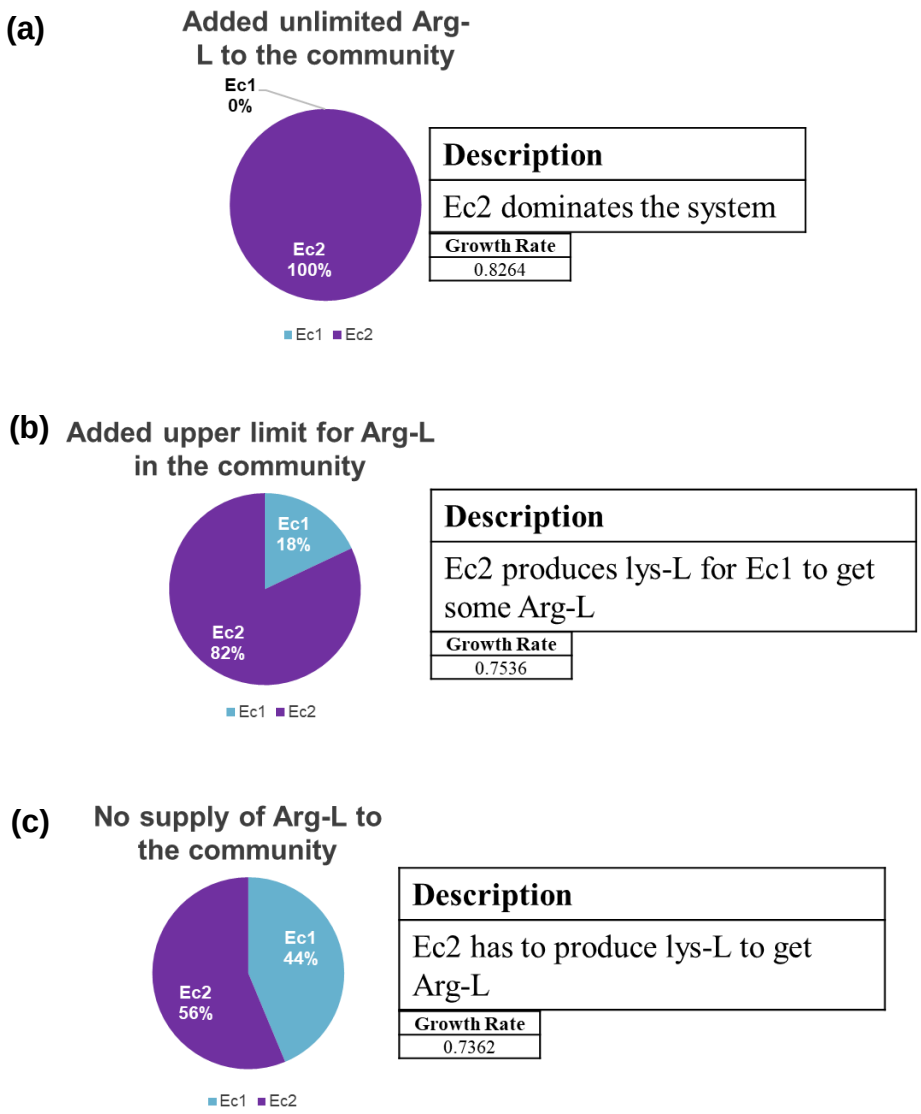

Figure 33. Different scenarios and coculture GEM model prediction results of the *E. coli* toy system

5.4 GEM models of *A. platensis – M. buryatense* 5GB1 system

As it is mentioned, the coculture GEM model was developed by SteadyCom and MMT for predicting metabolic flux distributions for a growth rate of the coculture. The experimental data from Experiment A (Chapter 4) was used to test and validate the GEM models.

5.4.1 SteadyCom

Just CO_2 and photon were used as constraints for the coculture model. **Table 14** shows the constraints for the modeling. O_2 constraint for the community was set to zero for lower and upper bound, which means the only oxygen source is from production by cyanobacteria and all of it must be consumed by methanotroph, since there was not any oxygen remained in the coculture systems (experimental data).

Table 14. Constraints implemented in the SteadyCom GEM model

	CO_2	Photon
Case A	Constraint	
	mmol/gDCW/hr	
	0.680	6.98*

***** This amount is the photon was received by the cells in unit of mmol/gDCW/hr (in the GEM model) which estimated by performing several *in silico* experiments in order to produce the proper amount of Oxygen for methanotroph.

(a)

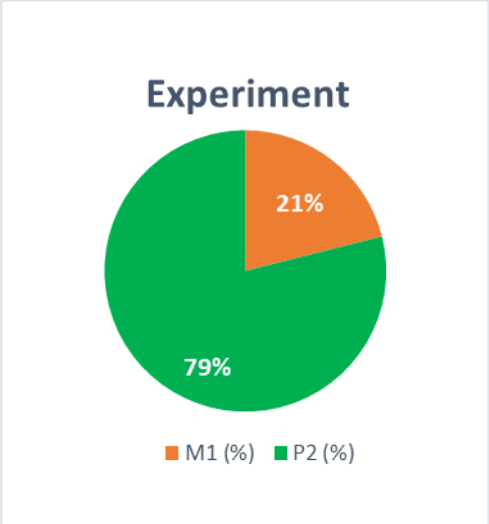

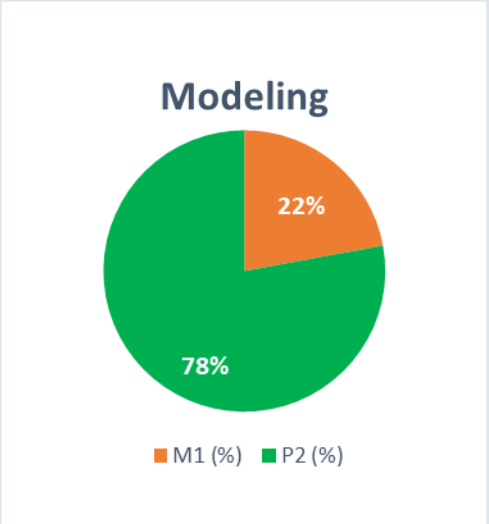

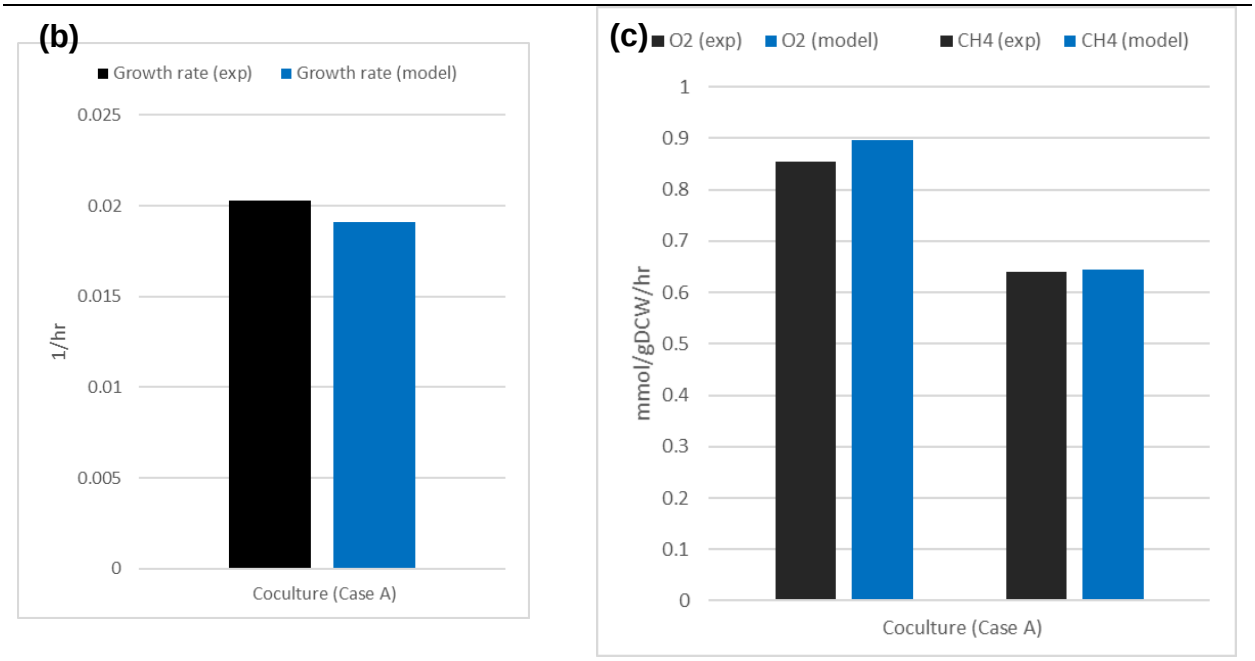

Figure 34. Comparison between the experimental data (Case A) and SteadyCom GEM model prediction of **(a)** population ratio; **(b)** growth rate; **(c)** Oxygen (O_2) and methane (CH_4) consumption, in the coculture system.

As it is shown in **Figure 34**, the model could accurately predict biomass ratio of photoautotroph over methanotroph and growth rate of the coculture. The consumption rate of O_2 and CH_4 also agree with experimental data for methanotroph in the coculture.

Table 15 shows the metabolic interactions between photoautotroph and methanotroph predicted by the model. The table is ordered based on higher to lower flowrate that depicts the contribution of each metabolite in this interaction. It is worth to mention that some metabolites are the major metabolites in TCA cycle (**Table 15** in red color) and need to be excluded from metabolic links or just one or two of them can be included, otherwise the solution for the GEM models is infeasible. Decision on which major metabolites should be included in the metabolic links makes several scenarios. Therefore, at this case, just Malate was included in metabolic links and other major metabolites were excluded (in red font).

Table 15. Potential metabolic links in the coculture predicted by SteadyCom (When "malate" is allowed to exchange). The amount shows the flow rate (mmol/gDCW/hr) with different color for each strain.

No.	Metabolite	Name	Amount
1	NH_4	ammonium	0.1601
2	glu-L	L-glutamate	0.0664
3	cit	citrate	0.0652
4	for	formate	0.049
5	mal-L	L-malate	0.0311
6	gln-L	L-glutamine	0.0241
7	ser-L	L-serine	0.0118
8	leu-L	L-leucine	0.0083
9	phe-L	L-phenylalanine	0.0034
10	tyr-L	L-tyrosine	0.0034
11	ala-L	L-alanine	0.0025
12	sucr	sucrose	0.0018
13	val-L	L-valine	0.0014
14	thr-L	L-threonine	0.0011
15	ile-L	L-isoleucine	0.0011
16	lys-L	L-lysine	0.001
17	trp-L	L-tryptophan	0.0008
18	arg-L	L-arginine	0.0008
19	pro-L	L-proline	0.0008
20	met-L	L-methionine	0.0005
21	his-L	L-histidine	0.0002
22	cys-L	L-cysteine	0.0001
23	ac	acetate	2E-05
	succ	Succinate	
	pyr	Pyruvate	
	mal-L	L-malate	

Produced by *platensis* and consumed by 5GB1
Produced by 5GB1 and consumed by platensis
No participation in metabolic links

A visualization for the coculture system was made to show all the reactions quickly and clearly. This coculture visualization shows the main carbon fluxes and metabolite exchange between the organisms (**Figure 35**). Therefore, it is easy to keep track of the consumption and production of metabolites. The dash black line shows the whole community compartment, where both cells are present, getting their feed (CH_4, CO_2, photon) from bulk, and able to exchange their

metabolites. The left green solid line shows the photoautotroph, and the right orange solid line shows the methanotroph.

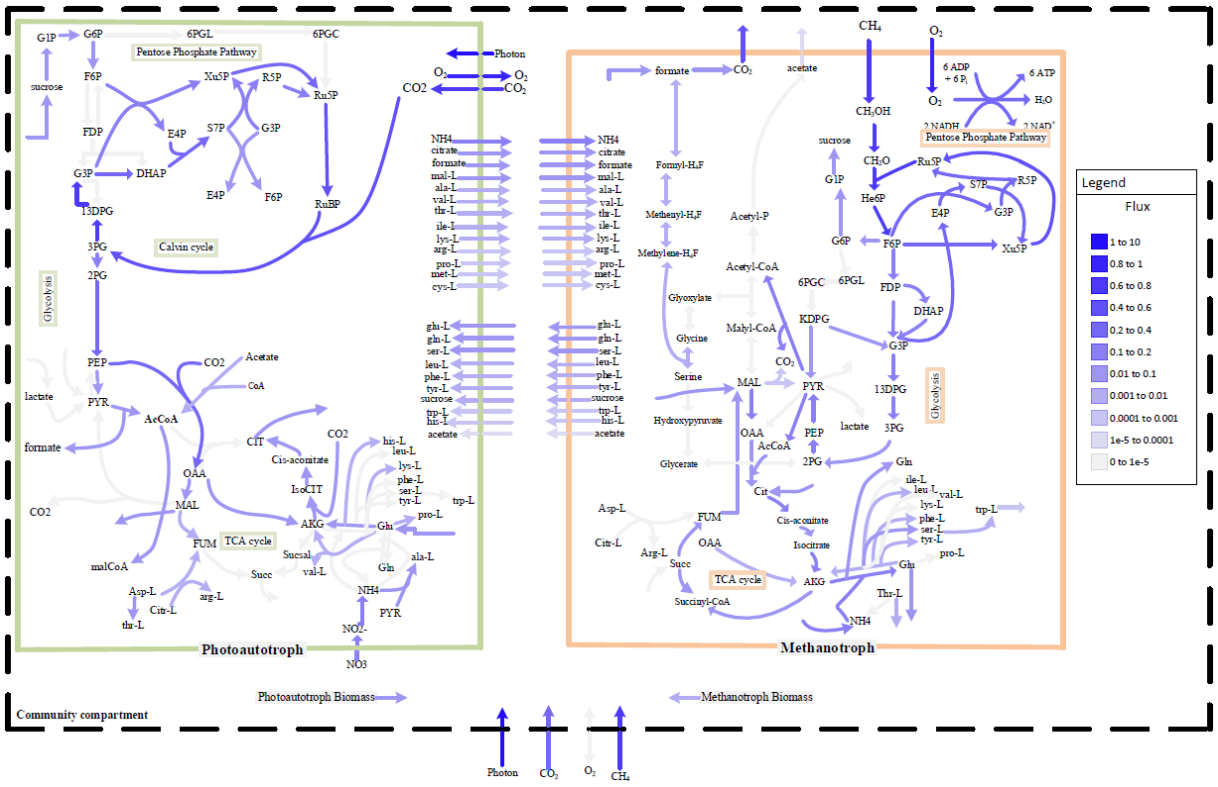

Figure 35. Schematic representation of the simulated metabolism of the coculture system when cells are allowed to exchange the metabolites.

As it is shown, cyanobacteria (shown with green line, left) mainly consumed photon and carbon dioxide, and produce oxygen for methanotroph (shown with orange line, right). Calvin, pentose phosphate cycle are active in cyanobacteria and the TCA cycle is half active as it has been shown by other studies [129].

5.4.1.1 Coculture GEM modeling without metabolic links

In order to demonstrate the importance of metabolic links in the GEM modeling, all the metabolic links were blocked, except oxygen and carbon dioxide, so the strains cannot exchange any metabolites. **Figure 36** shows the visualization of central carbon pathways when the metabolic links are blocked (a) and the comparison of the coculture growth rate between the SteadyCom models when metabolic links exist and when it does not exist (b).

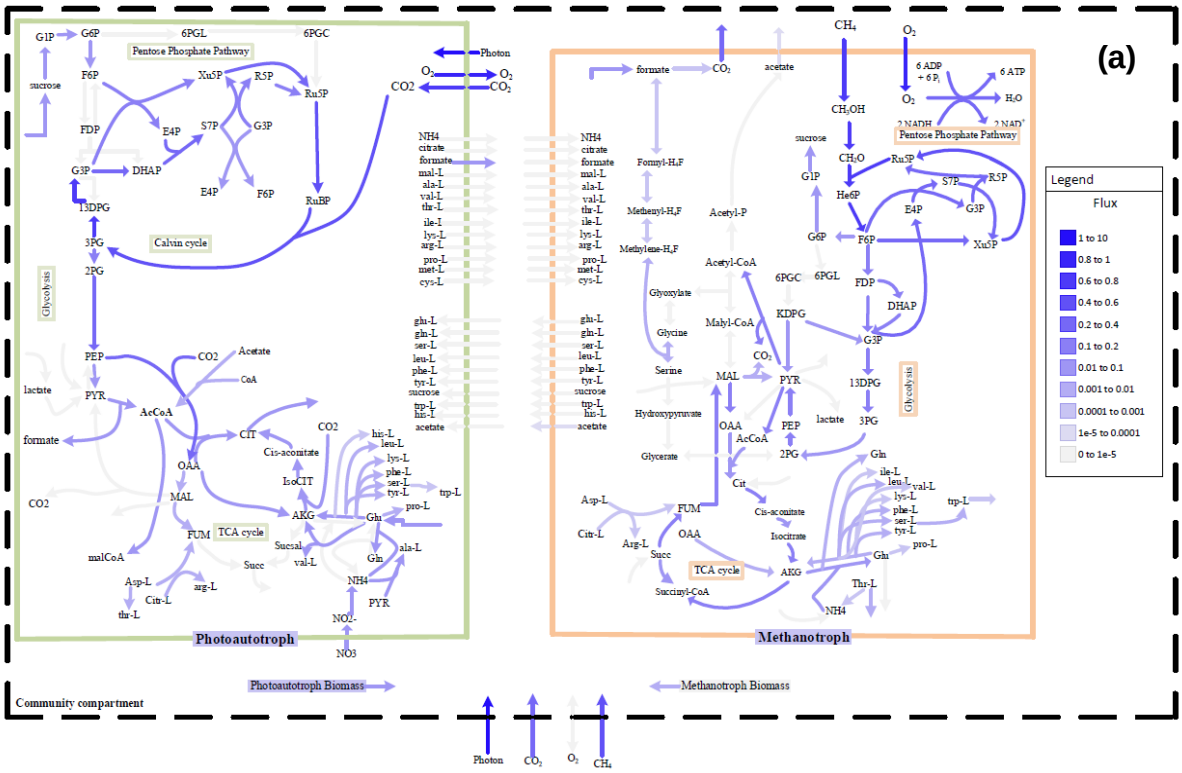

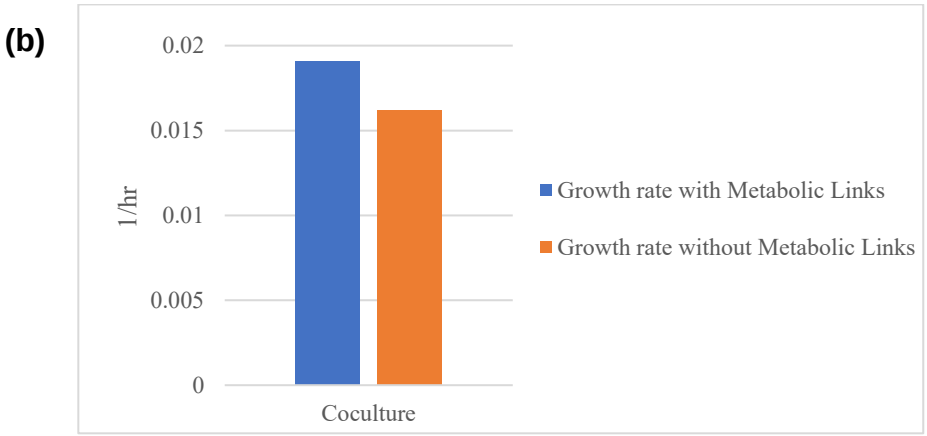

Figure 36. The visualization of central carbon pathways and the growth rate of the coculture system when strains are not allowed to exchange any metabolites.

As it is shown, there is no exchange of metabolites between the strains. Photoautotroph produced "formate" and methanotroph produced "acetate", but the other strain was not allowed to use it, then the produced metabolites accumulated in bulk (medium). Each strain has to produce all amino acids by itself since there is not any metabolic links. Moreover, the GEM model predicted a lower growth rate for the coculture when they cannot exchange any metabolites which proves the importance and contribution of the metabolic links in the coculture system.

5.4.2 Microbe-microbe interactions/ Microbiome Modeling Toolbox (MMT)

The constraints for each microbe (CO_2 for photoautotroph and CH_4 for methanotroph) should be added to the microbe-microbe interaction in MMT GEM model, otherwise, the model could not be solved. In general, the results of MMT were more accurate than SteadyCom, therefore, we used MMT model for the next chapter. **Table 16** shows the constraints for the modeling. O_2 constraint for the community was set to zero for lower and upper bound, which means the only O_2 source is O_2 produced by cyanobacteria and all of it must be consumed by methanotroph, since there was not any O_2 remained in the coculture systems (experimental data).

Table 16. Constraints implemented in the MMT GEM model

	CO_2	**CH_4**
Case A	Constraint	
	mmol/gDCW/hr	
	0.680	0.640

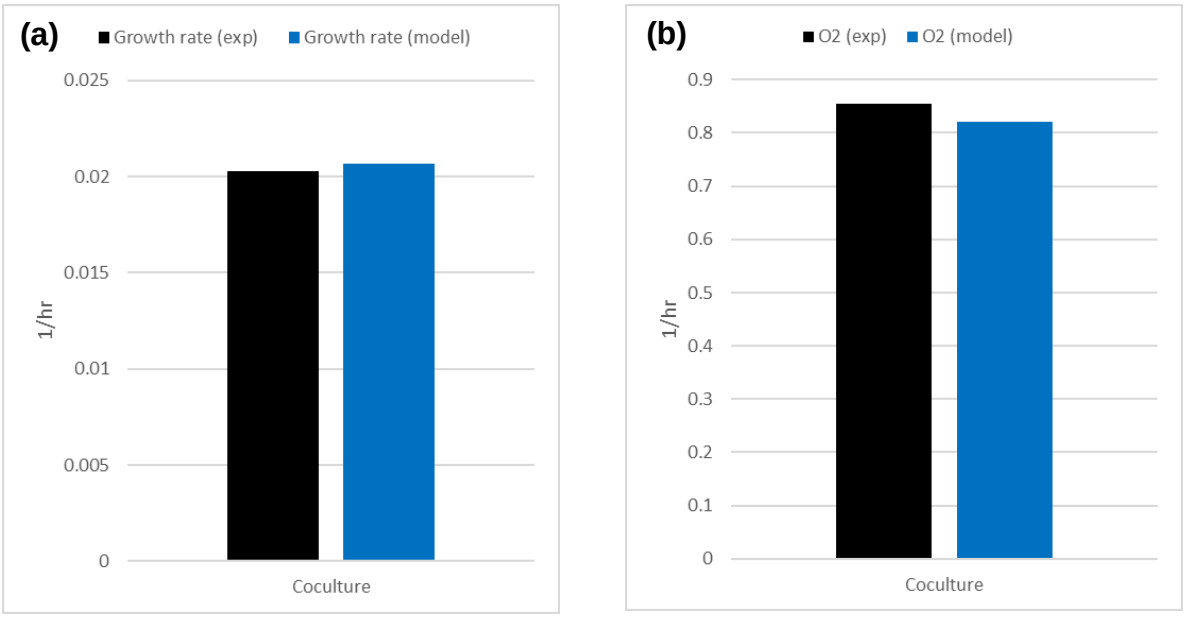

Figure 37. Comparison between the experimental data (Case A) and MMT GEM model prediction of **(a)** growth rate; and **(b)** Oxygen (O_2) consumption, in the coculture system.

Table 17. Potential metabolic links in the coculture predicted by MMT (When "malate" is allowed to exchange). The amount shows the flow rate (mmol/gDCW/hr) with different color for each strain.

No.	Metabolite	amount
1	NH3	0.1015
2	mal-L	0.0925
3	cit	0.0857
4	lac	0.0848
5	glu-L	0.073
6	for	0.0614
7	gln-L	0.0246
8	sucr	0.0089
9	thr-L	0.0083
10	leu-L	0.0081
11	val-L	0.0067
12	ser-L	0.0065
13	ile-L	0.0052
14	ala-L	0.0036
15	phe-L	0.0033
16	tyr-L	0.0033
17	lys-L	0.0015
18	arg-L	0.0012
19	pro-L	0.0012
20	trp-L	0.0008
21	met-L	0.0007
22	his-L	0.0005
23	cys-L	0.0002

24	ac	2E-05
	fum	
	succ	
	pyr	
	oaa	
	akg	

Produced by *platensis* and consumed by 5GB1
Produced by 5GB1 and consumed by platensis
No participation in metabolic links

As it is shown in **Figure 37**, the model could accurately predict growth rate and consumption rate of O_2 in the coculture system. This validated the accuracy of the model in molecular level for predicting of strains behavior in the coculture. **Table 17** shows the potential metabolic interactions between photoautotroph and methanotroph predicted by the MMT model. The table is ordered based on higher to lower flowrate that depicts the contribution of each metabolites in this interaction. At this case, just "malate" was included in metabolic links and other major metabolites were excluded (in red font).

Figure 38 (a) shows the visualization of central carbon pathways where and the comparison of the coculture growth rate between the SteadyCom models when metabolic links exist versus when it does not exist. The whole idea is to see if the GEM coculture model also differentiate the effect of metabolic links on coculture growth. Figure 32 (a) The GEM model predicted a lower growth rate for the coculture when they cannot exchange any metabolites which proves the importance and contribution of the metabolic links in the coculture system.

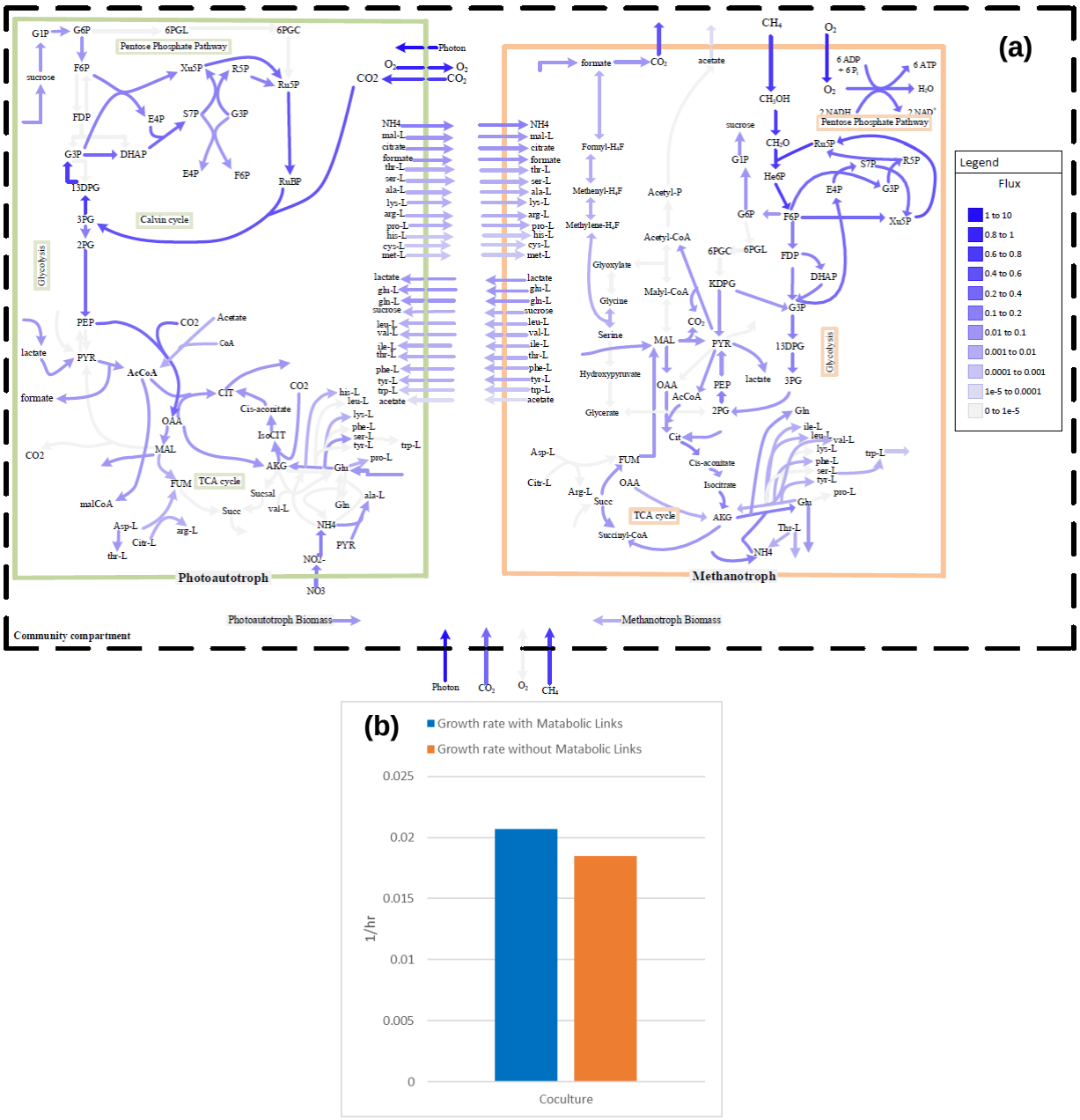

Figure 38. **(a)** Schematic representation of the simulated metabolism of the coculture system when cells are allowed to exchange the metabolites; **(b)** the comparison of the coculture growth rate between the MMT models when metabolic links exist and when it does not exist.

5.4.3 Comparison of SteadyCom and MMT

Both SteadyCom and microbe-microbe interactions (MMT) coculture GEM could accurately capture the coculture growth rate, the population ratio and main product consumption

/productions of the coculture under different conditions. However, it seems MMT was more accurate and consistent in predicting the coculture behavior. **Table 18** shows models prediction of the exchange metabolites for two different scenarios: 1- succinate and pyruvate are included in the metabolic links (malate is excluded), 2- just pyruvate is included in the metabolic links (succinate/malate are excluded). Considering the prediction for potential metabolic links, even though the order and flowrate of the metabolites was slightly different between the models,

Table 18. Models' prediction of the exchange metabolites for two different scenarios

1- pyr/succ				
Microbe-microbe model			**SteadyCom model**	
No.	Metabolite	amount		No.
1	succ	0.3982	0.5489	1
2	lac	0.1944	0	
3	NH4	0.1613	0.1572	3
4	sucr	0.0565	0.0553	5
5	cit	0.0453	0.0369	7
6	for	0.0437	0.0528	6
7	glu-L	0.0406	0.0363	8
8	pyr	0.0288	0.3411	2
9	gln-L	0.0233	0.0247	
10	ser-L	0.0082		
11	leu-L	0.0075		
12	val-L	0.0062		
13	thr-L	0.0049		
14	ile-L	0.0049		
15	ala-L	0.0044		
16	pro-L	0.0043		
17	lys-L	0.0037		
18	phe-L	0.0031		
19	tyr-L	0.0031		
20	arg-L	0.0015		
21	trp-L	0.0008		
22	ac	0.0007		
23	his-L	0.0006		
24	cys-L	0.0004		
25	met-L	0.0003		
	asp-L	0	0.1365	4

2- pyr				
Microbe-microbe model			**SteadyCom model**	
No.	Metabolite	amount		No.
1	cit	0.159	0.0747	3
2	NH4	0.1518	0.1555	1
3	for	0.1378	0.0475	4
4	glu-L	0.0666	0.0759	2
5	sucr	0.053	0	
6	pyr	0.0383	0.0246	5
7	gln-L	0.0258	0.0234	6
8	leu-L	0.0087	0.008	7
9	thr-L	0.0081	0.0011	
10	val-L	0.0072		
11	ser-L	0.006		
12	ile-L	0.0056		
13	pro-L	0.0049		
14	phe-L	0.0035		
15	tyr-L	0.0035		
16	ala-L	0.0029		
17	lys-L	0.0012		
18	arg-L	0.001		
19	trp-L	0.0009		
20	ac	0.0007		
21	cys-L	0.0005		
22	his-L	0.0004		
23	met-L	7E-05		
	lac	0	0	

however, interestingly top predicted exchange metabolites were always similar between the models. “lactate” and “aspartic acid” are examples of different metabolite prediction between the models. lactate production happens in microbe-microbe model by methanotroph, however the prediction of lactate by SteadyCom is zero. The similarity between the models investigated by metabolites and also their exchange which means they produce by the same organism. The color in the table shows the production of the metabolites by photoautotroph or methanotroph. As it is shown, the top exchange metabolites are similar between two models.

Table 18 comparison of the order of predicted potential exchange metabolites between microbe-microbe model (MMT) and SteadyCom model, for two different scenarios: 1- succinate and pyruvate are included in the metabolic links (malate is excluded), 2- just pyruvate is included in the metabolic links (succinate/malate are excluded). Amounts in orange color are produced metabolite by methanotroph and amounts in green color are produced metabolites by photoautotroph.

Table 19. Top predicted exchanged metabolite from SteadyCom and microbe-microbe interactions models

succinate	NH3	formate	citrate
sucrose	glutamate	pyruvate	glutamine

This result agrees with literatures that used microbe-microbe interaction modeling. They found metabolite in TCA cycle and amino acids as the main cross-fed metabolites [137]. It is worth to mention that we included “succinate” and “pyruvate”, as the major metabolite in TCA cycle, in the metabolic link and excluded “malate” since we found more evidence in literature that formers are more possible options [137,138]. **Table 19** shows the top predicted exchange metabolites and

Figure 39 depicts the central carbon pathway along with potential metabolic links between photoautotroph and methanotroph based on our most recent knowledge and analysis.

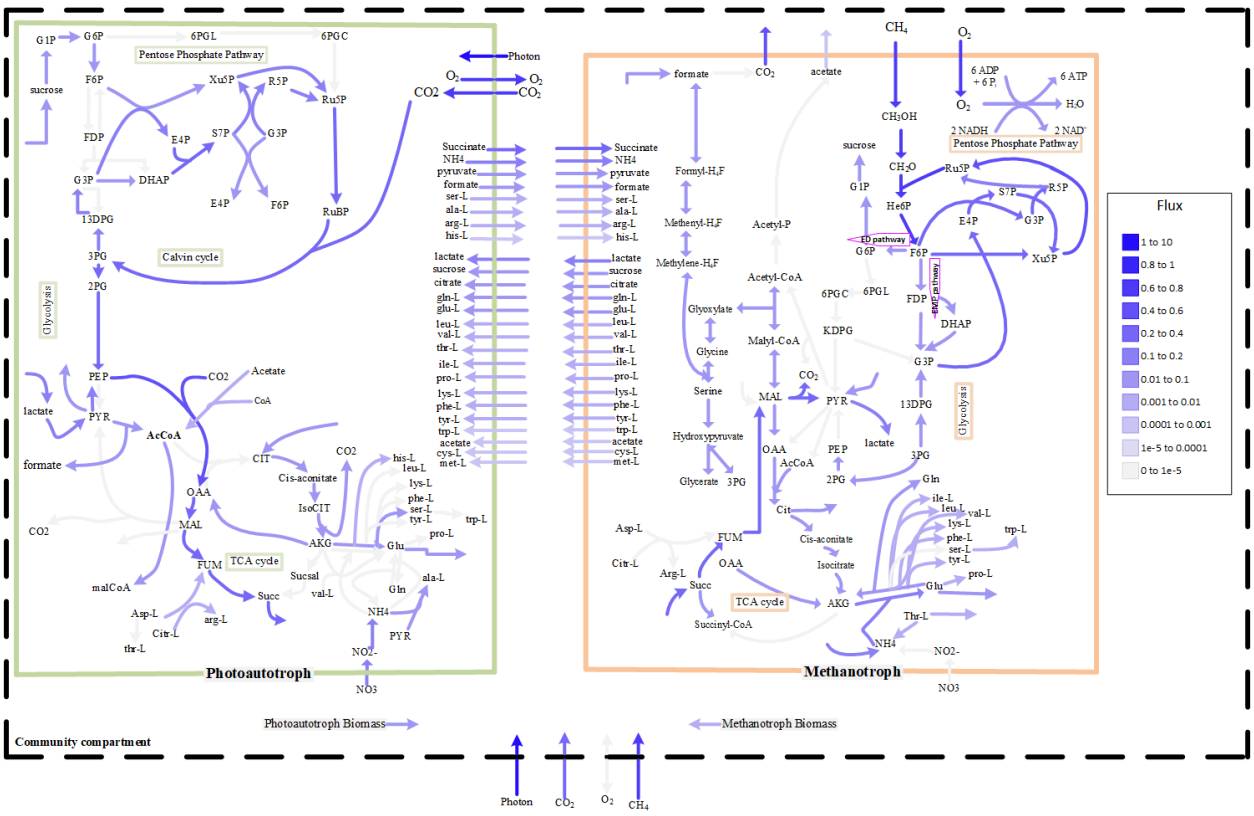

Figure 39. Schematic representation of the simulated metabolism of the coculture system when cells are allowed to exchange the metabolites ("Succinate" and "pyruvate" are allowed to exchange at the major metabolites in TCA cycle).

The GEM models identified key metabolites links in the coculture. Although microbial social interaction spans over a wide range of sophistication, even the simplest cooperative interaction can be difficult to explain when it brings population benefits but comes at the expense of individuals. Xavier [139] mentioned that a good illustration of this conflict is the trade-off between slow growth rates with a high yield versus fast but wasteful growth. The trade-off can be a consequence of irreversible thermodynamics on heterotrophic cell metabolism and has important consequences for populations. Higher yields make a more economic use of limited resources, and

therefore can be beneficial to the entire population. The population benefit comes at the expense of individual-level restraint, as cells could grow faster with lower yields. This exactly could happen in photoautotroph-methanotroph cooperation.

As it is shown in **Figure 39**, photoautotroph provides main favourable carbon source and nitrogen source, such as succinate and ammonium respectively, for methanotroph. In response, methanotroph produce more amino acids for both organisms. We believe the reason is that methanotroph can produce most of the amino acids less expensive biologically/thermodynamically than photoautotroph. Some literatures mentioned the advantageous of methanotroph for the production of TCA-derived products [140,141]. Hillesland and Stahl [142] have showed in their study that strains in a coculture with mutualistic relationship adapt themselves to use resources more efficiently. When populations first engage in a mutualistic relationship, they must adapt to new growth conditions, and they most likely use preexisting traits for new functions. Thus, one of the first adaptations for mutualism may be optimization of these traits for mutualistic performance. In support of this hypothesis, both species in nearly every studied coculture appear to have substituted mutations that improved the overall productivity of syntropy. Cocultures could grow faster and produce more cells even though the resources remained constant throughout the experiment. Each species contributed to one or both of these community-level changes, presumably because they were able to more efficiently use the available resources and hence acquire more energy for growth.

Moreover, though empirical testing of the simulation we performed is inaccessible at this time (we need to test coculture medium with metabolomic analysis to quantify all metabolites and compare with metabolites in the single culture), we note that experimental data from previously published work supports key portions of our predictions. We reviewed the literatures to find the

evidence of production or exchange of the predicted metabolites in order to validate the possibility of the predicted exchange metabolites between photoautotroph and methanotroph (next section).

5.5 Evidence and explanation on interactions between photoautotroph and bacteria

We are interested here in interactions between free-living species. One example is the two-species aggregate *Chlorochromatium aggregatum* (**Figure 40**), in which nonmotile, photosynthetic sulfur bacteria attach to motile β-proteobacteria, providing them with fixed organic carbon in exchange for a ride toward sulfide-rich areas.

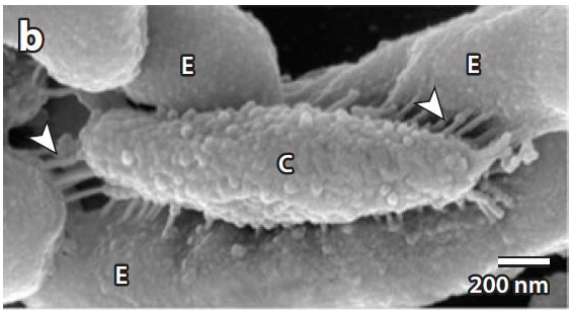

Figure 40. Electron microscopy image of the two-species aggregate *Chlorochromatium aggregatum*, showing photosynthetic sulfur bacteria (E) attached to a betaproteobacterial cell (C) by thin filaments (arrows) [143].

However, because of difficulties in cultivating the aggregate or its individual species, it remains unclear whether the interaction does indeed result in overall fitness gains for both parties. Attachment also occurs between the bacterium *Pelotomaculum thermopropionicum* and the methanogenic archeaon *Methanothermobacter thermautotrophicus*, whereby *P. thermopropionicum* uses its flagella to attach to *M. thermautotrophicus*, with flagella attachment inducing the latter to exchange metabolic services with the former. This example illustrates some key elements that are likely to be important for a cooperative interaction to stably emerge between species. First, the two species have very different metabolisms, which limits ecological

competition between them. Second, their metabolism is so different that one species can live off of the hydrogen produced by the other. Finally, the two species are physically attached to one another and respond to each other metabolically, which suggests that anything that a focal cell does to the other genotype is likely to feedback on itself. The prevalence of physical attachment in all of these examples may suggest that it is a particularly important component of between-genotype cooperation [143].

To discuss the previous study on our coculture pair, it is worth to compare their key hypothesis in our case. In our coculture system, cyanobacteria use CO_2 and methanotroph use CH_4 as carbon source, which eliminate competition between them for the main carbon source. Cyanobacteria produce oxygen and needs to get rid of it because it inhibits its metabolism and methanotroph live off the oxygen produced as byproduct by cyanobacteria. Finally, both strains could be physically attached to one another and respond to each other metabolically as it has been seen methanotroph around cyanobacteria cells under microscope (unfortunately SEM pictures are unavailable at this moment).

Generally, photoautotroph provide O_2 and organics through photosynthesis for bacterial consumption, whereas the bacteria produce CO_2 and inorganic substances through respiration to sustain photoautotroph growth [144]. The definition of photoautotroph covers all unicellular and simple multi-cellular microorganisms including prokaryotic microalgae (cyanobacteria), eukaryotic microalgae, and diatoms. Due to the mutually beneficial interactions of CO_2 and O_2, capital costs with regard to the oxygenation of activated sludge tanks and the risk of volatilization can obviously be reduced [145]. Besides, it is now acknowledged that bacteria secrete micronutrient metabolites such as vitamin B12, phytohormones (IAA, abscisic acid, cytokinins,

ethylene, and gibberellins), thiamine derivatives, and siderophores to accelerate photoautotroph metabolism and biomass growth [146,147].

As it mentioned before, in order to investigate the metabolic links, we need to first focus on oxygen which is the main metabolic link in this coculture and could be a significant force or trigger for more cooperation between the organisms. As Heinken and Thiele [137] have shown that microbe-microbe interactions with and without oxygen differed significantly in microbiota environment. In fact, all but one of the mutualistic interactions observed without oxygen were abolished in the presence of oxygen. These results highlight that in the presence of oxygen, most microbes were able to efficiently extract energy from the supplied dietary nutrients and did not rely on metabolites secreted by other microbes. In the absence of oxygen, however, the microbes were forced to cooperate to achieve optimal growth by exchanging metabolites with each other. Accordingly, mutualistic pairs switched to parasitic giver-consumer interactions in the presence of oxygen.

The substrate exchange is not limited to micronutrients. Macronutrients such as nitrogen-mediated interactions also occur between photoautotroph and bacteria. In photoautotroph, nitrate assimilation is performed by two transport and two reduction steps: First, nitrate is transported into the cell, then a cytosolic Nitrate Reductase (NR) catalyzes nitrate reduction to nitrite, which subsequently is transported into the chloroplast, where the enzyme Nitrite Reductase (NiR) catalyzes its reduction to ammonium [148,149]. Finally, ammonium is incorporated to carbon skeletons by rendering glutamate, through the glutamine synthetase/glutamine oxoglutarate amino transferase or glutamate synthase (GS/GOGAT) cycle [150]. First, ammonium is incorporated as the amide group of glutamine in a reaction involving glutamate and ATP (catalyzed by GS); then,

the amide group is transferred reductively to a-oxoglutarate to form two molecules of glutamate [151].

Recently, de-Bashan et al. [152] clearly showed that co-evolution is not a prerequisite for a functioning synthetic mutualism between a microalga and a bacteria. Using highly specific analytical tools capable of analyzing single cells within the association such as NanoSIMS isotopic imaging and fluorescent in situ hybridization (FISH), combined with enforcing initial proximity between cells of the two species in alginate beads, they directly showed that C and N containing compounds were exchanged during interaction and association, which is beneficial to both microorganisms as demonstrated by their mutually enhanced growth. Furthermore, because this association was man-made and created almost spontaneously without lengthy co-evolution, it challenges a basic paradigm of mutualism. This association arises relatively fast and forms a stable association lasting for at least 10 days.

Moreover, a recent study investigated a stable mutualism between winery wastewater isolated *C. sorokiniana* and *S. cerevisiae* under synthetic growth conditions. They observed mutualistic relationship based on carbon (C) and nitrogen (N) cross-feeding which involves the reciprocal exchange of C in the form of CO_2 to the microalgae and ammonium (derived from inaccessible nitrite) as N to the yeast [153]. Ammonium is the preferred N source due to its reduced state and energetically favorable assimilation. It is well-established that ammonium has a negative effect on nitrate assimilation [149]

Research has been shown production of formate by cyanobacteria through the action of pyruvate formate lyase (PFL). PFL catalyzes CoA-dependent cleavage of pyruvate to form acetyl-CoA without the associated production of NADH or reduced ferredoxin according to the following reaction [154]:

$$CH_3COCOOH + CoASH \rightarrow CH_3COOCoA + CHOOH \quad (30)$$

This reaction notably does not result in the production of NADPH or reduced ferredoxin and allows for ATP synthesis from acetyl-CoA through the combined action of phosphotransacetylase and acetate kinase [154,155].

One question here could be whether the strain is able to recognize presence of amino acid in the bulk (produced by methanotroph) and most importantly whether the strain is able to manage the production or quenching of amino acids. Riccardi et al. [156] have shown the amino acid regulation in cyanobacteria in response to external effect that help us to explain the relationship of strains in the coculture. They showed in their review that biosynthetic pathways are highly responsive to some specific exogenous amino acids. Some idea of the importance of amino acid biosynthesis in the carbon economy of the cell can be obtained from the estimate that 59% of the carbon assimilated from glucose by *E. coli* is in the form of amino acids. For growth in a glucose minimal medium, the diversion of this large component of assimilated carbon to amino acids is essential. However, there would be a strong selective pressure for mechanisms allowing a complete quenching of amino acid biosynthesis in the presence of an exogenous source of preformed amino acids. The extent to which such quenching occurs depends on the organism and on the pathway involved.

Another question could be the ability of the strains for execration of the metabolites. To answer this question, we refer a study that has illustrated cyanobacteria as sources of bioactive compounds with interesting biological activities, for example, antibacterial, antifungal, antiviral, antialgal, anticancer, anti-inflammatory, and so forth. These bioactive compounds include lipopeptides (40%), amino acids (5.6%), fatty acids (4.2%), macrolides (4.2%), and amides (9%). The excretion of bioactive compounds by cyanobacteria into the aquatic environments is possible

allelopathy strategy used by cyanobacteria to outcompete other microorganisms within the same ecosystem [157]. Furthermore, many studies have shown that a wild type [158] and mutant [159,160] cyanobacteria can excrete amino acids and other compounds if there is overproduction/accumulation of the metabolite [161]. For example, previously it has been proved that knockout of the glycogen synthesis pathway could effectively promote accumulation and excretion of pyruvate in cyanobacteria [162], thus the strains can secrete any metabolite if the condition is provided.

Moreover, Riccardi et al. [156] have shown that mutants of *Spirulina platensis* resistant to phenylalanine, which excrete phenylalanine, produce concentrations of amino acids that are up to 50-fold higher than those produced by the parental strain. Only about 45% of the amino acid over-produced is released into the medium during growth while the rest (> 50%) remains in the cell and is released only at cell lysis. From the other side, produced citrate, lactate and sucrose by methanotroph is consumed by cyanobacteria. Cyanobacteria used sucrose as a carbon source to increase the fluxes of PPH pathway and Calvin cycle; and used citrate and lactate to produce more glutamate and beside it some other required aminoamides.

Zhu et al. [163] have been shown releasing of citrate by methanotrophs. Briefly, CH4 is initially catalyzed by methane monooxygenase (MMO), soluble MMO (sMMO) or particulate MMO (pMMO), to produce methanol as the first intermediate. Afterwards, methanol is transformed into formaldehyde by methanol dehydrogenase. Formaldehyde may be assimilated into biomass through the ribulose monophosphate pathway or the serine pathway, releasing multi-carbon intermediates such as acetate and citrate; Or formaldehyde can be dissimilated to CO2 via formate for energy production.

Gilman et al. [164] showed that *M. buryatense* 5GB1 has able to produce lactate and succinate.

But et al. [165] have investigated the biochemical pathways for sucrose metabolism in methanotroph *Methylomicrobium alcaliphilum* 20Z and showed the ability of the organism for sucrose production. It worth mentioning that until recently, sucrose was thought to be accumulated mainly in phototrophic organisms, including plants, unicellular algae, and cyanobacteria. However, studies have shown that a number of methylotrophic bacteria utilizing methane, methanol, or methylated amines can accumulate sucrose as a primary or secondary solute. The methanotroph synthesizes sucrose in response to the increased salinity of growth media.

In conclusion, the coculture GEM models were able to predict the growth rate, ratio of organisms and metabolic links that make sense for reaching a stable mutual coculture. Moreover, cross-fed metabolites have been seen and confirmed by other studies as it discussed in this section.

Chapter 6: Dynamic genome-scale metabolic modeling suggests the establishment of mutualism without co-evolution within a synthetic microbiome

6.1 Introduction

GEMs work under a pseudo-steady state assumption and utilize linear optimization to extract feasible flux distributions. These fluxes are integrated over time in dynamic GEM. There is this possibility to predict the changes of initial conditions over time such as the consumption and production of metabolites, changes in biomass, and shifts in metabolism in response to environmental changes. Dynamic GEM simulates a whole time of experiment, as opposed to standard GEM that just provide a single snapshot of the steady state condition [166]. The schematic diagram of dynamic GEM in **Figure 41** clearly shows integration of fluxes and other characterization that was explained. As shown in **Figure 41**, bioreactor dynamic model integrates the substrate uptake rate and feeds it to the steady state genome scale modeling for each strain, then the genome modeling provides product and growth rate and feeds those back to the dynamic model for integrating over next time segment. In fact, dynamic GEM just captures the bioreactor dynamics which is coupled to steady state genome scale modeling. The sequential product rate will be fed back to the bioreactor dynamic model from the genome modeling.

The use of linear optimization requires an objective function, but more importantly a biologically relevant objective function. Most standard GEM applications use maximization of an artificial biomass equation representing the production of metabolic constituents of biomass as the objective function. However, in the dynamic GEM, metabolites, species abundance and metabolic states are free to change by changing the environment or response to interactions. Thus, there is no need to a community objective function (still we need objective function for each strains) and proper bounds on interspecies fluxes to be defined, since the proper kinetic parameters are given to the model. As an example, Hanly and Henson [167] were performed dynamic flux balance

modeling of a coculture (*Escherichia coli* and *Saccharomyces cerevisiae).* Each microbe consumes a unique sugar (glucose or xylose), objective function was maximizing summation of biomass of the strains and the whole simulation was used to optimize ethanol production. Zhuang et al. [168] developed the dynamic multispecies metabolic modeling (DyMMM) framework, which is an alternative form of dynamic GEM for community modeling, to model the competition of two acetate oxidizing and Fe(III) reducer. Challenges with the implementation of dynamic GEM are inserting the kinetic parameters such as Michaelis–Menten kinetics (constants), particularly uptake rates of limiting metabolites such as methane, carbon dioxide and oxygen in our study.

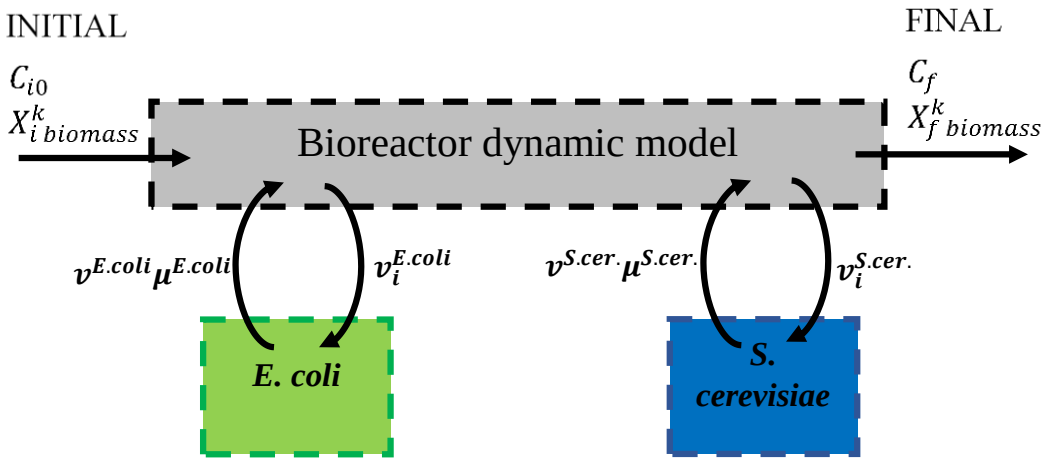

Figure 41. Schematic diagram of dynamic GEM

In this work, it was decided to first reproduce the results generated by Hanly and Henson study [167]. A Matlab based simulator developed by Barton group [169] named DFBAlab was used for modeling. This model uses the LP feasibility problem to obtain an extended system, and also lexicographic optimization to yield unique exchange fluxes. The performances are comparable to DyMMM.

6.2 Dynamic GEM modeling using DFBAlab

6.2.1 Reproduction of a published results

The Dynamic GEM of *E.coli* and *Saccharomyces cerevisiae* co-culture from the Hanly and Henson's paper [167] was built and compared with experimental data. The rebuilt model prediction was almost matched with the paper's result as it shown in **Figure 42**.

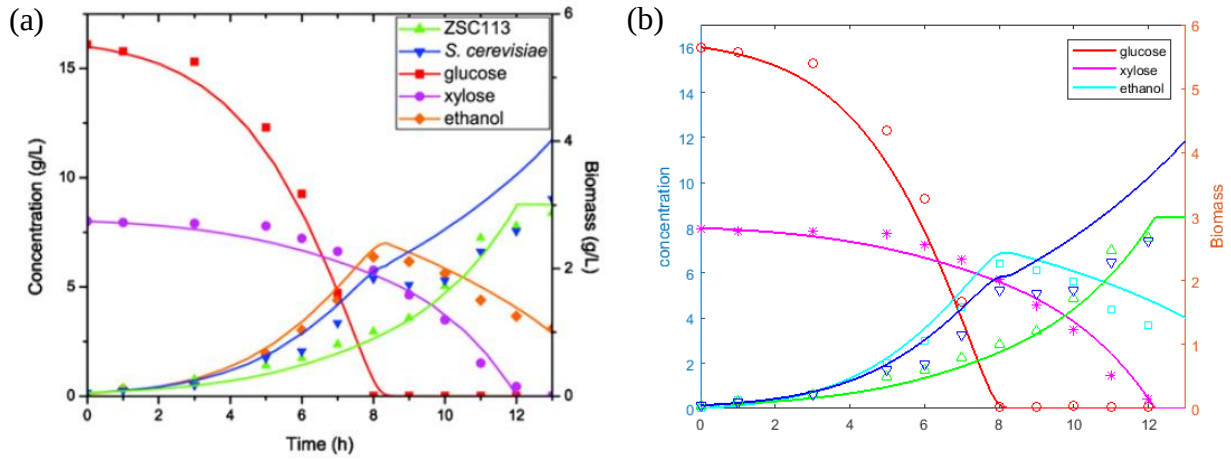

Figure 42. Experimental data (points) and coculture prediction (lines) by model for aerobic batch fermentation (a) The result from the literature [167], (b) The result generated in this work.

The literature used the fix oxygen uptake rate; however, it was decided to improve the prediction ability since the model is unable to catch most of yeast biomass production (*S. cerevisiae*) specifically after depletion the glucose in the system.

The concentration of dissolved oxygen depends on the oxygen transfer rate from the air bubbles to liquid phase, the oxygen uptake rate of cells for growth, maintenance, and the metabolite production by the cells. The mass balance of the dissolved oxygen in the assumed well mixed liquid phase was written in equation 31.

$$\frac{dC_{o2}}{dt} = k_l a\,(C^* - C^{t1}) - q_{o2}.X \qquad (31)$$

where $\frac{dC_{o2}}{dt}$ is the accumulation of oxygen in the liquid phase, the first term on the right hand side is the oxygen transfer rate, (C^{t1} is the oxygen concentration at time 1), the second term is the oxygen uptake rate which can be expressed by q_{o2} (specific oxygen uptake rate), and X is the biomass concentration. Most of the studies have used Michaelis-Menten equation for specific oxygen uptake rate ($q_{O2} = \frac{v_m \times C_{O2}}{K_m + C_{O2}}$) as it was explained at previous sections. The $k_l a$ was obtained from literature [170]. Hence the system is coculture and both strains need oxygen to grow, the uptake by both strains was considered in the equation (Equation 32).

$$\frac{dC_{o2}}{dt} = k_l a\,(C^* - C^{t1}) - q_{o2,1}.\,X_1 - q_{O2,2}X_2 \qquad (32)$$

It is a valid consideration that when oxygen concentration is low, the change of dissolved oxygen in the coculture system by time is zero ($\frac{dC_{o2}}{dt} = 0$), and it is assumed that specific uptake rate for both strains is almost the same ($q_{o2,1} = q_{o2,2}$). The updated specific oxygen uptake rate shows in equation 33.

$$q_{o2} = \frac{k_l a\,(C^* - C^{t1})}{X_1 + X_2} \qquad (33)$$

The mass transfer formula was used and implemented into the model and the better match with experimental data was achieved.

(a)

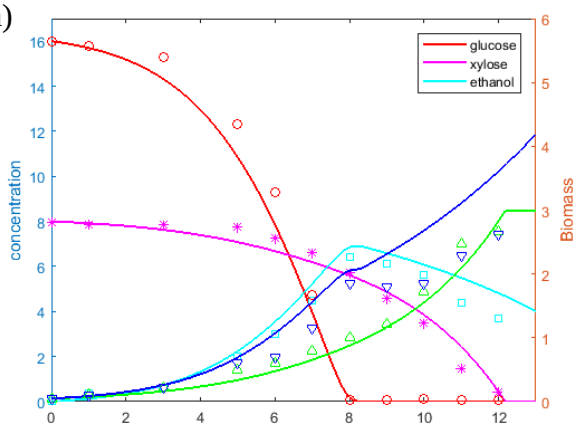

(b)

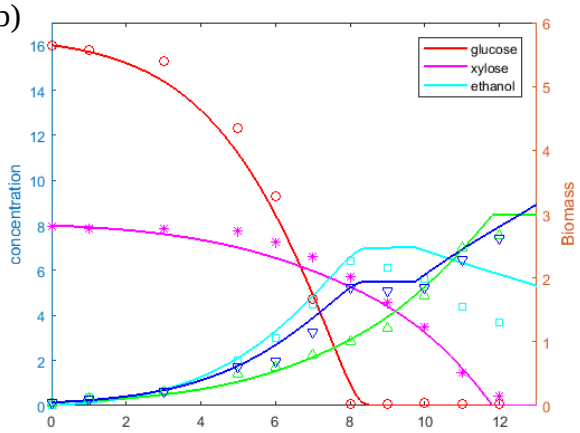

Figure 43. Comparison between dynamic GEM modeling with fixed specific oxygen uptake rate and changeable specific oxygen uptake rate.

Figure 43 shows the improvement after implementing the specific oxygen uptake rate into the model. As shown, there has been a great improvement in prediction of *S. cerevisiae* biomass compare to before. Next step was using this dynamic GEM model and simulating the photoautotroph-methanotroph coculture system.

6.2.2 M-P coculture system

As it is mentioned, challenges with the implementation of dynamic GEM are inserting the kinetic parameters such as Michaelis–Menten kinetics and constants, particularly for uptake rates of limiting metabolites such as methane, carbon dioxide and oxygen in our study. The prediction of single culture using DFBAlab was tested first to make sure the models were worked properly (**Figure 44**).

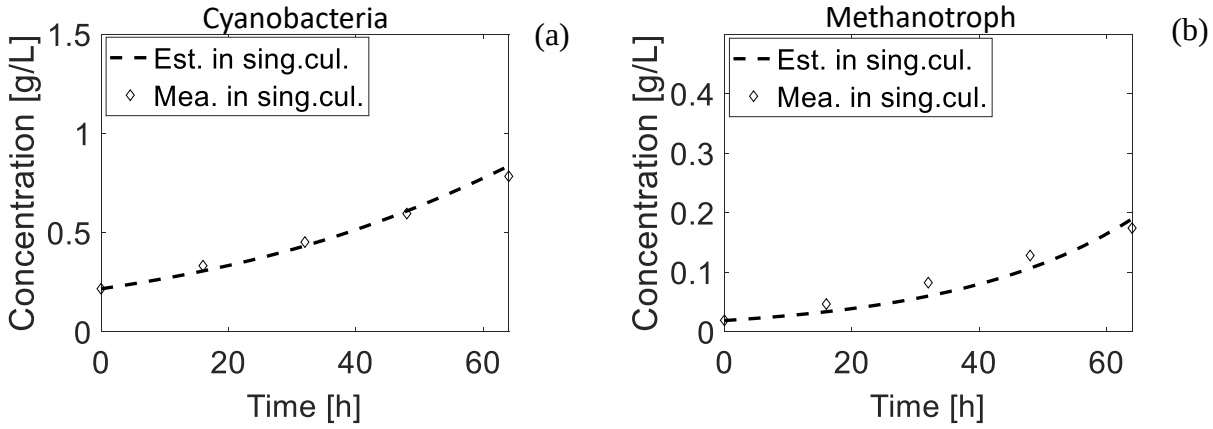

Figure 44. DFBAlab prediction for biomass concentration of (a) cyanobacteria single culture and (b) methanotroph single culture.

Beside the kinetics and constant parameters, which are difficult to find and fairly dependent on experimental conditions, one the most significant shortcoming of DFBAlab is absence of a common compartment, which means the metabolites cannot freely exchange between

species in the coculture. Therefore, we had to rely on Growth associated maintenance (GAM) and Non-growth associated maintenance (NGAM) to capture the effect of those molecular interactions that are not captured by the dynamic GEM model. As it is shown in the **Table 20**, the GAM and NGAM values had to decrease in order to predict the biomass concentration of individual strains in the coculture. It means that strains need less energy to grow when they are presence in the coculture system. **Figure 45** shows the prediction of the DFBAlab after modification. However, we still could not predict any metabolic links here, and we again proved the effect of the metabolic links.

Table 20. The GAM and NGAM values used in DFBAlab model.

GAM&NGAM	***Cyanobacteria***		***Methanotroph***	
	GAM	**NGAM**	**GAM**	**NGAM**
Single Culture	60	0.6	23	10.6
Coculture	40	0.05	23	5.6

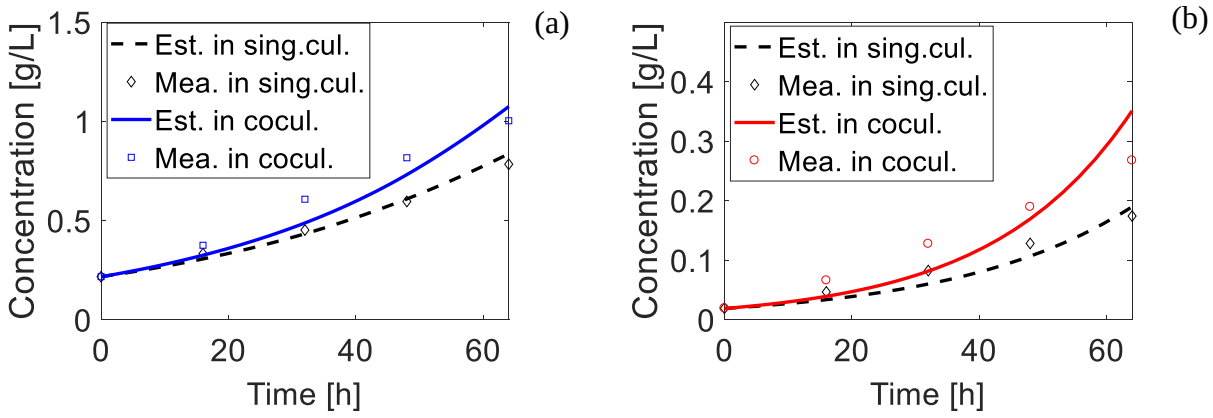

Figure 45. Comparison of biomass concentration of individual strain in the coculture versus single culture by DFBAlab for (a) cyanobacteria, (b) methanotroph.

To overcome these shortcomings, we decided to approach the issue from a different angle by developing a new dynamic GEM.

6.3 Developed dynamic GEM

While several GEM modeling approaches have been developed for microbial communities, little emphasis has been placed on the need for actual and reliable constraints of these complex systems, especially when the behavior of these communities is dynamic. Moreover, metabolic flux predictions based on constraint-based approaches can be inaccurate, as they often disagree with experimentally measured fluxes using techniques such as ^{13}C metabolic flux analysis, as was shown recently for *E. coli*. [171].

To address these challenges, we employ the validated semi-structured kinetic model to provide the cross-membrane fluxes, i.e., substrate pickup rates, product excretion rates and biomass growth rates, as constraints to the coculture GEM. These constraints not only allow the reduction of the feasible solution space of the GEM model, but also enables the simulation of the dynamic GEM, which can significantly improve metabolic flux predictions. Because the gene-regulation is much faster than the bioreactor dynamics, we can assume that the cellular metabolism is always in a pseudo-steady-state. Therefore, we can use the substrate uptake rates predicted by the kinetic model as constraints to the GEM, and use the steady-state GEM to determine the metabolic flux profile under then given pseudo-steady state. In this way, by integrating the kinetic model with the steady-state GEM for the coculture, we were able to obtain the dynamic metabolic flux changes over time. **Figure 46** shows our proposed dynamic GEM model.

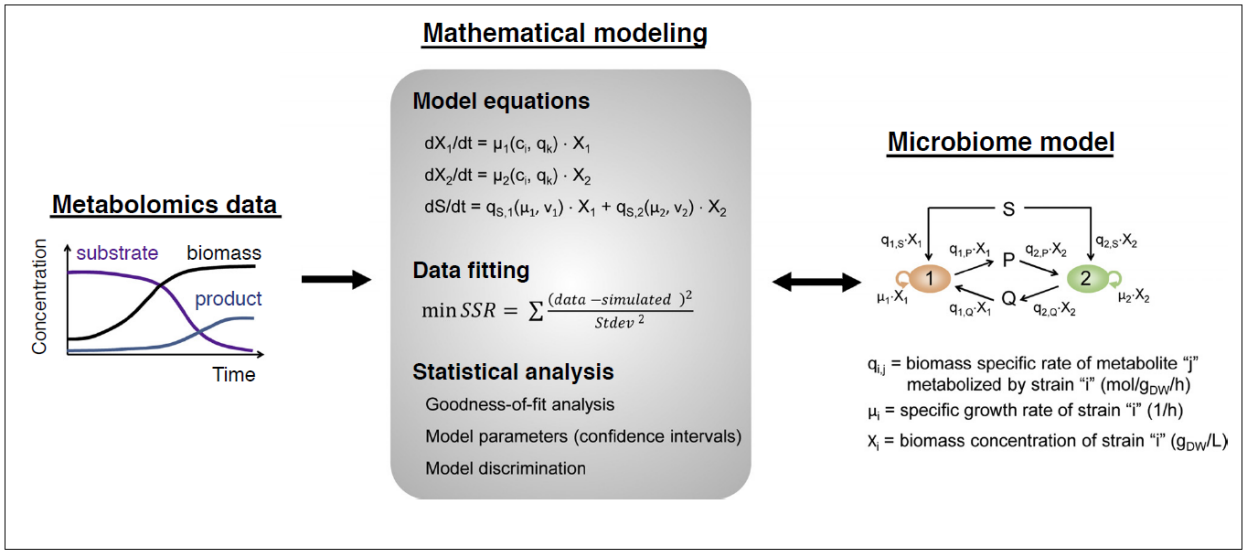

Figure 46. Mathematical models of microbial communities provide critical tools for generating and testing biological hypotheses. New computational approaches and software tools are needed that can promote fundamental understanding of microbial communities through comprehensive model-based analysis of omics data sets across multiple scales, from intracellular metabolism, to metabolite cross-feeding interactions between cells, to the emergent behaviors, structures and functions of microbial communities (adapted from Antoniewicz 2020 [64]).

6.4 Material and Methods

Microbe-microbe interaction (MMT) was implemented for pseudo-steady-state GEM of the dynamic GEM model. Experimental data of Experiment C (for different gas composition in coculture), condition (b) (Gas composition of 60%CH_4, 30%CO_2, 10%N_2) (Chapter 4, **Table 5**) was used as experimental data to run in the developed dynamic GEM model. As it is mentioned, the integration is a continuous process, however in order to reduce the volume of the results and be able to interpret the results easier, several time steps were chosen as an output of the dynamic GEM. The picked times are shown in **Figure 47**. Since the uptake rate of CH_4 and CO_2 are the two major constraints for the GEM model, the time steps were chosen to cover all range and irregularity of these variables (time steps: 2,5.5,8,14,20,26,32,38,42,50,58,64,74,82,90).

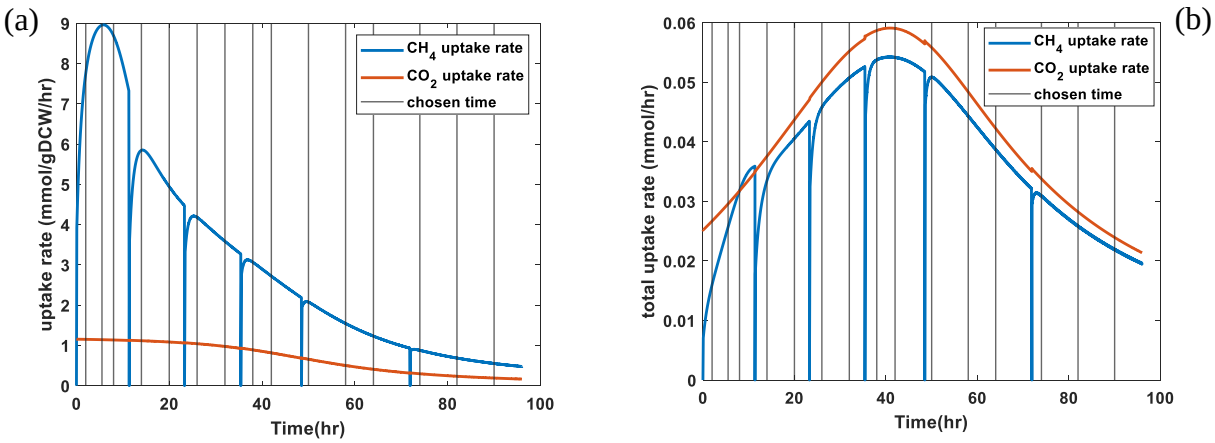

Figure 47. Chosen time steps for dynamic GEM model according to the behavior of the coculture uptake rates. All the black lines are the picked time shown in (a) uptake rate and (b) total uptake rate plots. Time: 2,5.5,8,14,20,26,32,38,42,50,58,64,74,82,90.

6.5 Results and discussion

The following figures show the visualization results of the coculture behavior and their metabolic interaction in progress with time steps by using dynamic GEM. This means CH_4 and CO_2 uptake rates from semi-structure kinetic model at each time step was put in MMT coculture model and generated the solution for the coculture system. The solution of the simulation at each time step was depicted below for observation of the pathway changes and further investigation.

Time= 2 hrs

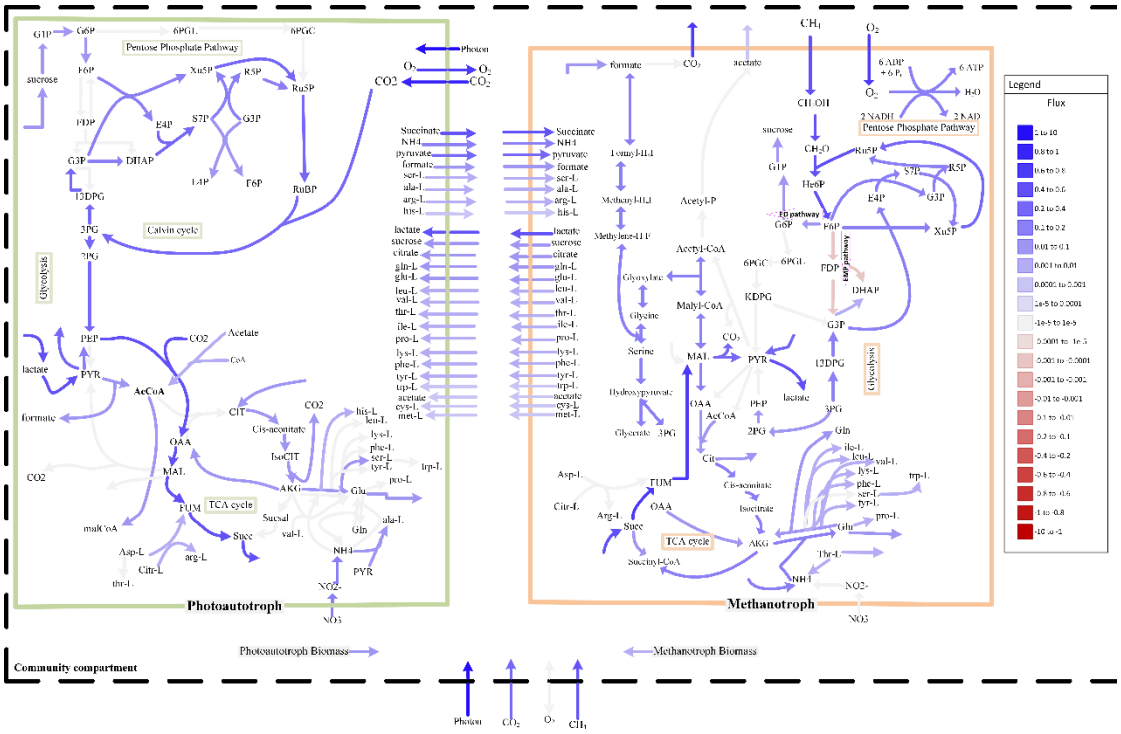

Time= 5.5 hrs

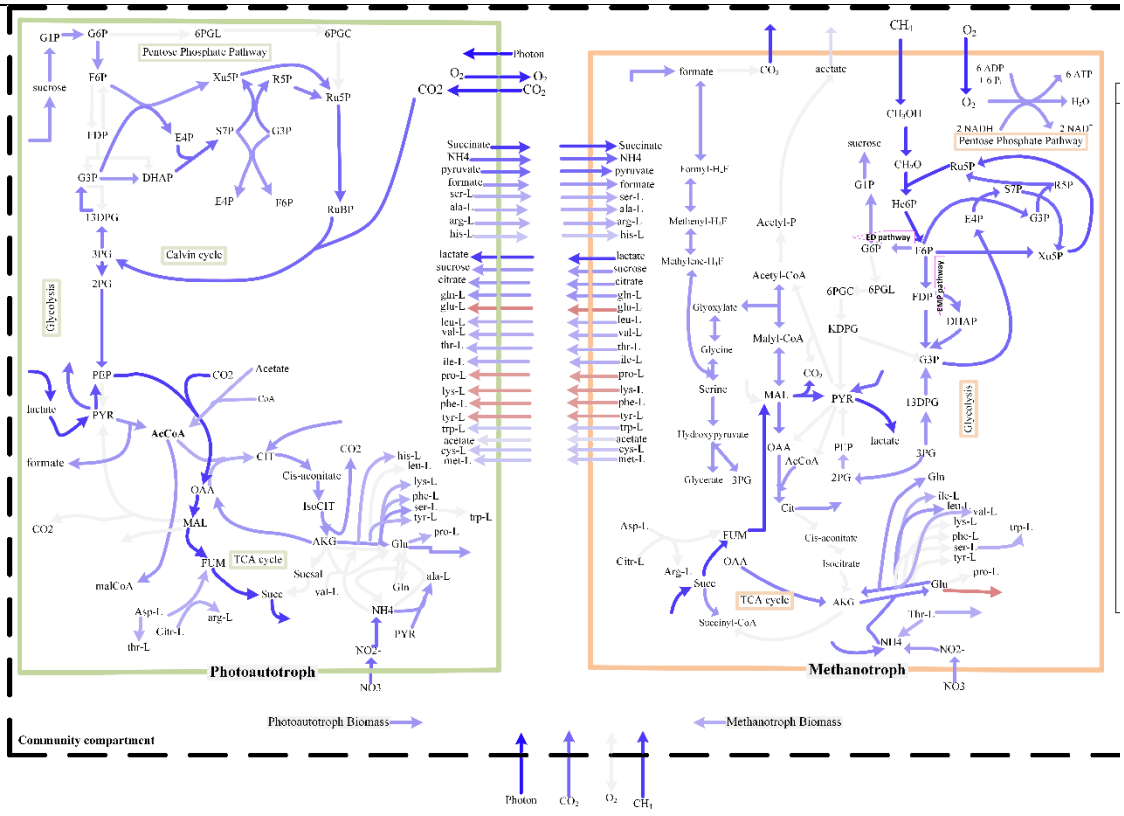

Time= 8 hrs

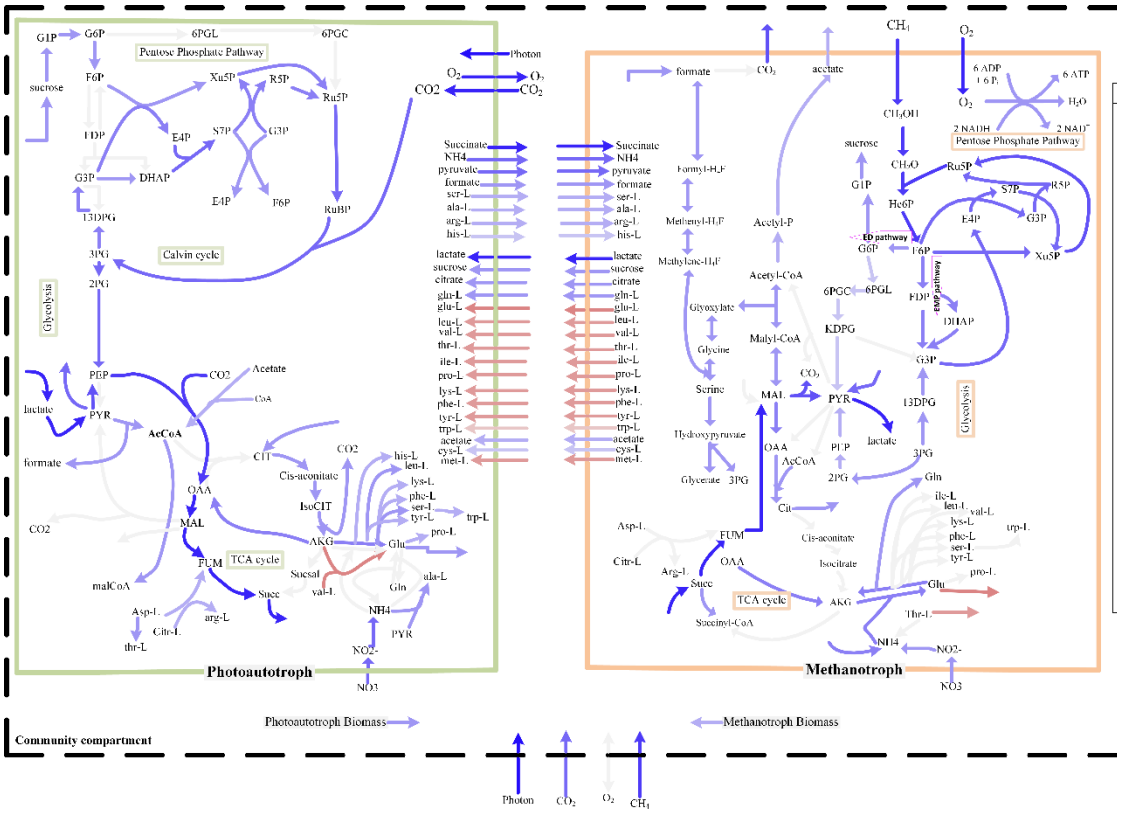

Time= 14 hrs

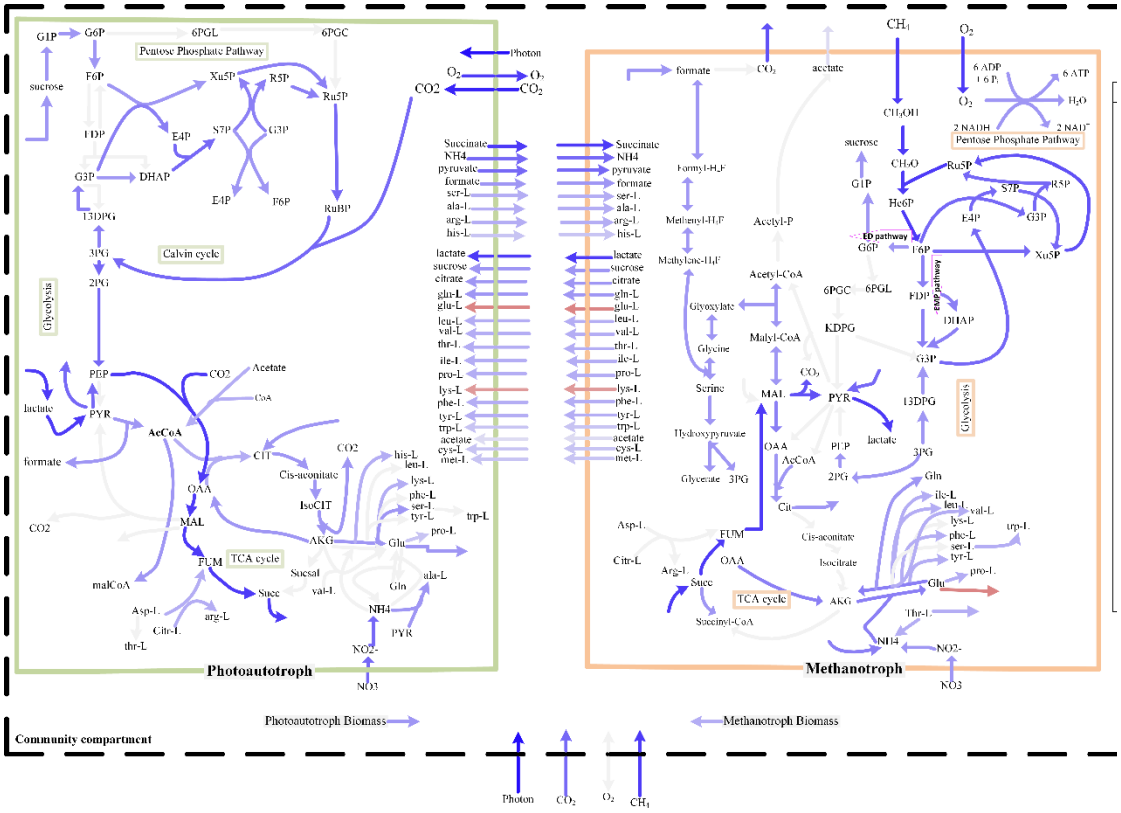

Time= 20 hrs

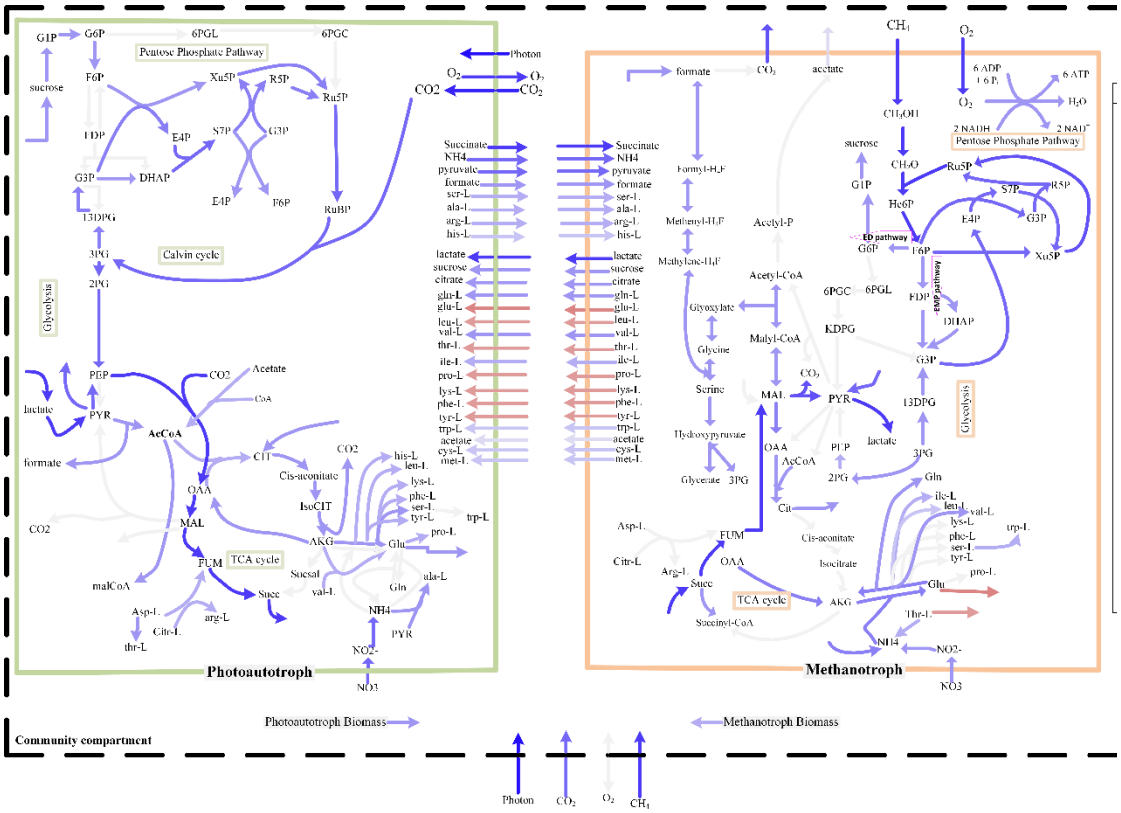

Time= 26 hrs

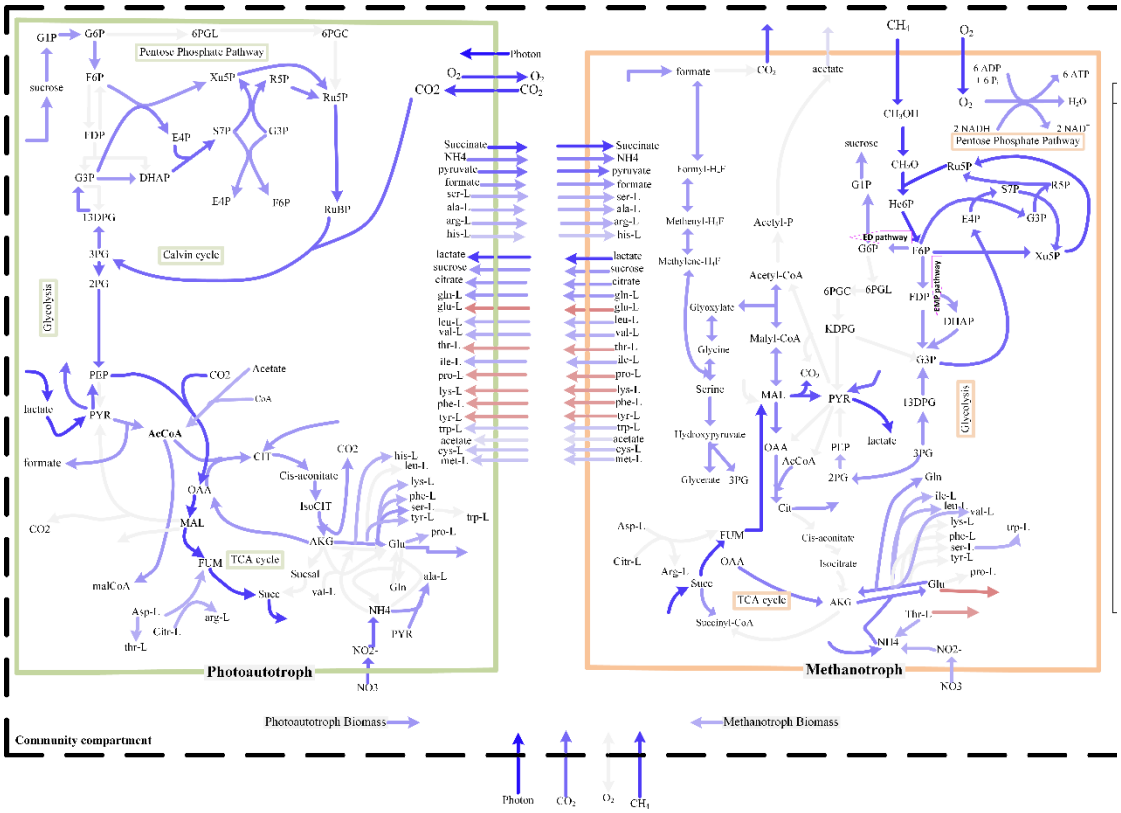

Time=
32 hrs

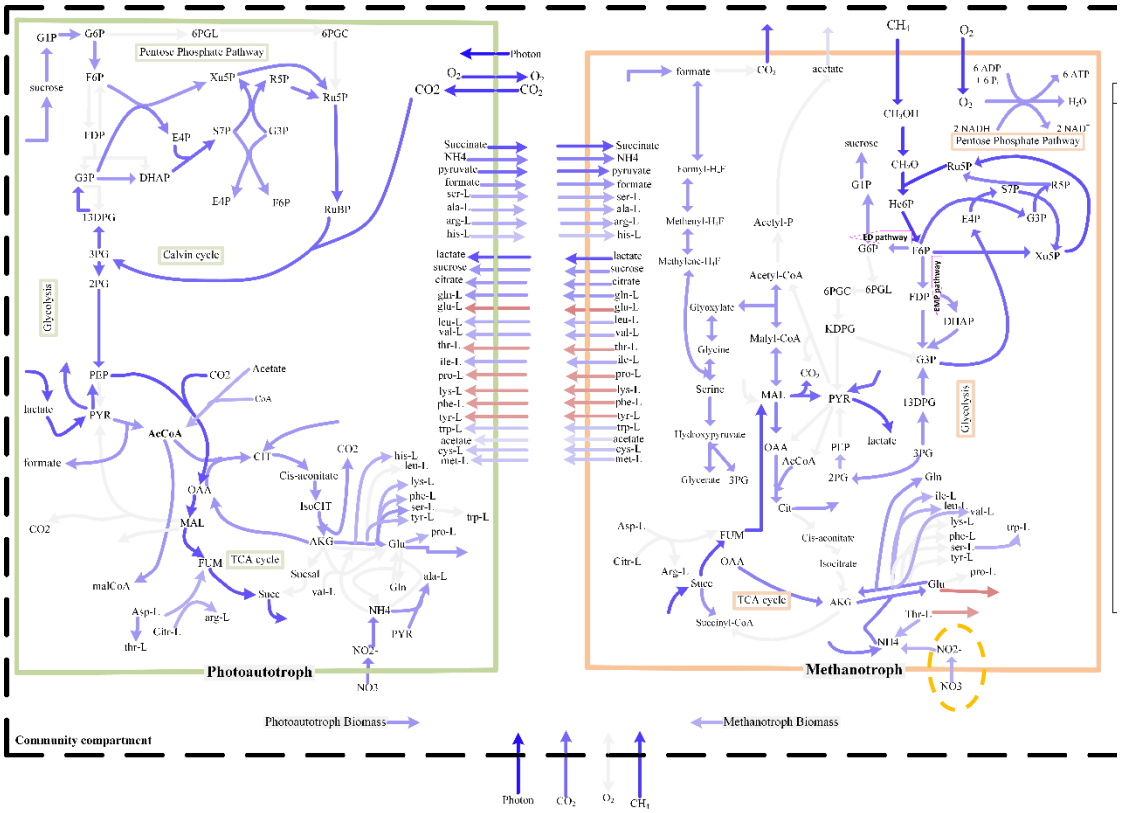

Time=
38 hrs

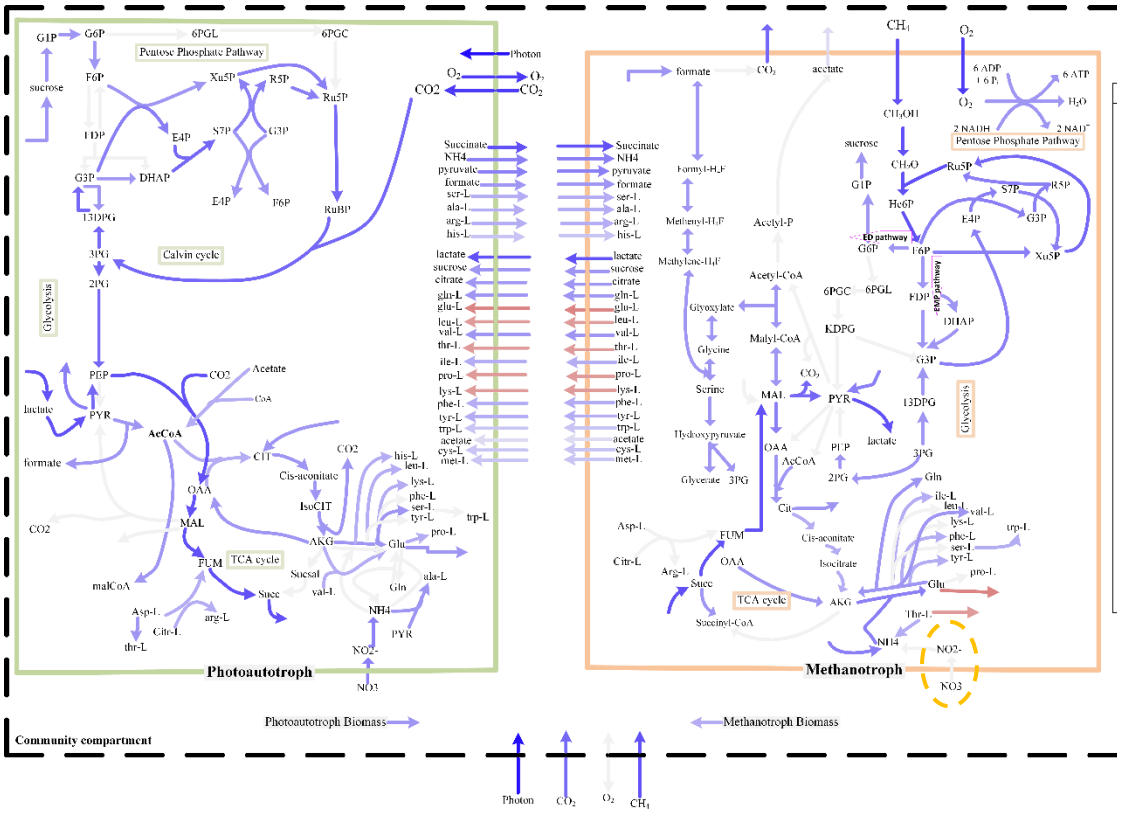

Time= 42 hrs

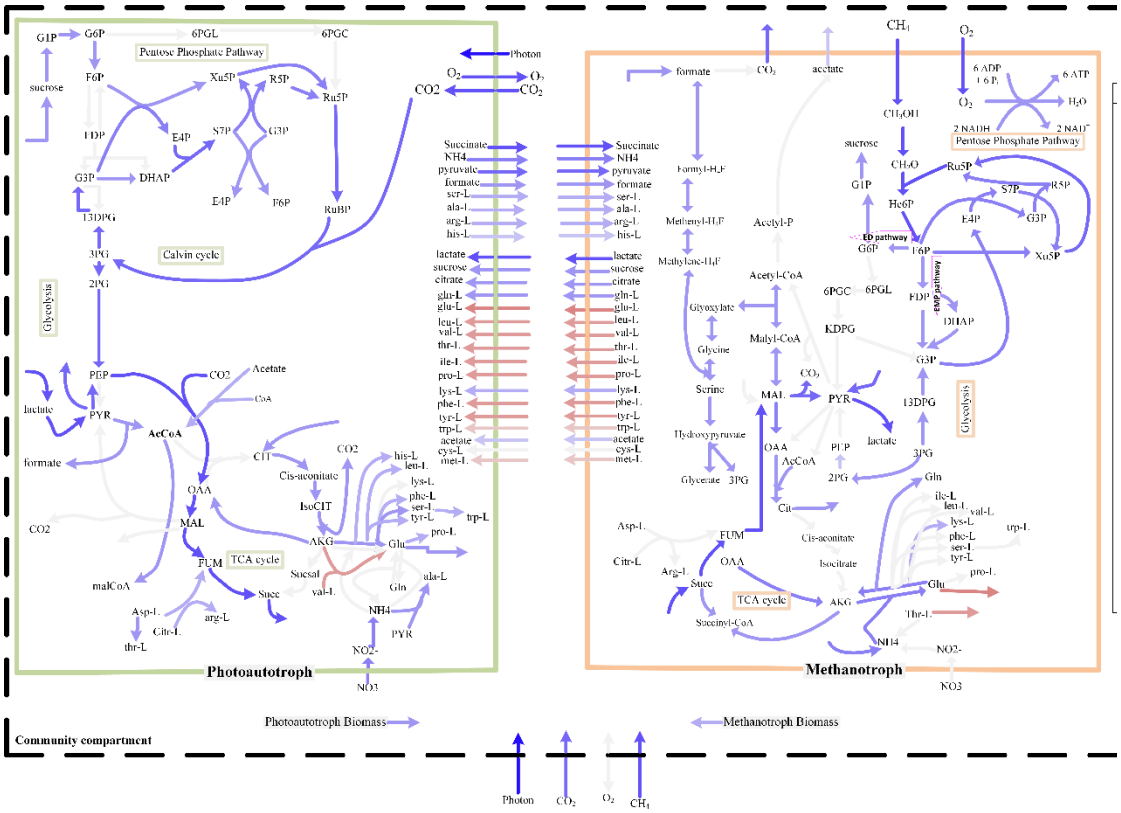

Time= 50 hrs

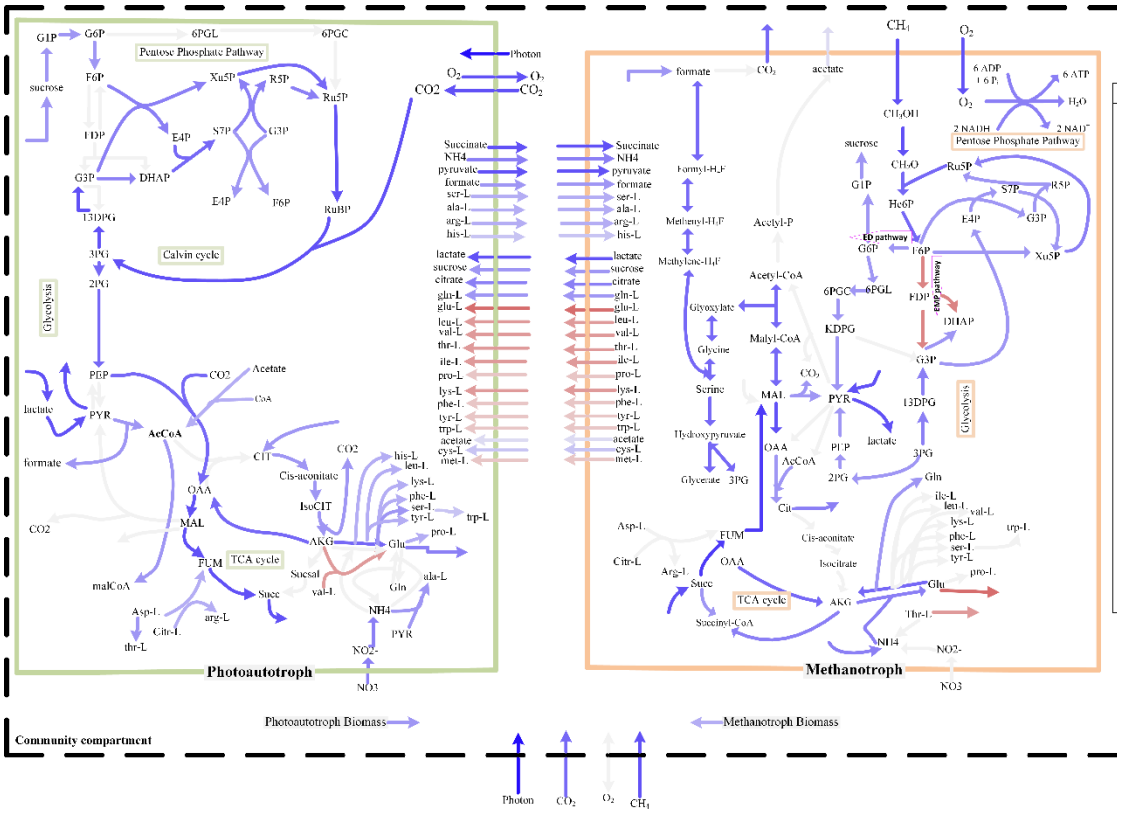

Time= 58 hrs

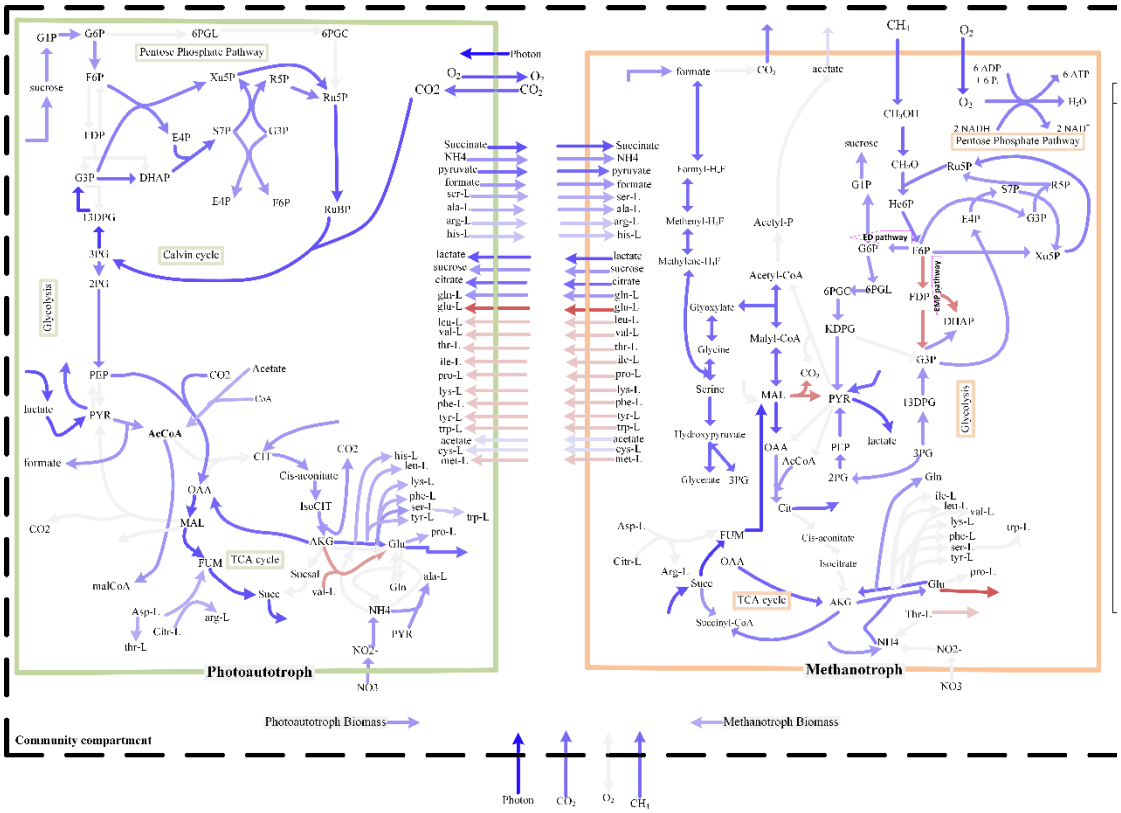

Time= 64 hrs

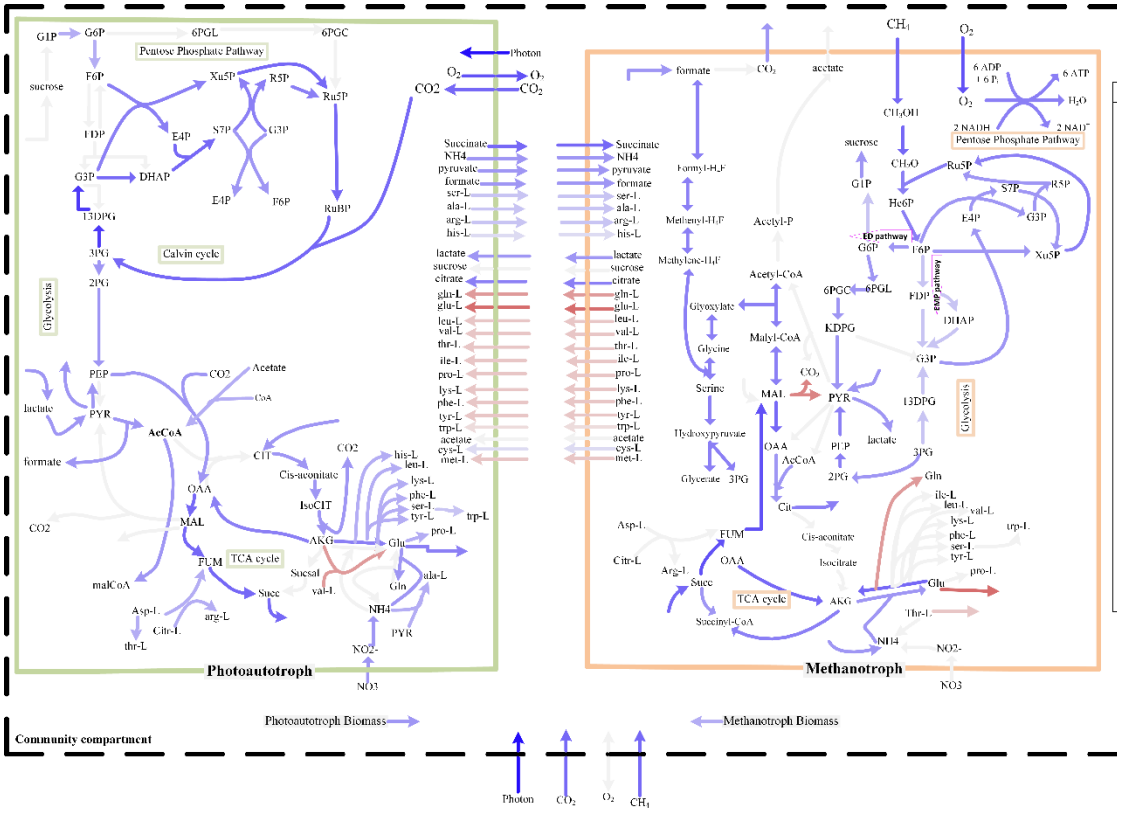

Time= 74 hrs

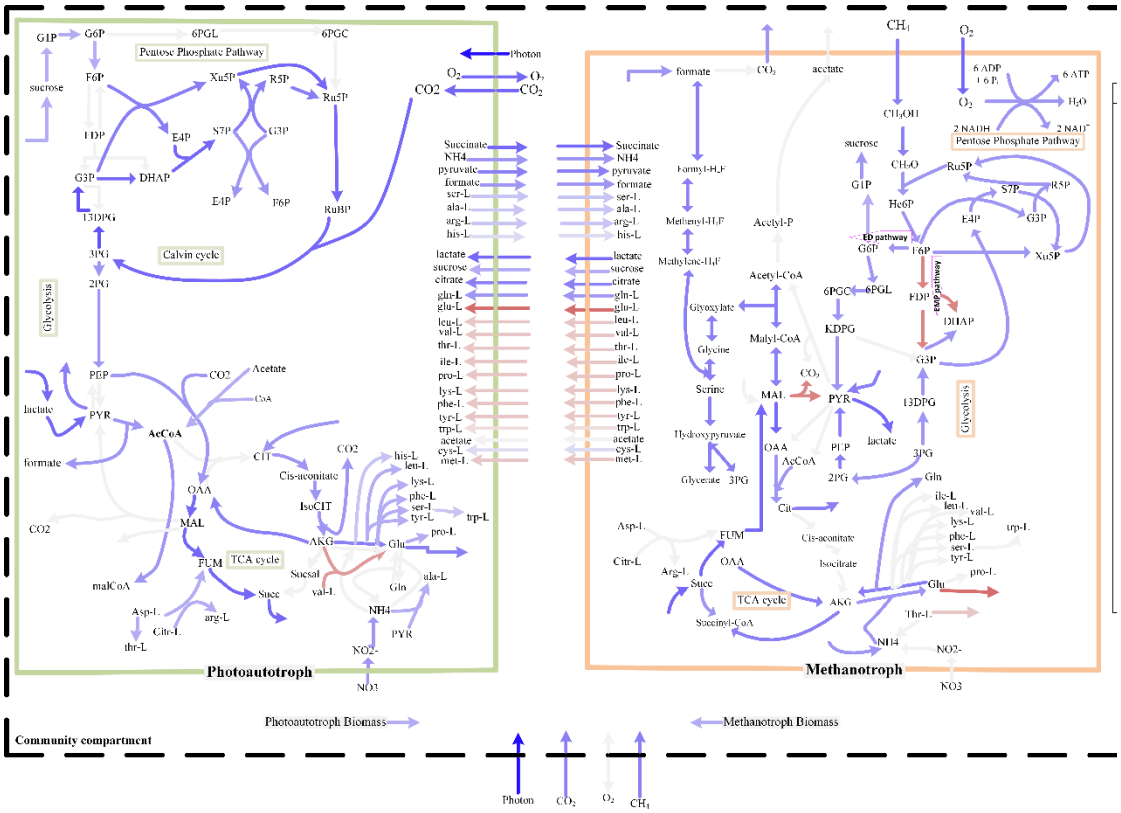

Time= 82 hrs

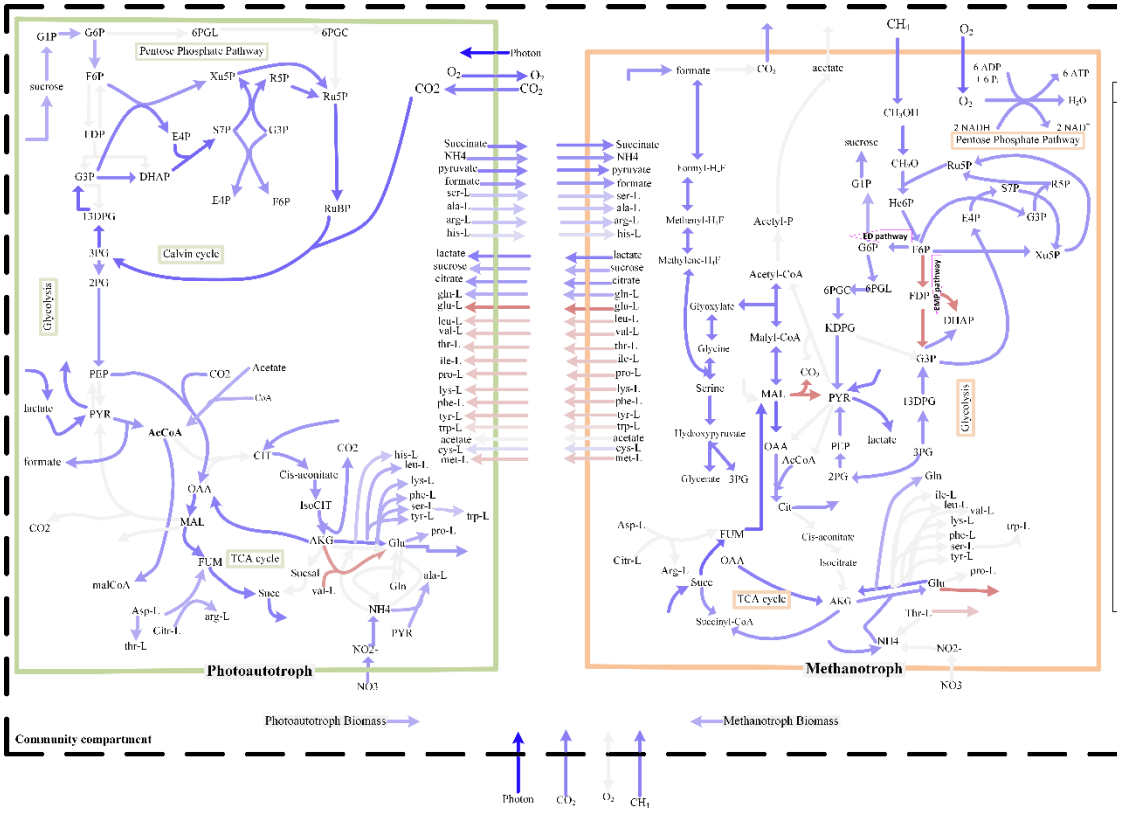

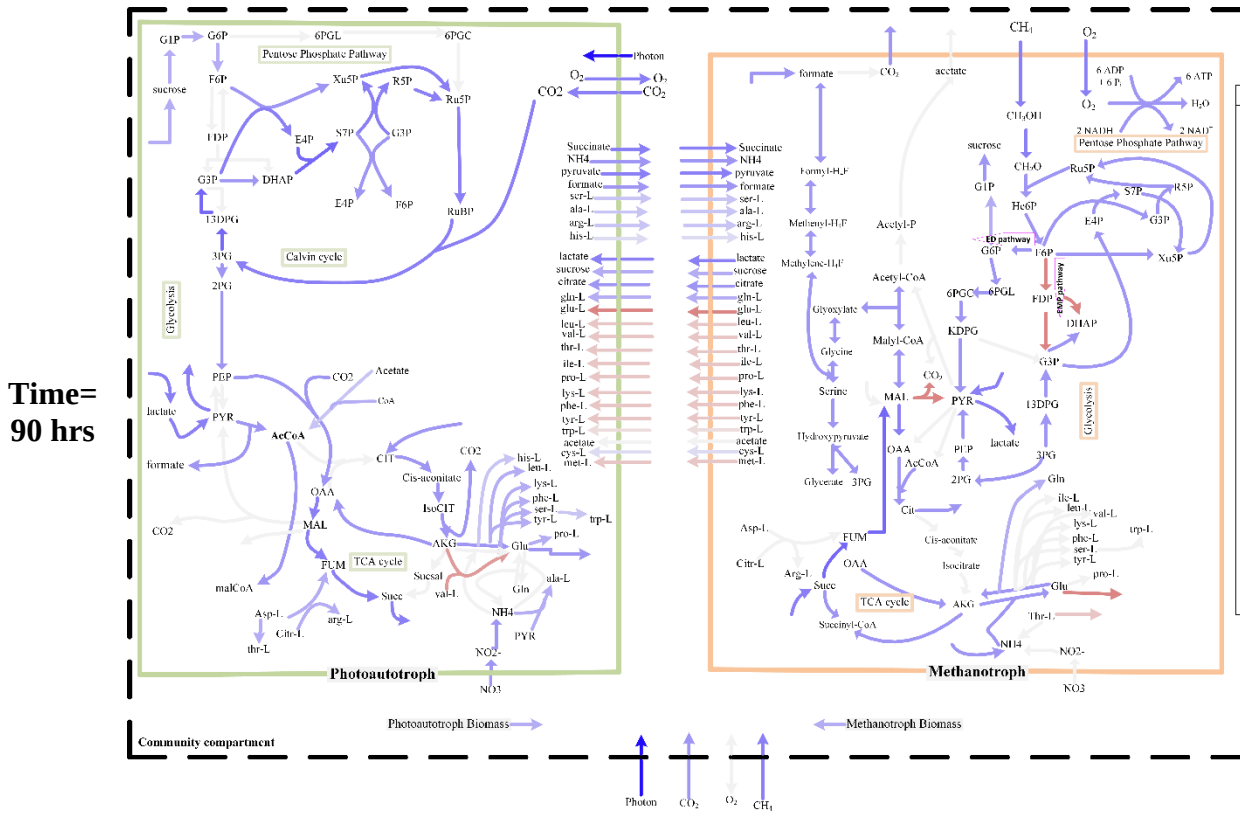

Figure 48. Schematic representation of the simulated metabolism of the coculture system by dynamic coculture GEM for 15-time steps.

Our extensive simulations under various *in silico* setups with the GEM consistently predicted the same top exchanged metabolites, as shown in **Figure 48**. The top exchanged metabolites were plotted for each 15 time steps to demonstrate their change and significant by time (**Figure 49**). CH_4 and CO_2 consumption were included in the plot to depict the comparison between the main carbon sources and the exchanged metabolites. **Figure 49** (a) shows the flowrates normalized by CH_4 uptake rate (mmol X/mmol CH_4) where X is a metabolite. **Figure 49** (b) shows the flowrates normalized by total growth rate (mmol X/gDCW). The metabolites (except CH_4) showed above zero line are produced by methanotroph, and the metabolites (except CO_2) below zero line are produced by photoautotroph. As it is shown there are some abnormalities in the exchanged metabolites at time 2 and 64 which could be inaccurate model prediction. Both plots

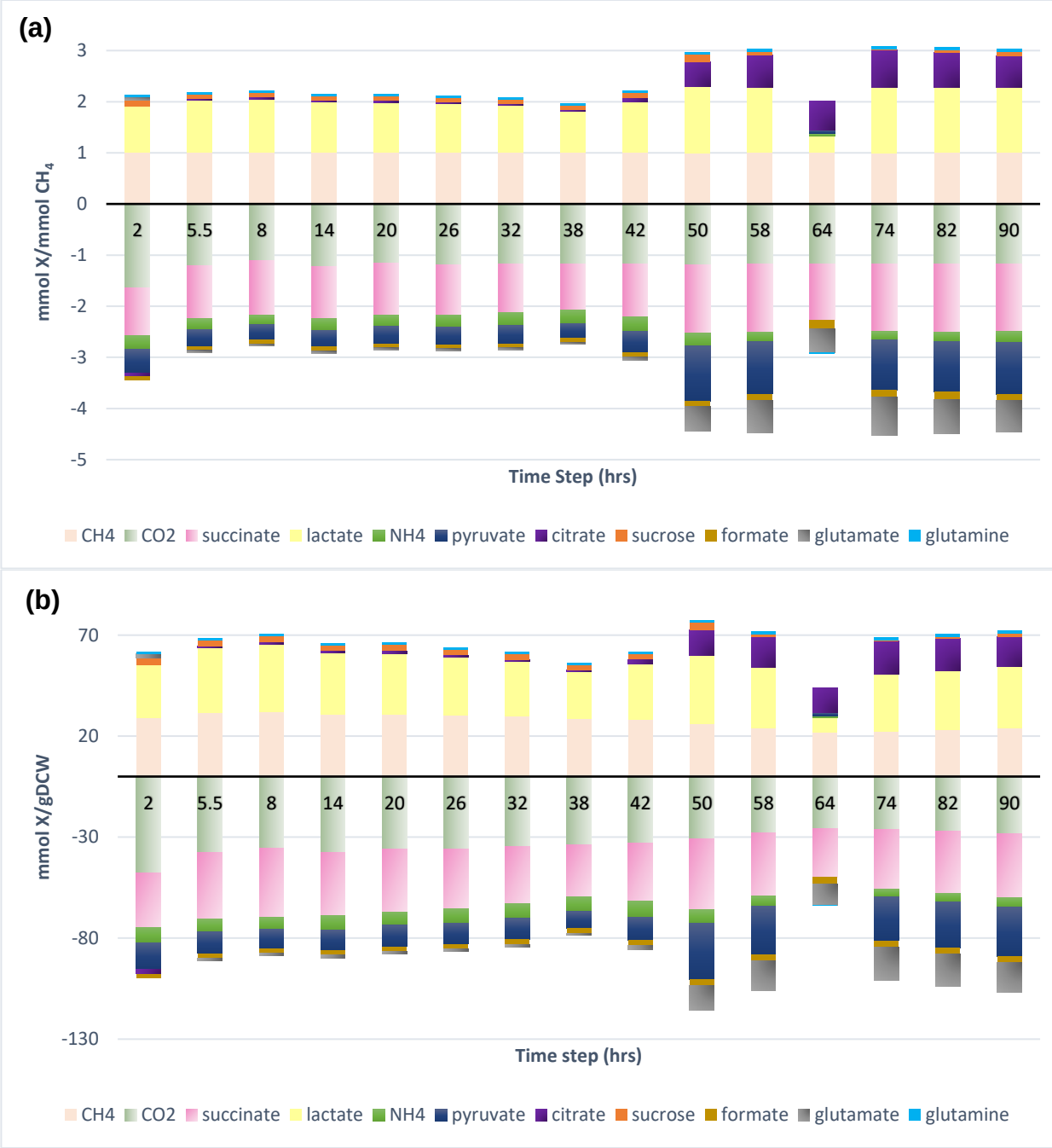

Figure 49. Top exchanged metabolites for each 15-time steps. (a) the flowrates normalized by CH_4 uptake rate (mmol X/mmol CH_4), (b) the flowrates normalized by total growth rate (mmol X/gDCW) where X is a metabolite. The metabolites (except CH_4) showed above zero line are produced by methanotroph, and the metabolites (except CO_2) below zero line are produced by photoautotroph.

show a similar trend and a meaningful prediction for the top 9 exchanged metabolites. It seems after 38 hours (establishing the mutualistic relationship), photoautotroph produced more pyruvate

and glutamate and kept providing NH_4, succinate and formate for methanotroph. From the other side, methanotroph produced more citrate and slightly more glutamine and kept providing lactate and sucrose for photoautotroph.

It is also interesting to point out that the dynamic coculture GEM predicts the establishment of the mutualistic relationship between the methanotroph and cyanobacteria. Specifically, the dynamic GEM predicts an emergent N-exchange being established when *M. buryatense* and *A. platensis* are cocultured together. After the establishment of the mutualistic interaction, only the cyanobacteria uptakes nitrate, while the methanotroph consumes ammonium excreted by the cyanobacteria. This phenomena has been observed and validated experimentally (using nanoscale secondary ion mass spectrometry image analysis) before in the coculture of cyanobacteria-heterotroph [172] which the cyanobacteria at some point uptake nitrate and produce ammonium for heterotrophs [173]. And then heterotroph stop up taking nitrate and just consume ammonium since it is the preferred N source due to its reduced state and energetically favorable assimilation [149]. In this study, the establishment of this mutualism can be shown clearly by observing the methanotroph nitrate uptake in **Figure 48** until time = 32 hours, where nitrate uptake by the methanotroph is significant. And then after establishing a mutualistic relationship as it is shown in **Figure 48** at time =38 hours until the end of the experiment, the only Nitrogen source come from the cyanobacteria by providing ammonium where nitrate uptake by the methanotroph is zero.

Chapter 7: Conclusions and Recommendations for Future Work

7.1 Understanding on M-P coculture for biogas conversion

Anaerobic digestion (AD) produced biogas (in which CH_4 is a valuable fuel) can be used to produce energy, including electricity, heat and high-density fuels. In addition to economic benefits from energy generation, AD offers many environmental benefits, including reducing greenhouse gases (GHGs) emission, significant reduction of soil, water and air pollutions, plus odor and pathogen controls. CO_2 and CH_4 are the two leading GHGs that cause global warming and many detrimental effects to the earth's ecosystem, and AD enables the containment of biogas produced from waste degradation that otherwise would be released into atmosphere. The low value of biogas is the main factor that hinders the wide adoption of AD and exploration of biogas potential as a feedstock for production of high-density fuels and commodity chemicals. To tap into the immense potential of biogas produced from waste streams, effective biotechnologies that can operate at ambient pressure, temperature and are economically viable at small to mid-scale are needed. In addition, the technologies that can co-utilize both CH_4 and CO_2 are particularly attractive.

Recent studies have demonstrated that natural microbial communities have developed a highly efficient way to recover the energy and capture carbon from both CH_4 and CO_2 through metabolic coupling of methane oxidation to oxygenic photosynthesis. Inspired by these research findings, different methanotroph-photoautotroph (M-P) cocultures have been examined recently for biogas conversion. These recent developments clearly demonstrated that M-P cocultures offer a highly promising biotechnology platform for biogas conversion. However, existing results are limited to qualitative proof-of-concept experiments, and there is a lack of understanding on the growth and interaction of species in systematic and molecular levels. One of the key challenges in

microbiome research is identifying and manipulating cross-feeding interactions between community members that drive system dynamics and functions. Even for a simple two-member system there are a large number of possible interactions. To better understand microbiomes and make quantitative predictions, some advanced methods were established in this work. The availability of a kinetic model for the coculture growth is one of the prerequisites for developing coculture-based biotechnology, as it provides a foundation for design and scale-up of the bioreactor, as well as the optimization of operation conditions. In addition, currently how to quickly and accurately characterize mixed culture in real-time is still an unsolved problem, which is likely one major obstacle in developing kinetic models for the M-P cocultures. For the M-P coculture, besides tracking the individual biomass concentrations, an added difficulty is how to determine the substrate consumption rates and product excretion rates for each strain.

To address these limitations, this work proposes an experimental-computational (E-C) protocol that can deliver accurate characterization of the M-P cocultures in real time, which only require commonly measured variables such as gas composition, total optical density of the coculture and the inorganic carbon in the liquid broth. The accuracy of the proposed E-C protocol was validated by cell counting approach using flow cytometry. In addition, by comparing the predicted total OD from the individual biomass concentration with the measured total OD, this work shows that the E-C protocol provided better accuracy than the cell counting approach through statistical testing.

With the real-time characterization of the M-P coculture, this work proposes a semi-structured kinetic model that can accurately predict the growth rate, as well as the consumption/production rates of O_2 and CO_2 for the methanotroph and photoautotroph in the coculture. The proposed kinetic model is termed “semi-structured”, because the exchange of *in*

situ produced O_2 and CO_2 between the two species were explicitly modelled. Using the semi-structure dynamic modeling and the designed experiment, this work confirms that there exist other emergent interactions within the methanotroph-photoautotroph coculture, and quantified the effect of these emergent interactions, albeit unknown, on the growth of each species.

The structured Genome-scale metabolic (GEM) models have been used to predict population behaviors based on each organism's capabilities and potential competitive or cooperative interactions in microbial communities. In GEM modeling approaches, the quality of the reconstruction of complex community model depends on highly curated reconstructions of single organisms. Therefore, the GEM model for the *A. platensis* was refined to incorporate recent finding on photosynthetic electron transport components. The model predicted oxygen production and biomass growth showed a better agreement with experimental data after the refinements. The GEM model for *M. buryatense* 5GB1 was curated manually based on recent knowledge and validated using several sets of batch and continuous experiments. This work proposes the very first coculture GEM that is capable to predict potential "metabolic links"; because of these metabolic links, the individual growth rate predicted by the coculture GEM showed excellent agreement with experimental value without changing the model parameters, i.e., growth-associated and non-growth associated maintenance energy.

Moreover, this work proposes a dynamic GEM model by employing the validated semi-structured kinetic model to provide the cross-membrane fluxes, i.e., substrate pickup rates, product excretion rates and biomass growth rates, as constraints to the coculture GEM. These constraints not only allowed the reduction of the feasible solution space of the GEM model, but also enabled the simulation of the dynamic GEM, which could significantly improve metabolic flux predictions. In this way, by integrating the kinetic model with the steady-state GEM for the coculture, we were

able to obtain the dynamic metabolic flux changes over time. Both coculture GEM and dynamic GEM models consistently predicted the same top exchanged metabolites under different conditions contributing to enhanced coculture growth. It is also interesting to note that the dynamic coculture GEM predicted the establishment of the mutualistic relationship between the methanotroph and cyanobacteria. Specifically, the dynamic GEM predicted an emergent N-exchange being established when *M. buryatense* and *A. platensis* were cocultured together. After the establishment of the mutualistic interaction, only the cyanobacteria consumed nitrate, while the methanotroph consumed ammonium excreted by the cyanobacteria.

7.2 Recommendations for Future Work

While the GEM models developed and utilized in this work enable us to develop hypotheses about metabolic interactions of the micro-organisms studied, there are still many questions that need to be answered. The investigation into the potential metabolic interactions identified several interdependencies. Experimentally validation of these cross-feeding interactions is required. The validation of the predicted metabolic exchanges can be achieved by running the dynamic transcriptomic analysis. This method should capture at least top metabolic links and validate accuracy of the prediction. Another idea for validating the predicted coculture GEM model is designing and performing experiments using isotopes labeling ^{13}C and ^{15}N, NanoSIMS or combination of the mentioned methods. These methods can reveal the stablished mutual interactions in the coculture. Furthermore, using collected experimental data on the coculture, one can revise and improve the coculture GEM model for more accurate prediction.

To test the presence of the metabolic links, the medium of the coculture could be examined using metabolomic analysis and be compared with supernatant of individual single cultures. It may capture some residual or difference of metabolites between coculture and single culture. Moreover,

supernatant of single cyanobacteria can be used for culturing the single methanotroph and vice versa. By comparing the results with growth in standard medium, some difference could be seen that needs more investigation such as transcriptomic analysis in order to recognize the metabolic links.

Since some species need physical contact in their cell membrane, as it was mentioned in Chapter 5, coculture biomass samples can be taken at different time steps during establishment of the mutual interaction and the images of the samples will be produced by scanning electron microscope (SEM). The pictures can validate the hypothesis about the need of physical contact for metabolic interactions.

Ultimately, it is envisioned that integrated model of microbiomes will enhance our fundamental understanding of microbial communities and establish new theories and mechanisms that govern the structure and function of these complex biological systems.

References

[1] National Academy of Engineering, Policy Implications of Greenhouse Warming, 1991. https://books.google.com/books?id=-iEs4ZFoW8UC&pg=PT15&lpg=PT15&dq=Because+of+this+asymmetry,+the+earth,+its+atmosphere,+and+its+oceans+are+warmer+than+they+would+be+in+the+absence+of+such+gases&source=bl&ots=TG0oYnGhx8&sig=ACfU3U3ABHjasY-hNxA-ZcDXJH5U0gI (accessed June 25, 2021).

[2] E. Britannica, Causes of Global Warming, Saving Earth, (n.d.). https://www.britannica.com/explore/savingearth/global-warming-problem (accessed June 25, 2021).

[3] US EPA, Greenhouse Gas (GHG) Emissions, (n.d.). https://www.epa.gov/ghgemissions (accessed May 24, 2021).

[4] IPCC, AR5 Climate Change 2013: The Physical Science Basis, (n.d.). https://www.ipcc.ch/report/ar5/wg1/ (accessed May 24, 2021).

[5] US EPA, Inventory of U.S. Greenhouse Gas Emissions and Sinks, Greenhouse Gas (GHG) Emissions, (n.d.). https://www.epa.gov/ghgemissions/inventory-us-greenhouse-gas-emissions-and-sinks (accessed June 25, 2021).

[6] US EPA, Overview of Greenhouse Gases, Greenhouse Gas (GHG) Emissions, (n.d.). https://www.epa.gov/ghgemissions/overview-greenhouse-gases (accessed June 25, 2021).

[7] IPCC, AR4 Climate Change 2007: Synthesis Report, (n.d.). https://www.ipcc.ch/report/ar4/syr/ (accessed May 24, 2021).

[8] Department of Primary Industries and Regional Development's Agriculture and Food, Carbon farming: reducing methane emissions from cattle using feed additives, (n.d.). https://www.agric.wa.gov.au/climate-change/carbon-farming-reducing-methane-emissions-cattle-using-feed-additives (accessed July 13, 2021).

[9] US EPA, Basic Information about Landfill Gas, Landfill Methane Outreach Program (LMOP), (n.d.). https://www.epa.gov/lmop/basic-information-about-landfill-gas (accessed June 25, 2021).

[10] National Research Council, What We Know About Climate Change and Its Interactions with People and Ecosystems, in: Adv. Sci. Clim. Chang., National Academies Press, 2011: pp. 1–526. https://doi.org/10.17226/12782.

[11] U. Forest Service, United States Department Of Agriculture Forest Service Pacific Northwest Research Station, 2010. http://www.fs.fed.us./pnw/ (accessed June 25, 2021).

[12] NOAA Climate.gov, Teaching Essential Principle 6: Human activities are impacting the climate system, (n.d.). https://www.climate.gov/teaching/essential-principles-climate-literacy/teaching-essential-principle-6-human-activities-are (accessed June 25, 2021).

[13] NASA, Arctic Sea Ice Shrinks To New Low In Satellite Era, (n.d.). https://www.nasa.gov/topics/earth/features/arctic-seaice-2012.html (accessed June 25, 2021).

[14] The National Academies, Climate change 2008 edition, 2008.

[15] National Academies of Sciences, Negative Emissions Technologies and Reliable Sequestration, National Academies Press, 2019. https://doi.org/10.17226/25259.

[16] H. Eldardiry, E. Habib, Carbon capture and sequestration in power generation: review of impacts and opportunities for water sustainability, Energy. Sustain. Soc. 8 (2018) 1–15. https://doi.org/10.1186/s13705-018-0146-3.

[17] Environmental and Energy Study Institute (EESI), Fact Sheet, Biogas: Converting Waste to Energy, White Papers, (n.d.). https://www.eesi.org/papers/view/fact-sheet-biogasconverting-waste-to-energy (accessed June 25, 2021).
[18] Y. Shen, J.L. Linville, M. Urgun-Demirtas, M.M. Mintz, S.W. Snyder, An overview of biogas production and utilization at full-scale wastewater treatment plants (WWTPs) in the United States: Challenges and opportunities towards energy-neutral WWTPs, Renew. Sustain. Energy Rev. 50 (2015) 346–362. https://doi.org/10.1016/j.rser.2015.04.129.
[19] U.S. AgSTAR, Market Opportunities Report for Biogas Recovery in the Agriculture Sector, US EPA. (2018). https://www.epa.gov/sites/production/files/2018-06/documents/epa430r18006agstarmarketreport2018.pdf (accessed June 11, 2021).
[20] W. Zhang, X. Ge, Y.F. Li, Z. Yu, Y. Li, Isolation of a methanotroph from a hydrogen sulfide-rich anaerobic digester for methanol production from biogas, Process Biochem. 51 (2016) 838–844. https://doi.org/10.1016/j.procbio.2016.04.003.
[21] J.P. Sheets, X. Ge, Y.F. Li, Z. Yu, Y. Li, Biological conversion of biogas to methanol using methanotrophs isolated from solid-state anaerobic digestate, Bioresour. Technol. 201 (2016) 50–57. https://doi.org/10.1016/j.biortech.2015.11.035.
[22] E. Ryckebosch, M. Drouillon, H. Vervaeren, Techniques for transformation of biogas to biomethane, Biomass and Bioenergy. 35 (2011) 1633–1645. https://doi.org/10.1016/j.biombioe.2011.02.033.
[23] M. Bahr, I. Díaz, A. Dominguez, A. González Sánchez, R. Muñoz, Microalgal-biotechnology as a platform for an integral biogas upgrading and nutrient removal from anaerobic effluents, Environ. Sci. Technol. 48 (2014) 573–581. https://doi.org/10.1021/es403596m.
[24] Z. Rasouli, B.V. Pérez, M. D'Este, D. De Francisci, I. Angelidaki, B. Valverde-Pérez, M. D'Este, D. De Francisci, I. Angelidaki, Nutrient recovery from industrial wastewater as single cell protein by a co-culture of green microalgae and methanotrophs, Biochem. Eng. J. 134 (2018) 129–135. https://doi.org/10.1016/j.bej.2018.03.010.
[25] J. Masojídek, G. Torzillo, M. Koblízek, Photosynthesis in Microalgae, in: Handb. Microalgal Cult. Appl. Phycol. Biotechnol. Second Ed., wiley, 2013: pp. 21–36. https://doi.org/10.1002/9781118567166.ch2.
[26] H.L. MacIntyre, T.M. Kana, T. Anning, R.J. Geider, Photoacclimation of photosynthesis irradiance response curves and photosynthetic pigments in microalgae and cyanobacteria, J. Phycol. 38 (2002) 17–38. https://doi.org/10.1046/j.1529-8817.2002.00094.x.
[27] A. Benson, M. Calvin, The dark reductions of photosynthesis, Science (80-.). 105 (1947) 648. https://doi.org/10.1126/science.105.2738.648.
[28] M. Calvin, The photosynthetic carbon cycle, J. Chem. Soc. (1956) 1895. https://doi.org/10.1039/jr9560001895.
[29] G.E. Lakatos, K. Ranglová, J.C. Manoel, T. Grivalský, J. Kopecký, J. Masojídek, Bioethanol production from microalgae polysaccharides, Folia Microbiol. (Praha). 64 (2019) 627–644. https://doi.org/10.1007/s12223-019-00732-0.
[30] S. Behera, R. Singh, R. Arora, N.K. Sharma, M. Shukla, S. Kumar, Scope of Algae as Third Generation Biofuels, Front. Bioeng. Biotechnol. 2 (2015) 90. https://doi.org/10.3389/fbioe.2014.00090.
[31] K.W. Chew, J.Y. Yap, P.L. Show, N.H. Suan, J.C. Juan, T.C. Ling, D.J. Lee, J.S. Chang, Microalgae biorefinery: High value products perspectives, Bioresour. Technol. 229 (2017) 53–62. https://doi.org/10.1016/j.biortech.2017.01.006.

[32] M.I. Khan, J.H. Shin, J.D. Kim, The promising future of microalgae: Current status, challenges, and optimization of a sustainable and renewable industry for biofuels, feed, and other products, Microb. Cell Fact. 17 (2018) 36. https://doi.org/10.1186/s12934-018-0879-x.
[33] W. Qu, C. Zhang, Y. Zhang, S.H. Ho, Optimizing real swine wastewater treatment with maximum carbohydrate production by a newly isolated indigenous microalga Parachlorella kessleri QWY28, Bioresour. Technol. 289 (2019) 121702. https://doi.org/10.1016/j.biortech.2019.121702.
[34] G. Goswami, B.B. Makut, D. Das, Sustainable production of bio-crude oil via hydrothermal liquefaction of symbiotically grown biomass of microalgae-bacteria coupled with effective wastewater treatment, Sci. Rep. 9 (2019) 1–12. https://doi.org/10.1038/s41598-019-51315-5.
[35] H. Cao, Z. Zhang, X. Wu, X. Miao, Direct biodiesel production from wet microalgae biomass of chlorella pyrenoidosa through in situ transesterification, Biomed Res. Int. 2013 (2013). https://doi.org/10.1155/2013/930686.
[36] A. Ritala, S.T. Häkkinen, M. Toivari, M.G. Wiebe, Single cell protein-state-of-the-art, industrial landscape and patents 2001-2016, Front. Microbiol. 8 (2017). https://doi.org/10.3389/fmicb.2017.02009.
[37] S.W. Jones, A. Karpol, S. Friedman, B.T. Maru, B.P. Tracy, Recent advances in single cell protein use as a feed ingredient in aquaculture, Curr. Opin. Biotechnol. 61 (2020) 189–197. https://doi.org/10.1016/j.copbio.2019.12.026.
[38] S. Rasoul-Amini, M.H. Morowvat, G. Younes, Single Cell Protein: Production and Process Anticancer compounds View project Effect of Fibrin Packing on Managing Hepatic Hemorrhage and Liver Wound Healing in a Model of Liver Stab Wound in Rat View project CITATIONS SEE PROFILE, Artic. Am. J. Food Technol. (2011). https://doi.org/10.3923/ajft.2011.103.116.
[39] D. Putri, A. Ulhidayati, I.A. Musthofa, A.K. Wardani, Single cell protein production of Chlorella sp. using food processing waste as a cultivation medium, in: IOP Conf. Ser. Earth Environ. Sci., Institute of Physics Publishing, 2018: p. 012052. https://doi.org/10.1088/1755-1315/131/1/012052.
[40] P.J. Strong, M. Kalyuzhnaya, J. Silverman, W.P. Clarke, A methanotroph-based biorefinery: Potential scenarios for generating multiple products from a single fermentation, Bioresour. Technol. 215 (2016) 314–323. https://doi.org/10.1016/j.biortech.2016.04.099.
[41] N. Renuka, A. Guldhe, R. Prasanna, P. Singh, F. Bux, Microalgae as multi-functional options in modern agriculture: current trends, prospects and challenges, Biotechnol. Adv. 36 (2018) 1255–1273. https://doi.org/10.1016/j.biotechadv.2018.04.004.
[42] Y. Lu, J. Xu, Phytohormones in microalgae: A new opportunity for microalgal biotechnology?, Trends Plant Sci. 20 (2015) 273–282. https://doi.org/10.1016/j.tplants.2015.01.006.
[43] E. Yilmaz, M. Sönmez, The role of organic/bio–fertilizer amendment on aggregate stability and organic carbon content in different aggregate scales, Soil Tillage Res. 168 (2017) 118–124. https://doi.org/10.1016/j.still.2017.01.003.
[44] K. Swarnalakshmi, R. Prasanna, A. Kumar, S. Pattnaik, K. Chakravarty, Y.S. Shivay, R. Singh, A.K. Saxena, Evaluating the influence of novel cyanobacterial biofilmed biofertilizers on soil fertility and plant nutrition in wheat, Eur. J. Soil Biol. 55 (2013) 107–

116. https://doi.org/10.1016/j.ejsobi.2012.12.008.
[45] J. Coppens, O. Grunert, S. Van Den Hende, I. Vanhoutte, N. Boon, G. Haesaert, L. De Gelder, The use of microalgae as a high-value organic slow-release fertilizer results in tomatoes with increased carotenoid and sugar levels, J. Appl. Phycol. 28 (2016) 2367–2377. https://doi.org/10.1007/s10811-015-0775-2.
[46] N. Renuka, R. Prasanna, A. Sood, R. Bansal, N. Bidyarani, R. Singh, Y.S. Shivay, L. Nain, A.S. Ahluwalia, Wastewater grown microalgal biomass as inoculants for improving micronutrient availability in wheat, Rhizosphere. 3 (2017) 150–159. https://doi.org/10.1016/j.rhisph.2017.04.005.
[47] H. Mazur, A. Konop, R. Synak, Indole-3-acetic acid in the culture medium of two axenic green microalgae, J. Appl. Phycol. 13 (2001) 35–42. https://doi.org/10.1023/A:1008199409953.
[48] K.O. Romanenko, I. V. Kosakovskaya, P.O. Romanenko, Phytohormones of microalgae: Biological role and involvement in the regulation of physiological processes. Pt II. Cytokinins and gibberellins, Int. J. Algae. 18 (2016) 179–201. https://doi.org/10.1615/InterJAlgae.v18.i2.70.
[49] K. Minamisawa, H. Imaizumi-Anraku, Z. Bao, R. Shinoda, T. Okubo, S. Ikeda, Are symbiotic methanotrophs key microbes for N acquisition in paddy rice root?, Microbes Environ. 31 (2016) 4–10. https://doi.org/10.1264/jsme2.ME15180.
[50] M.A. Zeller, R. Hunt, A. Jones, S. Sharma, Bioplastics and their thermoplastic blends from Spirulina and Chlorella microalgae, J. Appl. Polym. Sci. 130 (2013) 3263–3275. https://doi.org/10.1002/app.39559.
[51] V. Piemonte, Bioplastic Wastes: The Best Final Disposition for Energy Saving, J. Polym. Environ. 19 (2011) 988–994. https://doi.org/10.1007/s10924-011-0343-z.
[52] L. Zhang, P. Chen, J. Huang, G. Yang, L. Zheng, Ways of strengthening biodegradable soy-dreg plastics, J. Appl. Polym. Sci. 88 (2003) 422–427. https://doi.org/10.1002/app.11718.
[53] U.S. AgSTAR, Market {Opportunities} for {Biogas} {Recovery} {Systems} at {U}.{S}. {Livestock} {Facilities}, (2018) 42. https://www.epa.gov/agstar/agstar-market-opportunities-report.
[54] C.A. Jones, C. Coker, K. Kirk, L. Reynolds, Food Waste Co-Digestion at Water Resource Recovery Facilities: Business Case Analysis, 2019. www.waterrf.org (accessed May 31, 2021).
[55] N. Kip, J.F. Van Winden, Y. Pan, L. Bodrossy, G.J. Reichart, A.J.P. Smolders, M.S.M. Jetten, J.S.S. Damsté, H.J.M. Op Den Camp, Global prevalence of methane oxidation by symbiotic bacteria in peat-moss ecosystems, Nat. Geosci. 3 (2010) 617–621. https://doi.org/10.1038/ngeo939.
[56] J. Milucka, M. Kirf, L. Lu, A. Krupke, P. Lam, S. Littmann, M.M.M. Kuypers, C.J. Schubert, Methane oxidation coupled to oxygenic photosynthesis in anoxic waters, ISME J. 9 (2015) 1991–2002. https://doi.org/10.1038/ismej.2015.12.
[57] A.A. Raghoebarsing, A.J.P. Smolders, M.C. Schmid, W.I.C. Rijpstra, M. Wolters-Arts, J. Derksen, M.S.M. Jetten, S. Schouten, J.S. Sinninghe Damsté, L.P.M. Lamers, J.G.M. Roelofs, H.J.M. den Camp, M. Strous, Methanotrophic symbionts provide carbon for photosynthesis in peat bogs, Nature. 436 (2005) 1153–1156. https://doi.org/10.1038/nature03802.
[58] D. Van Der Ha, L. Nachtergaele, F.M. Kerckhof, D. Rameiyanti, P. Bossier, W.

Verstraete, N. Boon, Conversion of biogas to bioproducts by algae and methane oxidizing bacteria, Environ. Sci. Technol. 46 (2012) 13425–13431. https://doi.org/10.1021/es303929s.
[59] E.A. Hill, W.B. Chrisler, A.S. Beliaev, H.C. Bernstein, A flexible microbial co-culture platform for simultaneous utilization of methane and carbon dioxide from gas feedstocks, Bioresour. Technol. 228 (2017) 250–256. https://doi.org/10.1016/j.biortech.2016.12.111.
[60] Z. Khan, P. Bhadouria, P. Bisen, Nutritional and Therapeutic Potential of Spirulina, Curr. Pharm. Biotechnol. 6 (2005) 373–379. https://doi.org/10.2174/138920105774370607.
[61] T. Kaji, Y. Fujiwara, Y. Inomata, C. Hamada, C. Yamamoto, S. Shimada, J.B. Lee, T. Hayashi, Repair of wounded monolayers of cultured bovine aortic endothelial cells is inhibited by calcium spirulan, a novel sulfated polysaccharide isolated from Spirulina platensis, Life Sci. 70 (2002) 1841–1848. https://doi.org/10.1016/S0024-3205(01)01555-7.
[62] A.W. Puri, S. Owen, F. Chu, T. Chavkin, D.A.C. Beck, M.G. Kalyuzhnaya, M.E. Lidstrom, Genetic tools for the industrially promising methanotroph Methylomicrobium buryatense, Appl. Environ. Microbiol. 81 (2015) 1775–1781. https://doi.org/10.1128/AEM.03795-14.
[63] N. Roberts, M. Hilliard, Q.P. He, J. Wang, A Microalgae-Methanotroph Coculture is a Promising Platform for Fuels and Chemical Production From Wastewater, Front. Energy Res. 8 (2020) 230. https://doi.org/10.3389/fenrg.2020.563352.
[64] M.R. Antoniewicz, A guide to deciphering microbial interactions and metabolic fluxes in microbiome communities, Curr. Opin. Biotechnol. 64 (2020) 230–237. https://doi.org/10.1016/j.copbio.2020.07.001.
[65] J. Friedman, L.M. Higgins, J. Gore, Community structure follows simple assembly rules in microbial microcosms, Nat. Ecol. Evol. 1 (2017) 1–7. https://doi.org/10.1038/s41559-017-0109.
[66] J.C. Wooley, A. Godzik, I. Friedberg, A primer on metagenomics, PLoS Comput. Biol. 6 (2010) e1000667. https://doi.org/10.1371/journal.pcbi.1000667.
[67] J.J. Faith, N.P. McNulty, F.E. Rey, J.I. Gordon, Predicting a human gut microbiota's response to diet in gnotobiotic mice, Science (80-.). 333 (2011) 101–104. https://doi.org/10.1126/science.1206025.
[68] C. Zuñiga, L. Zaramela, K. Zengler, Elucidation of complexity and prediction of interactions in microbial communities, Microb. Biotechnol. 10 (2017) 1500–1522. https://doi.org/10.1111/1751-7915.12855.
[69] K.Z. Coyte, J. Schluter, K.R. Foster, The ecology of the microbiome: Networks, competition, and stability, Science (80-.). 350 (2015) 663–666. https://doi.org/10.1126/science.aad2602.
[70] Market Opportunities for Biogas Recovery Systems at U.S. Livestock Facilities, 2018. www.epa.gov/agstar (accessed June 11, 2021).
[71] A.A. Raghoebarsing, A.J.P. Smolders, M.C. Schmid, W.I.C. Rijpstra, M. Wolters-Arts, J. Derksen, M.S.M. Jetten, S. Schouten, J.S.S. Damsté, L.P.M. Lamers, J.G.M. Roelofs, H.J.M. Op Den Camp, M. Strous, Methanotrophic symbionts provide carbon for photosynthesis in peat bogs, Nature. 436 (2005) 1153–1156. https://doi.org/10.1038/nature03802.
[72] E.A. Hill, W.B. Chrisler, A.S. Beliaev, H.C. Bernstein, A flexible microbial co-culture platform for simultaneous utilization of methane and carbon dioxide from gas feedstocks,

Bioresour. Technol. 228 (2017) 250–256. https://doi.org/10.1016/j.biortech.2016.12.111.
[73] J. Wang, Q.P. He, Methanotroph-microalgae coculture, US Provisional Pat. Appl. 62/664,565. (2018).
[74] K. Badr, M. Hilliard, N. Roberts, Q.P. He, J. Wang, Photoautotroph-Methanotroph Coculture – A Flexible Platform for Efficient Biological CO2-CH4 Co-utilization, IFAC-PapersOnLine. 52 (2019) 916–921. https://doi.org/10.1016/j.ifacol.2019.06.179.
[75] Z. Rasouli, B. Valverde-Pérez, M. D'Este, D. De Francisci, I. Angelidaki, Nutrient recovery from industrial wastewater as single cell protein by a co-culture of green microalgae and methanotrophs, Biochem. Eng. J. 134 (2018) 129–135. https://doi.org/10.1016/j.bej.2018.03.010.
[76] W. Sabra, D. Dietz, D. Tjahjasari, A.-P. Zeng, Biosystems analysis and engineering of microbial consortia for industrial biotechnology, Eng. Life Sci. 10 (2010) 407–421.
[77] D. Spiegelman, G. Whissell, C.W. Greer, A survey of the methods for the characterization of microbial consortia and communities, Can. J. Microbiol. 51 (2005) 355–386.
[78] K.A. Stone, Q.P. He, J. Wang, Two Experimental Protocols for Accurate Measurement of Gas Component Uptake and Production Rates in Bioconversion Processes, Sci. Rep. 9 (2019) 5899. https://doi.org/10.1038/s41598-019-42469-3.
[79] I.R. Akberdin, M. Thompson, R. Hamilton, N. Desai, D. Alexander, C.A. Henard, M.T. Guarnieri, M.G. Kalyuzhnaya, Methane utilization in Methylomicrobium alcaliphilum 20Z R: a systems approach, Sci. Rep. 8 (2018) 2512.
[80] H.C. Bernstein, R.S. McClure, E.A. Hill, L.M. Markillie, W.B. Chrisler, M.F. Romine, J.E. McDermott, M.C. Posewitz, D.A. Bryant, A.E. Konopka, others, Unlocking the constraints of cyanobacterial productivity: acclimations enabling ultrafast growth, MBio. 7 (2016) 949.
[81] A.M.J. Kliphuis, M. Janssen, E.J. van den End, D.E. Martens, R.H. Wijffels, Light respiration in Chlorella sorokiniana, J. Appl. Phycol. 23 (2011) 935–947.
[82] I.R. Akberdin, M. Thompson, R. Hamilton, N. Desai, D. Alexander, C.A. Henard, M.T. Guarnieri, M.G. Kalyuzhnaya, Methane utilization in {Methylomicrobium} alcaliphilum {20ZR}: a systems approach, Sci. Rep. 8 (2018). https://doi.org/10.1038/s41598-018-20574-z.
[83] N. Scarlat, J.F. Dallemand, F. Fahl, Biogas: Developments and perspectives in Europe, Renew. Energy. 129 (2018) 457–472. https://doi.org/10.1016/j.renene.2018.03.006.
[84] B.C. Murray, C.S. Galik, T. Vegh, Biogas in the United States: estimating future production and learning from international experiences, Mitig. Adapt. Strateg. Glob. Chang. 22 (2017) 485–501. https://doi.org/10.1007/s11027-015-9683-7.
[85] P. Kumaran, D. Hephzibah, R. Sivasankari, N. Saifuddin, A.H. Shamsuddin, A review on industrial scale anaerobic digestion systems deployment in Malaysia: Opportunities and challenges, Renew. Sustain. Energy Rev. 56 (2016) 929–940. https://doi.org/10.1016/j.rser.2015.11.069.
[86] (WBA) World Bioenergy Association, Global Bioenergy Statistics 2020 WBA, (2020). https://www.worldbioenergy.org/uploads/201210 WBA GBS 2020.pdf (accessed June 10, 2021).
[87] American Biogas Council, Championing the biogas industry, advancing a biogas future, (2017). https://americanbiogascouncil.org/ (accessed June 10, 2021).
[88] A. Aebiom, A Biogas Road Map for Europe Content, (2010). https://www.big-east.eu/downloads/Brochure_BiogasRoadmap_WEB%5B1%5D.pdf (accessed June 10,

2021).
[89] REN21, Renewables 2015 Global Status Reports, Renewable Energy Policy Network for the 21st Century, (2017). https://www.ren21.net/reports/global-status-report/ (accessed June 10, 2021).
[90] L. Jingming, The Future of Biogas in China. Biogas World, in: Biogas World Berlin, Ger. April 1, 2014, (2014). https://silo.tips/download/the-future-of-biogas-in-china#modals (accessed June 10, 2021).
[91] K. Badr, W. Whelan, Q.P. He, J. Wang, Fast and easy quantitative characterization of methanotroph–photoautotroph cocultures, Biotechnol. Bioeng. 118 (2021) 703–714. https://doi.org/10.1002/bit.27603.
[92] C. Zarrouk, Contribution a l'etude d'une Cyanophycee. Influence de Divers Facteurs Physiques et Chimiques sur la croissance et la photosynthese de Spirulina mixima., Thesis. Univ. Paris, Fr. (1966).
[93] Q. Béchet, A. Shilton, B. Guieysse, Modeling the effects of light and temperature on algae growth: State of the art and critical assessment for productivity prediction during outdoor cultivation, Biotechnol. Adv. 31 (2013) 1648–1663. https://doi.org/10.1016/j.biotechadv.2013.08.014.
[94] P.H. Ravelonandro, D.H. Ratianarivo, C. Joannis-Cassan, A. Isambert, M. Raherimandimby, Improvement of the growth of {Arthrospira} ({Spirulina}) platensis from {Toliara} ({Madagascar}): {Effect} of agitation, salinity and {CO2} addition, Food Bioprod. Process. 89 (2011) 209–216. https://doi.org/10.1016/j.fbp.2010.04.009.
[95] G. Cogne, J.-B. Gros, C.-G. Dussap, Identification of a metabolic network structure representative ofarthrospira (spirulina) platensis metabolism, Biotechnol. Bioeng. 84 (2003) 667–676. https://doi.org/10.1002/bit.10808.
[96] T.M. Sobczuk, F.G. Camacho, F.C. Rubio, F.G.A. Fernández, E.M. Grima, F.G. Fernandez, E.M. Grima, Carbon dioxide uptake efficiency by outdoor microalgal cultures in tubular airlift photobioreactors, Biotechnol. Bioeng. 67 (2000) 465–475. https://doi.org/10.1002/(SICI)1097-0290(20000220)67:4<465::AID-BIT10>3.0.CO;2-9.
[97] A. de la Torre, A. Metivier, F. Chu, L.M.L. Laurens, D.A.C. Beck, P.T. Pienkos, M.E. Lidstrom, M.G. Kalyuzhnaya, Genome-scale metabolic reconstructions and theoretical investigation of methane conversion in {Methylomicrobium} buryatense strain {5G}({B1}), Microb. Cell Fact. 14 (2015). https://doi.org/10.1186/s12934-015-0377-3.
[98] M.G. Kalyuzhnaya, S. Yang, O.N. Rozova, N.E. Smalley, J. Clubb, A. Lamb, G.A.N. Gowda, D. Raftery, Y. Fu, F. Bringel, S. Vuilleumier, D.A.C. Beck, Y.A. Trotsenko, V.N. Khmelenina, M.E. Lidstrom, Highly efficient methane biocatalysis revealed in a methanotrophic bacterium, Nat. Commun. 4 (2013). https://doi.org/10.1038/ncomms3785.
[99] S. Kasiri, A. Ulrich, V. Prasad, Kinetic modeling and optimization of carbon dioxide fixation using microalgae cultivated in oil-sands process water, Chem. Eng. Sci. 137 (2015) 697–711. https://doi.org/10.1016/j.ces.2015.07.004.
[100] P. van Bodegom, F. Stams, L. Mollema, S. Boeke, P. Leffelaar, Methane {Oxidation} and the {Competition} for {Oxygen} in the {Rice} {Rhizosphere}, Appl. Environ. Microbiol. 67 (2001) 3586–3597. https://doi.org/10.1128/AEM.67.8.3586-3597.2001.
[101] R. Sander, Compilation of {Henry}'s law constants (version 4.0) for water as solvent, Atmos. Chem. Phys. 15 (2015) 4399–4981. https://doi.org/10.5194/acp-15-4399-2015.
[102] A. AlSayed, A. Fergala, S. Khattab, A. Eldyasti, Kinetics of type I methanotrophs mixed culture enriched from waste activated sludge, Biochem. Eng. J. 132 (2018) 60–67.

https://doi.org/10.1016/j.bej.2018.01.003.
[103] R. Mariyana, M.S. Kim, C. Il Lim, T.W. Kim, S.J. Park, B.K. Oh, J. Lee, J.G. Na, Mass transfer performance of a string film reactor: A bioreactor design for aerobic methane bioconversion, Catalysts. 8 (2018) 490. https://doi.org/10.3390/catal8110490.
[104] Y. Yu, J.A. Ramsay, B.A. Ramsay, On-line estimation of dissolved methane concentration during methanotrophic fermentations, Biotechnol. Bioeng. 95 (2006) 788–793. https://doi.org/10.1002/bit.21050.
[105] M.A. Babcock, D.F. Pegelow, C.A. Harms, J.A. Dempsey, Effects of respiratory muscle unloading on exercise-induced diaphragm fatigue, J. Appl. Physiol. 93 (2002) 201–206. https://doi.org/10.1152/japplphysiol.00612.2001.
[106] Y. Fu, L. He, J. Reeve, D.A.C. Beck, M.E. Lidstrom, Core metabolism shifts during growth on methanol versus methane in the methanotroph methylomicrobium buryatense 5GB1, MBio. 10 (2019). https://doi.org/10.1128/mBio.00406-19.
[107] B.Ø. Palsson, Systems Biology: Properties of Reconstructed Networks, 1st ed., Cambridge University Press, 2006.
[108] R. Agren, L. Liu, S. Shoaie, W. Vongsangnak, I. Nookaew, J. Nielsen, The RAVEN Toolbox and Its Use for Generating a Genome-scale Metabolic Model for Penicillium chrysogenum, PLoS Comput. Biol. 9 (2013) e1002980. https://doi.org/10.1371/journal.pcbi.1002980.
[109] J. Schellenberger, R. Que, R.M.T. Fleming, I. Thiele, J.D. Orth, A.M. Feist, D.C. Zielinski, A. Bordbar, N.E. Lewis, S. Rahmanian, J. Kang, D.R. Hyduke, B.Ø. Palsson, Quantitative prediction of cellular metabolism with constraint-based models: the COBRA Toolbox v2.0, Nat. Protoc. 6 (2011) 1290–1307. https://doi.org/10.1038/nprot.2011.308.
[110] J. Zanghellini, D.E. Ruckerbauer, M. Hanscho, C. Jungreuthmayer, Elementary flux modes in a nutshell: Properties, calculation and applications, Biotechnol. J. 8 (2013) 1009–1016. https://doi.org/10.1002/biot.201200269.
[111] J.D. Orth, I. Thiele, B.Ø. Palsson, What is flux balance analysis?, Nat Biotech. 28 (2010) 245–248. https://doi.org/10.1038/nbt.1614.
[112] N.E. Lewis, H. Nagarajan, B.O. Palsson, Constraining the metabolic genotype-phenotype relationship using a phylogeny of in silico methods, Nat. Rev. Microbiol. 10 (2012) 291–305. https://doi.org/10.1038/nrmicro2737.
[113] R. Ramakrishna, J.S. Edwards, A. McCulloch, B.O. Palsson, Flux-balance analysis of mitochondrial energy metabolism: consequences of systemic stoichiometric constraints, Am. J. Physiol. Integr. Comp. Physiol. 280 (2001) R695–R704. https://doi.org/10.1152/ajpregu.2001.280.3.R695.
[114] J. Lee, H. Yun, A.M. Feist, B.Ø. Palsson, S.Y. Lee, Genome-scale reconstruction and <{Emphasis} {Type}="{Italic}">in silico</{Emphasis}>analysis of the <{Emphasis} {Type}="{Italic}">{Clostridium} acetobutylicum</{Emphasis}>{ATCC} 824 metabolic network, Appl Microbiol Biotechnol. 80 (2008) 849–862. https://doi.org/10.1007/s00253-008-1654-4.
[115] C.B. Milne, J.A. Eddy, R. Raju, S. Ardekani, P.-J. Kim, R.S. Senger, Y.-S. Jin, H.P. Blaschek, N.D. Price, Metabolic network reconstruction and genome-scale model of butanol-producing strain {Clostridium} beijerinckii {NCIMB} 8052, BMC Syst Biol. 5 (2011) 130. https://doi.org/10.1186/1752-0509-5-130.
[116] M.B. Biggs, G.L. Medlock, J.A. Papin, Metabolic network modeling of microbial communities, WIREs Syst Biol Med. 7 (2015) 317–334.

https://doi.org/10.1002/wsbm.1308.
[117] M.B. Biggs, G.L. Medlock, G.L. Kolling, J.A. Papin, Metabolic {Network} {Modeling} of {Microbial} {Communities}, Wiley Interdiscip Rev Syst Biol Med. 7 (2015) 317–334. https://doi.org/10.1002/wsbm.1308.
[118] B.J. Sánchez, J. Nielsen, Genome scale models of yeast: towards standardized evaluation and consistent omic integration, Integr. Biol. 7 (2015) 846–858.
[119] A.L. Damiani, Q.P. He, T.W. Jeffries, J. Wang, Comprehensive evaluation of two genome-scale metabolic network models for Scheffersomyces stipitis, Biotechnol. Bioeng. 112 (2015) 1250–1262.
[120] M. Hilliard, A. Damiani, Q.P. He, T. Jeffries, J. Wang, Elucidating redox balance shift in Scheffersomyces stipitis' fermentative metabolism using a modified genome-scale metabolic model, Microb. Cell Fact. 17 (2018) 140. https://doi.org/10.1186/s12934-018-0983-y.
[121] T. Österlund, I. Nookaew, J. Nielsen, Fifteen years of large scale metabolic modeling of yeast: Developments and impacts, Biotechnol. Adv. 30 (2012) 979–988.
[122] D. McCloskey, A.M. Palsson Bernhard Øand Feist, Basic and applied uses of genome-scale metabolic network reconstructions of Escherichia coli, Mol. Syst. Biol. 9 (2013).
[123] A. de la Torre, A. Metivier, F. Chu, L.M.L. Laurens, D.A.C. Beck, P.T. Pienkos, M.E. Lidstrom, M.G. Kalyuzhnaya, Genome-scale metabolic reconstructions and theoretical investigation of methane conversion in Methylomicrobium buryatense strain 5G(B1), Microb. Cell Fact. 14 (2015) 188. https://doi.org/10.1186/s12934-015-0377-3.
[124] A. Gilman, Y. Fu, M. Hendershott, F. Chu, A.W. Puri, A.L. Smith, M. Pesesky, R. Lieberman, D.A.C. Beck, M.E. Lidstrom, Oxygen-limited metabolism in the methanotroph Methylomicrobium buryatense 5GB1C, PeerJ. 5 (2017) e3945. https://doi.org/10.7717/peerj.3945.
[125] I.R. Akberdin, M. Thompson, R. Hamilton, N. Desai, D. Alexander, C.A. Henard, M.T. Guarnieri, M.G. Kalyuzhnaya, Methane utilization in Methylomicrobium alcaliphilum 20ZR: a systems approach, Sci. Rep. 8 (2018) 2512. https://doi.org/10.1038/s41598-018-20574-z.
[126] C.A. Henard, H. Smith, N. Dowe, M.G. Kalyuzhnaya, P.T. Pienkos, M.T. Guarnieri, Bioconversion of methane to lactate by an obligate methanotrophic bacterium, Sci. Rep. 6 (2016) 21585. https://doi.org/10.1038/srep21585.
[127] A. Gilman, L.M. Laurens, A.W. Puri, F. Chu, P.T. Pienkos, M.E. Lidstrom, Bioreactor performance parameters for an industrially-promising methanotroph Methylomicrobium buryatense 5GB1, Microb. Cell Fact. 14 (2015) 182. https://doi.org/10.1186/s12934-015-0372-8.
[128] A. Gilman, Development of a Promising Methanotrophic Bacterium as an Industrial Biocatalyst, University of Washington, 2017.
[129] K. Yoshikawa, S. Aikawa, Y. Kojima, Y. Toya, C. Furusawa, A. Kondo, H. Shimizu, Construction of a Genome-Scale Metabolic Model of Arthrospira platensis NIES-39 and Metabolic Design for Cyanobacterial Bioproduction, PLoS One. 10 (2015) e0144430. https://doi.org/10.1371/journal.pone.0144430.
[130] K. Yoshikawa, Y. Toya, H. Shimizu, Metabolic engineering of Synechocystis sp. PCC 6803 for enhanced ethanol production based on flux balance analysis, Bioprocess Biosyst Eng. 40 (2017) 791–796. https://doi.org/10.1007/s00449-017-1744-8.
[131] M. Toyoshima, Y. Toya, H. Shimizu, Flux balance analysis of cyanobacteria reveals

selective use of photosynthetic electron transport components under different spectral light conditions, Photosynth Res. 143 (2020) 31–43. https://doi.org/10.1007/s11120-019-00678-x.
[132] G. Peltier, E.-M. Aro, T. Shikanai, {NDH}-1 and {NDH}-2 {Plastoquinone} {Reductases} in {Oxygenic} {Photosynthesis}, Annu Rev Plant Biol. 67 (2016) 55–80. https://doi.org/10.1146/annurev-arplant-043014-114752.
[133] S.H.J. Chan, M.N. Simons, C.D. Maranas, {SteadyCom}: {Predicting} microbial abundances while ensuring community stability, PLOS Comput. Biol. 13 (2017) e1005539. https://doi.org/10.1371/journal.pcbi.1005539.
[134] F. Baldini, A. Heinken, L. Heirendt, S. Magnusdottir, R.M.T. Fleming, I. Thiele, The {Microbiome} {Modeling} {Toolbox}: from microbial interactions to personalized microbial communities, Bioinformatics. 35 (2019) 2332–2334. https://doi.org/10.1093/bioinformatics/bty941.
[135] R.A. Khandelwal, B.G. Olivier, W.F.M. Röling, B. Teusink, F.J. Bruggeman, Community {Flux} {Balance} {Analysis} for {Microbial} {Consortia} at {Balanced} {Growth}, PLoS One. 8 (2013) e64567. https://doi.org/10.1371/journal.pone.0064567.
[136] A.M. Feist, B.Ø. Palsson, The {Growing} {Scope} of {Applications} of {Genome}-scale {Metabolic} {Reconstructions}: the case of {E}. coli, Nat Biotechnol. 26 (2008) 659–667. https://doi.org/10.1038/nbt1401.
[137] A. Heinken, I. Thiele, Anoxic {Conditions} {Promote} {Species}-{Specific} {Mutualism} between {Gut} {Microbes} {In} {Silico}, Appl. Environ. Microbiol. 81 (2015) 4049–4061. https://doi.org/10.1128/AEM.00101-15.
[138] K. Zecher, K.R. Hayes, B. Philipp, Evidence of Interdomain Ammonium Cross-Feeding From Methylamine- and Glycine Betaine-Degrading Rhodobacteraceae to Diatoms as a Widespread Interaction in the Marine Phycosphere, Front. Microbiol. 11 (2020) 2431. https://doi.org/10.3389/fmicb.2020.533894.
[139] J.B. Xavier, Social interaction in synthetic and natural microbial communities, Mol. Syst. Biol. 7 (2011) 483. https://doi.org/10.1038/msb.2011.16.
[140] Y. Fu, Y. Li, M. Lidstrom, The oxidative {TCA} cycle operates during methanotrophic growth of the {Type} {I} methanotroph {Methylomicrobium} buryatense {5GB1}, Metab. Eng. 42 (2017) 43–51. https://doi.org/10.1016/j.ymben.2017.05.003.
[141] D.T.N. Nguyen, O.K. Lee, S. Hadiyati, A.N. Affifah, M.S. Kim, E.Y. Lee, Metabolic engineering of the type {I} methanotroph {Methylomonas} sp. {DH}-1 for production of succinate from methane, Metab. Eng. 54 (2019) 170–179. https://doi.org/10.1016/j.ymben.2019.03.013.
[142] K.L. Hillesland, D.A. Stahl, Rapid evolution of stability and productivity at the origin of a microbial mutualism, PNAS. 107 (2010) 2124–2129. https://doi.org/10.1073/pnas.0908456107.
[143] S. Mitri, K. Richard Foster, The {Genotypic} {View} of {Social} {Interactions} in {Microbial} {Communities}, Annu. Rev. Genet. 47 (2013) 247–273. https://doi.org/10.1146/annurev-genet-111212-133307.
[144] J.-H. Wang, T.-Y. Zhang, G.-H. Dao, X.-Q. Xu, X.-X. Wang, H.-Y. Hu, Microalgae-based advanced municipal wastewater treatment for reuse in water bodies, Appl Microbiol Biotechnol. 101 (2017) 2659–2675. https://doi.org/10.1007/s00253-017-8184-x.
[145] F.G. Acién, C. Gómez-Serrano, M.M. Morales-Amaral, J.M. Fernández-Sevilla, E. Molina-Grima, Wastewater treatment using microalgae: how realistic a contribution might

it be to significant urban wastewater treatment?, Appl. Microbiol. Biotechnol. 100 (2016) 9013–9022. https://doi.org/10.1007/s00253-016-7835-7.
[146] R. Ramanan, B.H. Kim, D.H. Cho, H.M. Oh, H.S. Kim, Algae-bacteria interactions: Evolution, ecology and emerging applications, Biotechnol. Adv. 34 (2016) 14–29. https://doi.org/10.1016/j.biotechadv.2015.12.003.
[147] B. Zhang, W. Li, Y. Guo, Z. Zhang, W. Shi, F. Cui, P.N.L. Lens, J.H. Tay, Microalgal-bacterial consortia: {From} interspecies interactions to biotechnological applications, Renew. Sustain. Energy Rev. 118 (2020) 109563. https://doi.org/10.1016/j.rser.2019.109563.
[148] E. Fernandez, A. Galvan, Inorganic nitrogen assimilation in Chlamydomonas, in: J. Exp. Bot., J Exp Bot, 2007: pp. 2279–2287. https://doi.org/10.1093/jxb/erm106.
[149] E. Fernandez, A. Galvan, Nitrate assimilation in Chlamydomonas, Eukaryot. Cell. 7 (2008) 555–559. https://doi.org/10.1128/EC.00431-07.
[150] B.J. Miflin, P.J. Lea, Glutamine and asparagine as nitrogen donors for reductant dependent glutamate synthesis in pea roots, Biochem. J. 149 (1975) 403–409. https://doi.org/10.1042/bj1490403.
[151] E. Sanz-Luque, A. Chamizo-Ampudia, A. Llamas, A. Galvan, E. Fernandez, Understanding nitrate assimilation and its regulation in microalgae, Front Plant Sci. 6 (2015). https://doi.org/10.3389/fpls.2015.00899.
[152] L.E. de-Bashan, X. Mayali, B.M. Bebout, P.K. Weber, A.M. Detweiler, J.P. Hernandez, L. Prufert-Bebout, Y. Bashan, Establishment of stable synthetic mutualism without co-evolution between microalgae and bacteria demonstrated by mutual transfer of metabolites (NanoSIMS isotopic imaging) and persistent physical association (Fluorescent in situ hybridization), Algal Res. 15 (2016) 179–186. https://doi.org/10.1016/j.algal.2016.02.019.
[153] J.R. Oosthuizen, R.K. Naidoo, D. Rossouw, F.F. Bauer, Evolution of mutualistic behaviour between Chlorella sorokiniana and Saccharomyces cerevisiae within a synthetic environment, J. Ind. Microbiol. Biotechnol. 47 (2020) 357–372. https://doi.org/10.1007/s10295-020-02280-w.
[154] B.R. Crable, C.M. Plugge, M.J. McInerney, A.J.M. Stams, Formate {Formation} and {Formate} {Conversion} in {Biological} {Fuels} {Production}, Enzyme Res. 2011 (2011) 1–8. https://doi.org/10.4061/2011/532536.
[155] M. Ihara, Y. Kawano, M. Urano, A. Okabe, Light {Driven} {CO2} {Fixation} by {Using} {Cyanobacterial} {Photosystem} {I} and {NADPH}-{Dependent} {Formate} {Dehydrogenase}, PLoS One. 8 (2013). https://doi.org/10.1371/journal.pone.0071581.
[156] G. Riccardi, E. de Rossi, A. Milano, Amino acid biosynthesis and its regulation in cyanobacteria, Plant Sci. 64 (1989) 135–151. https://doi.org/10.1016/0168-9452(89)90018-6.
[157] N.-S. Lau, M. Matsui, A.A.-A. Abdullah, Cyanobacteria: {Photoautotrophic} {Microbial} {Factories} for the {Sustainable} {Synthesis} of {Industrial} {Products}, Biomed Res Int. 2015 (2015). https://doi.org/10.1155/2015/754934.
[158] L.J. Stal, R. Moezelaar, Fermentation in {cyanobacteria1Publication} 2274 of the {Centre} of {Estuarine} and {Coastal} {Ecology}, {Yerseke}, {The} {Netherlands}.1, FEMS Microbiol. Rev. 21 (1997) 179–211. https://doi.org/10.1016/S0168-6445(97)00056-9.
[159] X. Liu, J. Sheng, R.C. Iii, Fatty acid production in genetically modified cyanobacteria, PNAS. 108 (2011) 6899–6904. https://doi.org/10.1073/pnas.1103014108.

[160] J. Zhou, H. Zhang, Y. Zhang, Y. Li, Y. Ma, Designing and creating a modularized synthetic pathway in cyanobacterium {Synechocystis} enables production of acetone from carbon dioxide, Metab. Eng. 14 (2012) 394–400. https://doi.org/10.1016/j.ymben.2012.03.005.
[161] C.J. Knoot, J. Ungerer, P.P. Wangikar, H.B. Pakrasi, Cyanobacteria: {Promising} biocatalysts for sustainable chemical production, J. Biol. Chem. 293 (2018) 5044–5052. https://doi.org/10.1074/jbc.R117.815886.
[162] G. Luan, Y. Qi, M. Wang, Z. Li, Y. Duan, X. Tan, X. Lu, Combinatory strategy for characterizing and understanding the ethanol synthesis pathway in cyanobacteria cell factories, Biotechnol Biofuels. 8 (2015) 184. https://doi.org/10.1186/s13068-015-0367-z.
[163] J. Zhu, X. Xu, M. Yuan, H. Wu, Z. Ma, W. Wu, Optimum {O2}:{CH4} {Ratio} {Promotes} the {Synergy} between {Aerobic} {Methanotrophs} and {Denitrifiers} to {Enhance} {Nitrogen} {Removal}, Front. Microbiol. 8 (2017). https://doi.org/10.3389/fmicb.2017.01112.
[164] A. Gilman, Y. Fu, M. Hendershott, F. Chu, A.W. Puri, A.L. Smith, M. Pesesky, R. Lieberman, D.A.C. Beck, M.E. Lidstrom, Oxygen-limited metabolism in the methanotroph {Methylomicrobium} buryatense {5GB1C}, PeerJ. 5 (2017). https://doi.org/10.7717/peerj.3945.
[165] S.Y. But, V.N. Khmelenina, A.S. Reshetnikov, I.I. Mustakhimov, M.G. Kalyuzhnaya, Y.A. Trotsenko, Sucrose metabolism in halotolerant methanotroph {Methylomicrobium} alcaliphilum {20Z}, Arch Microbiol. 197 (2015) 471–480. https://doi.org/10.1007/s00203-015-1080-9.
[166] M.B. Biggs, G.L. Medlock, G.L. Kolling, J.A. Papin, Metabolic network modeling of microbial communities, Wiley Interdiscip. Rev. Syst. Biol. Med. 7 (2015) 317–334. https://doi.org/10.1002/wsbm.1308.
[167] T.J. Hanly, M.A. Henson, Dynamic flux balance modeling of microbial co-cultures for efficient batch fermentation of glucose and xylose mixtures, Biotechnol. Bioeng. 108 (2011) 376–385. https://doi.org/10.1002/bit.22954.
[168] K. Zhuang, M. Izallalen, P. Mouser, H. Richter, C. Risso, R. Mahadevan, D.R. Lovley, Genome-scale dynamic modeling of the competition between {Rhodoferax} and {Geobacter} in anoxic subsurface environments, ISME J. 5 (2010) 305–316. http://dx.doi.org/10.1038/ismej.2010.117.
[169] J.A. Gomez, K. Höffner, P.I. Barton, {DFBAlab}: a fast and reliable {MATLAB} code for dynamic flux balance analysis, BMC Bioinformatics. 15 (2014). https://doi.org/10.1186/s12859-014-0409-8.
[170] H.O. Buhr, S.B. Miller, A dynamic model of the high-rate algal-bacterial wastewater treatment pond, Water Res. 17 (1983) 29–37.
[171] C.P. Long, M.R. Antoniewicz, Metabolic flux responses to deletion of 20 core enzymes reveal flexibility and limits of E. coli metabolism, Metab. Eng. 55 (2019) 249–257. https://doi.org/10.1016/j.ymben.2019.08.003.
[172] J.K. Cole, J.R. Hutchison, R.S. Renslow, Y.M. Kim, W.B. Chrisler, H.E. Engelmann, A.C. Dohnalkova, D. Hu, T.O. Metz, J.K. Fredrickson, S.R. Lindemann, Phototrophic biofilm assembly in microbial-mat-derived unicyanobacterial consortia: Model systems for the study of autotroph-heterotroph interactions, Front. Microbiol. 5 (2014) 109. https://doi.org/10.3389/fmicb.2014.00109.
[173] R.S. Renslow, S.R. Lindemann, J.K. Cole, Z. Zhu, C.R. Anderton, Quantifying element

incorporation in multispecies biofilms using nanoscale secondary ion mass spectrometry image analysis, Biointerphases. 11 (2016) 02A322. https://doi.org/10.1116/1.4941764.
[174] N. Global Monitoring Laboratory, Carbon cycle greenhouse gases, (2020). https://www.esrl.noaa.gov/gmd/ccgg/trends/mlo.html (accessed April 22, 2021).
[175] G. Kim, W. Choi, C.-H. Lee, K. Lee, Enhancement of dissolved inorganic carbon and carbon fixation by green alga {Scenedesmus} sp. in the presence of alkanolamine {CO2} absorbents, Biochem. Eng. J. 78 (2013) 18–23. https://doi.org/10.1016/j.bej.2013.02.010.
[176] J.C.M. Pires, F.G. Martins, M.C.M. Alvim-Ferraz, M. Simões, Recent developments on carbon capture and storage: {An} overview, Chem. Eng. Res. Des. 89 (2011) 1446–1460. https://doi.org/10.1016/j.cherd.2011.01.028.
[177] C. Stewart, M.-A.A. Hessami, A study of methods of carbon dioxide capture and sequestration—the sustainability of a photosynthetic bioreactor approach, Energy Convers. Manag. 46 (2005) 403–420. https://doi.org/10.1016/j.enconman.2004.03.009.
[178] S. Holloway, Carbon dioxide capture and geological storage, Philos. Trans. R. Soc. A Math. Phys. Eng. Sci. 365 (2007) 1095–1107. https://doi.org/10.1098/rsta.2006.1953.
[179] J.C. Abanades, M. Akai, S. Benson, S. Leone, R. Doctor, J. Gale, D. Keith, M. Mazzotti, B. Metz, L. Meyer, B. Osman-Elasha, A. Palmer, E. Rubin, This summary, approved in detail at the {Eighth} {Session} of {IPCC} {Working} {Group} {III} ({Montreal}, {Canada}, 22-24 {September} 2005), represents the formally agreed statement of the {IPCC} concerning current understanding of carbon dioxide capture , (n.d.) 16.
[180] L. de Lary, A. Loschetter, O. Bouc, J. Rohmer, C.M. Oldenburg, Assessing health impacts of {CO2} leakage from a geological storage site into buildings: {Role} of attenuation in the unsaturated zone and building foundation, Int. J. Greenh. Gas Control. 9 (2012) 322–333. https://doi.org/10.1016/j.ijggc.2012.04.011.
[181] C. Yao, J. Ai, X. Cao, S. Xue, W. Zhang, Enhancing starch production of a marine green microalga Tetraselmis subcordiformis through nutrient limitation, Bioresour. Technol. 118 (2012) 438–444. https://doi.org/10.1016/j.biortech.2012.05.030.
[182] D. Cheng, D. Li, Y. Yuan, L. Zhou, X. Li, T. Wu, L. Wang, Q. Zhao, W. Wei, Y. Sun, Improving carbohydrate and starch accumulation in Chlorella sp. AE10 by a novel two-stage process with cell dilution, Biotechnol. Biofuels. 10 (2017) 75. https://doi.org/10.1186/s13068-017-0753-9.
[183] M. Qi, C. Yao, B. Sun, X. Cao, Q. Fei, B. Liang, W. Ran, Q. Xiang, Y. Zhang, X. Lan, Application of an in situ {CO2}–bicarbonate system under nitrogen depletion to improve photosynthetic biomass and starch production and regulate amylose accumulation in a marine green microalga {Tetraselmis} subcordiformis, Biotechnol Biofuels. 12 (2019) 184. https://doi.org/10.1186/s13068-019-1523-7.
[184] H. Khatoon, N. Abdu Rahman, S. Banerjee, N. Harun, S.S. Suleiman, N.H. Zakaria, F. Lananan, S.H. Abdul Hamid, A. Endut, Effects of different salinities and pH on the growth and proximate composition of Nannochloropsis sp. and Tetraselmis sp. isolated from South China Sea cultured under control and natural condition, Int. Biodeterior. Biodegrad. 95 (2014) 11–18. https://doi.org/10.1016/j.ibiod.2014.06.022.
[185] W. Liu, J. Wang, T. Liu, Low pH rather than high CO 2 concentration itself inhibits growth of Arthrospira, Sci. Total Environ. 666 (2019) 572–580. https://doi.org/10.1016/j.scitotenv.2019.02.312.
[186] R.D. Gardner, E. Lohman, R. Gerlach, K.E. Cooksey, B.M. Peyton, Comparison of CO2 and bicarbonate as inorganic carbon sources for triacylglycerol and starch accumulation in

Chlamydomonas reinhardtii, Biotechnol. Bioeng. 110 (2013) 87–96. https://doi.org/10.1002/bit.24592.
[187] R.D. Gardner, K.E. Cooksey, F. Mus, R. Macur, K. Moll, E. Eustance, R.P. Carlson, R. Gerlach, M.W. Fields, B.M. Peyton, Use of sodium bicarbonate to stimulate triacylglycerol accumulation in the chlorophyte Scenedesmus sp. and the diatom Phaeodactylum tricornutum, J. Appl. Phycol. 24 (2012) 1311–1320. https://doi.org/10.1007/s10811-011-9782-0.
[188] C.F. Knud-Hansen, Pond Fertilization: Ecological Approach and Practical Applications, in: Pond Dynamics/Aquaculture Collaborative Research Support Program, 1998: p. 20.
[189] Oxyacid - Carbonic acid and carbonate salts | Britannica, (n.d.). https://www.britannica.com/science/oxyacid/Carbonic-acid-and-carbonate-salts#ref1000415 (accessed May 11, 2021).
[190] K.G. Schulz, U. Riebesell, B. Rost, S. Thoms, R.E. Zeebe, Determination of the rate constants for the carbon dioxide to bicarbonate inter-conversion in {pH}-buffered seawater systems, Mar. Chem. 100 (2006) 53–65. https://doi.org/10.1016/j.marchem.2005.11.001.
[191] K. Ying, J. Gilmour, W.B. Zimmerman, Effects of CO 2 and pH on Growth of the Microalga Dunaliella salina, J Microb Biochem Technol. 6 (2014) 167–173. https://doi.org/10.4172/1948-5948.1000138.
[192] S. Van Den Hende, H. Vervaeren, N. Boon, Flue gas compounds and microalgae: (Bio-)chemical interactions leading to biotechnological opportunities, Biotechnol. Adv. 30 (2012) 1405–1424. https://doi.org/10.1016/j.biotechadv.2012.02.015.
[193] A. Kumar, S. Ergas, X. Yuan, A. Sahu, Q. Zhang, J. Dewulf, F.X. Malcata, H. van Langenhove, Enhanced CO2 fixation and biofuel production via microalgae: Recent developments and future directions, Trends Biotechnol. 28 (2010) 371–380. https://doi.org/10.1016/j.tibtech.2010.04.004.
[194] K. Kumar, D. Banerjee, D. Das, Carbon dioxide sequestration from industrial flue gas by Chlorella sorokiniana, Bioresour. Technol. 152 (2014) 225–233. https://doi.org/10.1016/j.biortech.2013.10.098.
[195] Y.-S. Yun, S.B. Lee, J.M. Park, C.-I. Lee2, J.-W. Yang3, Carbon Dioxide Fixation by Algal Cultivation Using Wastewater Nutrients, 1997. https://doi.org/10.1002/(SICI)1097-4660(199708)69:4.
[196] C. Yoo, S.Y. Jun, J.Y. Lee, C.Y. Ahn, H.M. Oh, Selection of microalgae for lipid production under high levels carbon dioxide, in: Bioresour. Technol., Elsevier Ltd, 2010: pp. S71–S74. https://doi.org/10.1016/j.biortech.2009.03.030.
[197] F.F. Li, Z.H. Yang, R. Zeng, G. Yang, X. Chang, J.B. Yan, Y.L. Hou, Microalgae capture of CO2 from actual flue gas discharged from a combustion chamber, Ind. Eng. Chem. Res. 50 (2011) 6496–6502. https://doi.org/10.1021/ie200040q.
[198] K. Maeda, M. Owada, N. Kimura, K. Omata, I. Karube, CO2 fixation from the flue gas on coal-fired thermal power plant by microalgae, Energy Convers. Manag. 36 (1995) 717–720. https://doi.org/10.1016/0196-8904(95)00105-M.
[199] X. Zhang, Microalgae removal of CO 2 from flue gas, 2015. www.iea-coal.org (accessed May 13, 2021).
[200] M.G. de Morais, J.A.V. Costa, Isolation and selection of microalgae from coal fired thermoelectric power plant for biofixation of carbon dioxide, Energy Convers. Manag. 48 (2007) 2169–2173. https://doi.org/10.1016/j.enconman.2006.12.011.

[201] B. Zhao, Y. Su, Process effect of microalgal-carbon dioxide fixation and biomass production: {A} review, Renew. Sustain. Energy Rev. 31 (2014) 121–132. https://doi.org/10.1016/j.rser.2013.11.054.
[202] C. Jansson, T. Northen, Calcifying cyanobacteria—the potential of biomineralization for carbon capture and storage, Curr. Opin. Biotechnol. 21 (2010) 365–371. https://doi.org/10.1016/j.copbio.2010.03.017.
[203] X. Ji, J.M.H. Verspagen, D.B. de Waal, B. Rost, J. Huisman, Phenotypic plasticity of carbon fixation stimulates cyanobacterial blooms at elevated {CO} $_{\textrm{2}}$, Sci. Adv. 6 (2020) eaax2926. https://doi.org/10.1126/sciadv.aax2926.
[204] M.R. Badger, G.D. Price, {CO2} concentrating mechanisms in cyanobacteria: molecular components, their diversity and evolution, J Exp Bot. 54 (2003) 609–622. https://doi.org/10.1093/jxb/erg076.
[205] G.D. Price, S.I. Maeda, T. Omata, M.R. Badger, Modes of active inorganic carbon uptake in the cyanobacterium, Synechococcus sp. PCC7942, in: Funct. Plant Biol., CSIRO, 2002: pp. 131–149. https://doi.org/10.1071/pp01229.
[206] M. Shibata, H. Ohkawa, H. Katoh, M. Shimoyama, T. Ogawa, Two CO2 uptake systems in cyanobacteria: Four systems for inorganic carbon acquisition in Synechocystis sp. strain PCC6803, in: Funct. Plant Biol., CSIRO, 2002: pp. 123–129. https://doi.org/10.1071/pp01188.
[207] G. Amoroso, D. Sültemeyer, C. Thyssen, H.P. Fock, Uptake of {HCO3}− and {CO2} in {Cells} and {Chloroplasts} from the {Microalgae} {Chlamydomonas} reinhardtii and {Dunaliella} tertiolecta, Plant Physiol. 116 (1998) 193–201. https://www.ncbi.nlm.nih.gov/pmc/articles/PMC35158/ (accessed November 4, 2020).
[208] S.I. Maeda, M.R. Badger, G.D. Price, Novel gene products associated with NdhD3/D4-containing NDH-1 complexes are involved in photosynthetic CO2 hydration in the cyanobacterium, Synechococcus sp. PCC7942, Mol. Microbiol. 43 (2002) 425–435. https://doi.org/10.1046/j.1365-2958.2002.02753.x.
[209] M.R. Badger, D. Hanson, G.D. Price, Evolution and diversity of CO2 concentrating mechanisms in cyanobacteria, in: Funct. Plant Biol., CSIRO, 2002: pp. 161–173. https://doi.org/10.1071/pp01213.
[210] A. Solovchenko, I. Khozin-Goldberg, High-CO2 tolerance in microalgae: Possible mechanisms and implications for biotechnology and bioremediation, Biotechnol. Lett. 35 (2013) 1745–1752. https://doi.org/10.1007/s10529-013-1274-7.
[211] X. Ji, J.M.H. Verspagen, M. Stomp, J. Huisman, Competition between cyanobacteria and green algae at low versus elevated {CO2}: who will win, and why?, J Exp Bot. 68 (2017) 3815–3828. https://doi.org/10.1093/jxb/erx027.

Appendices

A. Carbon dioxide uptake mechanism and growth of cyanobacteria and microalgae under complex conditions: A mini review

A.1 Introduction

Carbon dioxide (CO_2) emission to the atmosphere has been increased dramatically in the last decade to 417ppm [174] due to many different sources including fossil fuels utilization and wastewater treatment facilities. Nature has a way to reduce this effect by absorption through trees, which overcutting forests has been making the reduction of CO_2 concentration hard for nature. Man-made activities have happened in order to control the CO_2 emission rate to the stable, safe and environmentally acceptable level, including application of Amine absorbents [175][176], desiccant absorption[177], geological storage [178] and ocean storage [179]. However, bio-reduction of CO_2 by microalgae and cyanobacteria has been more attractive due to lack of serious challenges such as high energy consumption for regeneration (e.g. Amine), large space requirements and the risk of CO_2 leakage over time concerning geological and ocean storage [180]. Furthermore, bio-reduction has affirmative characteristics such as converting water and CO_2 to organic compounds, oxygen and biomass for various applications without additional energy consumption and secondary pollution. However, some factors such as economic aspects, physicochemical and hydrodynamic parameters, various type of species and their complicated mechanisms for capturing CO_2 have made the bio-reduction process much slower at industrial level.

Unlike other gases, CO_2 has some unique factors. When CO_2 is passed into the aqueous solution, it can convert to chemicals such as carbonate, bicarbonate, and carbonic acid besides the aqueous form of CO_2 (dissolved CO_2-dCO_2) reducing the pH. pH is the major determinant in relative CO_2 concentration in water and could affect availability of carbon for photoautotroph organisms.

A completed and systematic review regarding the carbon uptake mechanism of photoautotrophs, especially in various environments and conditions, has not yet been reported. This work attempts to summarize and review the studies that investigated the relationship of photoautotroph growth with experimental variables such as CO_2 concentration, pH, and presence of other forms of inorganic carbon. Furthermore, we discuss the reason of photoautotrophs behavior in response to different conditions in detail, both on systematic and molecular levels.

A.1.1 Photoautotroph growth on different form of inorganic carbon

Overall, the studies related to growth of photoautotrophs have focused on the supplementation of inorganic carbon in the form of gas (Carbon dioxide-CO_2) or solid substrate (Sodium bicarbonate-$NaHCO_3$) that can be taken up and utilized by microalgae or cyanobacteria. The solid bicarbonate has been found to be easier to transport and cost-effective compared to gaseous inorganic carbon sources. One of the most common conditions that has been investigated is the growth of photoautotrophs under nutrient (nitrate and phosphate) depleted conditions to simulate harsh and common environmental situations.

Photoautotrophs tend to accumulate large quantities of starch with usually more than 50% gDCW (gram dry cell weight) in their biomass when they are under stressful situations such as nutrient deprivation and high irradiance [181]. Therefore, nitrogen depletion or nitrogen limitation has been used for the improvement of starch production. A “two-stage” process has been proposed using Nitrogen depletion condition (stage 1), which applies very small amounts of nitrogen supply, short cultivation time, and high light availability, with Nitrogen limitation condition (stage 2), which needs longer cultivation time and gets more biomass, in order to maximize the starch production

[182]. The carbon supply is one of the main factors for photoautotroph growth and as a result starch productivity in these studies.

In general, photoautotrophs use CO_2 as the primary carbon source for photosynthesis and growth; however, it provides low biomass productivity if the system only depends on air as a gas source because of the low percentage of carbon dioxide (%0.04), or if pH environment is acidic and undesirable (pH<5) because of high percentage of carbon dioxide in the gas source. As mentioned, bicarbonate salt is another form of carbon supply that most photoautotrophs are able to utilize. It has been shown that bicarbonate has high water solubility and could generate a favorable pH environment for growth of *Tetraselmis subcordiformis* under nitrogen depletion [183]. Addition of bicarbonate to the medium increased the pH level. Average pH reached 5.2, 6.7, 7.7 and 8.3 by adding 0, 0.2, 1 and 5 g/L $NaHCO_3$ respectively (Figure A1c). The best biomass production was obtained with the addition of 1g/L bicarbonate where pH was at 7.7 (Figure A1), which is in the optimal range of conditions for biomass production of *T. suecica.* Dramatically lower cell growth was observed in the culture without bicarbonate addition in which the pH was around 5.2. It has been shown that the low pH has inhibition effect on biomass production of *Tetraselmis* [184] and *Arthrospira platensis* [185]. Low pH can deactivate some critical enzymes in photosynthesis for carbon assimilation which can inhibit growth and biomass production. From the other side, the systems with the addition of bicarbonate have lower concentrations of dCO_2 compared to the 2% CO_2 aeration culture. This suggests the higher amount of dCO_2, 2.9-4.1 mmol/kg water, which is 13 to 52 times higher than in the culture with the 1 g/L $NaHCO_3$ addition, could be another reason for growth inhibition (Figure A1d).

However, it has been shown that high concentration of bicarbonate (in the culture with the addition of 5 g/L $NaHCO_3$) inhibited the growth of *T. subcordiformis* compared to 1g/L $NaHCO_3$, without

any notable difference in pH. It has been discussed the high concentration of bicarbonate could disrupt the energy dependent metabolism and photosynthetic CO_2 bio-fixation since bicarbonate assimilation needs an active transport in photoautotroph which is energy consuming and bioenergetically disadvantaged.

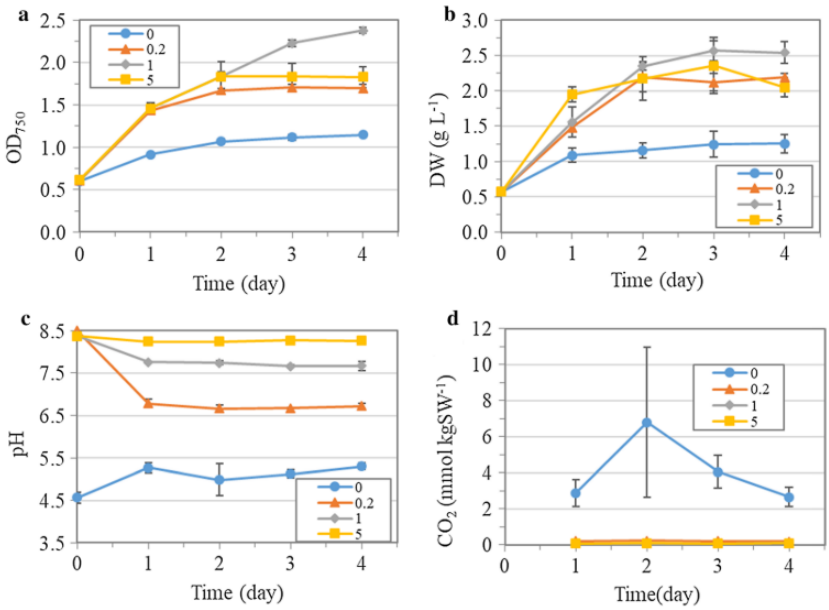

Figure A1. Cell growth (OD_{750}, a), biomass production (dry weight, b), pH variations (c), dissolved CO_2 concentration (dCO2, d) of *T. subcordiformis* cultures with different amounts of $NaHCO_3$ addition (0, 0.2, 1 and 5 g L^{-1}) under nitrogen depletion [183].

A CO_2-bicarbonate system was critical to have a proper pH and provide enough carbon source without inhibition effect of high dCO_2 for the adequate photosynthetic efficiency and improvement of biomass productivity in the microalgae *T. subcordiformis* under nutrient depletion cultivation (2.1 fold with addition of 1g/L $NaHCO_3$ compared with the system without bicarbonate and just aerated by 2%CO_2) [183].

Another study has been focused on triacylglycerol production, using a CO_2-bicarbonate system, but it has been shown that using bicarbonate ceased the growth of photoautotroph [186]. The effect

of different forms of inorganic carbon on physiological changes of *C. reinhardtii* and its triacylglycerol (TAG) and starch accumulation has been investigated and can provide more insight into potential industrial application of photoautotroph for biofuel production. The culture with aeration of 5% CO_2 had a better growth (1.7 times more) than the cultures with addition of bicarbonate, both with ammonium as the nitrogen source. During growth there was a characteristic decrease in pH, which is consistent for photoautotroph growth on ammonium and high CO_2 levels. During ammonium depletion, *C. reinhardtii* accumulated TAG and starch as carbon storage compounds when either 5% CO_2 gas-sparge or bicarbonate were used. However, the highest TAG accumulation was observed when the system was sparged with 5% CO_2. While the 50 mM bicarbonate amended cultures to accumulate starch and TAG at a slightly slower rate. Previous studies on the *Chlorophyte scenedesmus* sp. WC-1 showed the same result upon adding 50 mM bicarbonate compared to the system with sparged CO_2 [187]. The systems with added bicarbonate caused a change in metabolism and shifted from biomass production to a product formation as evident by lower growth and higher biomass yield compared to no-bicarbonate system.

As discussed in this section, the conclusion regarding which kind of inorganic carbon is utilizable and favorable for photoautotrophs are different among various studies. There are several factors that affect the growth of photoautotrophs that we discuss in following sections.

A.2 Main reactions and effects of dissolved carbon dioxide on growth

The following reaction happens when gaseous CO_2 is absorbed into water:

$$CO_{2\,(l)} + H_2O \leftrightarrow H_2CO_3 \leftrightarrow HCO_3^- + H^+ \leftrightarrow CO_3^{2-} + 2H^+ \quad \text{(A1)}$$

According to the equation, there is dCO_2, bicarbonate (HCO_3^-) and carbonate (CO_3^{2-}) production and an increase of hydrogen ions (H^+). This H^+ production has a significant role on pH in solution,

just as produced OH^- by adding CO_3^{2-} and HCO_3^- has, since pH is a measure of the equilibrium between H_2O and concentrations of H^+ and OH^-.

$$H_2O \leftrightarrow H^+ + OH^- \quad \text{(A2)}$$

For example, in a microalgae culture, when CO_2 is produced through respiration, total dissolved inorganic carbon (DIC) concentration is increased, and pH is dropped. On the other hand, microalgae uptake of CO_2 during photosynthesis increases OH^- concentration and, as a result, raises the pH of the water. The relationship between pH and the relative percentage of DIC including dCO_2, HCO_3^- and CO_3^{2-}, in equilibrium at 25°C has been shown in Table A1 [188].

Table A1. Relationship between pH and approximate relative percentages of total dissolved inorganic carbon (DIC), based on equilibrium reactions between dissolved carbon dioxide (dCO_2), bicarbonate (HCO_3^-), and carbonate (CO_3^{2-}) at 25°C [188].

PH	dCO_2	HCO_3^-	CO_3^{2-}
5	95.7	4.3	0
6	69.2	30.8	0
7	18.3	81.6	0
8	2.2	97.4	0.5
9	0.2	95.3	4.5
10	0	68.1	31.9
11	0	17.6	82.4

The main question here is what forms of DIC are utilizable by the microalgae and cyanobacteria. It has been shown that all microalgae and cyanobacteria can take up dCO_2 readily, and HCO_3^- can be utilized by many algal species. CO_3^{2-}, however, is not usable for photoautotrophs (Table A2). This does not create any significant issues when pH is 8 or less, but for higher pH such as 10, almost half (40%) of DIC is CO_3^{2-} in equilibrium (Table A1).

Table A2. Identification of different forms of dissolved inorganic carbon (DIC) in relation to total alkalinity and forms of inorganic carbon generally available for photoautotroph uptake [188].

	dCO_2	HCO_3^-	CO_3^{2-}

DIC	X	X	X
Alkalinity		X	X
Utilized by Photoautotroph	X	X	

Therefore, a main problem for culturing microalgae and cyanobacteria is how to accurately quantify usable and available DIC for photoautotroph uptake, since it changes with pH, temperature and time. The effect of pH has been shown clearly, and the temperature affects this problem by changing the solubility of CO_2 in water. To better explain the effect of time, the main reactions and their relative speed have been shown. Consider carbonic acid as a diprotic form of bicarbonate and carbonate. For example, at a pH less than 8, the reaction speed of converting dCO_2 to carbonic acid is slow as follows [189]:

$$dCO_2 + H_2O \leftrightarrow H_2CO_3 \ (slow) \quad \text{(A3)}$$

$$H_2CO_3 + OH^- \leftrightarrow HCO_3^- + H_2O \ (fast) \quad \text{(A4)}$$

And for pH above 10, the speed of conversion of dCO_2 to bicarbonate is slow:

$$dCO_2 + OH^- \leftrightarrow HCO_3^- \ (slow) \quad \text{(A5)}$$

$$HCO_3^- + OH^- \leftrightarrow CO_3^{2-} + H_2O \ (fast) \quad \text{(A6)}$$

Even though in the range of pH 8 to 10 the amount of dCO_2 in the liquid is limited and most of the carbon is in bicarbonate (Table A1), the reactions show that conversion of dCO_2 to carbonic acid and bicarbonate is slow and, as a result, dCO_2 is distinguishable between other forms of dissolved carbon at a wide range of pH (5-11) for algal culturing before it reaches equilibrium. Therefore, there is enough time and opportunity for photoautotrophs to uptake dCO_2 from the medium if it is desirable.

Some studies have shown the speed of conversion of dCO_2 to bicarbonate qualitatively and quantitatively. The k_+ value of reaction of equation (7) has been calculated by adding CO_2 to seawater (about $15 \mu mol/kg$) at different pH values ranging from 7 to 9 and different temperatures

of 11,16, and 26 °C as shown in the Figure A2. There have been some difficulties in this reaction for pH more than 8.5. The correlation between measured and calculated became less clear because of unreliable pH determination. Hence, after additions of known amounts of $NaHCO_3$ to the sea water, the change of dCO_2 concentration was negligible in the measurement system [190].

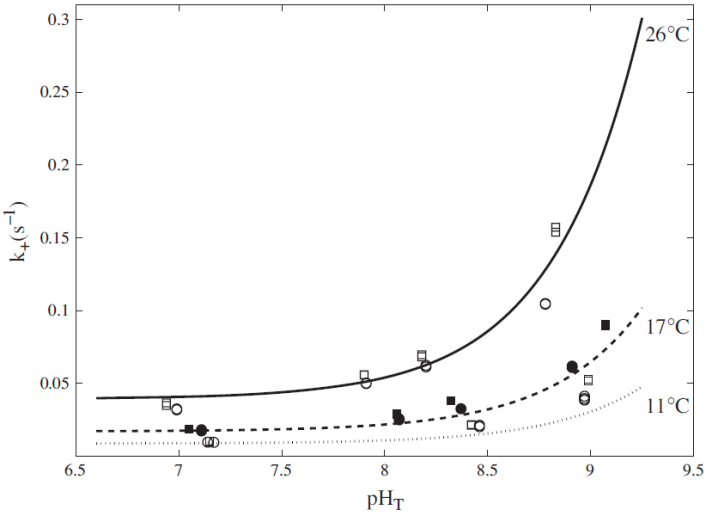

Figure A2. Graphical illustration of the k_+ values determined with the fitting procedure by additions of ~15 µmol CO_2 /kg seawater at different temperatures and seawater pH (total scale). Squares and circles denote seawater with two different buffer solutions [190].

$$H_2O + CO_2 \overset{k_+}{\rightarrow} HCO_3^- + H^+ \quad \text{(A7)}$$

It has been shown that the concentration of dCO_2 is independent of bicarbonate concentration and only depends on $\%CO_2$ in gas supply. The $[CO_2]^*$ (the equilibrium concentration of dCO_2 under a constant bubbling condition) did not change with variation of $NaHCO_3$ concentration when the $\%CO_2$ was fixed (Figure A3). This phenomenon has been supported by showing that the equilibrium dissolved concentration of a gas is in a direct proportion to the partial pressure of the gas over the solution (Henry's law). A correlation between equilibrium pH, $NaHCO_3$ concentration and $\%CO_2$ in gas supply was found (eq.(8)) [191].

$$pH^* = 7.65 + 0.41\ln(CO_2\%) - 0.46\ln(NaHCO_3)_{mol/L} \quad \text{(A8)}$$

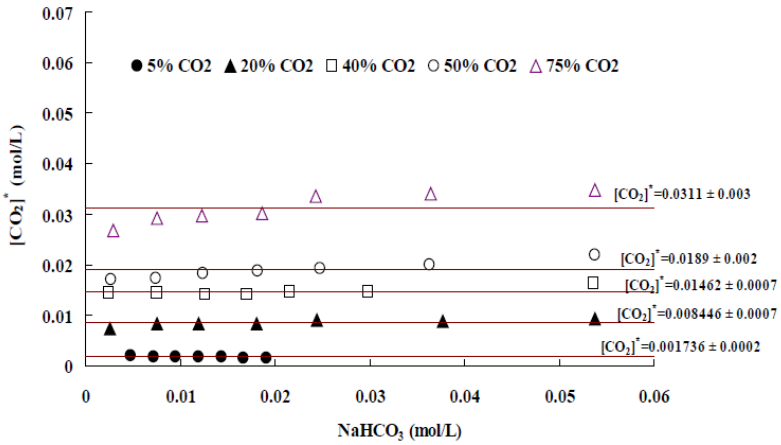

Figure A3. Plots of [CO2]* versus $NaHCO_3$ concentration for different CO_2 stream concentrations.

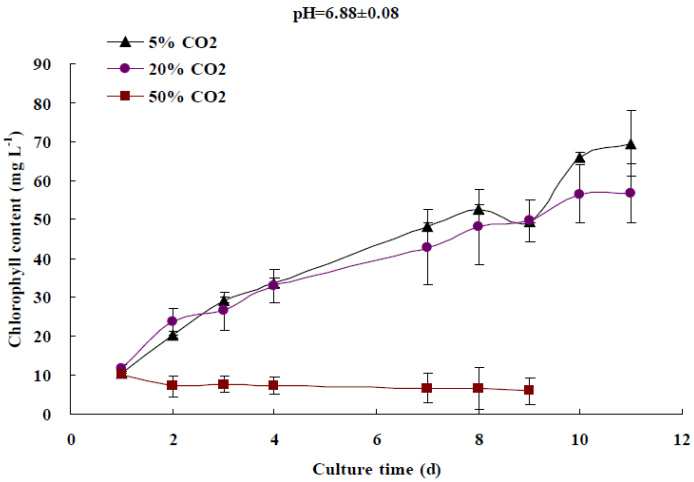

Figure A4. The plot of daily chlorophyll content against culture time for different CO_2 stream concentrations.

This correlation was used to study the effect of different pH on *D. salina* in the same dCO_2 for each culture. It was speculated that the intracellular CO_2 concentration was the same for each culture according to the two-film theory, which suggested the same intracellular equilibrium pH for each culture. The results showed even though the intracellular pH was identical for all cultures, the extracellular pH affected the photoautotroph growth, possibly because the pH gradient across the cell membrane.

The effect of different %CO_2 (5, 20 and 50%) in the gas supply on growth of *D. salina* in pH 7 was tested (Figure A4). The growth and photosynthesis of the microalgae was inhibited at the condition with 50% CO_2 with possible explanation of the intracellular pH can be affected by changing the equilibrium concentration of extracellular CO_2 despite the extracellular pH is constant, and as a result has damaged and hindered the enzymes involved in photosynthesis [191]. As it is shown the correlation between %CO_2, DIC and pH is very complicated and has various effects on growth of photoautotroph.

A.3 Photoautotrophs have different tolerance for amount of dCO_2

In this section, application of different %CO_2 in photoautotroph growth experiments has been reviewed. Most photoautotrophs, similar to some studies in section 2, showed a growth inhibition to high %CO_2, but this percentage could be different for different species for potential reasons that will be discussed. It is worth mentioning that the gas flow rate for %CO_2 in all the studies reviewed here are enough to reach the saturation and equilibrium between gas and liquid phases in the reactor. When low gas flow rates are applied, even high CO_2 concentrations in the gas phase can lead to low inorganic carbon loading in the liquid phase and low concentrations of dissolved inorganic carbon in the reactor [192].

It has been found that using 2% CO_2 is the optimal amount for *Chlorella sorokiniana* growth, while at 10% CO_2 there was a decrease in the specific growth rate compare to 2% [193,194]. The highest growth of *Chlorella vulgaris* was found at 5% CO_2 and a growth inhibition at 15% CO_2 was observed [195]. *Botryococcus braunii* had a higher growth rate at 5.5% CO_2 compared to 10% CO_2. While, *Scenedesmus sp.* could grow similarly on 5.5% and 10% CO_2 [196]. *Scenedesmus obliquus* was able to tolerate industrial flue gas with 12% CO_2 with an optimal removal efficiency of 67% in the pilot plant system [197].

From the other side, some strains have better ability for consuming CO_2. Several experiments have been carried out at high percentages of CO_2 on *Chlorella sp*. It was confirmed that *Chlorella sp*. can tolerate up to 100% CO_2 concentration, but the maximum growth rate was obtained when using 10% CO_2, even though, no significant decrease in the growth rate up to 50% CO_2 concentration was observed [198].

As discussed above, most photoautotrophs grow only at low CO_2 concentration levels, but some can grow under higher CO_2 concentrations (typically 20–50%). Few photoautotroph species are able to tolerate extremely high CO_2 levels up to 70% or even 100%. Adaptation to higher CO_2 concentrations during their evolution or previous generations is one of the main factors for defining the photoautotroph tolerance to $\%CO_2$. Isolation of photoautotroph strains from lakes or ponds in the vicinity of coal-fired power plants is a useful strategy to obtain photoautotrophs tolerant to the harsh conditions prevalent in the area, as such organism tend to have the ability to grow in the presence of the combustion gases produced by the power plants [199]. For instance, the microalgae *Scenedesmus obliquus* and *Chlorella kessleri* isolated from the waste treatment ponds of a coal-fired power plant and cultivated with 6% and 12% CO_2. It was found that with a gradual increase in CO_2 concentration, they grew better on 12% CO_2 [200]. High density of cell inoculums in photoautotrophs also lead to higher tolerance towards CO_2 and a faster growth rate. This is because the high density of inoculums could minimize the initial lag phase resulting in an immediate exponential growth of photoautotroph in the presence of a high concentration of CO_2 [199].

Overall, the CO_2 tolerance of microalgae and cyanobacteria is mainly dependent on pH and species selection, but other factors such as cell density, nutrients and light can also affect it. CO_2 tolerance depends on pH because the culture pH decease as the CO_2 concentration increases due to formation and accumulation of large amount of HCO_3^- and H^+ as discussed before. This low pH value

weakens carbon bio-fixation performance of photoautotrophs. Moreover, CO_2 tolerance depends on species because some photoautotrophs can adapt to low pH situation by, for instance, gene regulation and increasing the energy allocation proportion to maintain the pH stability inside the cell.

Essentially, photoautotroph growth and CO_2 fixation are strongly related to the inorganic carbon concentrating mechanism (CCM). The low pH value created by high CO_2 concentration inhibits carbonic anhydrase activity which plays an important catalytic role in the interchange between CO_2 and HCO_3^- and is regarded as an important factor of CCM. However, when a high CO_2 concentration decreases the pH value of the growth medium, some photoautotroph cells are able to adapt by, for example, gene regulation and increasing the energy allocation proportion. These methods can temporarily reduce the synthesis of organic carbon and simultaneously provide more adenosine triphosphate (ATP) to maintain the pH stability inside the cell, enabling it to tolerate extremely high CO_2 concentrations [201].

A.4 Inorganic carbon concentrating mechanism (CCM) in microalgae and cyanobacteria

So far, this review has provided the information about dissolved CO_2 reactions and their general effects on different microalgae and cyanobacteria growth as well as some potential reasons. In this section, CO_2 up-taking principle inside the cell and the effect of dCO_2 on cell growth will be discussed in detail.

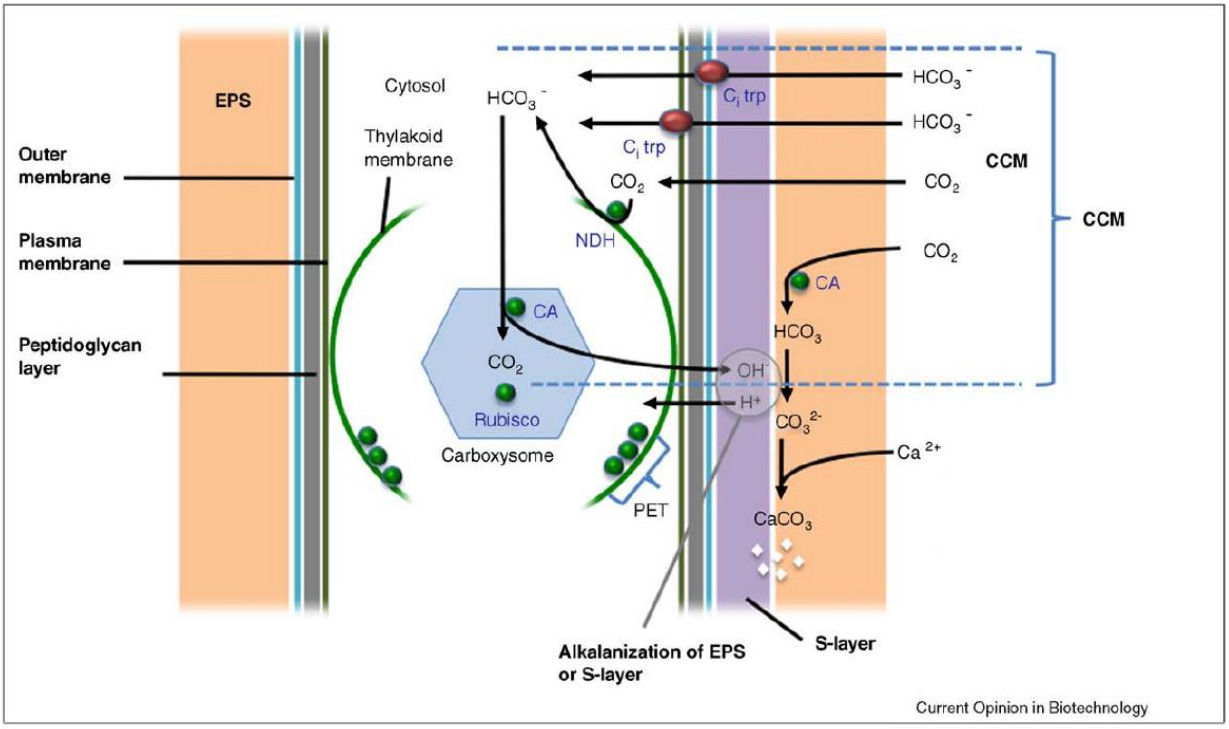

Figure A5. Model of the carbon-concentrating mechanism (CCM) in a photoautotroph cell. CO_2 enters the cells mainly via active transport of HCO_3^- and also through diffusion of dCO_2, which is converted to HCO_3^- during the uptake. Cytosolic HCO_3^- is subsequently imported to the carboxysome. CA, carbonic anhydrase; C_i, inorganic carbon; EPS, exopolysaccharide sheath; NDH, NADPH dehydrogenase; and PET, photosynthetic electron transport [202].

A photoautotroph cell components of the CCM can be illustrated in Figure A5. As it is shown, carboxysome is the center of the photoautotroph function, which is a protein within the cell that contains the Rubisco of the cell together with a carboxysomal carbonic anhydrase (CA). The CA converts the accumulated HCO_3^- in cytosol into CO_2 for Rubisco within the carboxysome. Most inorganic carbon taken up (dCO_2 or HCO_3^-) by the cell is first converted to HCO_3^- in cytosol, transported to carboxysomes, converted back to CO_2 and fixed into organic carbon by the Rubisco enzyme [203].

A.4.1 Inorganic Carbon transporters

The evidence suggests that HCO_3^- is the species accumulated within cytoplasm, regardless of which form of inorganic carbon is presented to the cells (HCO_3^- or dCO_2). One of the differences between accumulated HCO_3^- and dCO_2 in the cell is that HCO_3^- is much less permeable to lipid membranes due to its ionic structure and leaks much slower than the uncharged dCO2 molecule.

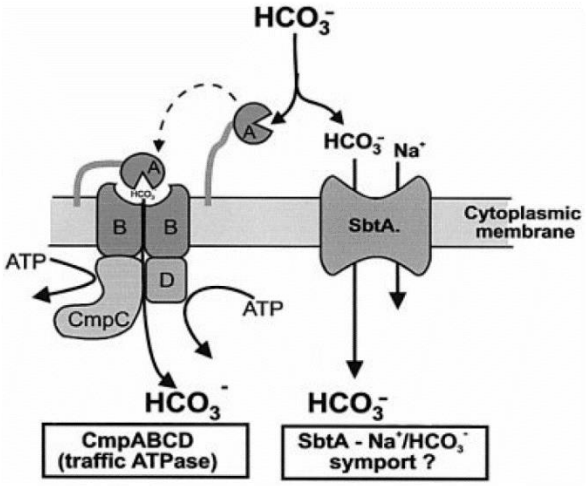

Figure A6. Models of two HCO_3^- transport systems identified in photoautotrophs. BCT1, the high-affinity traffic ATPase is shown on the left. SbtA, a potential Na^+/HCO_3^- symport system is shown on the right [204].

The substrate for the carboxysome, HCO_3^-, is accumulated in the cytosol by the operation of a number of active CO_2 and HCO_3^- transporters (Figure A6). There are five different inorganic carbon uptake systems, including three HCO_3^- uptake systems (BCT1, BicA, and SbtA) and two CO_2 uptake systems (NDH-1_3 and NDH-1_4) [203,205]. One of the first identified inorganic carbon transporters was BCT1, an inducible high affinity HCO_3^- transporter, which needs ATP to function. SbtA is a medium affinity inorganic carbon transporter that uptakes HCO_3^- and operates using Na+ gradient. Some photoautotrophs such as *Synechocystis* PCC6803 use this transporter under inorganic carbon limitation [206]. For example, BicA has a low affinity for bicarbonate but high

flux rate, whereas SbtA has a medium affinity but low flux rate. The meaning of the affinity here is the desire of the cells in consumption of a specific form of inorganic carbon, indicating that cells modify their transport mechanism to more efficiently uptake inorganic carbon after habituation to low CO_2 environment rather than increasing the number of their transport components [207].

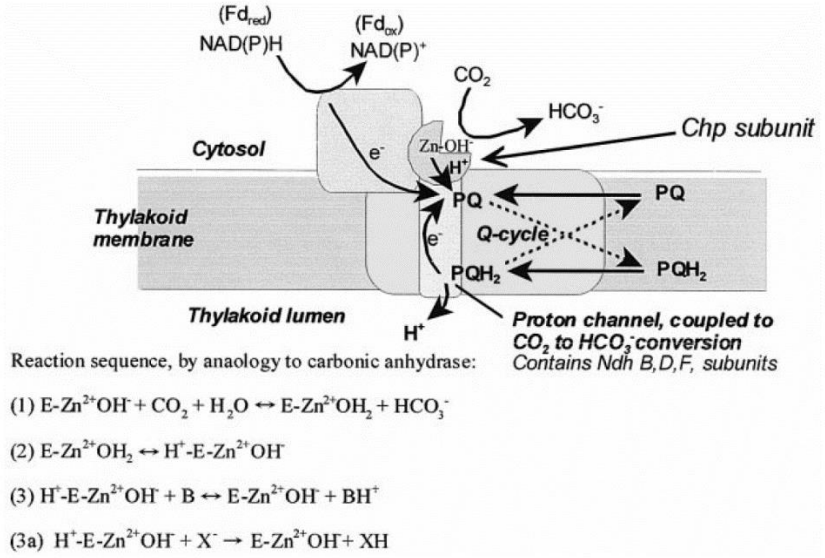

Figure A7. A speculative model for the functioning of a specialized NDH-$1_{3/4}$ -type complex to hydrate CO_2 to HCO_3^-. The hydration is coupled to electron flow such as that supported by PSI cyclic electron transport. The model is based on the proposal of Price et al. (2002) [205]. It is postulated that ChpX and Y subunits are CO_2 hydration proteins bound to the cytoplasmic face of NDH-$1_{3/4}$ complexes. The NdhF4/F3 and NdhD4/D3 subunits form part of the proton translocation channel. This specialized NDH-1 complex is proposed to drive the net hydration of CO_2 to HCO_3^- when coupled to photosynthetic electron transport. Here both NADPH and Fd_{red} are depicted as being potential electron donors to the NDH-$1_{3/4}$ complexes. The energetics of CO_2 conversion may be further improved through the operation of a Q cycle similar to that operating in the *bf* complex. Equations 1-3 (in the figure A7) describe the reaction sequence proposed to occur in conventional CA enzymes (E); the steps are (1) generation of a reactive hydroxyl group combined with spontaneous conversion of CO_2 to HCO_3^-, (2) binding a water molecule to Zn and (3) abstraction of a protons to a nearby His residue and then conduction along a proton wire to a buffer molecule (B) in the bulk medium. The essential part of this proposal is that the last step (3a) be coupled to electron-driven translocation of protons to the thylakoid lumen, making hydroxyl-mediated net hydration of CO_2 largely irreversible in the light [204].

The thylakoid-located NDH-1 dehydrogenase complex is a key component of the cyclic-electron-transfer around photosystem I pathway and involved in enabling CO_2 uptake by photoautotroph. NDH-1_3 and NDH-1_4 (NDH-$1_{3/4}$) are two specialized forms of a thylakoid-located NDH-1 complex. They can directly uptake dCO_2 and convert it to HCO_3^-. NDH-1_3 is a constitutive system for dCO_2 uptake and NDH-1_4 is inducible at limited inorganic carbon conditions and exhibits a higher uptake affinity for dCO_2 [208]. This unit uses electron, which takes it from NADPH and Fd_{red} (reduced ferredoxin), to operate [205]. A potential reaction sequence for the conversion of CO_2 to HCO_3^- is shown in Figure A7 and explained in the legend [204].

It is worth mentioning that even though these transporters are common and general between most of photoautotrophs but still the existence of them can be different depending on the species (species selection). For example, there are two main groups of cyanobacteria: α-cyanobacterial and β-cyanobacterial species, and the combination of mentioned transporters is different between them. There may be a number of distinct types of NDH-1 complexes (NDH-1_4 and NDH-1_3) within the cell of β -cyanobacterial species; however, some of α -cyanobacterial are lacking NDH-1_3. The bicarbonate transport systems in α-cyanobacteria also may be quite different from β-cyanobacteria. BCT1 and sbtA transporters are absent in *Prochlorococcus*, which is a marine α-cyanobacteria. This suggests that different types of HCO_3^- transporters have evolved independently between α and β cyanobacteria, since all have at least one type of dCO_2 transporter and they diverged in their evolution prior to the development of the HCO_3^- uptake system [204,209]. The difference between CO_2 and HCO_3^- transport systems in photoautotroph species also can be explained by the differences between high and low affinity transport systems.

Any difference between transport systems makes an inorganic carbon more favorable for growth. For example, the ability of chloroplast on taking up dCO_2 and HCO_3^- at high and low $\%CO_2$ for

two algae strains *C. reinhardtii* and *D. tertiolecta* has been studied [207]. The results provided enough evidence that chloroplast from both algal species are able to transport CO_2 and HCO_3^- simultaneously, regardless of the CO_2 concentration provided during growth. However, each species prefers one inorganic carbon type more depending on its CCM. *C. reinhardtii,* photosynthesis was supported by taking up both dCO_2 and HCO_3^- at the same percentage over the entire range of inorganic carbon concentration. And for *D. tertiolecta,* HCO_3^- seemed to be the more dominant substrate, with utilization of dCO_2 and HCO_3^- with contribution of 20% and 80% respectively.

A.4.2 Carbon dioxide uptake mechanism at high and low CO_2 percentage

To answer in detail the question why some cyanobacteria and microalgae cannot tolerate high CO_2 concentration conditions (>50 $\%CO_2$), one might look at the CCM. Under high $\%CO_2$, and as a result low internal pH, rubisco will be inhibited due to hindering the photosynthesis electron transport chain [202]. It is believed that high $\%CO_2$ tolerance of photoautotrophs is achieved by preventing acidification of the cytoplasm to maintain sufficient activity of the Rubisco, the enzyme involved in the first major step of carbon fixation. This happens by 1- increasing ATP generation which is spent on maintaining a suitable pH by active transport, 2- turning off/on the CCM operation rapidly and reversibly, 3- adjusting in lipid metabolism for optimal balance of source and sink under stressful conditions, as well as for swift rearrangements of photosynthetic apparatus membranes [210]. This can be shown in a mutant version of cyanobacteria where the constitutive and inducible CO_2 uptake/conversion systems are blocked, and the strain can just uptake HCO_3^-. Such mutant can grow at high CO_2 concentrations but not under CO_2-limiting conditions [202]. With certain photoautotroph species, the addition of bases such as NaOH to compensate for CO_2

acidification enhances CO_2 tolerance. Photoautotroph growth can be sustained even at 100% CO_2, suggesting that it is mainly acidification that inhibits photoautotroph growth [199]. At very low $\%CO_2$ (<50ppm CO_2), photoautotrophs activate inducible transport systems (HCO_3^- transporter) and increase in Rubisco activity and carboxysome content. Furthermore, when there is enough dCO_2 (high CO_2 concentrations), cells preferentially take up inorganic carbon directly using dCO_2 rather than HCO_3^-. The conversion of CO_2 during transport to cytosol produce H^+ that need to be neutralized, possibly via export to the medium [202].

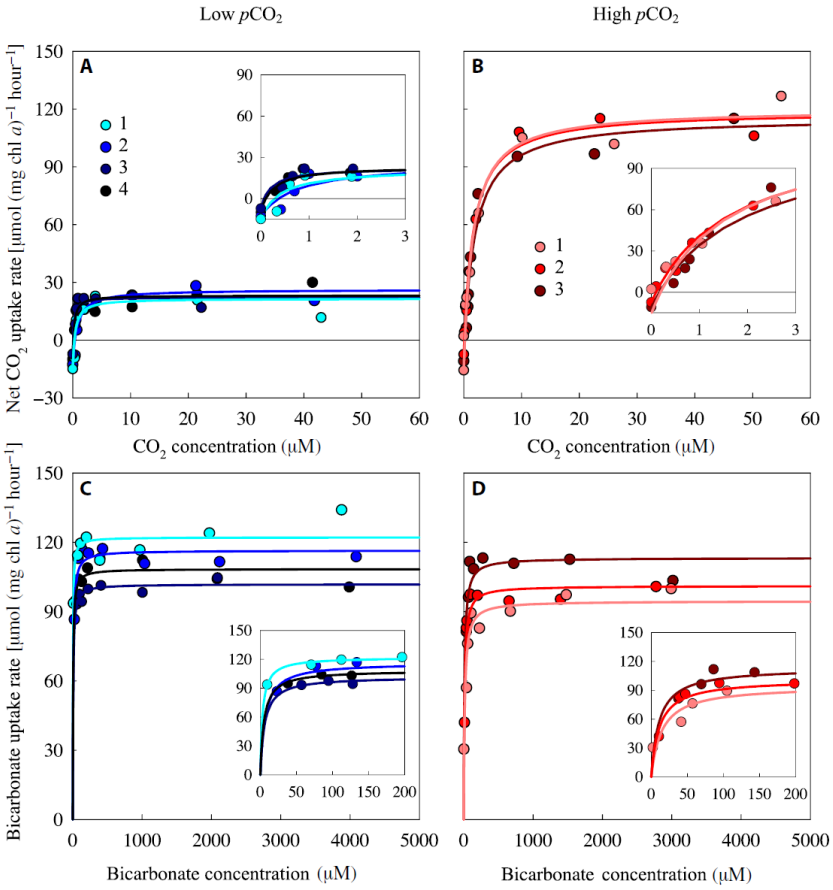

Figure A8. Carbon uptake kinetics of *Microcystis* PCC 7806 acclimated to either low or high $\%CO_2$. (A and B) Net CO_2 uptake rate as function of the dCO2 concentration, after acclimation to (A) low $\%CO_2$ and (B) high $\%CO_2$. (C and D) Bicarbonate uptake rate as function of the bicarbonate concentration, after acclimation to (C) low $\%CO_2$ and (D) high $\%CO_2$. Carbon uptake kinetics were measured after ~20 days of acclimation to the steady-state conditions in the chemostats. Measurements were replicated fourfold at low $\%CO_2$

and threefold at high %CO_2, as indicated by the different colors. Lines are Michaelis-Menten fits to each of the replicates [203].

In general, after acclimation to high %CO_2, photoautotrophs have achieved a higher maximum dCO_2 uptake rate and a lower HCO_3^- uptake rate and produced more biomass, than before habituation. For *Microcystis* PCC 7806 and *Trichodesmium erythraeum* IMS101 the maximum dCO_2 uptake rate was more than five time higher at high %CO_2 than at low %CO_2 as shown by Ji et al. 2020 in Figure A8. Moreover, it produced much higher steady-state biomass at high than at low %CO_2. However, the maximum HCO_3^- rate was not significantly affected by CO_2 percentage. A similar phenomenon happened for *Microcystis* PCC 7941, *Synechocystis* PCC 6803, and *Synechococcus* PCC 7942 that the maximum dCO_2 uptake rate was 1.8 times higher, whereas the maximum HCO_3^- rate was 40% lower at high percentage of CO_2 than at low %CO_2. To explain the phenomena in more details, at low %CO_2, strains relied 100% on HCO_3^- uptake and the net dCO_2 uptake rate was negative in the experiments at steady states, since the dCO_2 concentration was depleted. From the other side, carbon fixation in the high pCO_2 experiments relied ~50% on dCO_2 uptake and ~50% on HCO_3^- uptake [203].

The change of HCO_3^- uptake rates of the strains in response to high %CO_2 are different which may be related to different composition of their HCO_3^- uptake system. The photoautotrophs in which maximum HCO_3^- uptake rates were reduced at high %CO_2 all contain the low-flux bicarbonate transporter SbtA, whereas photoautotrophs in which maximum HCO_3^- uptake rates did not respond to changes in %CO_2 all contain the high-flux bicarbonate transporter BicA but lack SbtA. This absent of the high-affinity HCO_3^- uptake system SbtA makes the strain a poor competitor at low %CO_2 (inorganic carbon-limited) conditions [203]. Previous results have shown the high affinity HCO_3^- uptake system BCT1 is strongly down regulated at high %CO_2 (high dCO_2 concentration), which is a reasonable response in the view of the energetic costs as the HCO_3^-uptake system is an

ATP dependent system and energetically quite expensive. This clearly explains the low HCO_3^- uptake efficiency at high $\%CO_2$ when higher dCO_2 is accessible.

Dense cyanobacterial blooms often deplete dCO_2 concentration in the surface of water since the $\%CO_2$ in the air above the surface is only about 0.04%. This dCO_2 depletion increase the pH value to above 9 or even 10. At these pH values, most of DIC is in bicarbonate and carbonate form. Cyanobacteria have developed an efficient way to uptake the remaining bicarbonate as an inorganic carbon source at this low $\%CO_2$ condition [211]. This preference for different inorganic carbon components has been explained by the environmental conditions of past generations such as under high or low pH, salinity and HCO_3^-:CO_2 ratio in the medium. Thus, cells can adapt and modify their inorganic carbon transport system after acclimation to the environment for several generations.

A.5 Discussion

The results presented in this paper indicate that photoautotrophs prefer up-taking dCO_2 since it is less expensive for cells. However, high amount of dCO_2 can inhibit the growth of the cells since dCO_2 reduces the pH of outside and inside the cells. Therefore, only the habituated species with low pH and the species with more efficient transport system for dCO_2 can grow at high dCO_2 concentration.

And finally, by looking into evolution of the cyanobacteria, the mechanism of uptaking of dCO_2 and HCO_3^- will be much clearer. Cyanobacteria first just had the ability to consume dCO_2. However, they evolved to be more efficient and additionally consume HCO_3^- in order to take enough carbon. Nevertheless, they preferred utilization of dCO_2 since there is no cost for the cells to uptake it.

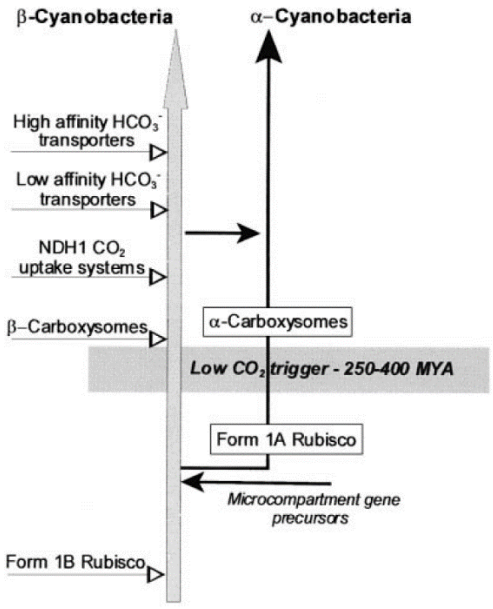

Figure A9. A speculative pathway for the evolution of the CCM and its components in α and β-cyanobacteria [204].

Past atmospheric CO_2 levels were 100 times higher than current conditions when cyanobacteria first arose. Moreover, O_2 level was much lower, which means the original cyanobacteria would not need a CCM system to uptake inorganic carbon and achieve effective photosynthesis. This changed and triggered cyanobacteria developing a CCM when the concentration of CO_2 and O_2 in the atmosphere had changed and caused CO_2 to be a limiting factor for photosynthetic activity and accordingly the Rubisco oxygenase reaction to become a main issue. There is no clear record of CO_2 and O_2 level before about 600 million years ago, however it has been inferred that O_2 was near the same and CO_2 level have been 20 times more than present day conditions [209].

In the initial stage of declination of CO_2 level, the first step for developing a CCM was construction of a carboxysome for Rubisco (Figure A9). This structure was the main component of CCM that all other additions would have revolved around. A carboxysome carbonic anhydrase was required to convert HCO_3^- to CO_2 at higher rates. The development of the NDH-1 based low and high affinity CO_2 uptake systems started as the CO_2 limitation became more severe. These systems

maintained enough HCO_3^- inside the cells and provided adequate CO_2 levels around Rubisco in the carboxysome [204]. The processes for development of these systems have been based on the modification of an existing respiratory NDH-1 complex to efficiently recycle the leaked CO_2 as well as net acquisition of CO_2 from outside the cell. And finally, as more extreme CO_2 limitation happened, the cells evolved the low and high affinity bicarbonate uptake systems.

B. Comparative study of oxygen-limited and methane-limited growth phenotypes of *Methylomicrobium buryatense* 5GB1

Kyle Stone*, Matthew Hilliard, Kiumars Badr, Alisabeth Bradford, Q. Peter He and Jin Wang

* Currently employed as a Bioprocess Development Scientist at Dupont.

Highlights

- O_2 partial pressure determines the cell growth rate for batch growth;
- Cell growth rate has to be controlled to achieve different phenotypes;
- For continuous culture, cells' prior growth condition affects current physiology;
- Carbon-limited growth condition produces more organic compounds;
- The current GEM lacks key metabolic routes to explain different phenotypes.

Abstract

Methylomicrobium buryatense 5GB1 has been identified as a promising biocatalyst for industrial methane conversion to produce value-added products. However, despite recent advancements in understanding the metabolism of 5GB1, existing knowledge on the differences between oxygen-limited and methane-limited phenotypes is still limited. In this work, both batch and continuous experiments were carried out to systematically examine the strain's oxygen-limited and methane-limited phenotypes. Total carbon balances were performed to ensure the obtained measurements of CH_4 and O_2 consumption rates and CO_2 production rate were accurate. Our results showed that the feed gas composition alone does not dictate the strain's growth phenotype. In order to achieve a desired phenotype, both feed gas composition and cell growth rate have to be controlled. In addition, contrary to the common belief that oxygen-limited conditions lead to increased production of organic compounds, our results suggest that it is the methane-limited condition that has higher yield for organic compounds. Knowledge of these differences could provide key

understanding into how *M. buryatense* 5GB1 regulate its carbon flow among different pathways under different growth conditions, which will provide the key insights for both mutant design, and process design (e.g., culture conditions) for desired outcomes such as increased production of organic acids. Finally, using data collected in this work and those published in literature, we further validated a published genome-scale model under optimal growth condition. In addition, our results suggest that the current model lacks key metabolic routes to explain the surprisingly robust growth exhibited by the strain under wide substrate availability conditions.

Keywords: Methanotroph, *Methylomicrobium buryatense*, Methane metabolism, Methane-limited growth, Oxygen-limited growth, genome-scale metabolic model, carbon balance

1. Introduction

Methane (CH_4) is the second most abundant greenhouse gas (GHG), whose global warming potential is 72 times that of CO_2 within a 20 year period [1,2]. At the same time, CH_4 is a low-cost,rich source for carbon and energy, and an essential component of the global carbon cycle. Currently, CH_4 is mainly used for heating, cooking and electricity generation. In its compressed form, CH_4 can be used as a transportation fuel; however, such usage is constrained owing to its inherently low volumetric energy density and the lack of infrastructure required for its broader adoption. Therefore, it is desirable to convert CH_4 into other forms of liquid fuels. The dominant route for conversion of CH_4 into transportation fuels involves thermochemical gas-to-liquid (GTL) conversion technologies and subsequent conversion via the Fischer-Tropsch (FT) process. However, the technical complexity of the GTL-FT process results in exceptionally large-scale facilities (>$20 billion capital cost per facility) that cannot be economically scaled down [3], and therefore are not suitable for smaller, distributed biogas sites and natural gas wells.

In contrast to the thermochemical processes, microbial conversion of CH_4 at ambient temperatureand pressure is an attractive alternative, particularly for small scale conversions [4–6]. As a result,methanotrophs that use CH_4 as their sole carbon and energy source have drawn renewed interest due to their capability of converting CH_4 under ambient conditions in an environmentally benign fashion. Strong et al. provides a comprehensive review on the array of valuable bioproducts that could be produced by methanotrophs using natural gas or biogas as feedstock [7]. Among differentmethanotroph species, *Methylomicrobium buryatense* 5GB1 has been identified as a promising biocatalyst for industrial CH_4 conversion due to the following reasons. First, it is a fast-growing methanotroph, with a demonstrated growth rate of 0.224-0.239 h^{-1} [8]; second, it is not easily susceptible to contamination due to its haloalkaliphile nature (*i.e.*, it prefers a high pH, high salt growth condition) [8,9]; third, it is an unusually robust strain that can withstand a wide range of growth conditions [8]; finally, a suite of genetic tools and a genome-scale model have also been developed for the strain, enabling further metabolic engineering [9–11]. Recently, some baseline data of *M. buryatense* 5GB1 on its bioreactor performance as well as transcriptomic and ^{13}C labeling-based analyses have been reported [8,12,13]. Specifically, Gilman et al. have reported thestrain's growth performance under both fed-batch and continuous bioreactor runs for balanced growth, one oxygen-limited condition, and one methane-limited condition [8]. Using a modified ^{13}C tracer approach, Fu et al. provided direct evidence that a complete, oxidative TCA cycle operates during methanotrophic growth of *M. buryatense* 5GB1 [13]. Most recently, transcriptomic analysis revealed that *M. buryatense* 5GB1 exhibited very limited differential expression for key genes involved in the central carbon network between oxygen-limited and methane-limited growths, suggesting *M. buryatense* 5GB1 maintains a metabolic staterepresenting a combination of fermentation and respiration

metabolism [12].

These recent findings represent significant advancements towards a better understanding of the type I methanotroph's cellular metabolism; however, existing understanding on the difference of methane metabolism between oxygen-limited and methane-limited growth is still limited. In addition, these recent results were obtained at relatively low cell density and were constrained to a couple of gas substrate compositions, which provided limited insight into the cellular metabolism.In this work, using *M. buryatense* 5GB1 as the model system, we designed a set of experiments tosystematically examine the difference between oxygen-limited and methane-limited phenotypes. This work was made possible by our recently developed analytical protocols that enabled us to obtain accurate measurements of cross-membrane fluxes for gas components under both batch and

continuous operations [14]. Using an in-house developed gas mixing system and our gas measurement protocol, we were able to quantitatively examine the differences between oxygen-limited and methane-limited phenotypes under a wide range of substrate compositions and different cell growth rates, as well as at higher cell densities. Finally, with the measured substrate uptake rates and product secretion rates, we were able to validate a modified genome-scale metabolic model (GEM) under optimal growth conditions. Our experimental data suggest that thecurrent model lacks key metabolic routes to explain the surprisingly robust growth exhibited by the strain under both oxygen-limited and methane-limited conditions.

2. Methods

2.1 Strain handling and cultivation

Methylomicrobium buryatense 5GB1 was provided by Prof. Mary Lidstrom at the University of

Washington and grown in modified nitrate mineral salts (NMS2) medium as described by Puri et al. [10]. The inoculum was prepared by first pre-culturing cells in a 250ml serum vial containing 50mL medium with saturated gas phase of 35% CH_4, 35% O_2 and 30% N_2. These pre-culture vialswere incubated until mid-exponential growth phase in a Lab-Line Orbit Environ-shaker with a rotation speed of 200 rpm and temperature controlled at 30^oC. The vials that exhibited the best growth were harvested, centrifuged and suspended in fresh medium as inoculum.

2.2 Gas mixing system

In this work, a safe gas mixing system was designed to create various custom mixtures of O_2, CH_4, N_2 and He. By controlling the flow rate of each gas through mass flow controllers (MFCs) and funneling them through a static mixer, any feed gas composition can be achieved. Ball valves and check valves are used to prevent backflow of gases. The static gas mixer allows for the turbulent mixture to become uniform before entering the gas inlet for the vials or continuous reactors. A failsafe auto shut-off gas system was installed and consists of a flammable gas detector with a relay that is connected to the electronic MFCs and solenoid valves in the gas lines. In the case of a power failure or flammable gas leakage, the system will automatically shut off all gas flows.

2.3 Batch experiments

All batch growth experiments were conducted in 250 mL serum vials with 50 mL of medium. Before inoculation, the vials were bubbled with feed gas corresponding to the compositions listed in Table B1 for 10 minutes at 200 smL/min to ensure that the liquid phase is saturated with the gas mixture. Then an initial gas sample was taken, and the vials were bubbled with the same gas mixture for another 5 minutes. The prepared inoculum was then injected into each of the vials to create an initial concentration of 0.05-0.06 gDCW L^{-1}. After inoculation was complete, the first

liquid sample was taken, and the time was referred to as t = 0 hrs. After that, liquid samples were taken every 2 ~ 3 hours for the first 10 hours then every 4 hours afterwards during daytime for biomass concentration, total carbon (TC) and total inorganic carbon (TIC) analysis. At the end of the batch, besides the liquid sample, the gas phase is sampled following our recently established protocol [14].

2.4 Continuous experiments

All continuous experiments were conducted in a 3 L Eppendorf BioFlo 115 reactor with working volume of 1.5 L. The experimental setup is shown in Figure S2 in the Supplementary Information. Based on our prior study [4], agitation was kept at 500 rpm to achieve maximum mass transfer from gas to liquid, which avoids over-agitation effects while maximizing the rotational bubble flow for efficient gas transfer [15]. For different feed gas compositions (with N_2 as the balancing component), the gas mixing system delivered a constant flow of 300 smL min^{-1} through a microsparger. The temperature of the off-gas was measured via the online probe and software from Vernier Software and Technology. The BioFlo unit temperature was maintained at 30^{o}C and pH maintained at 9 via addition of 4 M NaOH. Struktol J 660R was used as antifoam. The antifoam was pumped in with New Era syinge pump at a flow rate of 18 µL h^{-1} to 24 µL h^{-1}. The culture medium was similar to the standard NMS2 medium, except with a higher concentration of nitrate (2×) and trace element solution (2×). The medium did not include carbonate buffer, as the pH wasmaintained via the BioFlo unit.

After inoculation, the bioreactor was operated under batch mode (with continuous gas feeding) to accumulate biomass and switched to continuous mode the next day. For each growth condition, once a steady-state was achieved, it was maintained for at least three days to allow multiple data points to be collected. If a variation of larger than 10% was observed in the data,

the steady-state was maintained for an additional day, after which the culture condition was switched to examine a different condition. In total, six steady-state growth conditions were examined, which consists of 3 different cell growth rates (controlled via dilution rate), and two feed gas compositions. The feed gas that contains 14% CH_4 (42sml/min) and 22.3% O_2 (70 sml/min) is denoted as the methane-limited condition; while the feed gas that contains 14% CH_4 (42sml/min) and 11.7% O_2 (35 sml/min) is denoted as the oxygen-limited condition. After inoculation, samples were taken 4-5 times a day during daytime every 3 ~ 4 hours. Both off-gas and liquid samples were taken and analyzed as described below.

Two independent continuous runs were performed. In continuous experiment #1 (CE1), the 6 steady-state conditions were examined in sequence according to the order given in Figure 4 (a) (Sec. 3.2.1). In continuous experiment #2 (CE2), 6 conditions were examined again in a different order: 2→3→6→5→4→1 (Supplementary Figure S3).The conditions tested in different runs are the same 6 conditions, but these conditions were carried out in different orders in order to test thehypothesis that the cells' prior growth condition has a noticeable effect on their current physiological state.

2.5 Measuring the amounts and rates of gas component consumption and production

The total amount of consumption/production (for batch culture) or consumption/production rates (for continuous culture) of the gas components (*i.e.*, CH_4, O_2 and CO_2) were determined following the developed protocols [14]. For batch experiments, a repressurization procedure was implemented to obtain accurate gas compositions, and the mass balances between the beginning and end of the batch experiment were conducted to calculate the gas consumption and production amounts. For continuous experiments, helium gas was used as an internal standard to accurately estimate the off-gas flow rate. Mass balances between different sample points were conducted to

calculate the gas component uptake rates and excretion rates. Due to the high pH condition, the majority of CO_2 is dissolved in the liquid phase, therefore, TIC was included in the calculation of the CO_2 production rate. Details of the developed protocol can be found in our previous work [14]. Gas samples (for batch experiment) and off-gas samples (for continuous experiment) were analyzed by a customized Agilent Technologies 7890B GC system equipped with a FID/TCD at 250^{o}C for CH_4, O_2, He and CO_2 concentrations.

2.6 Analysis of liquid samples

For liquid samples, biomass concentration, total organic carbon (TOC) and total inorganic carbon (TIC) were measured to track cell growth and production of organic compounds and CO_2. Total carbon (TC) and TIC of the liquid samples were analyzed via a Shimadzu TOC-VCSN analyzer. TOC was obtained by subtracting TIC from TC. Cell biomass was measured via a Beckman Coulter DU Life Science UV/Vis spectrophotometer. It is worth noting that it would be useful to determine the constituents of the TOC (*e.g.*, acetate, formate, etc.) using HPLC. However, the acetate amount was very small and its peak was crowded with the formate peak; therefore, it was not possible to determine the individual concentrations of acetate and formate. In addition, there were a large peak and a few smaller peaks that we could not associate with known metabolites. However, our results suggest that extracellular polysaccharides (more likely some kind of glycoprotein) represent the majority of the excreted organic compounds (M. Lidstrom, personal communication). For these reasons, we decided to report the TOC to account for the variety of organic carbon sources.

2.7 Metabolic network modeling and flux balance analysis

The metabolic network model of *M. buryatense* 5GB1 used in this study was derived based on a published GEM, iMb5G(B1) [9]. The stoichiometric matrix for the model was reduced by Prof. Marina Kalyuzhnaya's group at San Diego State University, with futile cycles and non-expressed

reactions removed. Further modifications made in this work include the following: the production of various organic acids were decoupled from biomass production, so that they can be freely excreted by the model, and the fermentation reactions reported in [12] were added to the model. After these modifications, the modified GEM consists of 442 reactions, 403 metabolites, 313 genes, 3 compartments (extracellular, periplasm, cytosol).

For the model used in this work, similar to iMb5G(B1), aerobic respiration was represented by a single summarization reaction where the ATP/NADH yield was assumed to remain at 3 as shown in Eqn. (B1).

$$2NADH/H^+ + O_2 + 6\ ADP + 6\ P_i + 8H^+ \leftrightarrow 2NAD^+ + 8H_2O + 6ATP \quad \text{(B1)}$$

Only direct coupling methane oxidation, *i.e.*, electrons produced in methanol dehydrogenase (MDH) reaction are supplied to methane monooxygenase (MMO), was evaluated in this study as redox arm and uphill transfer are far less efficient and the model prediction did not match experimentally measured growth rates [9]. The ratio of flux through the Embden–Meyerhof–Parnas (EMP) and Entner-Doudoroff (ED) pathways was left at the default 0.75/0.25 ratio.

Flux balance analysis (FBA) [16]was performed using the modified GEM to compare the model predictions with experimental measurements. In FBA, cellular metabolism is assumed to be in a quasi-steady state, as the dynamics of gene-regulations are considered to be significantly faster than that of the bioreactor. Therefore, mass balance equations can be established for all intracellular metabolites in the GEM, yielding a linear system of equations. In most applications of FBA, a biomass growth equation is developed to represent the production of metabolic constituents of the cellular biomass, and most often, this biomass growth equation is set as the objective function for the linear program. Finally, FBA uses linear optimization to identify solution sets that maximize the objective function (e.g., biomass growth rate) subject to the constraints

imposed on the model. In this work, the objective function for all *in silico* simulations using FBA was biomass production. Constraints imposed on the model include: methane uptake rate, oxygen uptake rate, non-growth associated ATP maintenance (NGAM), and growth associated ATP maintenance (set to 23.3 [9] unless otherwise noted). The GEM predicted cell growth rate and CO_2 production rate were compared with experimental measurements to validate the GEM.

2.8 Determining the non-growth associated ATP maintenance energy (NGAM):

In this work, we use the following relationship given in [17] to estimate the NGAM value.

$$q_{CH_4} = m_{CH_4} + \frac{\mu}{Y_{max}} \quad \text{(B2)}$$

where q_{CH_4} is the methane uptake rate; m_{CH_4} is the methane requirement for non-growth associated maintenance activity; Y_{max} is the maximum biomass yield including NGAM, and μ is the cell growth rate. The result clearly shows that the six conditions separate into 2 groups, corresponding to oxygen-limited and methane-limited conditions, respectively. Assuming an ATP yield of 6 mol ATP per mole of CH_4 consumed, NGAM can be calculated based on estimated m_{CH_4}. It is interesting to note that the NGAM obtained from different continuous runs are slightly different, especially for methane-limited growth. For CE1 the NGAM were estimated to be 15.53 and 10.60 mmolATP/(gDCW·hr) for methane-limited and oxygen-limited phenotypes respectively, while the values changed to 10.93 and 9.88 mmolATP/(gDCW·hr) for CE2.

3. Results and discussions

3.1 Batch culture

3.1.1 The effect of oxygen concentration on cell growth

In the literature it has been suggested that there exists an optimal feed gas composition, *i.e.*, O_2:CH_4 ratio, which enables the maximum growth rate for methanotrophs; however, our previous experiments have suggested that it is the concentration or partial pressure of O_2, not the ratio of

O_2:CH_4 in the feed gas, that plays a dominant role in determining cells' growth rate [78]. To confirm this, we designed two sets of vial experiments to examine *M. buryatense* 5GB1 growth under different headspace compositions. The initial pressure of the headspace was 1 atm for all vials, and the headspace compositions (in terms of partial pressures in atm) are listed in the top part of Table B1 (*i.e.*, Sets 1 & 2). N_2 was used as the balancing gas making up to 100% of mole fraction and 1 atm total pressure. For each condition, batch growth experiments were carried out with triplicate vials.

Table B1 Experimental conditions for Sets 1-4 (pO_2 and pCH_4 are partial pressures of O_2 and CH_4 in atm respectively). For vials that have $pCH_4 + pO_2 < 1$, N_2 was added to achieve a total pressure of 1 atm.

Set	Fixed	pCH_4	O_2:CH_4
1	pO_2=0.4	0.20	2:1
		0.30	1.33:1
		0.40	1:1
		0.60	0.67:1
	pO_2=0.6	0.20	3:1
		0.30	2:1
		0.40	1.5:1
2	pO_2=0.3	0.28	1.07:1
		0.36	0.83:1
		0.45	0.67:1
	pO_2=0.55	0.28	2:1
		0.36	1.53:1
		0.45	1.22:1
Set	**Fixed**	**pO_2**	**O_2:CH_4**
3	pCH_4=0.35	0.35	1:1
		0.42	1.2:1
		0.56	1.6:1
		0.63	1.8:1
4	pCH_4=0.2	0.20	1:1
		0.40	2:1
		0.60	3:1
		0.80	4:1

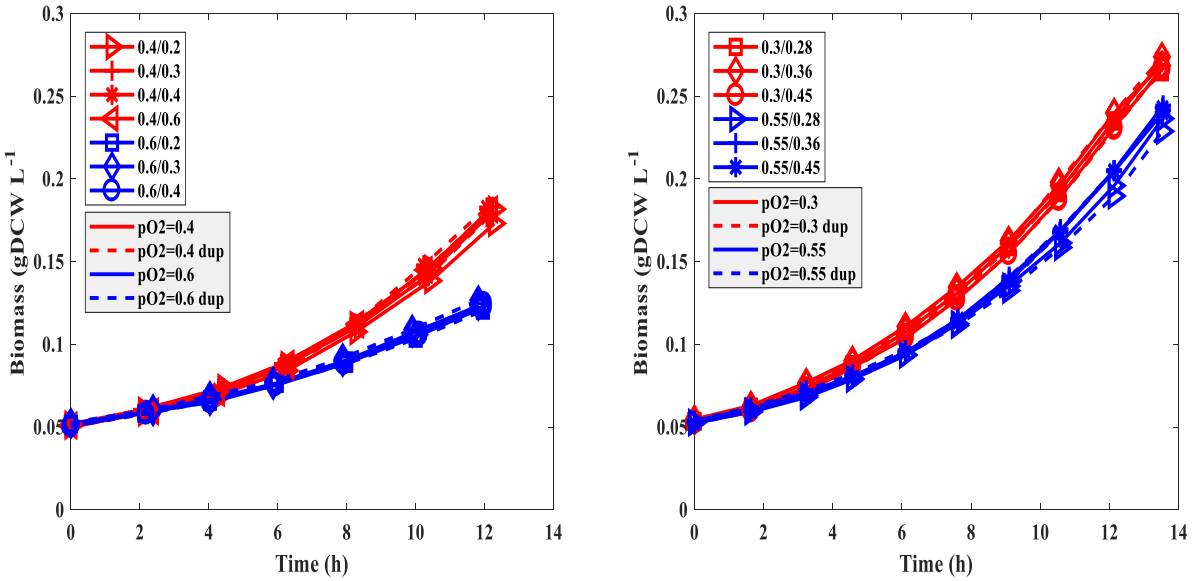

(a) (b)

Figure B1. Growth curves for experiments from Set 1 (a) and Set 2 (b). Red and blue lines in (a) denote experiments with pO_2=0.4 atm and pO_2=0.6 atm respectively, while different symbols correspond to conditions with different pCH_4, which does not make a significant difference in cell growth. Similarly, red and blue lines in (b) represent growth curves with pO_2=0.3 atm and pO_2=0.55 atm respectively, while different symbols correspond to different pCH_4.

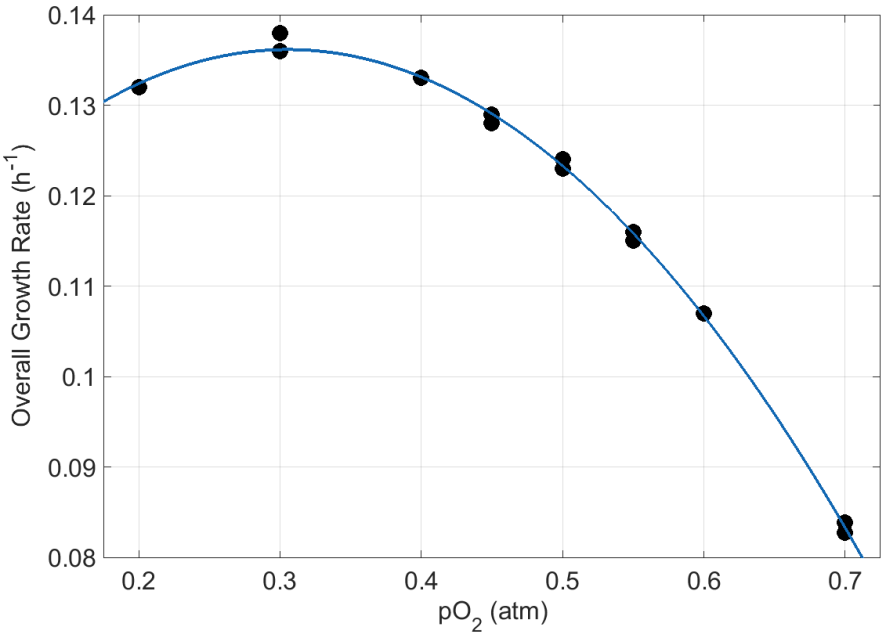

Figure B2. Overall growth rates vs oxygen partial pressure from additional experiments. The overall growth rates determined for each vial in the duplicate sets are represented as black dots while the trend line illustrates the overall behavior observed.

As shown in Table B1, experiments in Sets 1 and 2 consist of pair-wise headspace compositions with subgroups where each subgroup shares the same O_2 partial pressure but different CH_4 partial pressures. The headspace composition in these experiments covered a wide range of O_2:CH_4 ratios, from 0.67:1 to 3:1. The biomass accumulations for the first 12 hours, while cells were still in the exponential growth phase, are plotted in Figure B1(a) and 1(b) for Set 1 and Set 2 respectively. The results clearly indicate that the oxygen concentration (or partial pressure) in the feed gas is the dominant factor that dictated how fast cells grew during the exponential growth phase, and the slower cell growth rates at higher oxygen concentrations were most likely due to oxygen inhibition [7, 18]. In addition, compared to the oxygen concentration, the methane concentration or O_2:CH_4 ratio of the feed gas, had a much smaller effect on cell growth rate. Additional experiments were conducted to determine the range of oxygen partial pressures that would deliver optimal cell growth. The results are given in Figure B2, where pCH_4=0.2 for all conditions. From the conditions tested, pO_2=0.2~0.4 atm enabled optimal cell growth (pO_2 less than 0.2 atm was not tested).

3.1.2 The effect of feed gas composition on cell growth phenotype

Regarding the effect of feed gas composition on the cell's growth phenotype, it is commonly assumed that different feed gas compositions would result in different growth phenotypes, which would be distinguished by different product distributions. To confirm this, two additional sets of experiments (Sets 3 & 4 in Table B1) were designed with each set sharing the same CH_4 partial pressure but different O_2 partial pressure. After cell growth ceased, the yields of three major product groups (biomass, CO_2 and excreted organic compounds) were measured to determine whether the carbon distribution (or phenotype) was affected by the feed gas composition.

In this work, total carbon balances were conducted to confirm the accuracy and reliability of the measurements as well as the validity of the experimental results. Based on the mass balance, it is expected that the amount of carbon consumed ($N_{C,Consumed}$) should equal to the amount of carbon produced ($N_{C,Produced}$). In other words, the total amount of CH_4 assimilated during cell growth should equal to the carbon distributed in different products (*i.e.*, biomass, CO_2 and excreted organic carbon compounds). Therefore, by comparing total moles of carbon consumed with total moles of carbon produced, the accuracy of different measurements can be gauged. Details of the total carbon balance calculation can be found in our recent work [78], and a brief description of the protocol is provide in the Supplementary material.

Across all conditions tested in Sets 3 and 4, total carbon balances were 95.3 $\pm$ 1.8% and 98.9 $\pm$ 1.8% respectively, confirming the accuracy and reliability of the measurements for both batch experiments. For these results, the small deviations from 100% carbon accounted for were attributed to measurement error from the different sample measurements including headspace gas concentrations, biomass concentration, and total (in)organic carbon concentrations. The yields of biomass, CO_2 and organic compounds are shown in Figure B3 (a) for Set 3 experiments (pCH_4 = 0.45 atm), and Figure B3 (b) for Set 4 experiments (pCH_4 = 0.2 atm). As shown in these figures, under all headspace compositions, the yields of biomass, CO_2 and organic compounds remained relatively stable, with 44.96±1.33% for biomass, 49.01±2.00% for CO_2 and 3.23±1.49% for organic compounds.

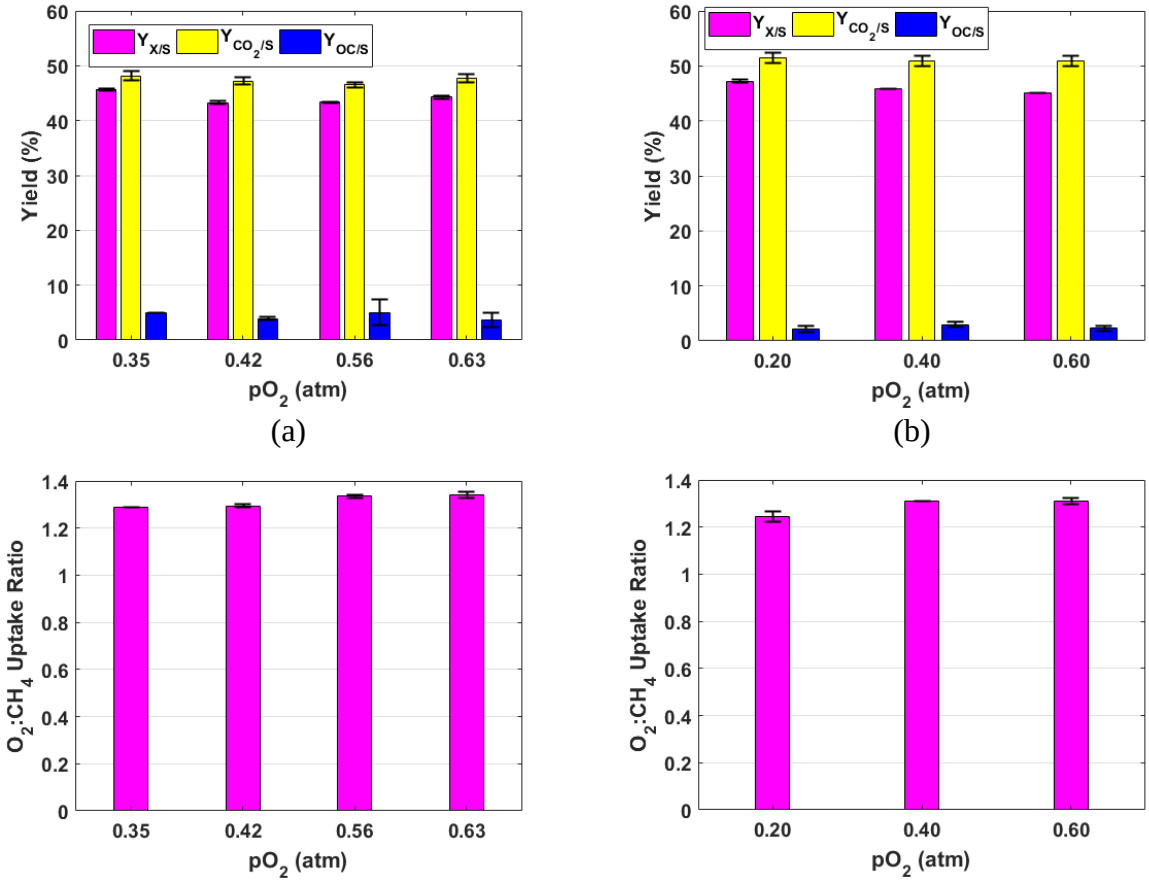

Figure B3: Yields of biomass, carbon dioxide, and organic carbon of the vials under various conditions listed in Table B1 for (a) Set 3 and (b) Set 4. Yields are in mmolC/(mmolCH_4 consumed). (c) & (d) O_2:CH_4 consumption ratios observed for vials in Set 3 and Set 4 respectively.

It should be noted that at the beginning of each batch growth, both methane and oxygen were unlimited due to low cell density. However, about 8 hours after inoculation cell growth rates started to drop, suggesting cell growth became mass transfer limited. Therefore, during the rest of the batch growth (about 27 hours), the availability of CH_4 and O_2 were determined by gas phase composition, and the majority of cell growth occurred under either oxygen-limited or methane-limited conditions. One-way multivariate analysis of variance (MANOVA) was performed to determine whether the O_2:CH_4 ratio in the headspace affects the yields of different products for all experiments in Sets 3 and 4 using Matlab® function *manova1*. In this work, we compare three

oxygen-limited gas compositions (*i.e.*, pO_2 = 0.35 and 0.42 in Set 3, and pO_2=0.2 in Set 4) vs. four carbon-limited gas compositions (*i.e.*, pO_2=0.56 and 0.63 in Set 3, and pO_2=0.4 and 0.6 in Set 4). MANOVA tests the hypothesis that the 3-dimensional mean vectors (*i.e.*, the three product yields) are equal for all experimental conditions versus the alternative hypothesis that one experimental condition (*i.e.*, oxygen-limited or carbon-limited gas composition) resulted in a yield profile that is different from the other in at least one dimension. The returning dimension variable d = 0 and p-value of 0.3956 from *manova1* both indicate that the differences among the yield profiles from the two groups of gas compositions are statistically insignificant at a 99% confidence level.

Further analysis revealed that the largely similar yield distributions from the tested conditions were possibly due to the similar O_2:CH_4 consumption ratios, as shown in Figure B3 (c) and (d), which were also obtained at the end of each batch experiment. In other words, under batch culture conditions, the headspace composition had little effect on the uptake ratio of O_2:CH_4. In addition, it is interesting to note that these uptake ratios were within the range of the optimal uptake ratio predicted by the modified GEM as discussed in section 3.3.1.

The results from all the batch experiments suggest that although the different pO_2 has a dominant role in determining the cell growth rate, it does not appear to dictate the cells growth phenotype; instead, cells grow optimally under batch conditions, regardless of methane-limited or oxygen-limited headspace. This is most likely the primary reason for the stable yield distribution across a wide range of headspace compositions. In order to obtain methane-limited and oxygen-limited growth phenotypes, we hypothesize that the cell growth rate must be controlled, in addition to manipulating feed gas compositions.

3.2 Continuous culture

In this section, we use continuous cultures to achieve oxygen-limited and methane-limited growth phenotypes by controlling both the cell growth rate and the feed gas composition. In addition, we compare the differences between the two phenotypes through yield distribution. In this section, we provide the details of the results obtained from CE1, as the conclusions obtained from CE2 are consistent with CE1. The results from CE2 are provided in Supplementary Information.

3.2.1 Experimental design and outcome

For CE1, the order of the six conditions is shown in Figure B4 (a) with CH_4 fixed at 42 smL/min while O_2 varied between two conditions (*i.e.*, 35 smL/min for oxygen-limited and 70 smL/min for methane-limited) at three different dilution rates. Examining cell growth under three different growth rates (through manipulating dilution rates) for each phenotype enabled a better understanding of methane metabolism and validation of the GEM under much broader conditions. In addition, an estimate of the non-growth associated maintenance energy was obtained with better accuracy.

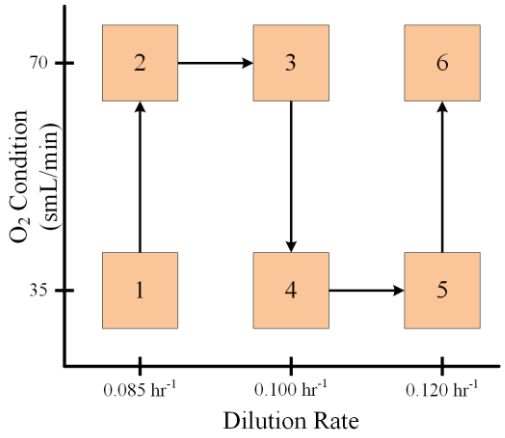

(a)

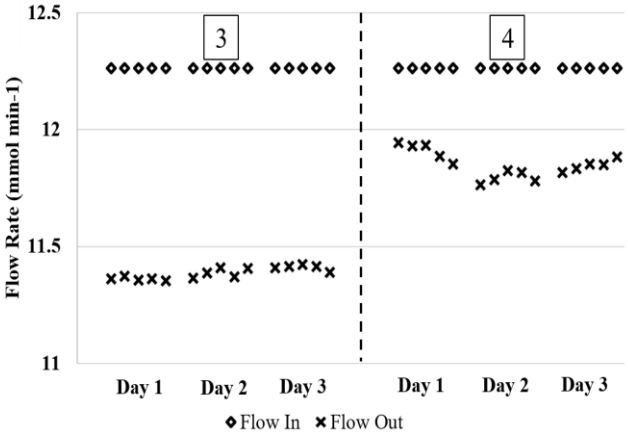

(b)

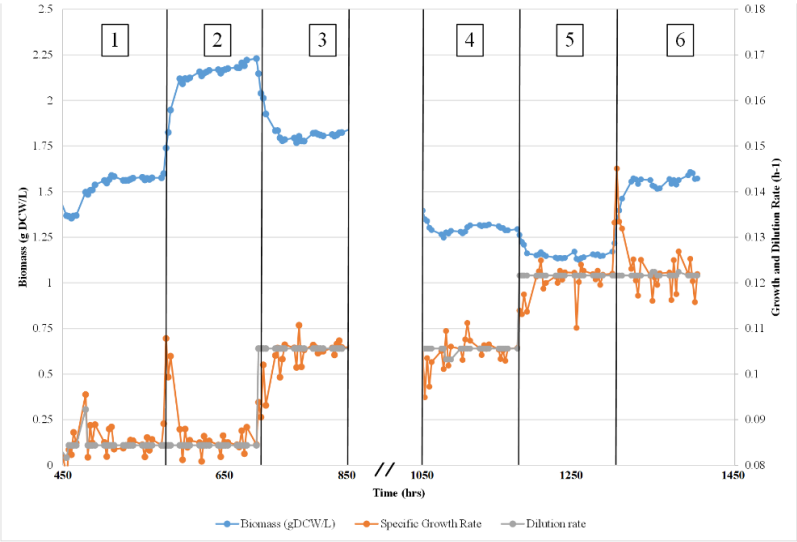

(c)

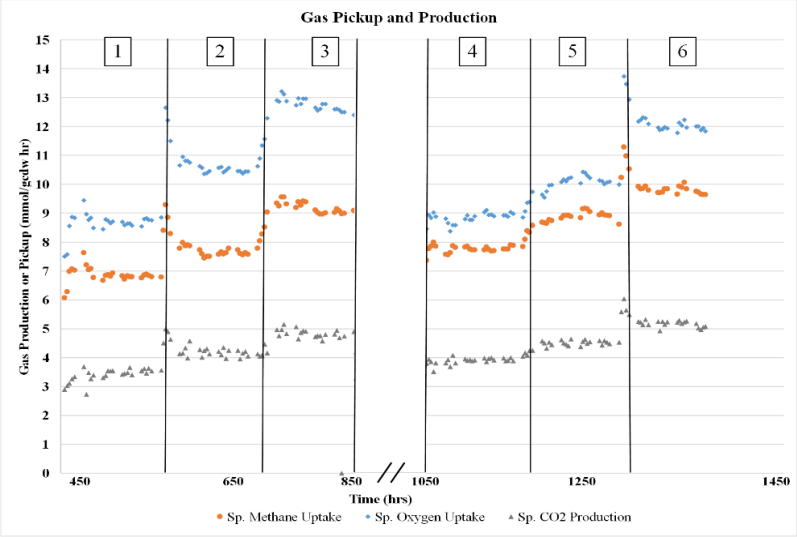

(d)

Figure B4: (a) Overview of experimental design for CE1 with 6 operating conditions: three growth rates (dilution rates) and two gas compositions (oxygen-limited and methane-limited) were tested. (b) Feed gas flow rate and off-gas flow rate for conditions 3 and 4 in CE1. N_2 was added and its flow rate was adjusted to make sure the feed gas flow rate was maintained at a constant rate for all conditions. (c) Biomass density, growth rate and dilution rate for all conditions tested during CE1. (d) Specific gas uptake rates for methane and oxygen, as well as the specific CO_2 production for all six conditions in CE1.

For continuous operation, the off-gas flow rates can be (significantly) different from that of the feed gas due to the consumption of gaseous substrates. To accurately measure the off-gas flow

rate, we have developed a protocol using helium (He) as an internal standard in the feed gas. Further details can be found in our recent work [14]. Figure B4 (b) compares the measured off-gas flow rate with feed gas flow rate for conditions 3 and 4. Figure B4 (b) shows that, as cells transition from methane-limited condition (condition 3) to oxygen-limited condition (condition 4), the off-gas flow rate increased noticeably, indicating less amount of the gas substrates were consumed under condition 4. In addition, the significant differences between the feed and off-gas flow rates for both conditions demonstrate the importance of accurate off-gas flow rate measurements, which play a critical role in computing substrate uptake rates and CO_2 production rates. To ensure that the measurements obtained through the developed protocols are reliable, total carbon balances across different chemostat conditions were conducted, and the carbon accounted for was consistently between 98% ~ 104%, again indicating accurate and reliable measurements of the cross-membrane fluxes.

In Figure B4 (c), the biomass concentration, dilution rate as well as calculated cell growth rate over the course of CE1 are plotted, and in Figure B4 (d) the estimated specific gas uptake or production rates are plotted. The vertical lines in Figure B4 (c) and (d) indicate when the switch of conditions was introduced. In CE1, several unexpected disturbances occurred during 850 – 1050 hours caused by a disruption due to severe weather, so the data for this period was omitted. As shown in Figure B4 (c), there were significant changes in biomass concentration upon transition into different oxygen conditions and/or dilution rates, which is how different cell growth rates could be achieved. For bioconversion with gas substrate(s), mass transfer from gas to liquid is usually the rate limiting step. When the dilution rate is increased or oxygen supply is reduced, cell growth rate would become smaller than the dilution rate and the cell density would decrease due to cell wash-out. As the total amount of CH_4 and O_2 transferred from the gas phase to the liquid

phase remains relatively stable, the specific methane and oxygen uptake rates would increase due to the reduced cell density, which would result in increased cell growth rate. Therefore, as biomass density keeps decreasing, cell growth rate would keep increasing until it matches the dilution rate and reaches the new steady-state. In this way, by adjusting dilution rate and feed gas composition, different cell growth rates can be obtained with different methane and oxygen uptake rates, enabling further examination of the differences between the methane-limited and the oxygen-limited growth phenotypes. As confirmed by Figure B4 (d), a wide range of specific CH_4 and O_2 uptake rates were achieved, which also resulted in changes in the specific CO_2 production rates.

3.2.2 Cells produce more organic compounds under carbon-limited phenotype

Biomass and CO_2 yields for the 6 different conditions are plotted in Figure B5 (a), with yield of organic compounds given in Figure B5 (b). The data is organized according to the feed gas composition: oxygen-limited conditions vs methane-limited conditions. As detailed in Section 3.3.3, phenotype phase plane analysis confirmed that cells under conditions 2 & 3 exhibited a carbon-limited phenotype, cells under conditions 4 & 5 exhibited an oxygen-limited phenotype, while cells under conditions 1 & 6 deviated from their expected phenotypes. In addition, Figure B5 (a) and (b) clearly show that the yield distribution varied within the same phenotype, depending on the carbon (CH_4) uptake rate. To determine whether different growth phenotypes result in different yield distributions pair-wise ANOVA was performed. Based on their carbon uptake rates, condition 2 is paired with condition 4, while condition 3 is paired with condition 5. Note that each pair has very similar CH_4 uptake rates. Separate ANOVA and multiple comparison tests were performed on the yields of biomass ($Y_{X/S}$), CO_2 ($Y_{X/S}$and organic compounds ($Y_{OC/S}$). The tests indicate that there are statistically significant differences between conditions 2 and 4 as well as

between conditions 3 and 5, for all three product yields, as all p-values were less than 0.001 as indicated on Figure B5 (a) and (b).

The yield difference caused by the transitions from condition 1 to 2, condition 5 to 6, as well as condition 3 to 4 were also investigated. It is interesting to see that despite the different yield distributions obtained under the same feed gas conditions (oxygen-limited vs methane-limited), the changes in yield distribution caused by the same environmental perturbation appear to be relatively consistent. During the switch from methane-rich to methane-limited feed gas composition, both transitions (*i.e.*, 1→2 and 5→6) resulted in a decrease of biomass yield (-5.5±0.8% and -4.2±0.7%), increase of CO_2 yield (2.6±1.1% and 2.2±0.8%) and increase of organic compounds yield (2.6±1.2% and 1.6±0.6%). In the reverse direction, the switch from a methane-limited condition to an oxygen-limited condition (*i.e.*, 3→4) resulted in an increase of biomass yield (6.6±0.8%) and decrease of CO_2 and organic compounds yields (-3.2±1.1% and -3.1±1.3% respectively).

The effect of feed gas composition on the consumption ratio between O_2 and CH_4 is plotted in Figure B5 (c). Different from the batch experiments, when cell growth rate is controlled, the feed gas composition had a clear effect on the O_2:CH_4 consumption ratio (Figure B5 c), which decreased from about 1.38 for the two methane-limited conditions (2 and 3) to about 1.13 for the two oxygen-limited conditions (4 and 5). ANOVA and multiple comparison tests were performed to compare the O_2:CH_4 consumption ratio under the different conditions. As shown in Figure B5 (c), the difference between conditions 2 and 3 is not statistically significant at 95% confidence, and neither is the difference between conditions 4 and 5. On the other hand, the difference between methane-

limited conditions (*i.e.*, conditions 2 and 3 combined) and oxygen-limited conditions (*i.e.*, conditions 4 and 5 combined) is statistically significant at 99.9% confidence.

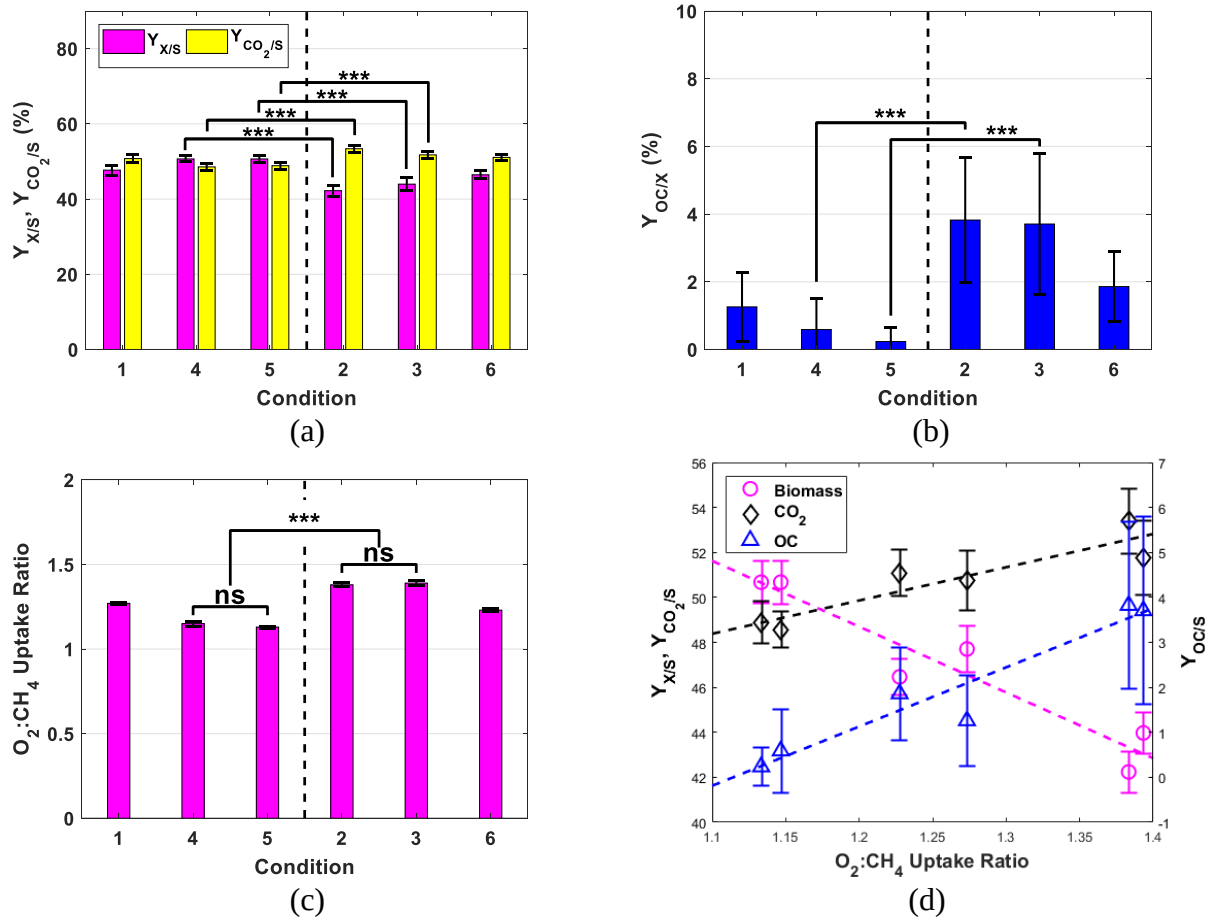

Figure B5: (a) Yields of biomass and CO_2 for conditions 1-6. Note that the order of the conditions does not match the chronological order as they are grouped by the feed gas composition. (b) Yield of organic compounds. (c) O_2:CH_4 consumption ratio. (d) Trends in carbon distribution correlated to the O_2:CH_4 consumption ratio. Biomass yield decreases as the O_2:CH_4 uptake ratio increases as indicated by the trend line. On the other hand, the CO_2 and organic carbon yields increase with the increase in O_2:CH_4 uptake ratio. ANOVA and multiple comparison tests p-values are denoted as: ns (not significant): $P>0.05$; *: $P\leq0.05$; **: $P\leq0.01$; ***: $P\leq0.001$.

Finally, it is important to note that these results suggest that it is the methane-limited condition, not the oxygen-limited condition, that pushes carbon toward the production of organic compounds. Under oxygen-limited conditions, lower yields for organic compounds and CO_2, and a higher yield

for biomass were observed when compared to the methane-limited conditions. This is consistent with Figure B5 (d) where the yields of different products are correlated with the O_2:CH_4 consumption ratios. These finding are confirmed by results obtained from CE2. Clearly the results from CE1 and CE2 indicate that it is the methane-limited phenotype that produces more organic compounds.

Currently, it is not clear why methane-limited phenotype produces more organic compounds and CO_2. It is possibly a result of natural selection, as the natural environment of *M. buryatense* 5GB1 is oxygen-limited and cells have been adapted to process methane more efficiently under oxygen-limited conditions. When excess amount of oxygen becomes available (*e.g.* transition from condition 1 to condition 2), cells are able to pick up more methane (~12% more when condition 2 is compared to condition 1) while maintaining the same growth rate. This suggests that the extra methane consumed by the cells was directed to CO_2 and organic compound production. Such metabolic shift is likely driven by a perturbation to the redox and energy balance as processing more oxygen requires more reducing power and generates more ATP. Further experiments are required to validate this explanation.

3.3 *In silico* analysis using a reduced genome-scale metabolic model (GEM)

To better understand the differences between the oxygen-limited and methane-limited growth phenotypes of *M. buryatense* 5GB1, a modified GEM was used to conduct *in silico* analysis by incorporating the measurements obtained from the continuous culture. One major application of metabolic network models, particularly GEMs, is to predict different growth phenotypes (*e.g.*, how fast cells grow, what products are excreted) in various genetic and environmental conditions. Developed by the Palsson Lab, phenotype phase plane (PhPP) analysis is a powerful tool that uses FBA with the model to provide a global perspective on the genotype-phenotype relationship, and

to help characterize different metabolic phenotypes [19]. In PhPP analysis, FBA is performed along two flux constraint dimensions (for this paper methane uptake rate and oxygen uptake rate), and the FBA results generated are used to construct a 2D or 3D (if growth rate is also considered) phase diagram. In order to conduct FBA with the reduced model, growth and non-growth associated ATP maintenance values are needed. The growth associated ATP maintenance value within the biomass equation was set at 23 ATP g DCW $^{-1}$ [9], which is considered as the low mode. The non-growth associated ATP maintenance (NGAM) was estimated using experimental data as shown in Section 2.8. It is worth noting that methane-limited phenotype requires higher NGAM, indicating higher metabolic burden to the cells. This is consistent with the experimental results of increased production of organic compounds under methane-limited conditions.

3.3.1 Phenotype phase plane analysis

PhPP analysis was performed using the modified GEM with custom scripts developed within the COBRA toolbox [16] framework. The objective function utilized in all *in silico* simulations was to maximize biomass production. For PhPP analysis, the oxygen and methane uptake rates were varied from 0 to 15 mmol/gCDW/hr. In addition to setting substrate uptake rate constraints, the NGAM was set to 10.6 mmolATP/(gDCW·hr) (obtained from CE1 for the oxygen-limited conditions), and the 3D PhPP plot is shown in Figure B6 (a). PhPP analysis reveals only two phenotypes are predicted by the model, which correspond to the two slanted surfaces: the blue surface represents the methane-limited phenotype and the yellow surface represents the oxygen-limited phenotype. The boundary between the two phenotypes (*i.e.*, the black line in the figure) is the line of optimality (LO), which represents the optimal relation between methane and oxygen uptake rates that allow for the maximal growth rate. In other words, along the LO, the optimal

amount of oxygen will be consumed to enable complete oxidation of CH_4 and achieve maximum cell growth.

In Figure B6 (a), methane and oxygen uptake rates corresponding to condition 1 in CE1 are marked. It is interesting to see that condition 1 is located on the LO, indicating that the cells maintained optimal growth under the oxygen-limited feed gas composition. One potential explanation for this unexpected optimal growth is that the cells' prior growth condition may have a significant impact on the new steady-state. Prior to condition 1, cells were cultured under batch mode to accumulate biomass. As discussed in the previous section, under batch operation, the gas phase composition has little effect on O_2:CH_4 consumption ratio, as cells tend to uptake the amount of O_2 and CH_4 to achieve optimal growth. Indeed, as shown later (Figure B8 a) the model predicted optimal cell growth rate and CO_2 production rate for condition 1 also show excellent agreement with experimental data. To further validate the impact of the previous growth condition on the current physiological state of the cells, continuous experiment CE2 was performed. The results of CE2 are further discussed in 3.3.3.

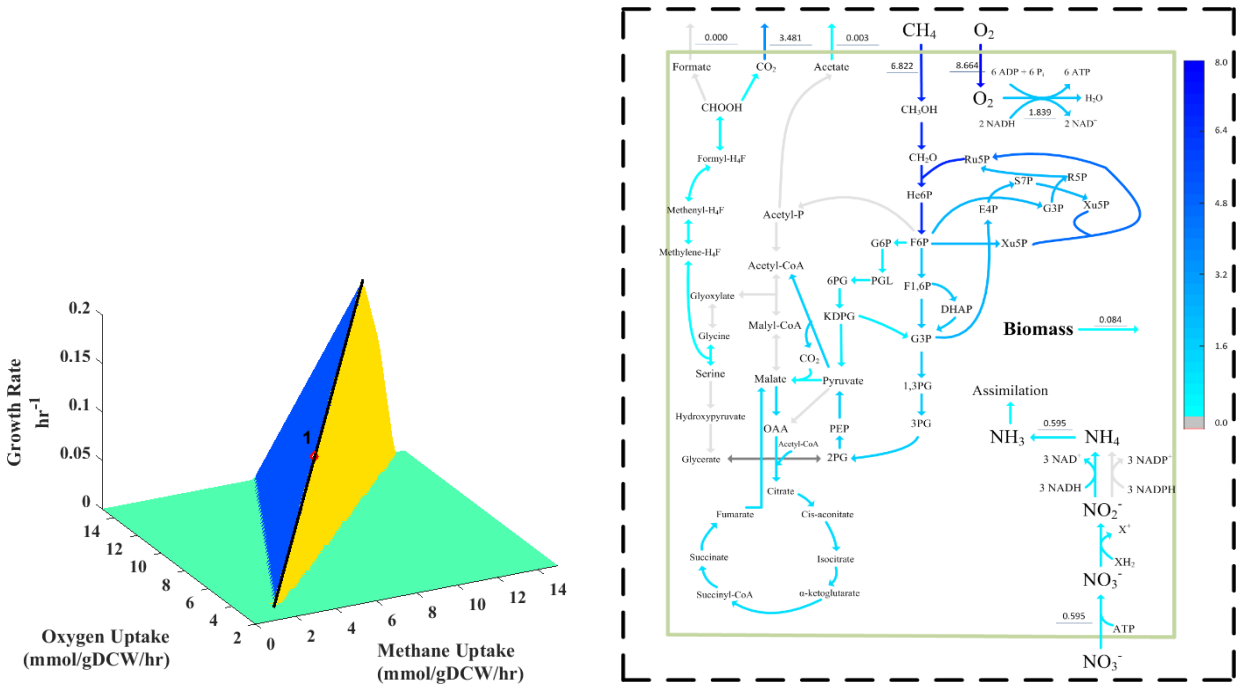

(a) (b)

Figure B6: (a) 3D PhPP diagram with NGAM set to 10.6 mmolATP/(gDCW·hr). The black line separating the blue and yellow phenotype phases represents the line of optimality (LO). The experimental methane and oxygen uptake rates as well as the growth rate for CE1-1 are plotted on the diagram (red circle), which lies on the LO. (b) Model predicted fluxes for the model's central carbon network (CCN) for CE1-1.

To further examine the distribution of the intracellular fluxes and validate the modified GEM, Figure B6 (b) plots the model predicted fluxes in the central carbon network (CCN) for condition 1. Figure B6 (b) shows that under optimal aerobic growth, *M. buryatense* 5GB1 operates a complete oxidative TCA cycle, which agrees with the experimental findings obtained through ^{13}C tracer analysis [13]. In addition, the model predictions suggest that about 85% of malate was produced from fumarate through the TCA cycle, while about 15% was produced from pyruvate through the malic enzyme. This trend in general agrees with the experimental finding which reported that about 46% of malate was produced from fumarate [13]. Finally, as shown in Figure

B6(b), the model prediction shows that the entry step of the serine cycle, *i.e.*, converting glyoxylate into glycine, and serine into hydroxypyruvate, are not active, which again agrees with experimental findings through ^{13}C tracer analysis [13]. Together, these results suggest that the modified GEM can capture the optimal aerobic growth of *M. buryatense* 5GB1 reasonably well, which offers confidence in the PhPP analysis results, and enables us to use the model to examine further intracellular details.

3.3.2 Analysis of the 6 growth conditions using PhPP

The 2D PhPP results, obtained by projecting the 3D PhPP plot onto the 2D plane defined by the CH_4 and O_2 uptake fluxes, are plotted in Figure B7 (a) - (d), corresponding to the oxygen-limited and methane-limited conditions for CE1 and CE2. The results plotted in Figure B7 (a) were generated with NGAM=10.60 mmolATP/(gDCW·hr), Figure B7 (b) with NGAM=15.53 mmolATP/(gDCW·hr), Figure B7 (c) with NGAM=9.88 mmolATP/(gDCW·hr) and Figure B7 (d) with NGAM=10.93 mmolATP/(gDCW·hr). The NGAM values used for modeling were derived from experimental data as described in section 2.8. It is worth noting that the NGAM value used in the model only affects the intercept of the LO without changing the slope of the LO, so the LO in Figure B7 (a) – (d) are parallel to each other. Specifically, the LO obtained for methane-limited conditions has a larger intercept than that of oxygen-limited conditions, as more ATP is needed to maintain the cellular functionality, therefore more O_2 is required to achieve optimal growth. At the same time, because neither LO crosses the origin, the O_2:CH_4 uptake ratio along the LO is not a constant. Instead, it decreases as the CH_4 uptake increases, and the optimal O_2:CH_4 uptake ratio ranges from 1.25 to 1.31 for the tested experimental conditions. This range agrees with the O_2:CH_4 uptake ratio observed in the batch experiments as well (1.23-1.35).

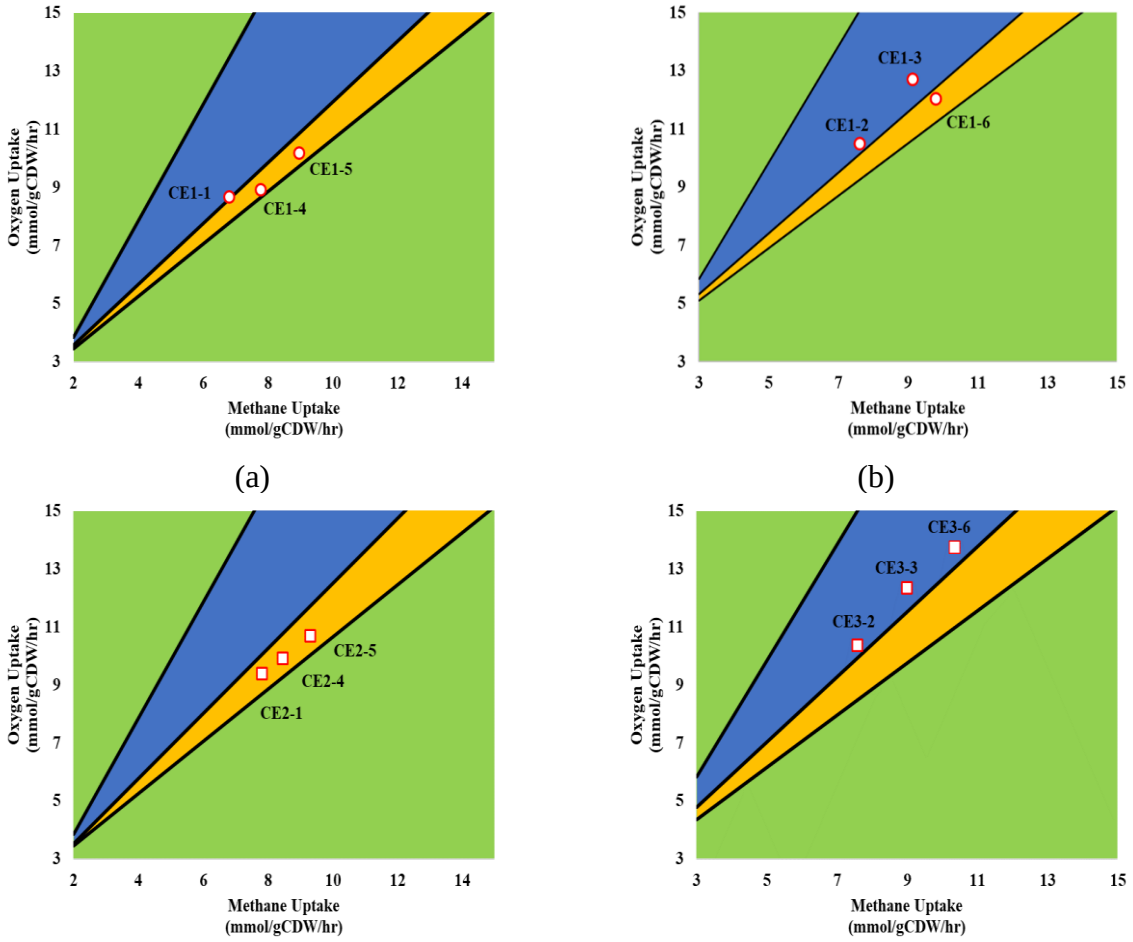

Figure B7: (a) 2D PhPP diagram for NGAM set to 10.6 mmolATP/(gDCW·hr). Experimental data for oxygen-limited conditions CE1-1, CE1-4, CE1-5 are plotted in red circles (b) 2D PhPP diagram for NGAM set to 15.53 mmolATP/(gDCW·hr). Experimental data for methane-limited conditions CE1-2, CE1-3, CE1-6 are plotted in red circles. (c) 2D PhPP diagram for NGAM set to 9.88 mmolATP/(gDCW·hr). Experimental data for oxygen-limited conditions CE2-1, CE2-4, CE2-5 are plotted in red squares. (d) 2D PhPP diagram for NGAM set to 10.93 mmolATP/(gDCW·hr). Experimental data for methane-limited conditions CE2-2, CE2-3, CE2-6 are plotted in red squares.

In Figure B7 (a), it can be seen that condition CE1-1 falls on the LO not in the oxygen-limited phenotype as expected, while in Figure B7 (b) CE1-6 falls in the oxygen-limited phenotype. As discussed previously, we believe such "mis-registered" phenotypes for conditions CE-1 and CE-6 could be attributed to the cells' prior growth conditions. For condition CE1-1 which followed batch

mode where cells grew optimally, cells exhibited optimal growth under the oxygen-limited feed gas composition; for condition CE1-6, which followed two oxygen-limited phenotypes (conditions 4 &5), cells did not pick up the extra oxygen provided in the feed gas and remained in the oxygen-limited phenotype while under methane-limited gas composition. It is important to note that the dissolved oxygen for condition CE1-6 was higher than 8%, which was consistent with conditions CE1-2 & CE1-3 where dissolved oxygen was about 7%, indicating that excessive amount of oxygen was available but the cells did not pick it up.

To confirm that the cells' prior growth condition has a noticeable effect on their current physiological state, we conducted an additional continuous run to test all 6 conditions in a different order, 2→3→6→5→4→1. The 6 conditions tested in CE2 are denoted CE2-1, CE2-2, CE2-3, CE2-4, CE2-5, and CE2-6. The results from this experiment are plotted in Fig. 7 (c) and (d) which further supports our hypothesis that the previous condition affects the growth phenotype of the current condition. More specifically, if we compare CE1-6 with CE2-6, we note that since CE1-6 followed CE1-5 (oxygen-limited), CE1-6 actually falls in the oxygen-limited phenotype; however, CE2-6 which followed CE2-3 (methane-limited) falls in the methane-limited phenotype as expected. It is worth noting that as each growth condition was only maintained for 3 to 4 days in this work, it is possible that the substrate uptake rates could change after prolonged culture under each condition.

3.3.5 The current GEM lacks key metabolic routes to maintain near-optimal growth under oxygen-limited and methane-limited phenotypes

To further examine the validity of the modified GEM, as well as to gain a better understanding of the methane-limited and oxygen-limited phenotypes, we compared the model predicted cell growth rate and CO_2 production rates for all six conditions with experimental measurements from CE1. Two *in silico* experimental setups were considered. In Setup I, only the measured CH_4 uptake

rate was used as the model input, while the O_2 uptake rate was determined via FBA by maximizing cell growth rate. In other words, simulation Setup I would result in a point located on the LO corresponding to the given CH_4 uptake on the 2D PhPP plot. In Setup II, both measured CH_4 and O_2 uptake rates were used as the model inputs. Figure B8 compares the *in silico* results (Setup I and II) with the experimental measurements for all six conditions, with cell growth rate in Figure B8 (a) and CO_2 production in Figure B8 (b). For FBA, the NGAM value was set to 10.6 and 15.53 mmolATP/(gDCW·hr) for the oxygen-limited and methane-limited phenotypes, respectively.

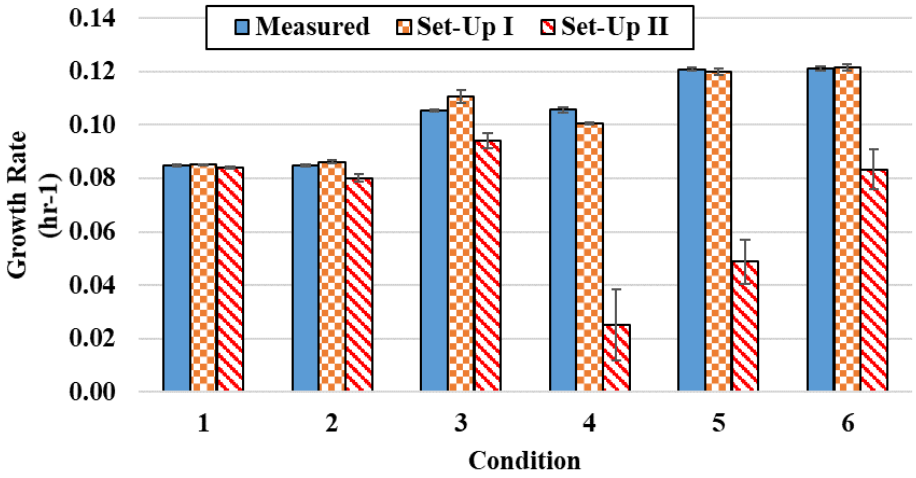

(a)

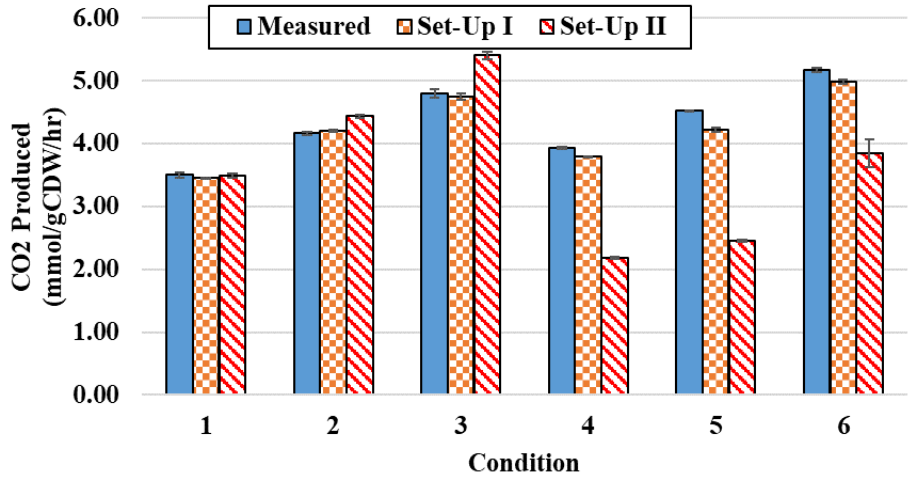

(b)

Figure B8: (a) Growth rate comparison for all six conditions using three different modeling approaches. NGAM set to 10.6 and 15.53 mmolATP/(gDCW·hr) for oxygen-limited and

methane-limited conditions, respectively. (b) Model predicted vs measured CO_2 production.

The *in silico* results show that across all six conditions, cells' actual growth rates were very close to the model predictions obtained in Setup I, *i.e.*, the maximum growth rate predicted by the LO for the given experimental CH_4 uptake rates. This result suggests that *M. buryatense* 5GB1 is extremely robust and capable of maintaining near-optimal growth under a wide range of oxygen availabilities.

However, under Setup II, where both measured CH_4 and O_2 uptake rates were used as model inputs, the model predicted cell growth rates are slightly lower than the experimental measurements for methane-limited phenotypes (condition 2 and 3), but significantly lower for oxygen-limited phenotypes (conditions 4, 5 and 6). For methane-limited growth phenotypes (conditions 2 and 3), the reduced cell growth rate predicted in Setup II is coupled with increased CO_2 production. Further analysis showed the model processes the increasing amount of O_2 through oxidative phosphorylation, and the increasing amount of electrons needed for phosphorylation is produced by increasing flux through TCA cycle. Such changes cause decreased flux to biomass and increased flux to CO_2. In addition, the model dissipates the excess amount of ATP produced through oxidative phosphorylation by uptaking and excreting metal ions (Cu^{2+}) because metal ion uptake consumes ATP while excretion does not. For the oxygen-limited phenotype, the reduced growth rate predicted by the model is coupled with significantly reduced CO_2 production as well. Further analysis shows that the GEM handles the reduced O_2 uptake by reducing flux through oxidative phosphorylation, which in turn causes the reduced flux through TCA cycle driven by the reduced demand of electrons. To cope with the reduced ATP production due to reduced oxidative phosphorylation, the model uses acetate production as the major route for ATP generation to support cell growth. The diversion of carbon leads to reduced biomass production as well as

significantly reduced CO_2 production. For example, the predicted acetate production accounted for about 40% of the CH_4 consumed by the model for condition CE1-4. It is worth mentioning that although acetate production was not observed in our experiments, it has been reported that under prolonged O_2-starvation in a closed vial, 10-fold increase of excreted acetate was observed [12]. However, even a 10-fold increase in acetate production is still far less than the flux predicted by the model.

This discrepancy between model prediction (Setup II) and experimental measurement suggests that the current model lacks key metabolic routes that the cells possess to handle a wide range of oxygen availability. As a result, the model predicts significantly reduced cell growth when the cells uptake excess or insufficient amounts of O_2 required for aerobic respiration, and the model cannot predict the near-optimal growth observed in the experiments.

Conclusion

To successfully deploy methanotrophs for industrial scale methane conversions, additional genetic and environmental manipulations are needed to significantly improve the conversion, yield and throughput. It has been well-recognized that a clear understanding on the strain's cellular metabolism and different growth phenotypes would offer insight and guidance for such manipulations. In this work, using *M. buryatense* 5GB1, a promising industrial methanotroph, as the model system, we use both batch and continuous cultures to investigate the differences between methane-limited growth vs oxygen-limited growth phenotypes. In addition, a reduced genome-scale metabolic model (GEM) is utilized to help understand the intracellular details of the two different phenotypes and for testing a hypothesis that could explain the experimental observations. As most obligate and facultative aerobic microbes produce various bio-products under oxygen-limited conditions, it is natural to expect that *M. buryatense* 5GB1 would produce more organic

compounds under oxygen-limited conditions. Indeed, among all published research on *M. buryatense* 5GB1, reducing oxygen supply in the feed gas has been used to induce an oxygen-limited, fermentative phenotype with the aim to shift carbon flux away from biomass production to desired organic compound production. In this work, using designed batch experiments with accurate gas phase measurements and control, we show that the cell growth rate is primarily determined by the concentration or partial pressure of oxygen in the gas phase, instead of the CH_4:O_2 ratio. In addition, cell growth rate must be controlled in order to drive the cells into different growth phenotypes. Using continuous culture, we were able to achieve both methane-limited and oxygen-limited growth phenotypes through manipulating feed gas composition while controlling cell growth rate; however, we found that even feed gas composition combined with cell growth rate cannot fully determine cells' growth phenotype, as their prior growth phenotype also has a significant impact on their current physiology. In addition, our results indicate that contrary to the common belief, it is the methane-limited condition, instead of oxygen-limited condition, that diverts more carbon flow towards organic compounds from biomass production. Additional research is needed to examine methane-limited conditions for potential chemical production through methane bioconversion.

To better understand the difference between methane-limited and oxygen-limited phenotypes, we use a modified GEM of *M. buryatense* 5GB1 to further examine our experimental findings. We first investigated the model performance along the line of optimality (LO) using our experiments, as well as the flux and transcriptomic data published in the literature. Next, using continuous experiments, we confirmed that *M. buryatense* 5GB1 exhibits surprisingly robust, near-optimal growth under a wide range of CH_4:O_2 uptake ratios. Such behavior cannot be predicted by the

modified GEM, suggesting that the strain has other routes not captured by the GEM to handle excess or insufficient amounts of oxygen to maintain near-optimal growth.

Author Contributions

JW and QH conceived the idea, lead the experimental design, wrote the initial draft and revised the manuscript. KS, MH and KB participated in the experimental design; KS carried out the batch experiments; KB, KS and AB carried out the continuous experiment. MH and KB carried out the *in silico* experiments. MH, KB and JW did the data analyses, QH did all the statistical analyses. MH, KB participated in manuscript revision. KS, MH, KB, AB, QH and JW read and approved the final manuscript.

Declaration of interests

The authors declare that they have no known competing financial interests or personal relationships that could have appeared to influence the work reported in this paper.

Acknowledgements

This material is based upon work supported by the U.S. Department of Energy, Office of Science, Office of Biological and Environmental Research, Genomic Science Program under Award Number DE-SC0019181 (for QH and JW); and by the U.S. Department of Education, Graduate Assistance in Areas of National Need Program under Award Number P200A150074 (for KS and MH). The authors gratefully acknowledge Dr. Mary Lidstrom for providing the strain and invaluable feedback on our draft. The authors also gratefully acknowledge Dr. Marina Kalyuzhnaya for providing the modified GEM of the strain.

References:

[1] P. Forster, P. Artaxo, D. Lowe, G. Raga, G. Bodeker, D. Etheridge, S. Kinne, D. Oram, N. Ramankutty, S. Solanki, R. Wang, Changes in Atmospheric Consituents and in Radiative Forcing, in: Clim. Chang. 2007. Phys. Sci. Basis, 2007.

[2] T. Dong, Q. Fei, M. Genelot, H. Smith, L.M.L. Laurens, M.J. Watson, P.T. Pienkos, A novel integrated biorefinery process for diesel fuel blendstock production using lipids from the methanotroph, Methylomicrobium buryatense, Energy Convers. Manag. 140 (2017) 62–70. https://doi.org/10.1016/J.ENCONMAN.2017.02.075.

[3] R.J. Conrado, R. Gonzalez, Envisioning the bioconversion of methane to liquid fuels, Science 343 (2014) 621–623. http://www.sciencemag.org/content/343/6171/621.short.

[4] K.A. Stone, M. V Hilliard, Q.P. He, J. Wang, A Mini Review on Bioreactor Configurations and Gas Transfer Enhancements for Biochemical Methane Conversion, Biochem. Eng. J. 107 (2017) 52–60.

[5] P. Strong, B. Laycock, S. Mahamud, P. Jensen, P. Lant, G. Tyson, S. Pratt, The Opportunity for High-Performance Biomaterials from Methane, Microorganisms. 4 (2016) 11. https://doi.org/10.3390/microorganisms4010011.

[6] O.K. Lee, D.H. Hur, D.T.N. Nguyen, E.Y. Lee, Metabolic engineering of methanotrophs and its application to production of chemicals and biofuels from methane, Biofuels, Bioprod. Biorefining. 10 (2016) 848–863. https://doi.org/10.1002/bbb.1678.

[7] P.J. Strong, M. Kalyuzhnaya, J. Silverman, W.P. Clarke, A methanotroph-based biorefinery: potential scenarios for generating multiple products from a single fermentation, Bioresour. Technol. 215 (2016) 314–323.

[8] A. Gilman, L.M. Laurens, A.W. Puri, F. Chu, P.T. Pienkos, M.E. Lidstrom, Bioreactor performance parameters for an industrially-promising methanotroph Methylomicrobium buryatense 5GB1, Microb. Cell Fact. 14 (2015) 1. http://microbialcellfactories.biomedcentral.com/articles/10.1186/s12934-015-0372-8.

[9] A. Torre, A. Metivier, F. Chu, L.M.L. Laurens, D.A.C. Beck, P.T. Pienkos, M.E. Lidstrom, M.G. Kalyuzhnaya, Genome-scale metabolic reconstructions and theoretical investigation of methane conversion in Methylomicrobium buryatense strain 5G (B1), Microb. Cell Fact. 14 (2015) 1.

[10] A.W. Puri, S. Owen, F. Chu, T. Chavkin, D.A.C. Beck, M.G. Kalyuzhnaya, M.E. Lidstrom, Genetic tools for the industrially promising methanotroph Methylomicrobium buryatense, Appl. Environ. Microbiol. 81 (2015) 1775–1781. http://aem.asm.org/content/81/5/1775.short.

[11] C.A. Henard, H. Smith, N. Dowe, M.G. Kalyuzhnaya, P.T. Pienkos, M.T. Guarnieri, Bioconversion of methane to lactate by an obligate methanotrophic bacterium, Sci. Rep. 6 (2016) 21585.

[12] A. Gilman, Y. Fu, M. Hendershott, F. Chu, A.W. Puri, A.L. Smith, M. Pesesky, R. Lieberman, D.A.C. Beck, M.E. Lidstrom, Oxygen-limited metabolism in the methanotroph *Methylomicrobium buryatense* 5GB1C, PeerJ. 5 (2017) e3945. https://doi.org/10.7717/peerj.3945.

[13] Y. Fu, Y. Li, M. Lidstrom, The oxidative TCA cycle operates during methanotrophic growth of the Type I methanotroph Methylomicrobium buryatense 5GB1, Metab. Eng. 42 (2017) 43–51. https://doi.org/10.1016/J.YMBEN.2017.05.003.

[14] K.A. Stone, Q.P. He, J. Wang, Two Experimental Protocols for Accurate Measurement of Gas Component Uptake and Production Rates in Bioconversion Processes, Sci. Rep. 9 (2019) 5899. https://doi.org/10.1038/s41598-019-42469-3.

[15] A. Bakker, J. Smith, K. Myers, How to Disperse Gases in Liquids, Chem. Eng. 101 (1994) 98.

[16] J. Schellenberger, R. Que, R.M.T. Fleming, I. Thiele, J.D. Orth, A.M. Feist, D.C. Zielinski, A. Bordbar, N.E. Lewis, S. Rahmanian, others, Quantitative prediction of cellular metabolism with constraint-based models: the COBRA Toolbox v2. 0, Nat. Protoc. 6 (2011) 1290–1307. http://www.nature.com/nprot/journal/v6/n9/abs/nprot.2011.308.html.
[17] I.R. Akberdin, M. Thompson, R. Hamilton, N. Desai, D. Alexander, C.A. Henard, M.T. Guarnieri, M.G. Kalyuzhnaya, Methane utilization in Methylomicrobium alcaliphilum 20Z R: a systems approach, Sci. Rep. 8 (2018) 2512.
[18] P.J. Strong, S. Xie, W.P. Clarke, Methane as a Resource: Can the Methanotrophs Add Value?, Environ. Sci. Technol. 49 (2015) 4001–4018.
[19] J.S. Edwards, R. Ramakrishna, B.O. Palsson, Characterizing the metabolic phenotype: a phenotype phase plane analysis, Biotechnol. Bioeng. 77 (2002) 27–36.